VRIJE UNIVERSITEIT

Chemistry in Water

First Principles Computer Simulations

ACADEMISCH PROEFSCHRIFT

ter verkrijging van de graad van doctor aan
de Vrije Universiteit Amsterdam,
op gezag van de rector magnificus
prof.dr. T. Sminia,
in het openbaar te verdedigen
ten overstaan van de promotiecommissie
van de faculteit der Exacte Wetenschappen
op dinsdag 7 januari 2003 om 10.45 uur
in de aula van de universiteit
De Boelelaan 1105

door

Berend Ensing

geboren te Delfzijl

promotor: prof.dr. E.J. Baerends

Chemistry in Water

First Principles Computer Simulations

Bernd Ensing

Beoordelingscommissie:

prof.dr. W.J. Briels
prof.dr. M. Sprik
dr. F. Buda
dr. E.J. Meijer
dr. M.C.M. Gribnau

Het promotieonderzoek beschreven in dit proefschrift werd financieel mogelijk gemaakt door de stichting Chemische Wetenschappen (NWO/CW) in het kader van het Prioriteits Programma Materialen–Computational Material Science (PPM–CMS).

I think computer viruses should count as life. I think it says something about human nature that the only form of life we have created so far is purely destructive. We've created life in our own image.

Stephen Hawking

Contents

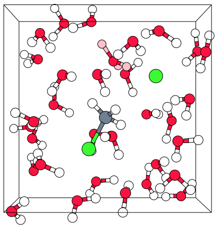

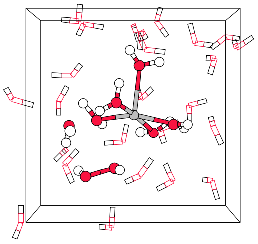

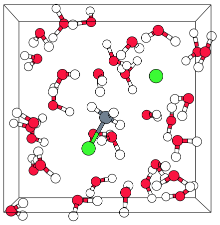

Chapter 1

Introduction

1.1 Chemistry in water

Water is one of the most plentiful and essential of compounds, which is vital to life, participating in virtually every process that occurs in plants and animals. In fact, life is believed to have originated in the worlds complex brews, the oceans. It is no wonder, that due to its prominence, water has long played an important religious and philosophical role in human history. The Chinese alchemist Tsou Yen (3$^{\text{rd}}$ century BC) placed water among the five divine elements (together with fire, earth, wood and metal) that make up the universe. And the Greek Thales of Miletus (6$^{\text{th}}$ century BC) regarded water as the sole fundamental building block of matter:

> It is water that, in taking different forms, constitutes the earth, atmosphere, sky, mountains, gods and men, beast and birds, grass and trees, and animals down to worms, flies and ants. All these are different forms of water. Meditate on water!

The great Aristotle included water among the four elements alongside earth, air and fire, which belief persisted for more than 2000 years until experiments in the second half of the 18$^{\text{th}}$ century showed that water is a compound made up of the elements hydrogen and oxygen. Unfortunately, nowadays practically none of us sees anymore the magic in such things as our planet being covered with oceans of liquid water, in solid rocks of ice floating on water, in sugar cubes disappearing in water whereas milk blends with water (not to mention the behavior of tea leaves in water), in clouds of water flying in the air or even in its beautiful appearance in a rainbow and in the water crystals in snowflakes. Yet, especially in the eyes of physicists and chemists, water is an extraordinary substance with very unique properties. For example, its boiling point of 100° C is nearly 200° C higher than would be expected by comparison with other molecules as small as the water molecule. The secret behind the unexpected properties of water lies in the electronic structure of the oxygen atom and the two hydrogen atoms which make up the bent water molecule (H_2O), as shown in figure 1.1. It causes the hydrogens to carry each a positive charge of about one third of an electron and the oxygen a negative charge of about two thirds on an electron, inducing a significant dipole moment in the water molecule. The

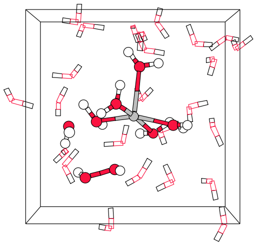

Figure 1.1: *In liquid and solid water (ice), the* H_2O *molecules form so-called hydrogen bonds between the partially positive hydrogen atoms (H) and partially negative oxygen atoms (O), forming a relatively strong tetrahedral network.*

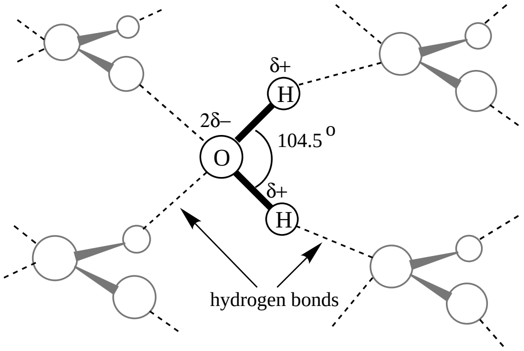

electronegative oxygen atom has two non-bonding electron pairs that attract hydrogens from adjacent water molecules, so that the water molecule associates strongly. The weak bonds that are this way formed between them, are called hydrogen bonds, which are also known to be responsible for the double helix shape of DNA, the working of soap, and the perfect mixing of ethanol and water, giving rise to the best mindboggling beverages known to man. In an ice crystal, the water molecules are tetrahedrally surrounded by neighbors and form an open highly ordered three-dimensional network of hydrogen bonds. The formed tetrahedrons give rise to puckered hexagonal rings of water molecules, which are responsible for the hexagonal symmetry of the ice crystals, *e.g.* in snowflakes. When the ice melts, the highly order structure breaks down and the molecules pack more closely together. This makes liquid water denser than ice which is why the solid floats on the liquid; another highly unusual property of water. However, also in the liquid, hydrogen bonding remains the important associative force, responsible for the unusually high values for the boiling point, the surface tension, the heat and entropy of vaporization and the viscosity, given the low molar mass of H_2O.

One of the most important properties of water is its ability to dissolve ionic and polar chemicals to form aqueous solutions. From ponts till oceans, the water masses contain a vast number of dissolved substances, which are vital to life. Moreover, in living organisms, water enables the transport of nutrients and trace elements. The solvation of compounds involves complex rearrangements in the solvent environment of the compound (*i.e.* the solvation shell), in which again the polar nature of the water molecule and the hydrogen bond making and breaking play the essential roles. The structure and dynamics in these solvation shells are closely connected to the way in which chemical reactions in water take place. For instance, many reactions only occur after water molecules have been removed from the solvation shells. Other examples are acid catalyzed reactions and radical reactions in aqueous solution, in which respectively protons and hydroxyl radicals rapidly move along hydrogen bond wires through the solvent by passing on hydrogens from water molecule to molecule. Still, the dynamic solvent effects and the versatile

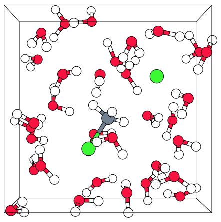

role of water in chemical reactions are poorly understood on a microscopic level, which complicates the understanding of biological processes and slows down the development of environmentally friendly industrial applications. This thesis is perhaps not likely to bring back any of the magic around the special behavior of water, but, no doubt, insight and understanding is gained of its involvement in chemistry.

1.2 Theoretical chemistry

If it were not for the too long wavelengths of visible light,[1] we could see through a microscope the chemical building blocks of all matter: atoms. At a magnification of twenty five million times, the smallest atom, hydrogen, would still seem to be about only one millimeter in size. Although, the word atom comes from the Greek word *atomos*, which means unbreakable[2], atoms are actually separable into a relatively small core with a positive charge and a cloud of negatively charged electrons, surrounding the core. In classical mechanics, a moving body with an electric charge (such as an electron) loses kinetic energy by radiating an electro-magnetic field. For an atom, this would imply that an electron flying around the core would be doomed to spiral down into a crash landing onto the core. That this apparently does not happen in reality is a quantum mechanical effect: the remarkable behavior of the electron around the core is in a way similar to a standing wave in a guitar string. The wave pattern of nodes and anti-nodes for an electron is called an orbital; it reflects the space in which the electron moves. According to quantum mechanical laws, one orbital can contain up to two electrons with opposite values for the quantum number s, called electron spin. The orbitals for an atom are classified in shells, with a principle quantum number n, and the orbitals in one shell can again be divided into sub-shells, each with a so-called angular momentum quantum numbers l and a magnetic quantum number m_l. From this buildup of the electrons, each with its unique set of the four quantum numbers $\{n, l, m_l, s\}$, *i.e.* from the electronic structure, the properties of the different atoms can be understood. The development of accurate quantum mechanical models and computer programs to calculate and understand the electronic structure and its derivable physical properties is one of the most important achievements in theoretical chemistry, for which John A. Pople and Walter Kohn were rewarded with the Nobel prize for chemistry in 1998.

In general, electrons prefer to group together as much as possible into completely filled orbitals, sub-shells and shells, because such configurations have the lowest energy. Consider for example, the first shell ($n = 1$), which has only one sub-shell, with only one orbital, so that it can contain just two electrons. For a hydrogen atom, which has only one electron, the first shell is thus half-filled. It can, however, lower its energy by sharing its electron with another hydrogen atom. Together, the atoms form a molecule by shaping a new (molecular) orbital, completely filled by the two electrons. The electrons shared by the atoms form a chemical bond. The energy release by this bond formation is significant;

---

[1] the shortest visible wavelength is about $390 \cdot 10^{-9}$ m (violet light), which is still more than 1000 times larger than the largest atom — instead of being reflected by a single atom, visible light oscillates around it

[2] *a* meaning "not" and *tomos* meaning "to cut", already proposed for the smallest thinkable particles about 440 BC, by the Greek philosopher Leucippus of Miletus and his pupil Democritos

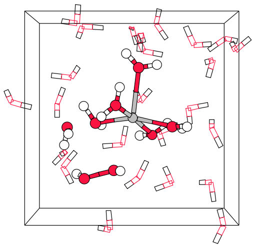

a 60 Watt light bulb could burn for one hour from the energy that would come free if we would have only one gram of hydrogen atoms transforming into hydrogen molecules. On the other hand, in helium, which has two electrons, the first shell is already completely filled so that it cannot further lower its energy by forming chemical bonds. Helium, and the other inert gasses (neon, argon, krypton, xenon and radon) are the only atoms with completely filled shells, which are therefore found as such in nature. All other atoms, are usually only found in nature to be chemically bound to other atoms, forming molecules, metals or crystals.

The relative stability of a molecule is given by its energy of formation (also: minus the atomization energy), which is the energy that would come free if the molecule is formed from bare atoms. In a chemical reaction, the atoms in one or more molecules (the reactants) regroup to form one or more new molecules (the products). The reaction energy is simply the difference between the energies of formation of the products and reactants. At room temperature, most chemical reactants are activated, *i.e.* one first has to inject energy into the reactants in order to start the chemical reaction, even if the reaction energy is negative. The existence of such energy barriers is actually very fortunate, and if they would suddenly disappear, this theses, for instance, would instantaneously react explosively with oxygen in the air to form carbon dioxide and water vapor, before you could reach to the scientific juicy parts — and that would have been even the least of your problems. For most chemical reactions between molecules in the gas-phase, the reaction rate constant, k, depends exponentially on the absolute temperature, T, as reflected by the well-known Arrhenius equation:

$$k = A \cdot e^{-E_a/RT} \tag{1.1}$$

Here, R is the universal gas constant, E_a is the activation energy and A is a pre-exponential factor whose dependence on the temperature is usually neglected. Within collision theory, this empirical equation is rationalized as the product of the (Boltzmann) fraction of collisions between the molecules with enough energy to react ($\propto e^{-E_a/RT}$) and A, which is related to the total number of collisions in the gas per second and the reactive cross section (*i.e.* the probability that the reactants have the required orientation to react). Alternatively, the activation energy, E_a, can be associated to the energetically most unfavorable geometric configuration, the so called transition state, which the reactants have to surpass when they transform into products. Now, the Boltzmann factor reflects the probability to find the system in the transition state, and A is a frequency factor connected to the decay of the transition state into products. The latter interpretation justifies Arrhenius-type reaction rates of reactions in solution, in which case the reactants do not actually collide at high velocities. Equation 1.1 predicts that storing meat in a refrigerator will slow down rotting processes and heating up an egg speeds up the chemical reaction that makes it solid. We can also understand that the addition of an extra chemical that stabilizes the transition state (*i.e.* a catalyst), thus lowering the activation energy, will speed up the chemical reaction. And finally, we see that the reaction rate of a specific reaction in solution will change when this reaction is performed in the gas phase or in another solvent, because the parameters A and E_a are dependent on the reaction environment.

Of course, we want to answer the ultimate question about life, the universe and everything from first principles by computer simulation [1]. For gas phase reactions, one

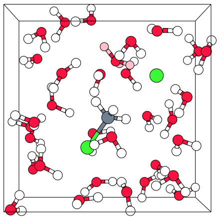

can nowadays calculate the structure of the reacting molecules along a reaction path together with the reaction and activation energies with only a few mouseclicks. Entropic contributions (in equation 1.1 concealed in A) can be estimated with a sum over states after calculating the molecular vibrations. For chemical reactions in solution however, computer simulation is a bit more involved. For instance, embedding the reactants by a few spheres of solvent molecules would hardly mimic the liquid after optimizing the geometry and also the calculation of the vibrations would become horribly cumbersome. Instead, one needs to sample over many solvent configurations, either stochastically within a Monte Carlo simulation or deterministic using molecular dynamics. The advantage of the latter is that it can also be used to study the reaction dynamics. And last but not least, the molecular dynamics trajectories can by visualized in illustrative movies, offering a realistic impression of the motions of the chemical building blocks which we can never see in reality, not even with the best microscope. Two examples of such visualizations, are found in the bottom corner of this thesis by rapidly flipping the pages, showing two chemical reactions in water (see also the caption on the last pages of this thesis).

1.3 Our model

The method of choice for the title study, *Chemistry in Water*, is the Car-Parrinello molecular dynamics (CPMD) simulation technique. CPMD embodies, in an efficient algorithm, the evaluation of the classical Newtonian equations of motion for the molecular dynamics with, simultaneously, the quantum mechanical calculation of the electronic structure, using density functional theory (DFT). The atomic interactions during the molecular dynamics are obtained from the electronic structure calculation, instead of from empirical forcefields, so that the CPMD method is commonly seen as an *ab initio* molecular dynamics method (AIMD).

The advantages of AIMD for our application are numerous, of which most importantly: 1) the molecular forcefield is obtained from first principles which makes it possible to simulate chemical reactions within molecular dynamics; 2) therefore, we have access to the electronic structure during the molecular dynamics, from which the chemistry can be understood; 3) the solvent effect on chemical reactions is included from the dynamics of explicit solvent molecules (in contrast to *e.g.* Langevin equation methods and polarizable continuum models), so that solvent behavior, such as changes in the hydrogen bonded network, during chemistry can be studied; 4) additional molecular dynamics techniques, such as periodic boundary conditions and thermostats, realistically mimic the bulk solvent, which carries the inclusion of solvent effects beyond those of microsolvation and cluster studies.

However, models are by definition not perfect. Important approximations in our model originate in the first place from the accuracy of the molecular interactions, which is dictated by the limits of DFT. Particularly, current electron exchange and correlation functionals are still under development and several cases are known where DFT fails. We will leave the construction of improved functionals to others, and use the established Becke-Perdew gradient corrected functional throughout our studies, as it has proven to be very reliable for predicting energies and geometries of molecules, condensed phase

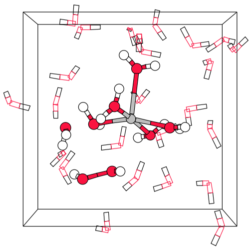

systems and transition metal complexes. Secondly, the computational demands of AIMD are very high, which limits the system size to 10-1000 atoms or equivalently, 30-3000 valence electrons and the trajectory lengths to 10-100 picoseconds. This is just enough to include the first and second solvation shells of solutes in water, but approximations have to be made on the long-range interactions. Other approximation of minor significance are 3) the neglect of quantum mechanical effects in the classical molecular dynamics, such as tunneling and zero-point motions; 4) the frozen core approximation; 5) neglect of relativistic effects; 6) the Born Oppenheimer approximation (*i.e.* the electron subsystem follows the nuclei adiabatically and always remains in the ground level) and 7) the neglect of pressure effects as the simulations are performed in the canonical ensemble. A large part of the work has therefore been dedicated to severe testing and critical comparison of our model to other methods and literature; only a small part of which is found back in this thesis. Nevertheless, AIMD is hands down the best method for the job, and this thesis gives a clear impression of the state-of-the-art on computer simulations of chemical reactions in the condensed phase.

1.4 This thesis

This thesis is about the study of chemical reactions in water without getting our hands wet. Solvent effects can have a very large influence on the thermodynamics and the kinetics of chemical reactions in water, but are usually poorly described or even neglected completely in theoretical models. Moreover, the understanding of solvation shell dynamics and solvent effects on chemistry on a microscopic level is in general still rather poor. Having said that, we will continue in the next chapter with the introduction of the techniques applied for our study. In particular, A) the Car-Parrinello technique which efficiently solves the problem of following the motions of the nuclei while simultaneously updating the electronic structure allowing for the simulation of chemical reactions in the condensed phase and B) the statistical thermodynamics techniques to solve the “rare event” problem of observing the crossing of a chemical reaction barrier whose height is several order of kT with the Car-Parrinello molecular dynamics technique. In chapter 3, we start with the investigation of the solvent effects on a textbook $\mathrm{S_N}2$ reaction. Chemically, this type of reaction is very well understood: the solvent effects are very large, leading to a decrease of the reaction rate of 13 orders of magnitude (!) in aqueous solution with respect to this reaction in the gas phase. We show that we can accurately calculate the solvent-solute interactions and compute the solvent effects on the reaction free energy barrier in aqueous solution. Moreover, we rationalize the strong solvent effects from the structural changes in the solvent during the reaction. After this prototype, yet very instructive, $\mathrm{S_N}2$ reaction, we move on to the study of transition metal catalyzed oxidation reactions in aqueous solution, a short introduction of which is given in chapter 4. In particular, we investigate the solvent effects on the catalyzed activation of hydrogen peroxide by iron(II) in chapter 5 and by iron(III) in chapter 6, also known as Fenton and Fenton-like chemistry, respectively. We show that in these cases the solvent molecules are actively involved in the reaction mechanisms, catalyzing the chemical transformations on the metal complexes via hydrogen and proton abstraction reactions. Spontaneous hydrolysis of the

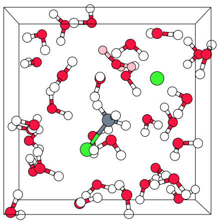

acidic metal complexes is seen to play an important role, again a process which cannot be observed without an accurate incorporation of the aqueous environment. We elucidate the surprisingly different reaction mechanisms for Fenton and Fenton-like chemistry in water and show that in the $\mathrm{Fe^{II}/H_2O_2}$ case the much contested $[\mathrm{Fe^{IV}O}]^{2+}$ ion is the predominant oxidative intermediate and not the hydroxyl radical as is generally believed. Instead, in the $\mathrm{Fe^{III}/H_2O_2}$ case, an $\mathrm{H^+}$ is donated to the solvent to produce the iron(III)hydroperoxo species as the primary intermediate. In these chapters (chapter 5 and 6), we present a number of illuminating and illustrative simulations of the dynamics of the Fenton and the Fenton-like reactions in aqueous solution at room temperature. However, concern is in place with the representativeness of such reactive trajectories, in view of the unphysical geometric constraints applied in the construction of the systems in order to overcome the earlier mentioned rare event problem. Therefore, chapter 7 is devoted to the generation of representative reactive trajectories with no memory of the artificial construction of the system by way of the new transition path sampling technique. In chapter 8, we study the oxidation of methane to methanol by the ferryl ion ($[\mathrm{Fe^{IV}O}]^{2+}$), *i.e.* the active intermediate proposed for the Fenton reaction in chapter 5 and find that again the water environment has a large effect on the chemistry via the hydrophobic interactions with the hydrocarbon species and the solvated metal oxo and hydroxo complexes. Also, we confirm the mechanistic similarities between the organic oxidations by Fenton's reagent and those by such enzymes as MMO (methane mono-oxygenase) and cytochrome P450, as was recently suggested in literature. This thesis ends with a summary (also in Dutch) and acknowledgments to the people who have contributed to this work.

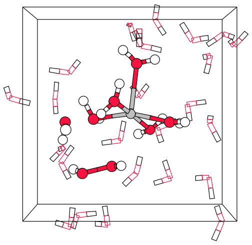

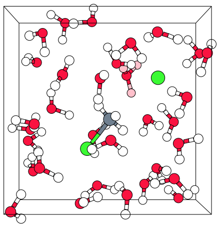

Chapter 2

Techniques

Consider a simple reaction (R $\longleftrightarrow$ P) in solution and the differential expressions for the reaction rate

$$\begin{aligned}
\frac{dc_R}{dt} &= -k_R c_R(t) + k_P c_P(t) \\
\frac{dc_P}{dt} &= k_R c_R(t) - k_P c_P(t) \qquad (2.1)
\end{aligned}$$

where $c_R(t)$ and $c_P(t)$ are the concentrations of the reactant R and the product P at time t and k_R and k_P are the rate constants for the forward and backward reactions, respectively. We assume k to be time independent (*cf.* ref 2 for a discussion of interesting cases for which k is a function of time). Furthermore, we assume that the temperature dependence of the reaction is Arrhenius-like, which means it can be written in the form:

$$k = A(T) \exp\left[-\Delta G^{\ddagger}/RT\right] \quad , \qquad (2.2)$$

$$\frac{\mathrm{d}\ln(k)}{\mathrm{d}(1/T)} \approx -\frac{\Delta H^{\ddagger}}{R} \qquad (2.3)$$

where $\Delta G^{\ddagger}$ and $\Delta H^{\ddagger}$, the activation free energy and activation enthalpy, respectively, are approximately independent of temperature and $A(T)$ is the pre-exponential factor with only a weak temperature dependence. The gas constant is $R = 8.31451$ J K^{-1}mol^{-1}. In the condensed phase, we can distinguish between the relatively strong intramolecular bonds, with bonding energies which are much higher than the energy associated with the thermal motions ($E_{\mathrm{intra}} \gg k_B T$) and the much weaker intermolecular solvent-solvent, solute-solute, and solute-solvent interactions, with binding energies in the order of that of the thermal motions ($E_{\mathrm{inter}} \approx k_B T$). Traditionally, the intramolecular bonds belong to the territory of the quantum chemists as the making and breaking of these bonds (*i.e.* chemistry) is governed by the electronic structure. The weak intermolecular interactions on the other hand, are in the dominion of statistical thermodynamics as these bonds are broken and formed continuously on the time scale of the thermal motions, so that measurements (computations) require averaging over the different configurations of the interacting particles. To appreciate the title study of *Chemistry in water*, in which the estimation of the rate constant k and its dependence of solvent effects belong to the important parameters, some background information is essential on both statistical thermodynamics and

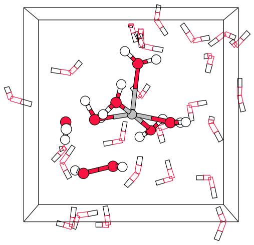

on electronic structure calculations. We will therefore start with elementary statistical thermodynamics in this section and the section hereafter, and then introduce the basics of the electronic structure calculations and the happy marriage of these two fields in the method of Car–Parrinello molecular dynamics in the sections 2.3 and 2.4.

2.1 Statistical thermodynamics

The number of different configurations of positions $\mathbf{r}^N$ and momenta $\mathbf{p}^N$ of N particles in a volume V at an absolute temperature T is for all but the simplest systems mindbogglingly large. In the canonical ensemble (*i.e.* at fixed N,V, and T), the probability P to find the system in some configuration $(\mathbf{r}^N, \mathbf{p}^N)$ depends on the total energy of the configuration given by the Hamiltonian $\mathcal{H}(\mathbf{r}^N, \mathbf{p}^N)$ according to the Boltzmann distribution:

$$P(\mathbf{r}^N, \mathbf{p}^N) = Q^{-1}(h^{3N}N!)^{-1} \exp[-\beta\mathcal{H}(\mathbf{r}^N, \mathbf{p}^N)] \tag{2.4}$$

with $\beta = 1/k_BT$. Boltzmann's constant is $k_B = 1.38066 \cdot 10^{-23}$ J/K and Planck's constant is $h = 6.62618 \cdot 10^{-34}$ J·s. Here, Q is the partition function given by

$$Q = (h^{3N}N!)^{-1} \iint \mathrm{d}\mathbf{r}^N \mathrm{d}\mathbf{p}^N \exp[-\beta\mathcal{H}(\mathbf{r}^N, \mathbf{p}^N)] \tag{2.5}$$

and the parenthesized reciprocal term on the right-hand-side of both equantion 2.4 and 2.5 connects the classical distribution to the quantum mechanical distribution. The macroscopic observable A is obtained by taking the ensemble average (denoted by the use of brackets $\langle \cdots \rangle$) of the microscopic property a,:

$$\langle a \rangle = \frac{\iint \mathrm{d}\mathbf{r}^N \mathrm{d}\mathbf{p}^N a(\mathbf{r}^N, \mathbf{p}^N) \exp[-\beta\mathcal{H}(\mathbf{r}^N, \mathbf{p}^N)]}{\iint \mathrm{d}\mathbf{r}^N \mathrm{d}\mathbf{p}^N \exp[-\beta\mathcal{H}(\mathbf{r}^N, \mathbf{p}^N)]} \tag{2.6}$$

This horrible expression can numerically be evaluated by sampling the configurations either stochastically, using the Monte Carlo method, or deterministically using molecular dynamics (MD). In the latter case, one makes use of the chaotic (ergodic) nature of the dynamics of the system. That is, during a sufficiently long MD simulation, a representative part of all possible configurations will be sampled, so that the time average of property a equals the naturally weighted ensemble average $\langle a \rangle$:

$$\langle a \rangle = \lim_{t\to\infty} \frac{1}{t} \int_0^t \mathrm{d}t' a(\mathbf{r}^N, \mathbf{p}^N) \tag{2.7}$$

An advantage of MD over Monte Carlo is that also dynamical properties can be evaluated. Onsager's regression hypothesis states that slow microscopic fluctuations around equilibrium on average decay according to the macroscopic laws. [3] For example, transport properties such as the diffusion coefficient of some species i, D_i, which is the macroscopic proportionality constant between the flux J_i of the diffusing species i and the gradient of its concentration c_i as given by Fick's law,

$$J_i = -D_i \nabla c_i \tag{2.8}$$

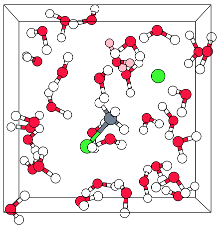

can be calculated from an equilibrium MD trajectory (*i.e.* without inducing a gradient in the concentration) from the microscopic fluctuations in the velocity of the species, when averaged over long enough times τ:

$$D_i = \int_0^\infty \mathrm{d}\tau \, \langle v_i(\tau) v_i(0) \rangle \tag{2.9}$$

Simulation of a chemical reaction and therefore the direct estimation of the rate constant k is in practice not possible using MD or Monte Carlo. The problem is, that for the system to move from the stable reactant state to the stable product state, it has to cross some transition state configuration associated with the relatively high activation energy, $\Delta E^\ddagger \gg k_B T$, of equation 2.2, which has a very low probability of being populated during a simulation, as follows from the exponential dependence in equation 2.4. This dynamical bottleneck makes the chemical reaction a rare event on the time scale of the thermal motions. Fortunately, there are a number of techniques available to circumvent this problem.

2.2 Reaction rate theory

Already in 1940, Hendrik Kramers understood well the mechanism of climbing the reaction barrier in solution as governed by the thermal (Brownian) motions of the solvent. The above mentioned rare event problem did not play a role in the description he used, as the solvent effect was not described by explicit molecules, but rather by Gaussian random fluctuations $f(t)$ and by a linear friction force $-\gamma m \frac{\mathrm{d}x}{\mathrm{d}t}$ working on a reaction coordinate x with a mass m. A one-dimensional asymmetric double-well potential $U(x)$ represents the reactant and product well and the separating barrier along by the reaction coordinate, which enter with the solvent forces Newton's equation of motion of x in the form of a Langevin equation:

$$m\frac{\mathrm{d}^2 x}{\mathrm{d}t^2} = -\frac{\mathrm{d}U(x)}{\mathrm{d}x} - \gamma m \frac{\mathrm{d}x}{\mathrm{d}t} + f(t) \tag{2.10}$$

Here, γ is a constant friction rate, and the fluctuating force $f(t)$ denotes Gaussian white noise with zero mean, which obeys the fluctuation-dissipation relation,

$$\begin{aligned} \langle f(t) \rangle &= 0 \quad , \\ \langle f(t) f(t') \rangle &= 2m\gamma k_B T \delta(t-t') \quad . \end{aligned} \tag{2.11}$$

The delta function in 2.11 ensures instantaneous dissipation, which is known as the Markov property. From the time evolution of the probability density $p(x, v, t)$, expressed in a so-called Fokker-Planck equation, he studied the reactant flux over the barrier for low and high friction γ (also referred to as damping, coupling or viscosity, and related to the diffusion coefficient via Einstein's relation: $\gamma = k_B T/D$). For moderate-to-strong friction he came to the cornerstone result in rate theory for the reaction rate constant [4]:

$$k_R = \frac{1}{\omega_b}\left(-\frac{\gamma}{2} + \sqrt{\frac{\gamma^2}{4} + \omega_b^2}\right)\left\{\frac{\omega_R}{2\pi}\exp\left[-\beta E_b\right]\right\} \tag{2.12}$$

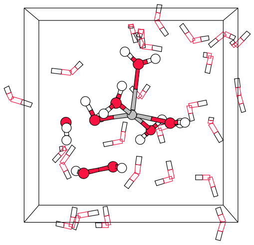

where ω_R and ω_b the frequencies that confine the parabolic reactant well and barrier top respectively, as they are both of the form $U(x) = U(x') - \frac{1}{2}m\omega'(x-x')^2$. In this expression (2.12), the part between the curly brackets gives the transition state theory (TST) result for the reaction rate, so that the expression in front of the curly brackets approximates the correction to the TST result, known as the transmission coefficient $\kappa = k_R/k_{\mathrm{TST}}$, for the moderate-to-strong solvent friction regime.

Transition state theory [5] is based on two assumptions, namely 1) thermodynamic equilibrium must prevail throughout the entire system for all degrees of freedom and 2) any transition pathway starting from the reactant state which crosses the dividing transition state surface will end up in the product state. For strong (over-damped) friction, $\gamma \gg \omega_b$, the expression for the rate constant simplifies to,

$$k_R = \frac{\omega_b}{\gamma}\frac{\omega_R}{2\pi}\exp\left[-\beta E_b\right] \tag{2.13}$$

so that the correction factor to TST, $\kappa = \frac{\omega_b}{\gamma}$ becomes inversely proportional to the solvent friction, and $\kappa \rightarrow 0$ as $\gamma \rightarrow \infty$. From equation 2.12, we can deduce that the transmission coefficient is always smaller than unity for any friction γ larger than zero, and that the transition state theory rate k_{TST} thus provides an upperbound for the true rate. Kramers simulations showed that the second TST assumption does not hold for a reaction which is strongly coupled to the thermal motions of a solvent, because the strong solvent friction forces the reaction coordinate into something like a random walk at the barrier top so that many transition pathways recross and do not end up in the product state. The result is referred to as *spatial-diffusion-controlled rate*.

In the low solvent friction limit, Kramers found

$$k_R = p\gamma\frac{I(E_b^+)}{k_B T}\left\{\frac{\omega_R}{2\pi}\exp\left[-\beta E_b^+\right]\right\} \tag{2.14}$$

where $I(E_b^+)$ is the action at the barrier top in the forward direction, E_b^+ the barrier top energy with respect to the reactant state and p the probability to thermalize in the product well. This probability equals $p = \frac{1}{2}$ for a symmetric double well potential. The transmission coefficient (again the terms in front of the curly brackets) in the small friction regime is thus proportional to the friction and it goes to zero as $\gamma \rightarrow 0$. This friction regime describes the *energy-diffusion-controlled rate*, because the reaction coordinate moving over the barrier top will recross many times from the product state to the reactant state and back before it loses enough energy to the solvent to thermalize in either stable state. At some intermediate friction, there will be a crossover between the spatial-diffusion regime and the energy-diffusion regime, known as Kramers turnover, which is highly system dependent.

Kramers reaction rate theory predicts that the solvent dynamics will always decrease the reaction rate, or that in the most favorable situation no barrier recrossings take place and the rate constant corresponds with that of Rice-Ramsperger-Kassel-Marcus (RRKM) rate theory, which gives the TST rate as a function of the collision rate for independent polyatomic molecules. However, for general realistic applications, Kramers' theory (and RRKM theory) fails when the time scale of barrier crossing (which is of course much faster than $1/k$) is in the same order or even slower than the time scale of the correlations

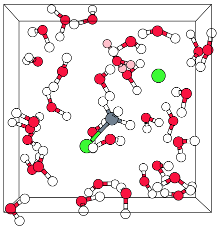

in the random solvent fluctuations. Moreover in RRKM theory, the reacting polyatomic molecules provide there own (infinitely fast) energy sinks, whereas in realistic applications the coupling of the reaction coordinate with these intramolecular modes can be weaker than the coupling (friction) with the solvent. In certain cases, the solvent dynamics can therefore *increase* the reaction rate, as it provides an extra energy dissipation source after barrier crossing. An important improvement on Kramers formulation is the generalization to non-Markovian solvents which introduces memory effects in the solvent fluctuations expressed by equation 2.11 (Grote-Hynes theory [6]). An excellent review of improvements on Kramers theory of barrier crossings in many-particle systems is found in ref 7.

From the phenomenological point of view, the Langevin equation and Fokker–Planck equation methods to describe barrier crossings in the condensed phase have been (and still are) very important for our understanding of solvent effects on the rate constant. A disadvantage of these methods is that they depend heavily on parameters such as the potential felt by the reaction coordinate $U(x)$, the coupling (friction) between the reactants and the solvent γ and the dissipative fluctuating force $f(t)$, which are not known for general applications. Moreover, we are also interested in the behavior of the solvent environment during a chemical reaction, which requires the inclusion of explicit molecules *via* molecular dynamics. We will therefore make use of an alternative microscopic expression for the reaction rate derived from the macroscopic equations (2.1) for which in equilibrium $k_R \langle c_R \rangle = k_P \langle c_P \rangle$. We introduce a microscopic reaction coordinate x and the Heavyside step-function $\Theta(x - x^\ddagger)$ which indicates whether the system finds itself in the reactant state or in the product state,

$$\Theta(x - x^\ddagger) = \begin{cases} 0 & \text{at the reactant side of the transition state } x^\ddagger \\ 1 & \text{at the product side of the transition state } x^\ddagger \end{cases}$$

The decay of a deviation at time zero, $\Delta\Theta(x(0) - x^\ddagger)$, from the equilibrium $\left\langle \Theta(x - x^\ddagger) \right\rangle$ can be written as [8]:

$$\begin{aligned} \Delta\Theta(x - x^\ddagger) &= \Theta(x - x^\ddagger) - \left\langle \Theta(x - x^\ddagger) \right\rangle & (2.15) \\ \Delta\Theta(x(t) - x^\ddagger) &= \Delta\Theta(x(0) - x^\ddagger) \exp[-(k_R + k_P)t] & (2.16) \end{aligned}$$

Applying again Onsager's hypothesis and taking the time derivative, we obtain equation 2.17 for the forward reaction rate constant [8–11]:

$$k_R(t) = \frac{\left\langle \delta(x(0) - x^\ddagger)\dot{x}(0)\Theta(x(t) - x^\ddagger) \right\rangle}{\left\langle \Theta(-x(0) + x^\ddagger) \right\rangle} \tag{2.17}$$

The rate constant is thus expressed as a time correlation function of the velocity along the reaction coordinate ($\dot{x} = \mathrm{d}x/\mathrm{d}t$) at the transition state at time zero, $\delta(x(0) - x^\ddagger)\dot{x}(0)$, with the probability that the system finds itself in the product state at time t, normalized by the fraction of transitions that started in the reactant state. A typical appearance of the rate constant as a function of time is shown in figure 2.1. For very short correlation times, $t \approx 0$, the system, crossing the transition state with a positive velocity $\dot{x}(0)$, will find itself in the product state ($\Theta(x(t) - x^\ddagger) = 1$), because it has not yet had the time to recross back. For t equals zero, we thus recover the transition state theory result for the rate

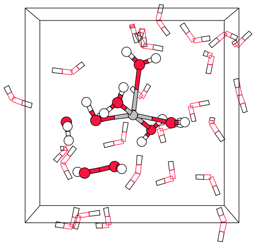

Figure 2.1: *Reaction flux rate constant as a function of time, as expressed by equation 2.17. Figure adapted from ref 12.*

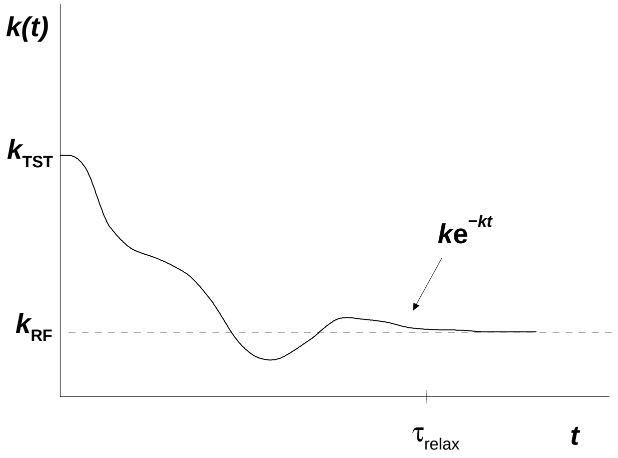

constant, k_{TST}. For larger correlation times, recrossings do take place, and $k(t)$ decreases. For very long times, in the order of the time scale of typical microscopic relaxation times τ_{relax}, $k(t)$ decays as $k\exp[-kt]$, as the system will have thermalized in one of the stable states and no further barrier recrossings take place until the system is reactivated. Since for this time scale $\exp[-kt] \approx 1$, $k(t)$ appears to reach a plateau value, which equals the macroscopic rate constant k.

In the shape of equation 2.17, apparently we still have to perform one prohibitively long simulation and wait for every occasion that the barrier top is reached to set our stopwatch to $t = 0$ and add a measurement of $\Theta(x(t) - x^{\ddagger})$ to our statistics, in order to obtain k. For practical calculations we therefore rewrite equation 2.17 by multiplying numerator and denominator with $\left\langle \delta(x(0) - x^{\ddagger})\dot{x}(0)\Theta(\dot{x}(0)) \right\rangle \left\langle \delta(x(0) - x^{\ddagger}) \right\rangle$, giving:

$$k_R(t) = \frac{\left\langle \delta(x(0) - x^{\ddagger})\dot{x}(0)\Theta(x(t) - x^{\ddagger}) \right\rangle}{\left\langle \delta(x(0) - x^{\ddagger})\dot{x}(0)\Theta(\dot{x}(0)) \right\rangle} \times \\ \times \frac{\left\langle \delta(x(0) - x^{\ddagger})\dot{x}(0)\Theta(\dot{x}(0)) \right\rangle}{\left\langle \delta(x(0) - x^{\ddagger}) \right\rangle} \frac{\left\langle \delta(x(0) - x^{\ddagger}) \right\rangle}{\left\langle \Theta(-x(0) + x^{\ddagger}) \right\rangle} \tag{2.18}$$

The last term at right-hand-side of equation 2.18 is simply the probability to find the system at the transition state relative to the probability of finding the system in the reactant state. The term in the middle gives the average forward crossing speed at the transition state, which equals together with the last term the transition state theory rate constant, k_{TST}. The first term at right-hand-side is again the transmission function, which corrects upon k_{TST} for long enough correlation times t, by giving the fraction of transitions that end up in the product state, irrespective of the crossing direction, relative

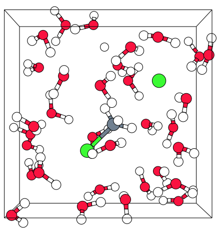

to the fraction that crosses in the forward direction. Or using Chandlers notation [10]:

$$k_R = \kappa \frac{1}{2} \left\langle |\dot{x}| \right\rangle_{\ddagger} \frac{\exp\left[-\beta \Delta G(x^{\ddagger})\right]}{\int_{-\infty}^{x^{\ddagger}} \mathrm{d}x \exp\left[-\beta \Delta G(x)\right]} \tag{2.19}$$

The separated terms can in principle all be computed using molecular dynamics. The transmission function κ, expressed by the time correlation function in the first term of eqation 2.18, is usually obtained by performing a dynamics run with the reaction coordinate constrained at the transition state $x^{\ddagger}$ to obtain a large number of starting configurations with a positive crossing velocity, which are then used to initiate unconstrained MD runs to evaluate $\Theta(x(t) - x^{\ddagger})$. The average crossing velocity (*i.e.* the second term) can be obtained from the initial constrained run. The last term, the probability to reach the transition state from the reactant state, can be obtained using a method to calculate free energy differences, such as umbrella sampling [13–15] or thermodynamic integration in combination with the method of constraint [16]. In the umbrella sampling method, the system is biased by addition of an (umbrella) potential $U(x)$, which approximately cancels the free energy barrier. In the MD run, the system can now move barrier-free back and forth from the reactant state to the product state. Accumulating the probability distribution $P(x)$ gives the desired free energy profile, $\Delta G(x) = -U(x) + k_B T \ln P(x)$. Using the method of constraint, one performs a number of constrained MD runs at different constraint values of the reaction coordinate. In each constrained run, one accumulates the force required to keep the reaction coordinate fixed. The obtained average constraint forces can be related to the thermodynamic force, $\mathrm{d}G(x)/\mathrm{d}x$, along the reaction coordinate [17], so that integration gives the desired free energy profile.

Summarizing, we see that chemical reactions are activated processes, and in particular that barrier crossings are, on the time scale of the thermal motions, rare but very important events. Performing the reaction in solution affects the reaction rate constant in two ways: 1) the static energy barrier is changed, due to different energies of solvation for the reactant state and the transition state (on the same ground the equilibrium constant $K = k_R/k_P$ can be changed by different energies of solvation for the reactant state and the product state) and 2) the solvent dynamics can alter the rate by providing an extra energy sink after barrier crossing (increasing the rate constant) or by forcing the reactants into recrossings at the barrier top region (decreasing the rate constant). By separating the rate constant in terms of the probability to reach the barrier top, the crossing velocity and the transmission coefficient, solvent effects on the reaction rate constant can be studied with molecular dynamics techniques.

2.3 Car–Parrinello molecular dynamics

The motion of small, but not too small, particles such as atoms and molecules is usually well described by Lagrangian mechanics, with the Lagrangian $\mathcal{L}$ defined as the kinetic energy minus the potential energy,

$$\mathcal{L} = T - V \tag{2.20}$$

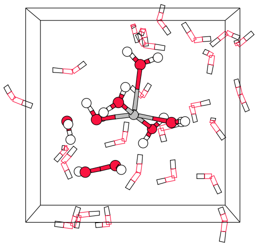

leading to the set of Newtonian equations of motion for each particle α, with mass m_α and cartesian coordinate $\mathbf{R}_\alpha$:

$$m_\alpha \frac{\mathrm{d}^2\mathbf{R}_\alpha}{\mathrm{d}t^2} = -\frac{\partial V}{\partial \mathbf{R}_\alpha} \tag{2.21}$$

Numerical integration of the equations of motion, taking small time steps Δt, results in a trajectory through the hyper-space of all possible positions and momenta of the particles, called phase-space. This simulation technique is known as molecular dynamics (MD).

The motion of even smaller particles, such as electrons, cannot be approximated with classical Newtonian dynamics, but instead has to be described with the more accurate quantum mechanical equations of motion derived from the time-independent Schrödinger equation:

$$\hat{\mathcal{H}}\Psi = E\Psi \tag{2.22}$$

That is, the Hamiltonian $\hat{\mathcal{H}}$, given as the sum of the kinetic and potential energy operators, operating on the many-electron wave function Ψ gives us the energy E. This rather simple and very famous equation can unfortunately not be solved analytically for a system of more than two electrons, and approximations on the Hamiltonian have to be introduced. Following Kohn and Sham's density functional theory (DFT) approach (see next section for the details on DFT), the exact density and the exact energy can be obtained from one-electron wave functions, the Kohn-Sham (KS) orbitals ψ_i, which are solutions in a local potential. The heart of this machinery lies in the notion that all properties, including the energy, of the electronic system are a functional of the electron density, ρ,

$$E = E[\rho] \tag{2.23}$$

The Kohn–Sham orbitals can be expanded in an orthogonal basis $\chi_1, \chi_2, \ldots$:

$$\psi_i = \sum_k c_k^i \chi_k \tag{2.24}$$

with c_k^i the expansion coefficients. The electron density ρ, given as

$$\rho(\mathbf{r}) = \sum_i f_i \left|\psi_i(\mathbf{r})\right|^2 \tag{2.25}$$

with f_i the occupation number of KS orbital i, gives us the probability to find an electron at position $\mathbf{r}$.

In DFT, the sets of coefficients c_k^i span a hyper-space $\mathcal{C}$, in which a point representing orthonormal KS orbitals ψ_i thus corresponds to an energy E, similar to a point in atomic coordinate space corresponding to a potential energy $V(\mathbf{R}^N)$. In fact, the iterative search for the one point in $\mathcal{C}$ that minimizes the energy to the physical ground-state energy E_0, resembles a molecular geometry optimization to minimize the potential energy. Since we want the one-electron functions ψ_i to be orthonormal, the trajectory through $\mathcal{C}$ during the energy minimization is constrained on a hyper-surface in $\mathcal{C}$ for which

$$\sum_k c_k^{i*} c_k^j = \delta_{ij} \quad \text{with} \quad \delta_{ij} = \begin{cases} 1 & \text{for } i = j \\ 0 & \text{for } i \neq j \end{cases} \tag{2.26}$$

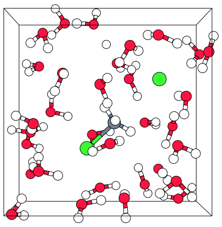

Taking the iteration steps as the analog of time steps, we can even formulate Newtonian equations of motion for the "dynamics" of changing coefficients:

$$\mu_k \frac{\mathrm{d}^2 c_k^i}{\mathrm{d}t^2} = -\frac{\partial E}{\partial c_k^{i*}} - \sum_j \lambda_{ij} c_k^j \tag{2.27}$$

Here, the μ_k are inertia parameters, usually called "fictitious masses", which control the acceleration of the coefficients, $-\frac{\mathrm{d}^2 c_k^i}{\mathrm{d}t^2}$ due to the force on the coefficients, on the right-hand-side. The last term arises from the constraint in equation 2.26, with λ_{ij} the undetermined Lagrange multipliers. The forces on the coefficients are given as

$$-\frac{\partial E[\{c_k^i\}, \{\mathbf{R}_\alpha\}]}{\partial c_k^i} = -\sum_l n_i H_{kl}^{\mathrm{KS}} c_l^i \tag{2.28}$$

which can amount to a considerable saving of computer time and memory with respect to techniques based on diagonalization of the full Hamiltonian matrix. In practice, the wave function coefficients are not known *a priori*, and we start from a random set of c_k^i, consistent with equation 2.26, associated with a meaningless energy E via equations 2.23 and 2.24. When we start to integrate the equations of motion (eq. 2.27), the coefficients will accelerate towards configurations with lower energies and gain "kinetic energy", until a dynamic equilibrium is reached. The electronic ground-state energy E_0 is found by damping the coefficient dynamics, so that kinetic energy is gradually removed and the coefficients eventually freeze in the ground-state configuration. This technique to optimize the wave function is known as "simulated annealing".

Car-Parrinello molecular dynamics (CPMD) is the integration of the fictitious wave function coefficient dynamics with the classical molecular dynamics by a single extended Lagrangian.

$$\begin{aligned} \mathcal{L} &= \sum_\alpha \frac{1}{2} m_\alpha \left| \frac{\mathrm{d}\mathbf{R}_\alpha}{\mathrm{d}t} \right|^2 + \sum_{i,k} \frac{1}{2} \mu_k \left| \frac{\mathrm{d}c_k^i}{\mathrm{d}t} \right|^2 \\ &- E[\{c_k^i\}, \{\mathbf{R}_\alpha\}] + \sum_{i,j} \lambda_{ij} (\sum_{k,l} c_l^i c_k^j S_{kl} - \delta_{ij}) \end{aligned} \tag{2.29}$$

Starting from some atomic configuration in the (optimized) electronic ground-state, we can calculate the forces on the atoms using the Hellmann–Feynman theorem,

$$-\frac{\partial E[\{c_k^i\}, \{\mathbf{R}_\alpha\}]}{\partial \mathbf{R}_\alpha} = \langle \Psi | \frac{\partial \mathcal{H}}{\partial \mathbf{R}_\alpha} | \Psi \rangle \tag{2.30}$$

to start the *ab initio* molecular dynamics. Initially, the forces on the coefficients equal zero as the electronic configuration is at its minimum, but after one time step the atomic positions have changed and the wave function is no longer up to date. However, since the electronic degrees of freedom c_k^i and the atomic positions $\mathbf{R}_\alpha$ are coupled via the potential energy (equation 2.29), the forces on the coefficients are no longer zero and the coefficients accelerate towards the new electronic ground-state. When the fictitious coefficient masses μ_k are chosen sufficiently small (*i.e.* $\mu_k \ll m_\alpha \forall k, \alpha$) the response of the coefficients to the changing nuclei α is so rapid that the electrons remain to a sufficiently high degree in the ground-state.

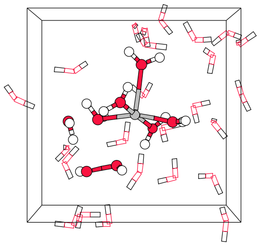

Figure 2.2: *Vibrational spectrum of the normal modes of the electronic coefficients (solid line) for a system with a large gap (periodic super cell containing 8 Si atoms in the diamond structure). The solid triangle indicates the position of the highest ionic frequency. The vertical bars below the spectrum represent the frequencies obtained from equation 2.31. Figure from ref 18.*

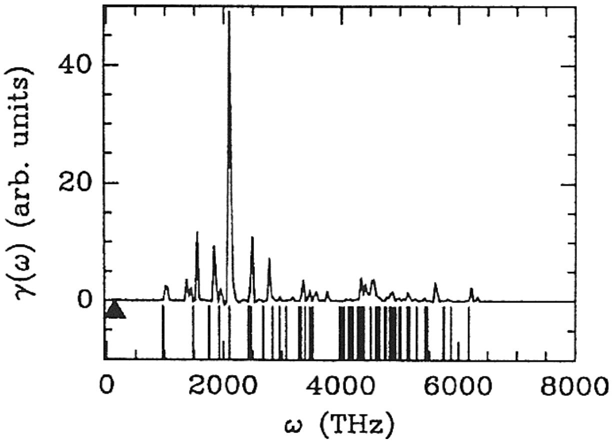

Of course, the dynamics of the nuclei in CPMD has only physical meaning if the electronic structure is close to its instantaneous ground-state at each step of the simulation. In other words, the dynamics of the electronic coefficients c_k^i has to remain relatively cold. However, since the two dynamic sub-systems of nuclei $\mathbf{R}_\alpha$ and electronic coefficients c_k^i are coupled, in principle energy can flow from the relatively hot nuclei sub-system, to the colder coefficients, which would lead to deviations from the Born-Oppenheimer (ground-state) surface. In many practical simulations, the energy flow between the sub-systems can be suppressed with a good choice for the fictitious coefficient masses μ_k, which can be rationalized by regarding the electronic coefficient dynamics for small deviations from the ground-state, described as a superposition of harmonic oscillations whose frequency is given by:

$$\begin{aligned} \omega_{ij}^{(1)} &= [f_j(\epsilon_i - \epsilon_j)/\mu]^{1/2} \\ \omega_{ij}^{(2)} &= [(f_j - f_i)(\epsilon_i - \epsilon_j)/2\mu]^{1/2} \end{aligned} \tag{2.31}$$

Here, ϵ_i indicates the eigenvalue of the ith unoccupied and ϵ_j the jth occupied level, and the fictitious coefficient masses μ_k are chosen equal for all k. As an illustration, let us refer to figure 2.2 from the illuminating study of ref 18, which shows the vibrational density of states of the electronic coefficients for an unrealistic but instructive model of crystalline silicon. The fictitious mass in this work was $\mu = 300$ au. The solid line is obtained from the Fourier transform of the velocity autocorrelation function

$$\nu(\omega) = \int_0^\infty \mathrm{d}t \cos(\omega t) \sum_{k,i} \left\langle \dot{c}_k^i(t) \dot{c}_k^i(0) \right\rangle \tag{2.32}$$

from a simulation of 3000 time steps ($\Delta t = 5$ au) and the vertical bars below are obtained from equation 2.31. The lowest electronic frequency (at about 1010 THz) results from the

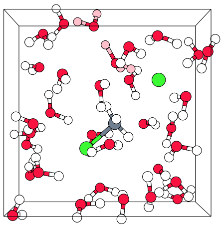

energy gap, which is in this model $E_g = 2.24$ eV, in good agreement with the estimate using equation 2.31: $\omega_{\mathrm{min}} = (2E_g/\mu)^{1/2} = 968$ THz. The highest ionic frequency for this model is 140 THz, indicated by the triangle in figure 2.2. This clear separation between the characteristic electronic and ionic frequencies, is the reason that the irreversible energy transfer from the slow to the fast degrees of freedom is minimal, and the main reason that CPMD works! Problems occur for systems with a small or vanishing bandgap, such as semiconductors and metals, because the heat transfer can no longer be controlled by choosing a small enough μ. A workable solution for these systems can be provided by coupling both dynamical sub-systems to thermostats which remove kinetic energy from the electronic coefficients while adding kinetic energy to the nuclei [19].

As the electronic coefficients rapidly fluctuate around their optimal values, the instantaneous values of the forces do not coincide with the Hellmann-Feynmann forces, however their average values do to a very high degree of accuracy. The high efficiency of the Car-Parrinello approach with respect to the so-called (real-) Born-Oppenheimer molecular dynamics (BOMD) method also lies in this respect. In BOMD, the electronic structure is self-consistently optimized after each time step in which only the relatively small number of nuclei positions are propagated. In practice, the convergence of the optimization has to be very high to avoid the accumulation of the small, but systematic (!), deviations in the Hellmann-Feynman forces, which makes BOMD computational more demanding than CPMD. This difference in efficiency is partly reduced by the larger time step that can be used in BOMD, as the maximum time step is limited by the proper integration of the equation of motions of the fastest (*i.e.* lightest) particles, which are the high frequency components of the fictitious dynamics in CPMD, whereas in BOMD, the lightest nuclei limit the time step maximum. A technique to accelerate CPMD further is known as mass-preconditioning [20], which is based on reducing these high frequency components of the fictitious dynamics by properly scaling the fictitious masses μ_k, so that a larger time step can be used. Excellent reviews of the Car–Parrinello molecular dynamics techniques are found in refs 21–23.

The first CPMD implementations used a basis set of plane waves, in combination with a pseudopotential [25–27], to expand the one-electron valence wave functions, which is the most widely used approach in electronic structure calculations in the field of solid state physics. Plane waves are of the form $\psi = N^{-1} \exp[i\mathbf{Gr}]$ ($i = (-1)^{1/2}$ and G the wave vector), which are the eigenfunctions of Schrödinger's equation (2.22) for an electron in vacuum with kinetic energy $E_{\mathrm{kin}} = G^2/2$. For electrons in an external field, such as in atoms, however, an expansion in plane waves is a rather poor choice, because these functions hardly mimic the rapid fluctuations of the one-electron wave functions in the neighborhood of the nucleus. Usually the low lying core electrons are kept "frozen" during an electronic structure calculation to reduce the computational cost, which is a good approximation since these states remain practically invariant from their atomic ground-state during the chemistry of bond breaking and making. For the chemically active valence wave functions a pseudopotential is used to describe the inner region (nucleus plus core electrons) of the atom, in a way that allows for replacing the rapid fluctuating functions by more smooth functions. Beyond this inner region, the smooth functions agree with the true wave functions. A disadvantage of the pseudopotential method is that they become "very hard" for first row elements and for systems with d and f electrons, so that

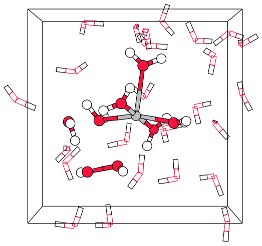

Figure 2.3: *Partial waves and projectors for Mn. Left panel: partial waves ϕ (solid lines) and pseudo partial waves $\tilde{\phi}$ (dashed and dash-dotted lines). The "first" pseudo partial wave is a dash-dotted line. Right panel: first (solid line) and second (dashed line) projector functions. (a) and (d) show the results for the first and second partial wave of the s angular momentum channel, respectively, (b) and (e) for the p channel and (c) and (f) for the d channel. 3s and 3p functions are treated as valence states. Figure from ref 24.*

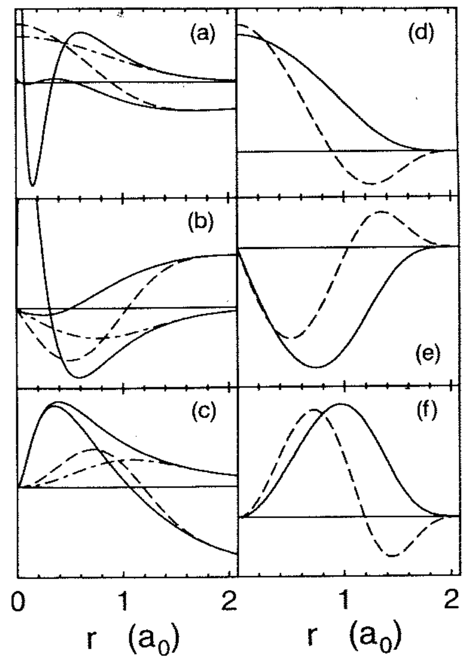

very large basis sets are required. An improvement on the traditional pseudopotentials was provided with the development of Vanderbilt's ultrasoft pseudopotentials [28, 29] by relaxing on the norm conserving condition that is usually imposed. The simulations described in this thesis were performed with Blöchl's CPMD implementation, named *projector augmented wave* or PAW [24], which is based on a generalization of both the pseudopotential approach and the linear augmented-plane wave method [30–32] (LAPW). In contrast to the pseudopotential approach, the LAPW technique utilizes the full one-electron valence wave function with the correct nodal structure. The wave function is subdivided into two regions; an inner (augmentation) region, which is expanded in a basis set of localized functions, and an outer region which is described by plane waves. At a certain (muffin-tin) sphere radius from the nucleus, the partial wave functions are matched together by value and derivative of the functions. Instead in PAW, a linear transformation between the one-electron valence wave functions ψ and fictitious pseudo wave functions $\tilde{\psi}$ is used, in Dirac's bra and ket notation:

$$|\psi >= \tilde{\psi} + \sum_i (|\phi_i > -|\tilde{\phi}_i >) < \tilde{p}_i|\tilde{\psi} > \qquad (2.33)$$

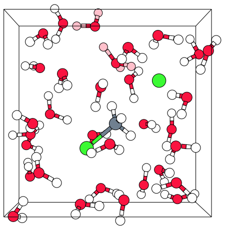

where $|\phi>_i$ are a complete set of partial waves (i referring to the atomic site R, the angular momentum quantum numbers $L = (l, m)$ and the index n for different partial waves per R and L). Each partial wave $|\phi>_i$ is connected to a pseudo partial wave $|\tilde{\phi}>_i$, which only differs from $|\phi>_i$ inside an augmentation region Ω_R, and a localized, so-called, projector function $< \tilde{p}_i|$ for which,

$$< \tilde{p}_i|\tilde{\phi} >= \delta_{ij}. \tag{2.34}$$

As an illustration, we use figure 2.3 from ref 24, which shows the partial waves and projector functions for manganese. The partial waves are functions on a radial grid, multiplied with spherical harmonics, which are obtained by radially integrating Schrödinger's equation for the isolated atom. The pseudo wave functions $\tilde{\psi}$ are expanded in plane waves. In practice, the partial waves $|\phi_i>$ and $|\tilde{\phi}_i>$ and the projector functions $< \tilde{p}_i|$ are imported from an atomic calculation at the start of a PAW molecular dynamics calculation. The main advantages of the PAW approach compared to the conventional norm-conserving pseudopotential methods is that the atomic partial and projector functions are better transferable than pseudopotentials and that the full wave function is accessible, which allows for the calculation of core dependent quantities such as hyperfine parameters and electric field gradients [33, 34]. Also a smaller plane wave basis set is required than with the norm conserving pseudopotential methods, which is most important for the present study as it cuts heavily on the computational expense. A very detailed description of the PAW technique and its relation to the traditional norm conserving pseudopotential method and the LAPW method is found in reference 24.

2.4 Density Functional Theory

In the previous section, we have shown that the "simulated annealing" technique can be used to minimize the electronic energy of a system by optimizing the electronic degrees of freedom, the coefficients c_k^i, or to minimize the atomic potential energy by optimizing the atomic degrees of freedom, the positions $\mathbf{R}_\alpha$. But we have not yet introduced the quantum mechanical relation between the energy and the electronic coefficients and atomic positions, to obtain the forces on the atoms and coefficients (eq. 2.30). The reason is, that in principle various quantum mechanical (or even semi-empirical methods) can be used, such as the Hartree-Fock method or the configurational interaction method. Hartree-Fock, however, lacks for many practical systems the desired chemical accuracy while on the other hand the configurational interaction method, although it can be highly accurate, is unpractical due to its dramatic scaling of the computational expense with the number of electrons. In practice, therefore, the energy and the forces are obtained from an electronic structure calculation using density functional theory (DFT), which is both accurate and has a favorable scaling.

Density functional theory is based on the notion that for a many–electron system there is a one-to-one mapping between the external potential and the electron density: $v(\mathbf{r}) \leftrightarrow \rho(\mathbf{r})$. In other words, the density is uniquely determined given a potential, and *vice versa*. All properties are therefore a functional of the density, because the density determines the potential, which determines the Hamiltonian, which determines the energy

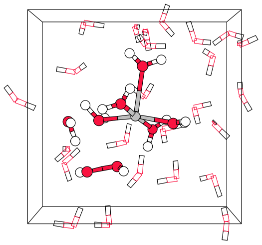

($E[\rho]$) and the wave function ($\Psi[\rho]$), from which all physical properties can be determined. This theorem was proven in 1964 by Hohenberg and Kohn, using the variational principle for systems with a non-degenerate ground-state. Hohenberg and Kohn also showed that for a given potential $v(\mathbf{r})$, which corresponds with a ground-state $\Psi_0[\rho]$ and ground-state energy $E_0[\rho]$, the energy functional $E_v[\rho]$ has its minimum equal to $E_0[\rho]$ at the ground-state density (second Hohenberg-Kohn theorem), or:

$$\left\langle \Psi[\rho] \left| \hat{\mathcal{H}} \right| \Psi[\rho] \right\rangle = \int \mathrm{d}\mathbf{r}\, v(\mathbf{r})\, \rho(\mathbf{r}) + T[\rho] + V_{\mathrm{ee}}[\rho] = E_v[\rho] \geq E_0[\rho] \tag{2.35}$$

with $T[\rho]$ the electronic kinetic energy functional and $V_{\mathrm{ee}}[\rho]$ the electron-electron interaction energy functional.

A prescription to obtain the energy from the N-electron density was given by Kohn and Sham in a one-electron formalism, posing that there exists an auxiliary system of N non-interacting electrons, feeling only a local potential $v_s(\mathbf{r})$ which yields exactly the same density as the system of interacting electrons with potential $v(\mathbf{r})$. The electron density is represented by the sum of the densities of the $N/2$ doubly occupied single-particle spatial orbitals,

$$\rho(\mathbf{r}) \quad = \quad 2 \sum_{i}^{occ} \left| \psi_i(\mathbf{r}) \right|^2 \tag{2.36}$$

and the Kohn-Sham (KS) expression for the electronic energy functional is given by:

$$E[\rho] = T_s[\rho] + V_{\mathrm{N}}[\rho] + J_{\mathrm{ee}}[\rho] + E_{\mathrm{xc}}[\rho] \tag{2.37}$$

Here, $T_s[\rho]$ is the kinetic energy of non-interacting electrons, $V_{\mathrm{N}}[\rho]$ describes the electron–nuclei interaction and the so-called Hartree term, $J_{\mathrm{ee}}[\rho]$, is the Coulombic interaction among the electrons:

$$\begin{aligned} T_s(\rho) &= -\frac{\hbar^2}{2m} \sum_{i}^{N} \int \mathrm{d}\mathbf{r}\, \psi_i^*(\mathbf{r}) \nabla^2 \psi_i(\mathbf{r}) && (2.38) \\ V_{\mathrm{N}}[\rho] &= \int \mathrm{d}\mathbf{r}\, v^{\mathrm{ext}}(\mathbf{r})\, \rho(\mathbf{r}) && (2.39) \\ J_{\mathrm{ee}}[\rho] &= \frac{e^2}{2} \int \mathrm{d}\mathbf{r} \int \mathrm{d}\mathbf{r}' \frac{\rho(\mathbf{r})\rho(\mathbf{r}')}{|\mathbf{r} - \mathbf{r}'|} && (2.40) \end{aligned}$$

The last term in equation 2.37 is the exchange correlation energy functional $E_{\mathrm{xc}}[\rho]$ which compensates for the electron-electron interaction V_{ee} being described only by the Coulomb interaction J_{ee} (thereby neglecting the exchange interaction and the electron correlation interaction) and for the kinetic energy functional which describes the kinetic energy for non-interacting electrons:

$$E_{\mathrm{xc}}[\rho] = V_{\mathrm{ee}} - J_{\mathrm{ee}}[\rho] + T[\rho] - T_s[\rho] \tag{2.41}$$

The exchange correlation energy functional also has to correct for a spurious self interaction arising from J_{ee}, which is in *ab initio* methods canceled exactly by the exchange term, but in DFT actually is the largest contribution to $E_{\mathrm{xc}}[\rho]$.

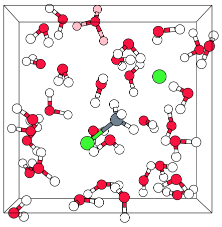

The electronic ground-state density is found by minimizing the Kohn-Sham energy functional, which is achieved by solving the Kohn-Sham equations:

$$\hat{\mathcal{H}}^{\mathrm{KS}}\psi_i = \left[-\frac{\hbar^2}{2m}\nabla^2 + v^{\mathrm{ext}} + \frac{e^2}{2}\int \mathrm{d}\mathbf{r}\frac{\rho(\mathbf{r}')}{|\mathbf{r}-\mathbf{r}'|} + \frac{\delta E_{\mathrm{xc}}[\rho]}{\delta\rho(\mathbf{r})}\right]\psi_i = \epsilon_i\psi_i \tag{2.42}$$

Thus far, the DFT expressions are exact. However, an exact expression for $E_{\mathrm{xc}}[\rho]$ is not known, and one is forced to use an approximate functional. Also, there is no straightforward way in which the exchange correlation functional can be systematically improved.

For an homogeneous electron gas or an electron gas with slow varying density, one can show that

$$E_{\mathrm{xc}}^{\mathrm{LD}} = \int \mathrm{d}\mathbf{r}\rho(\mathbf{r})\,\epsilon_{\mathrm{xc}}(\rho(\mathbf{r})) \tag{2.43}$$

The exchange correlation energy density function $\epsilon_{\mathrm{xc}}(\rho(\mathbf{r}))$ for the uniform electron gas is known to high accuracy from Monte Carlo calculations of Ceperly and Alder [35]. Several parameterizations were used for this type of functional, which are known as local density approximation (LDA) functionals. Especially in solid-state physics, LDA works surprisingly well despite its approximate nature. However, most chemical applications do not satisfy the restriction of slowly varying electron density and the LDA fails. Much better results are obtained by taking into account the density fluctuations, *via* the gradient of the density. This has led to the development of various so-called generalized gradient approximations (GGAs), of which the most popular is the Becke [36] exchange functional:

$$\epsilon_{\mathrm{xc}}^{\mathrm{B}} = -\beta\rho^{1/3}\frac{x^2}{(1+6\beta x\sinh^{-1}x)} \tag{2.44}$$

$$x = \frac{|\nabla\rho|}{\rho^{4/3}} \tag{2.45}$$

which has led to the acceptance of DFT as a valuable tool for computational chemistry, after its introduction in 1988. This functional contains one adjustable parameter β which was chosen so that the sum of the LDA and Becke exchange terms accurately reproduce the exchange energies of six noble gas atoms, $\beta = 0.0042$. A large number of other GGA functionals for both correlation and exchange have been developed, of which the most popular probably the 4 parameter LYP correlation functional [37] , the parameter-free Perdew86 correlation functional [38] and the Perdew91 exchange+correlation functional [39]. Throughout the present work, we will make use of Becke's exchange functional and the Perdew86 correlation functional. However, the search for the holy grail continues. Routes to improvement are for example the mixing in of exact (Hartree-Fock) exchange (so-called hybrid functionals, such as the B3LYP functional), the use of highly parameterized GGA functionals which are fitted to large sets of empirical molecular properties (*e.g.* the HCTH functional [40]), taking the Laplacian of the density into account (*e.g.* the BLAP functional [41]), correcting for the approximate kinetic energy term [42], correction for the spurious Coulombic self interaction (so-called SIC functionals [43]) and imposing of the correct asymptotic behavior (*e.g.* the VanLeeuwen-Baerends functional [44]). Other important progress, which makes DFT particularly popular by chemists, is made in the development of computer programs that calculate chemical and physical properties, such

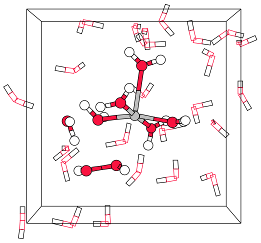

as spectroscopic observables, *a posteriori*, using the Kohn-Sham density. The reader interested in the technical details of density functional theory and its application in chemistry might wish to read references 45–48.

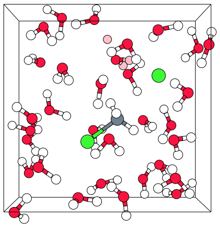

Chapter 3

Solvation effects on the S_N2 reaction between CH_3Cl and Cl^-, in water*

This chapter describes the Car–Parrinello molecular dynamics simulations which have been performed to investigate the solvation effects on the prototype S_N2 reaction between Cl^- and CH_3Cl. The free energy barrier for this reaction in water was calculated using constrained dynamics at a constant temperature of $T = 300$ K and a constant volume. Calculations on the isolated system (reaction in the gas phase at zero temperature) were performed for reference purposes. Qualitatively the calculations confirm that the double-well free energy profile of the reaction in the gas phase is converted into a single barrier by solvation, and that the height of the barrier increases significantly. Quantitatively, there are two error sources. At the electronic structure side the Becke–Perdew functional underestimates the barrier height by 8 kcal/mol. At the dynamics side there is a "hysteresis" effect - too slow adaptation of the solvent structure to changes in the reaction coordinate - yielding an estimated error of 3 kcal/mol in the free energy barrier height. After correction for these errors the calculated value of the free energy barrier is 27 kcal/mol. Considering the accuracy of the solvent-solvent and solvent-reactant interactions of ca. 1 kcal/mol, this compares very well with the experimental estimate of 26.6 kcal/mol. This indicates that the ab initio (DFT) MD very well captures the differential energetic as well as entropic effects of the solvation when going from the (solvated) reactants to the initial ion-dipole complex to the transition state.

3.1 Introduction

The presence of solvent can have a major impact on the thermodynamics and kinetics of chemical reactions. Aspects such as electrostatic interactions and steric hindrance can play an important role in this respect. Also, chemical binding of solvent molecules to the

---

*B. Ensing, E. J. Meijer, P. E. Blöchl, and E. J. Baerends, *J. Phys. Chem. A* **105**, 3300 (2001)

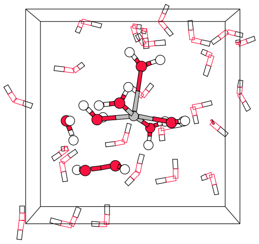

reacting species may have a strong effect. A detailed microscopic picture of these effects is of fundamental interest and provides insight for possible improvements with respect to the rate, balance, and selectivity of chemical reactions.

Molecular simulation is an appropriate tool to obtain such a detailed picture. A high-level quantitative molecular simulation of a chemical reaction in solution requires the use of accurate quantum chemical methods to describe the change in chemical bonding in combination with a statistical mechanical description of the effect of the rearrangement of solvent molecules. The Car–Parrinello (CP) method [49] satisfies these two requirements in a computationally efficient manner. It combines Density Functional Theory (DFT) to describe the electronic structure with Molecular Dynamics (MD) to incorporate the motion of the molecules. The forces on the molecules that govern their motion are obtained directly from the electronic structure calculation. Therefore the method may be regarded as an *ab initio* (DFT) Molecular Dynamics (AIMD) simulation. Of particular importance for the present work is that AIMD has proven to be applicable to the study of the structure and dynamics of water [50–53] and simple chemical reactions in aqueous solution. [54, 55]

The purpose of the present study is to gain microscopic insight in the energetics, mechanism, and structural aspects of the solvation effects on a prototype S_N2 reaction in water, with a minimal level of approximation and without use of empirical data. In particular we have investigated the effect of solvation in a dilute aqueous HCl solution of the bimolecular nucleophilic substitution (S_N2) reaction,

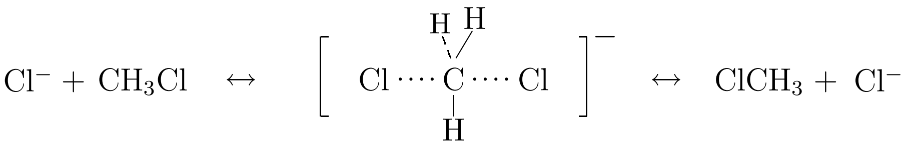

$$Cl^- + CH_3Cl \quad \leftrightarrow \quad \left[\; Cl \cdots \overset{H\;H}{\underset{H}{C}} \cdots Cl \;\right]^- \quad \leftrightarrow \quad ClCH_3 + Cl^- \qquad (i)$$

The S_N2 type of reaction is one of the most fundamental processes in organic chemistry and has been the subject of numerous theoretical [56–61] and experimental studies [62–64]. The energy profile for the gas phase reaction between methyl chloride and a chloride anion is commonly believed to have a symmetrical double-well shape with the two minima related to the ion–dipole complexes centered around a maximum at the transition state. However, experimental evidence shows that in aqueous solution the profile is unimodal and the reaction rate much lower compared to that of the gas phase reaction. Using classical Monte Carlo simulations, Chandrasekhar, Smith and Jorgensen [65] were the first to compute the barrier for the $Cl^- + CH_3Cl$ reaction in aqueous solution. They developed model potentials for the interactions between the water molecules and the solutes (Cl^- and CH_3Cl), and between water molecules, by fitting to *ab initio* calculations. It is an advantage of the Car–Parrinello simulation that these potentials are obtained directly. This is particularly important in a case like the present one where construction of good model potentials is difficult because of the changes in the charges on the attacking and leaving chloride ions, and hence in their solvation, along the reaction coordinate.

The reaction studied in the present work is activated. The experimental value for the activation energy is 27 kcal·mol^{-1}. [66] A successful reaction is therefore a rare event and outside the time scale accessible to *ab initio* Molecular Dynamics. To study such reactions by MD a reactive encounter must be forced on the system by some form of microscopic control of a suitable reaction coordinate. This is achieved by using the method

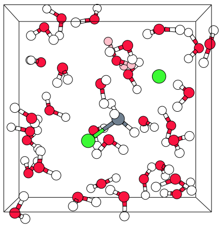

of constraint that allows for the evaluation of the free-energy profile along the reaction path. [16]

This paper is organized as follows: In section 3.2, we describe the computational details of the DFT and MD method, the method of constrained dynamics to calculate the reaction free energy, and the relevant parameters for the gas phase and aqueous solution calculations. Section 3.3 starts with the results of some preparatory simulations that serve to assess the accuracy of the methods used. The simulation results of the S_N2 reaction in gas phase and in aqueous solution are presented in sub-sections 3.3.3 and 3.3.4, respectively. In section 3.4 a discussion of our results for the solvation effect on the reaction barrier is given and we end with conclusions in section 3.5.

3.2 Method

3.2.1 Density Functional and Molecular Dynamics Method

The electronic structures were computed using density functional theory (DFT) (see *e.g.* ref 46). For the exchange–correlation functional we used the Perdew–Zunger [43] parameterization of the local density approximation (LDA) for this functional, which is based on the free-electron MC simulations by Ceperley and Alder [35]. Density gradient corrections were added, namely the Becke–88 gradient correction for exchange [67] and the Perdew–86 gradient correction for correlation. [38]

The Car–Parrinello (CP) method [49] was applied to perform both dynamic and static calculations. The method performs the classical MD and simultaneously applies DFT to describe the electronic structure, using an extended Lagrangian formulation. The characteristic feature of the Car–Parrinello approach is that the electronic wave function, *i.e.* the coefficients of the plane wave basis set, are dynamically optimized to be consistent with the changing positions of the atomic nuclei. The actual implementation involves the numerical integration of the equations of motion of second-order Newtonian dynamics. A crucial parameter in this scheme is the fictitious mass m_e associated with the dynamics of the electronic degrees of freedom. In practice, m_e has to be chosen small enough to ensure fast wave function adaptation to the changing nuclear positions on one hand and sufficiently large to have a workable large time step on the other. In the present work, the equations of motion were integrated using the Verlet [68] algorithm with a mass $m_\mathrm{e} = 1000$ a.u. $= 9.1093910^{-28}$ kg, which limits the time step to $\delta t = 0.19$ fs. To maintain a constant temperature of $T = 300$ K a Nosé thermostat [69] was applied with a period of 100 fs.

The CP simulations have been performed using the CP–PAW code package developed by Blöchl. It implements the ab-initio molecular dynamics together with the projector augmented wave (PAW) method. [24] The PAW method uses an augmented plane wave basis for the electronic valence wave functions, and, in the current implementation, frozen atomic wave functions for the core states. Thus it is able to produce the correct wave function and densities also close to the nucleus, including the correct nodal structure of the wave functions. The advantages compared to the pseudopotential approach are that transferability problems are largely avoided, that quantities such as hyperfine parameters and electric field gradients are obtained with high accuracy [33, 34] and, most important

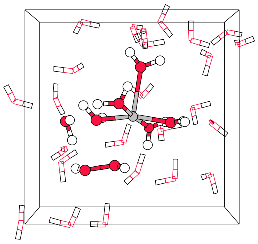

for the present study, that a smaller basis set as compared to traditional norm-conserving pseudopotentials is required. The frozen core approximation was applied for the 1s electrons of C and O, and up to 2p for Cl. For H, C and O, one projector function per angular-momentum quantum number was used for *s*- and *p*-angular momenta. For Cl, two projector functions were used for *s*- and one for *p*-angular momenta. The Kohn-Sham orbitals of the valence electrons were expanded in plane waves up to a kinetic energy cutoff of 30 Ry.

For reference, we also performed static DFT calculations using the atomic-orbital based ADF package. [70] In these calculations, the Kohn-Sham orbitals were expanded in an uncontracted triple-ζ Slater-type basis set augmented with one 2p and one 3d polarization function for H, 3d and 4f polarization functions for C, O, and Cl.

3.2.2 Free energy calculation

The reaction equilibrium constant and the transition state theory estimate of the reaction rate of a chemical reaction are determined by the free-energy profile along the reaction path. The free energy reaction barrier is the reversible work necessary to bring the system from the stable state of reactants (RS) to the transition state (TS). We will characterize these states by some order parameter, a reaction coordinate ξ, which is a function of the positions of the nuclei. As the reversible work is independent of the path, the precise choice of the reaction coordinate is not crucial, but a practical and physically appealing choice is one that incorporates the asymmetric stretch vibration along the Cl–C–Cl axis of the transition state complex CH_3Cl_2. Given a choice for the reaction coordinate, wa can obtain the free energy change $\Delta A(\xi)$ along the reaction path, using the technique of thermodynamic integration (see *e.g.* ref 71):

$$\Delta A(\xi) = \int_{\xi_{\mathrm{RS}}}^{\xi} \left\langle \frac{\partial H}{\partial \xi} \right\rangle_{\xi'} d\xi' \tag{3.1}$$

Here H is the Hamiltonian of the system of nuclei, defined as the sum of the kinetic and (Born-Oppenheimer) potential energy, and minus the integrand -$\langle \partial H/\partial \xi \rangle$ is usually called the mean force. The brackets denote an ensemble average and the subscript indicates that the integrand is evaluated at the point $\xi(\mathbf{r}) = \xi'$ along the reaction coordinate, where $\mathbf{r}$ denotes the total of nuclear coordinates.

The S_N2 reaction studied in the present work is an activated process, which implies that the barrier is too high for the reaction to take place spontaneously within the time scale accessible to an MD simulation. The probability to find the system close to the transition state is very small, and the reaction is therefore a rare event. To nevertheless be able to estimate the mean force at the reaction coordinate values of low probability, the method of constraint can be used, where the dynamics of the system is performed with the reaction coordinate fixed at a specified value ξ'. The theoretical framework of the study of activated processes in an MD simulation has been established some time ago in ref 10 and also ref 16, which provided a microscopic expression for the mean force. An approximate version of this method [72, 73], only valid for reaction paths controlled by special classes of constraints, has been successfully used in quite a number

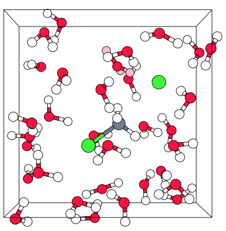

Figure 3.1: *The reaction coordinate (equation 3.2) is a function of the positions of the attacking chloride Cl′, the carbon atom C and the leaving chloride Cl. One characteristic of the chosen reaction coordinate is that for a particular value of the coordinate, the carbon is allowed to move only in a plane perpendicular to the line through the chlorine atoms.*

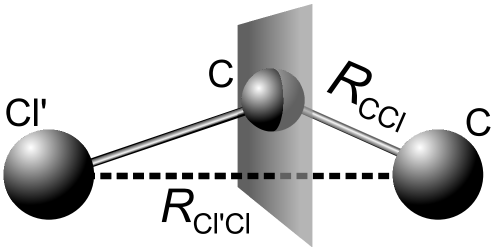

of simulations of reactions. [54, 74, 75] More recently, generally applicable expressions for the mean force have been outlined [17, 76], which include the explicit terms to correct for the bias introduced in the ensemble by applying the constraint (see also the appendix).

The reaction coordinate used in the present study is defined as the normalized projection of the C-Cl bond R_{CCl} on the Cl′-Cl bond $R_{\mathrm{Cl'Cl}}$ (see figure 3.1):

$$\xi = \frac{R_{\mathrm{CCl}} \cos(\angle_{\mathrm{CClCl'}})}{R_{\mathrm{ClCl'}}}. \tag{3.2}$$

Here $\angle_{\mathrm{CClCl'}}$ is the angle between the C-Cl and Cl′-Cl bonds. In the following we will refer to Cl′ and Cl as the attacking and leaving chloride, respectively. Since the reaction is symmetric, the transition state is at a point where both C-Cl distances are equal. At this transition state the value of the reaction coordinate (equation 3.2) is $\xi = 0.5$, whereas it approaches zero for separated reactants and one for separated products.

3.2.3 Gas phase computations

The CP–PAW calculations of the isolated compounds were performed in a cubic periodic unit cell of size $L = 10$ Å. A rectangular periodic unit cell of size 10x10x18 Å was used for the isolated (gas phase) reaction. These sizes are sufficiently large to ensure negligible overlap of the wave functions of the periodic images. To suppress the electrostatic

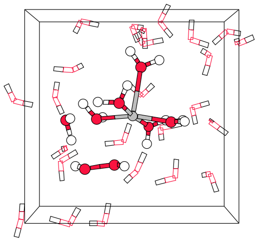

interaction among the periodic images, we used the method of electrostatic decoupling of ref 77.

For the ADF calculations, the finite-temperature reaction enthalpies at $T = 300$ K and the entropies were estimated using

$$
\begin{aligned}
\Delta H_{300K} &= \Delta E_0 + \Delta E_{\text{ZPE}} + \Delta E^{\text{v}}_T + \Delta E^{\text{t}} + \Delta E^{\text{r}} + \Delta(PV) && (3.3)\\
\Delta S &= R\ln(Q^{\text{t}}Q^{\text{r}}Q^{\text{v}}) && (3.4)
\end{aligned}
$$

with E_0 the sum of the electronic energy in a static nuclear field (Born–Oppenheimer approximation) and the nuclear electrostatic repulsion. The zero-point vibrational energy E_{ZPE} and the temperature dependent vibrational energy E^{v}_T were calculated from the unscaled DFT–BP frequencies, within the harmonic approximation. The change in translational energy ΔE^{t}, rotational energy ΔE^{r}, and PV were obtained using the ideal gas law, associating $\frac{1}{2}k_BT$ to each degree of freedom. The partition function Q is the product of translational, rotational and vibrational contributions (see *e.g.* chapter 20 in reference 78).

3.2.4 Aqueous solution computations

We performed Car–Parrinello molecular dynamics simulations of the following solutions: (a) HCl in water, (b) CH_3Cl in water and (c) both HCl and CH_3Cl in water. For reference, a CP–PAW calculation of a pure water sample of 32 H_2O molecules per unit cell was also done (d). All simulations were performed in a periodic system with the cubic unit cell containing one of each type of solute molecules (HCl or CH_3Cl or both) and 32 water molecules. The box sizes were: 9.9684, 10.1450, 10.2463 and 9.8650 Å for samples (a), (b), (c) and (d), respectively, yielding the experimental density of the solution at $T = 300$ K. The simulations of sample (c), the reactants in water, yield the central result of the present work. It involved the calculation of the free energy barrier for the $CH_3Cl + Cl^-$ reaction in water by a series of constrained CP–PAW runs at different values of the reaction coordinate (eqn 3.2). The starting configuration of the first run was created from a previous run of CH_3Cl in water, sample (b), at $T = 300$ K. A sphere-shaped cavity of radius 2 Å was created near the CH_3Cl molecule, in which HCl′ ($R_{\text{HCl}'} = 1.10$ Å) was placed at a distance from CH_3Cl equal to $R_{\text{CCl}'} = 4.00$ Å and with an angle $\angle_{HCl'C} = 180°$. With the angle $\angle_{\text{ClCCl}'} = 176°$ and the C–Cl distance in CH_3Cl $R_{\text{CCl}} = 1.871$ Ry and the C–Cl distance in CH_3Cl $R_{\text{CCl}} = 1.871$ Å, this corresponds to a value for our reaction coordinate in this initial snapshot of $\xi = 0.31848$. This value was constrained and equilibration was performed at $T = 300$ K until there was no longer a drift in the constraint force and the potential energy $E\,[\rho]$. Then a production run of 3–5 ps. was performed to collect statistics. After each production run, the constraint was moved to the next reaction coordinate value in a number of steps large enough to keep the induced atomic velocities very small compared to their average velocities at $T = 300$ K (typically 1000-2000 steps). This was again followed by equilibration and mean force sampling. Equilibrations took typically 1.5-3 ps.

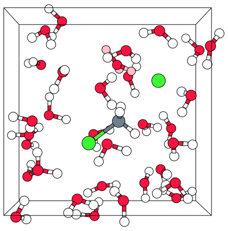

Table 3.1: *Comparison of bonding energies (kcal/mol) and geometries (Ångströms and degrees) calculated with the CP–PAW program and the ADF program with other calculations and experiment.*

Mol.	Prop.	PAW[a] 30Ry	PAW[a] 50Ry	ADF[a] TZDP	B3LYP[b] 6-31G*	G2[c] MP2/6-31G*	Exp.[d]
Cl_2	ΔE_{Bond}	-58.2	-58.2	-62.3		-56.56	58.0
	R_{ClCl} [Å]	2.065	2.065	2.023	2.042	2.015	1.988[e]
HCl	ΔE_{Bond}	-105.7	-106.0	-107.8		-106.7	106.3
	R_{HCl} [Å]	1.308	1.304	1.293	1.290	1.280	1.275[f]
H_2O	ΔE_{Bond}	-232.59	-234.46	-237.88		-232.5	232.2
	R_{OH} [Å]	0.985	0.979	0.971	0.969	0.969	0.957[g]
	$\angle_{\mathrm{HOH}}[^\circ]$	103.77	104.09	104.07	103.6	104.0	104.4[g]
CH_3Cl	ΔE_{Bond}	-401.9	-404.2	-402.2		-394.8	393.8
	R_{CH} [Å]	1.102	1.096	1.093	1.090	1.088	1.08[h]
	R_{CCl} [Å]	1.827	1.827	1.803	1.803	1.777	1.78[h]
	$\angle_{\mathrm{HOCl}}[^\circ]$	107.9	107.8	108.3	108.5	108.9	108.2[h]

[a] Our work, using the BP functional. [b] B3LYP 6-31G* geometries from ref 79. [c] G2 energies (effectively QCISD(T)/6-311+G(3*df*,2*p*) level) based on MP2/6-31G* geometries from ref [79]. [d] Experimental bonding energies minus the zero-point energy correction from refs 80, 81. [e] Ref 82. [f] Ref 83. [g] Ref 84. [h] Ref 85.

3.3 Results

In this section, we will present (1) reference calculations to assess the accuracy of the DFT approach and its implementation in the CP–PAW code; (2) results of calculations of a sample of 32 water molecules of pure water and the solvation of a single HCl molecule (*i.e.* the samples referred to as (a) and (d) in the previous section). These calculations serve as a validation of the theoretical approach and numerical methods used. Subsequently, we present the results of the gas phase S_N2 reaction (*i*) and the results of the CP–PAW calculations of the S_N2 reaction in water.

3.3.1 Structures and energies of isolated compounds

To test the accuracy of the DFT approach and the CP–PAW package we performed geometry optimizations of four small molecules and two small complexes (water dimer and water-chloride complex) relevant to reaction (*i*).

We optimized the structures of Cl_2, HCl, H_2O, and CH_3Cl with the CP–PAW program and compared these with results obtained with the ADF package and literature values. The results of the geometry optimizations are compiled in table 3.1. The first two columns show our CP–PAW results with two different plane wave basis sets.

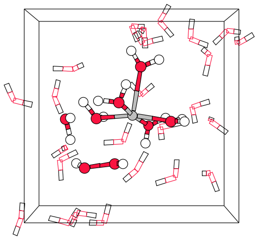

The geometry appears to be practically converged at the plane wave cutoff of 30 Ry. The largest bond distance discrepancy between the 30 Ry and the large 50 Ry basis set are found for R_{OH} and R_{CH}, namely 0.006 Å. Comparing the CP–PAW and ADF results there are larger differences. The largest discrepancy is found for the R_{CCl} (0.024) and R_{ClCl} (0.042) distances. After the simulations had been done, we have been able to trace the differences to the limited number of projector functions for Cl in the PAW method. Increasing the set of projector functions leads to very good agreement with the ADF results. Given the experimental uncertainties, the accuracy of the present CP–PAW results with the smaller set of projectors are satisfactory for our purposes. Bond lengths are slightly overestimated, with the largest errors for R_{ClCl} of 0.077 Å and R_{CCl} of 0.047 Å. Angles are correct within one degree.

Atomization energies obtained with CP–PAW are converged within 0–2 kcal/mol at a plane wave cutoff of 30 Ry. The differences between the CP–PAW energies and the ADF ones are somewhat larger, from 1–4 kcal/mol.

The water dimer H_2O–H_2O and the H_2O–Cl^- complex served as a second validation of CP–PAW. The water dimer has been extensively used as a test model for the hydrogen bond description. A small selection of literature data together with our results are compiled in table 3.2. Large basis set MP2 calculations yield an interaction energy of $\Delta E = -5.0$ kcal/mol [98] and an oxygen–oxygen distance of $R_{\mathrm{OO}} = 2.92$ Å. The best theoretical estimates are probably given by the CCSD(T)/aug-cc-pVTZ calculation of Halkier *et al.* [92] extrapolating for the CCSD(T) limit to $R_{\mathrm{OO}} = 2.90$ Å and $\Delta E = -5.0 \pm 0.1$ kcal/mol and also the CCSD(T) result by Schütz *et al.* ($R_{\mathrm{OO}} = 2.925$ Å and $\Delta E = -4.98 \pm 0.02$ kcal/mol) and Klopper *et al.* ($\Delta E = -5.057$ kcal/mol). The discrepancy of the experimental results ($\Delta E^{\mathrm{exp}} = -5.4 \pm 0.2$ kcal/mol, $R_{\mathrm{OO}}^{\mathrm{exp}} = 2.95$ Å) with these results is attributed by Schütz *et al.* to an underestimation of the anharmonicy corrections in the experimental result.

Compared to the high-level *ab initio* results, the computationally less demanding DFT methods yield similar results. Our CP–PAW results agree very well with the work of Sprik, Hutter and Parrinello [51], who recommended the BP (and BLYP) functional for water simulations. If the larger plane wave basis set of 50 Ry is used, the CP–PAW result for ΔE is 0.34 kcal/mol less negative than the BP/aug-cc-pVDZ result of Kim and Jordan [86] and the BP/TZVP work of Proynov, Sirois and Salahub [41]. Our ADF computation results in a 0.25 kcal/mol stronger interaction. The advanced BLAP3 functional (which combines Beckes GGA exchange functional [36] with the 4-parameter LAP3 correlation functional which includes also second order derivatives of the density) returns virtually the same interaction energy as the BP functional. Note that the oxygen–oxygen bond length is overestimated with BLAP3 even though the water dimer was included in the parameter fitting set. Using the Perdew–Wang exchange functional [99] in combination with LAP3 gives $R_{\mathrm{OO}} = 2.950$ Å [41]. We conclude that for the water dimer CP–PAW gives satisfactory results for our purposes.

A molecular simulation of the S_N2 reaction (*i*) involves the solvation of CH_3Cl, Cl^- and $[Cl\cdots CH_3\cdots Cl]^-$. An accurate simulation requires therefore a good description of the strong hydrogen bonds between water and the electronegative chlorine compounds. Combariza and Kestner [100] have pointed out that proposed empirical force fields for this interaction seem to have serious deficiencies. This is reflected in inaccurate geometries

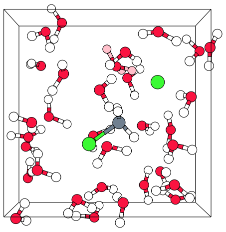

Table 3.2: *Water dimer bonding energy (kcal/mol) and geometry (deg and Å) calculated with PAW (two different plane wave cutoffs) and ADF compared to other Car–Parrinello calculations and accurate DFT, ab initio and experimental results.*

	$\Delta E_{\text{intermol.}}$	R_{OO}	R_{OH_b}	$R_{\text{H}_\text{b}\text{O}}$	$\angle_{\text{OHO}}$
PAW–BP 30Ry	-4.49	2.954	0.997	1.962	173.3
PAW–BP 50Ry	-4.35	2.938	0.990	1.955	171.6
ADF–BP/TZDP	-4.94	2.893	0.982	1.916	172.8
…………………………	…………………………				
CPMD–BP 70Ry[a]	-4.5	2.95			177
CPMD–BP 150Ry[a]	-4.3	2.94			177
DFT–BP/aug-cc-pVDZ*[b]	-4.69	2.886	0.985	1.908	172
DFT–BP/TZVP[c]	-4.69	2.885			
DFT–BLAP3/TZVP[c]	-4.63	2.979			
DFT–PLAP3/TZVP[c]	-4.68	2.950			
DFT–HCTH38/TZ2P[d]	-4.60	2.952			
DFT–B3LYP/aug-cc-pVTZ[b]	-4.57	2.917	0.970	1.953	172
DFT–B3PWa[e]	-3.629	2.950	0.962		
MP2[f]	-4.995	2.917	0.966	1.958	172
CASSCF/aug-cc-pVDZ[g]		3.084	0.948	2.143	172
CCSD(T)[h]	-4.98	2.925			175.7
CCSD(T)[i]	-4.96	2.895			
…………………………	…………………………				
Exp.	-5.4±0.7[j]	2.946[k]			174[l]
	-5.4±0.2[m]	2.952[n]			

[a] CP simulations with a norm conserving pseudo-potential and 70 Ry and 150 Ry plane wave cutoff [51] [b] Kim and Jordan [86]. [c] Proynov, Sirois and Salahub [41]. [d] GGA fitted to a set including the water dimer, BSSE corrected [87]. [e] Beckes hybrid exchange + Perdew-Wang correlation parameterized also for the water dimer, BSSE corrected [40]. [f] ΔE from ref [88] (MP2, 444 AOs, CP corrected) and geometry from ref [89](frozen core, counterpoise corrected); one of the many accurate MP2 results (see text). [g] Complete active space of 16 electrons in 12 orbitals (35793 configuration state functions) computation from ref 90. [h] Schütz *et al.* [91]. [i] Halkier *et al.* [92](aug-cc-pVTZ, frozen core, rigid monomers). [j] ref 93. [k] Experimental microwave result for $R_{0,\text{OO}}$ (=2.976 Å) corrected for anharmonicity, ref 94. [l] ref 95. [m] ref 96. [n] Another anharmonicity correction [97] based on the experiment of ref 94.

for small clusters $\text{Cl}^-(\text{H}_2\text{O})_n$ when compared to experimental evidence and correlated quantum chemical calculations on the MP2 or DFT level.

Here we will just consider the simplest (n=1) $\text{H}_2\text{O}\cdots\text{Cl}^-$ complex. Results are listed

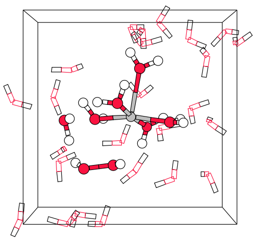

Table 3.3: *Water-chloride bonding energy (kcal/mol) and geometry (Å and deg) calculated with CP–PAW and ADF and compared to other methods.*

	$\Delta E_{\text{intermolec.}}$	R_{HCl^-}	R_{OH}	$R_{\text{OH}'}$	R_{OCl^-}	$\angle_{\text{OHCl}^-}$	$\angle_{\text{HOH}'}$
PAW–BP/30Ry	-15.48	2.090	1.028	0.984	3.115	174.9	101.6
ADF–BP/TZDP	-16.12	2.075	1.014	0.970	3.084	173.0	100.9
DFT–P86/DZVP[a]		2.15	1.01	0.98			
DFT–B3LYP[b]	-14.2	2.16	0.99	0.96	3.15	168.66	101.39
MP2/aug-cc-pVTZ[c]	-14.6	2.116	0.991	0.961	3.094	168.9	100.6
MP4/aug-cc-pVTZ[c]	-14.54	2.125	0.991	0.963	3.103	168.7	100.7
Exp.	-15.0[d] -15.2[e]						

[a] Ref 101 (the type of exchange functional remains unclear in the article). [b] DFT results using a 6-31++G(3*d*,*p*) basis on water and for Cl^- the basis set of McLean and Chandler augmented with diffuse *sp*-function and *d*-functions, ref 100. [c] BSSE corrected results from Xantheas [102]. [d] ΔH = -14.7 ± 0.6 kcal/mol from the mass spectroscopy results from ref 103 minus the zero point energy correction of $\Delta E^{\text{ZPE}} = 0.3$ kcal/mol from ref 102. [e] $\Delta H = -14.9$ kcal/mol both found by Sieck [104] and Yamabe *et al.* [105] using mass spectroscopy minus $\Delta E^{\text{ZPE}} = 0.3$ kcal/mol [102].

in table 3.3. The CP–PAW result for the interaction energy is 0.64 kcal/mol less than the prediction of ADF and the largest geometry difference is found for the R_{OCl^-} equal to 0.031 Å. DFT–BP slightly overestimates the interaction when compared to experiment and performs on the same level as DFT–B3LYP and MP2/MP4. The angle $\angle_{\text{OHCl}^-}$ found with DFT–BP agrees within 1 degree with other theoretical methods methods.

The overall conclusion is that for the water–water and water–anion interactions CP–PAW provides a sufficiently accurate DFT–BP result. In turn, DFT–BP performs as well as MP2/MP4/B3LYP, which results are all close to the experimental data.

3.3.2 Water and hydrochloric acid

The last two test cases, before actually treating the $\text{S}_\text{N}2$ reaction, deal with CP–PAW molecular dynamics simulations of water and hydrochloric acid (HCl) in water (*i.e.* cases (a) and (d) in section 3.2.4. The pure water sample consisted of 32 water molecules in a periodic cubic box with an edge of 9.8650 Å, which was taken from a previous empirical force-field MD simulation. After equilibrating for 15 ps to obtain natural distributions for the atomic positions and velocities at $T = 300$ K, we computed a trajectory of 8.6 ps, from which some structure and dynamics parameters for liquid water were calculated. The hydrochloric acid sample was obtained from the equilibrated water sample by inserting one HCl molecule and scaling the cubic box up to an edge of 9.9684 Å to yield the experimental density of a 1:32 ratio of HCl to H_2O molecules (1.66M) solution. The equilibration time for the HCl and 32 water molecules system was 10 ps and the following

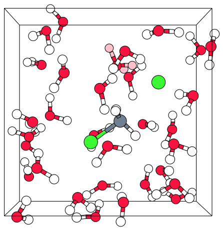

Figure 3.2: *Radial distribution of water at $T = 300$ K (*solid lines*) compared to the Car–Parrinello simulation from ref 51 (*dashed lines*) and the neutron diffraction data from ref 106 (*dotted lines*).*

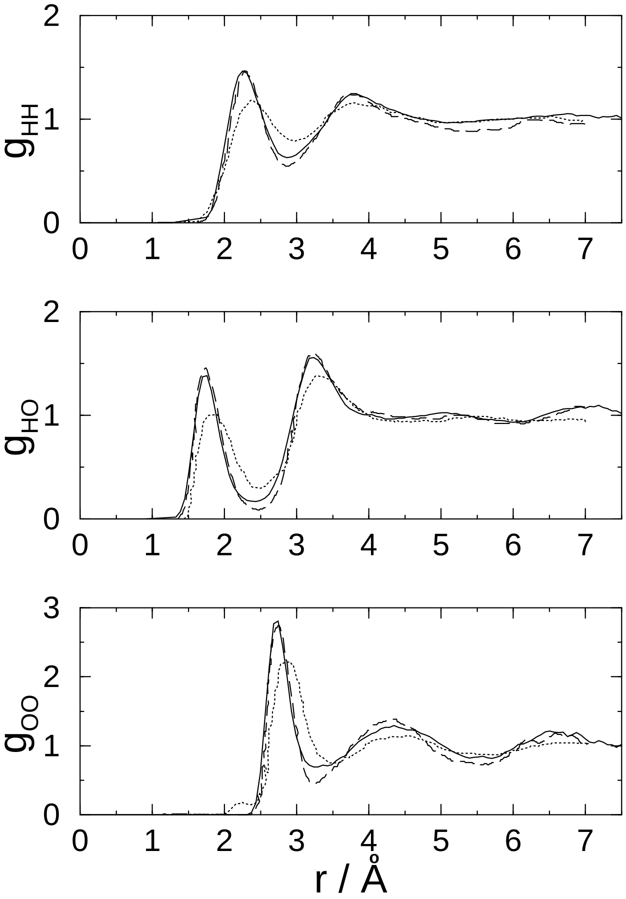

7.7 ps of trajectory was again used for analysis.

The calculated radial distribution functions of the pure water sample are shown in figure 3.2. As expected, our results obtained using the CP–PAW method are very similar to the CP–MD results by Sprik, Hutter and Parrinello [51], with a small discrepancy in the depth after the first peak in g_{OO}. When compared to neutron diffraction data, the peak values are overestimated and their positions shifted to smaller radii. The overall resemblance of the radial distribution is satisfactory, where we note that DFT–BP has a tendency to enhance structure of the liquid, as concluded earlier in ref 51. The peak positions and coordination numbers are listed in table 3.4. In view of the experimental numbers quoted for the coordination numbers, this seems to be a quantity that is difficult to measure. Nevertheless, it can be seen from the table that the CP–PAW simulation underestimates the H_2O coordination somewhat. Comparing the CP–PAW calculations to MD results obtained using the TIP4P or SSD force fields shows similar values for the O–O peak position. However, force field results for the O–H peak position and the

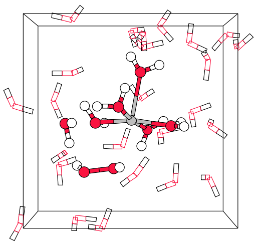

Table 3.4: *Some properties of liquid water compared. Peak maxima R_{OH} and R_{OO} are given in Å. The coordination numbers cn_{OH} and cn_{OO} were estimated for all methods by integration of the first peak of g_{OH} and g_{OO} up to the next minimum (at resp. 2.3/3.25 Å for the AIMD results and 2.5/3.5 Å for the other methods). The experimental self diffusion coefficient $D = 2.35 \cdot 10^{-5}$ cm^2/s [107].*

	R_{OH}	cn_{OH}	R_{OO}	cn_{OO}	D
CP–PAW	1.73	1.78	2.72	4.10	1.3 ± 0.7
SHP^a			2.72	3.9 ± 0.2	0.35 ± 30%
MC/MD(TIP4p)	1.9^b	1.9^b	2.75^c	5.1^b	3.3 ± 0.5^d
MD(SSD)^e	1.9	2.0	2.75	5.2	2.24 ± 2%
neutr. diff.^{f}	1.9	1.6-1.9	2.86	5.3	
X-ray^g			2.7-2.8	4.3	

[a] Ref 51 using Car–Parrinello MD simulations. R_{OO} was read from the graph. [b] From figure 1 in ref 108. [c] MD/TIP4 (transferable intermolecular potential-4 points) results from ref 109. [d] MD/TIP4 results from ref 110. [e] MD/SSD (soft sticky dipole model) results from ref 111 and 112. [f] Ref 106 using neutron diffraction. [g] Ref 113 and ref 114 using X-ray diffraction.

coordination numbers are larger than the CP–PAW results.

The self-diffusion coefficient D in the pure water sample was calculated from the mean-square displacement. Due to the short simulated trajectory of 8.6 ps, the statistical error, estimated from 1 ps block averages, is relatively very high. Our result of $D = 1.3 \pm 0.7 \cdot 10^{-5}$ cm^2/s lies between the experimental value [115] of $D^{\mathrm{exp}} = 2.35 \cdot 10^{-5}$ cm^2/s and the value of $D^{\mathrm{AIMD}} = 0.35 \pm 0.1 \cdot 10^{-5}$ cm^2/s from the CP–MD simulation of ref 51.

The results of the AIMD simulation of the dilute aqueous HCl solution are summarized in figure 3.3 and table 3.5 that show the Cl–H and Cl–O radial distribution functions and list the distribution peak positions and estimated coordination numbers, respectively.

AIMD simulations of aqueous HCl solutions have been reported earlier by Laasonen and Klein [117, 118]. They considered systems of similar size (32 molecules) at various concentrations, the most dilute one (mole ratio 1:31) comparable to ours. However, they focused on the dissociation and the effect of concentration and reported only little on structural properties. As far as comparison was possible, their results agree within the statistical error margins with our findings. Aqueous HCl solutions have also been studied by molecular simulation using (semi-)empirical force fields. Here we can distinguish between simple non-polarizable [119] and more advanced polarizable [116] water models. Note that the force-field studies considered solvation of a single Cl$^-$, leaving out the H$^+$ counter-ion. A comparison with our results is therefore only possible to a limited extent.

From figure 3.3 and table 3.5 we see that peak positions obtained with our AIMD simulations are shifted somewhat to smaller radii compared those of the experiment and

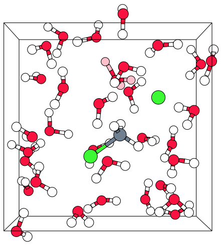

Figure 3.3: *Radial distribution around* Cl^- *at* $T = 300$ *K (*solid lines*) compared to the MD results using a polarizable semi-empirical force field from ref 116 (*dotted lines*).*

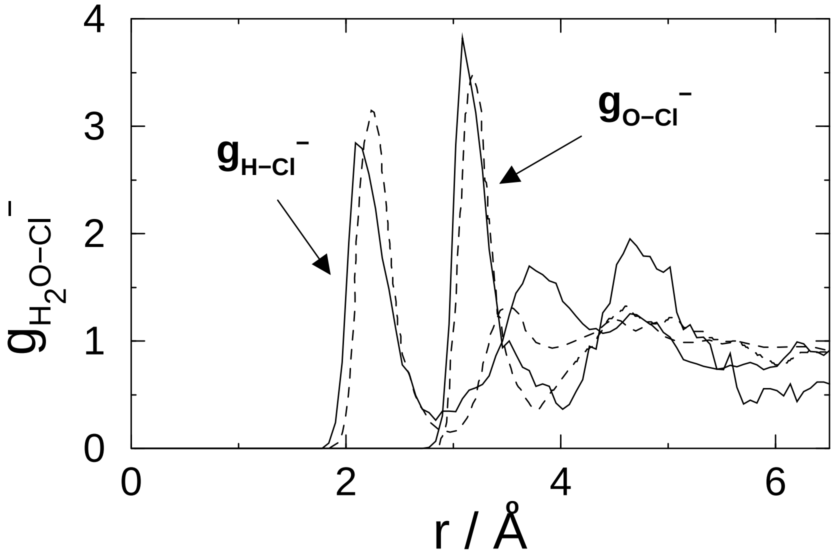

to the polarizable force-field MD simulation. Note also some enhanced structure of the second solvation shell, visible in the $g_{\mathrm{Cl-O}}$ distribution function beyond $r = 4$ Å and also in $g_{\mathrm{Cl-O}}$ beyond $r = 3.5$ Å. This structure is not present in the classical MD simulation. The observed differences need not be entirely due to the use of an *ab initio* (DFT) potential instead of an effective pair potential. It could also be attributed to the presence of the H^+ counter ion that resides on average in the second solvation shell. A second factor could be the small size of the periodic simulation box contributing to some extra structuring.

The coordination numbers listed in table 3.5 show that in our AIMD simulation Cl^- has on average 5 hydrogen bonds, in good agreement with the findings of the CP–MD simulation of ref 118 and the simulation with the advanced polarizable force field. Note that the non-polarizable force field overestimates the coordination of the hydrogens significantly. The oxygen coordination number from our AIMD simulation of 7.2 exceeds the results of the polarizable force field simulation by 1.1. Also the comparison with the experimental [122] range of 5.3-6.2 indicates an overestimate. The large value is due to the shoulder feature on the right of the first peak of the $g_{\mathrm{Cl--O}}$ radial distribution function. Inspections of snapshots indicates that the first solvation shell contains on average one water molecule that is not hydrogen bonded to the Cl^- ion. Again this feature might be attributed to the presence of the H^+ cation in the second solvation shell.

The excess proton is associated with a single water molecule, forming H_3O^+ in approximately 70% of the time, and shared between two water molecules, forming a $H_5O_2^+$ complex in approximately 30% of the time. This is in agreement with the CP–MD results of Tuckerman *et al.* [52, 53], from their study of the solvation and transport of H_3O^+ in

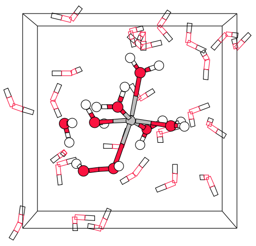

Table 3.5: *Structural parameters of Cl^- in water compared with other molecular simulation results and experiment.*

	$R_{\mathrm{Cl^-{-}H}}$	$cn_{\mathrm{Cl^-{-}H}}$	$R_{\mathrm{Cl^-{-}O}}$	$cn_{\mathrm{Cl^-{-}O}}$
CP–PAW	2.11	5.2	3.09	6.5(7.2)*
MC/TIP4p[a]	2.25	7.0	3.21	7.4
MD/TIP4p[b]	2.34	7.0	3.27	7.2
MD/pol.[c]	2.25	5.9	3.18	6.1
neutr. diff.[d]	2.22-2.26	-	3.20-3.34	5.3-6.2
X-ray[e]	-	-	3.10-3.35	5-11

[a] Ref 119 using Monte Carlo simulations with the TIP4p potential. [b] Ref 116 using Molecular Dynamics simulations with the TIP4p potential. [c] Ref 116 using Molecular Dynamics simulations with a polarizable model. [d] Ref 120 using neutron diffraction. [e] Ref 121 using X-ray diffraction. * Peak integrated up to: $r = 3.75$ Å as in literature, and in parenthesis: till the $g(r)$ minimum at $r = 4.0$ Å.

water at infinite dilution with 60% and 40% abundancies of the H_3O^+ and $H_5O_2^+$ hydronium complexes, respectively. (see for the criteria to distinguish between the complexes refs 52 and 53).

This difference might be attributed to the presence of the Cl^- ion in our work. The water structure surrounding the hydronium complexes is very similar to their results, which follows from the comparison of the radial distribution functions (data not shown).

From the calculations of the gas phase structures and the preparatory AIMD simulations of water and dilute hydrochloric acid, we may conclude that our numerical approach, using DFT–BP together with the Car–Parrinello technique as implemented in the PAW method, yields results consistent with results reported in the literature. These results also confirm reports in the literature that the CP–MD method is able to reproduce properties of aqueous solutions with an acceptable accuracy. An important technical detail is that, for accuracies of 1 kcal/mol for the energies and 0.03 Å for bond lengths of the systems in this study, the plane wave basis set can be kept as small as a 30 Ry kinetic energy cutoff.

3.3.3 S_N2 reaction in gas phase

To study the solvation effects on the reaction between CH_3Cl with Cl^-, we will first consider the gas phase reaction. Starting with separated reactants, the reaction energy $\Delta E(\xi)$ decreases as the attacking chloride anion approaches the dipolar CH_3Cl from the carbon side to form a reaction complex, with complexation energy ΔE^{RC} (see figure 3.4). Moving along to the product side, $\Delta E(\xi)$ increases until the reactants arrive at the D_{3h} symmetric transition state, with energy ΔE^{TS}. The product side of the profile is symmetric to the reactant side. The numerous attempts to estimate ΔE^{RC} and ΔE^{TS} have resulted, especially for the latter, in a variety of values for these quantities. A selection

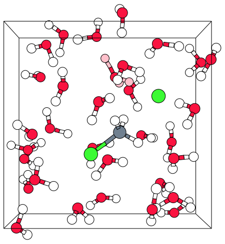

Figure 3.4: *The energy profile for the gas phase reaction calculated with ADF (triangles and solid line) and CP–PAW (crosses and dotted line). The zero-point energy and temperature contributions to the internal energy are very small at* $T = 300$ *K* ($\Delta H_{300\mathrm{K}}$, *circles and dashed line). Due to the much lower entropy of the reactant complex and transition state compared to the free reactants, the Gibbs free energy barrier* $\Delta G = \Delta H - T\Delta S$ *is much higher than the internal energy barrier (squares and solid line).*

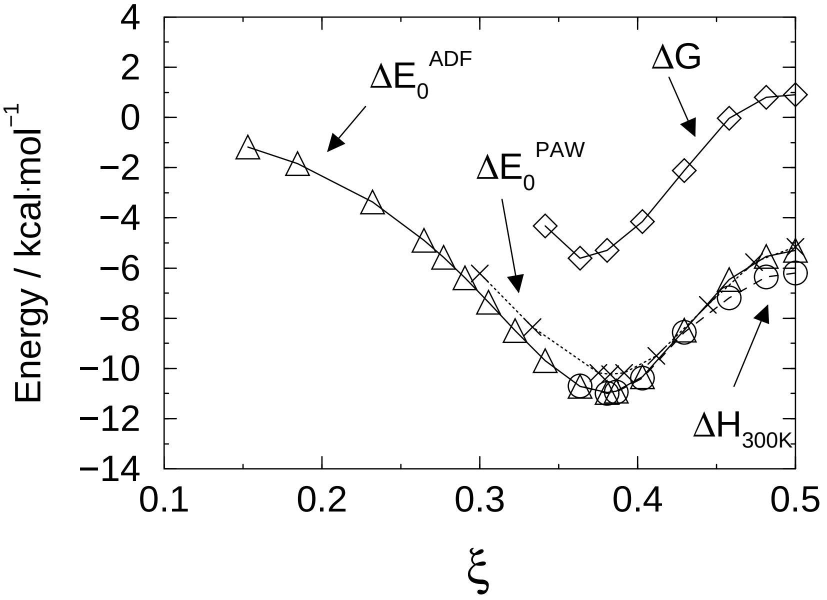

of these energies and the corresponding geometries found in the literature, as well as our own results are compiled in table 3.6. For the ion–dipole reaction complex energy, the best *ab initio* number is probably given by the G2 calculation of Glukhovtsev *et al.*: $\Delta E^{\mathrm{RC}} = -10.5$ kcal/mol. [58, 123] Our DFT results and the *ab initio* and DFT results from literature are all within 1 kcal/mol to this number. Also the experimental estimate by Larson and McMahon agrees within their error estimate with this value. Only the CISD (configurational interaction, including single and double excitations) result by Vetter and Zülicke is about 2 kcal/mol too low.

The results for the transition state energies, varying from -5.7 till 8.7 kcal/mol (see table 3.6) have lead to a number of conflicting views. For instance, Streitwieser *et al.* (ref 61) concluded: "the large differences in TS properties between MP2 and B3LYP suggest that the latter may not always be reliable for TS structures". And Deng *et al.* (ref 56) concluded that "the experimental data (for $\Delta E^{\mathrm{T}S}$ and $\Delta E^{\mathrm{barrier}}$) seem to fall in the region with the MP4 and NL-SCF (= DFT–BP) value as the upper and lower bounds, respectively." The highest-level *ab initio* result for $\Delta E^{\mathrm{T}S}$ is the CCSD(T) calculation by Botschwina, equal to 2.65 kcal/mol. The G2 estimate by Glukhovtsev *et al.* agrees very well with it, as well as the approximate experimental result of 1.0 ± 1.0 kcal/mol. This would imply that the DFT–BP result of -5.7 kcal/mol by Deng is just too low,

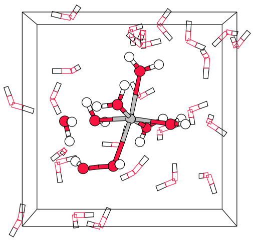

Table 3.6: *Bonding energy and geometry of the reaction complex (RC) and the transition state (TS) in gas phase at $T = 0$ K compared to other methods*

	Reaction complex			Transition state		
	ΔE^{RC} [kcal/mol]	R_{CCl} [Å]	$R_{\mathrm{CCl'}}$ [Å]	ΔE^{TS} [kcal/mol]	R_{CCl} [Å]	$\Delta E^{\mathrm{barrier}}$ [kcal/mol]
CP–PAW/BP	-10.39	1.91	3.01	-5.32	2.37	5.1
ADF–BP	-10.96	1.88	3.09	-5.30	2.35	5.7
DFT–BP[a]	-10.3	1.835	3.098	-5.7	2.342	4.6
MP2[a]	-10.5	1.808	3.266	3.5	2.316	14.0
MP4[a]	-10.6			1.8		12.4
MP2[b]				4.01	2.28	
CCSD(T)[b]				2.65	2.301	
G2[c]	-10.51	1.810	3.270	2.76	2.317	13.26
DFT–B3LYP[d]	-9.72	1.858	3.180	1.1	2.371	10.8
HF/CISD[e]	-8.7	1.823	3.384	8.7	2.408	17.5
MP2[f]	-9.66	1.808	3.267	7.68	2.316	17.34
B3LYP[f]	-9.52			-0.85		8.67
Expt.	-8.6 ± 0.2[g] -12.2 ± 2[i]			1. ± 1.[h]		13.2 ± 2.2[h]

[a] Ref 56 Deng and Ziegler 1994 6-31G(*d,p*). [b] Ref 57 Coupled cluster calculations by Peter Botschwina. [c] Ref 58 Glukhovtsev, Pross and Radom, at $T = 300$ K, G2 method effectively QCISD(T)/6-311+G(*3df,2p*) + ZPE correction for energies and MP2/6-311+G(*3df,2p*) for geometries. [d] Ref 59 Glukhovtsev, Bach, Pross and Radom, basis set: 6-311+G(*3df,2p*). [e] Ref 60 Vetter and Zülicke, geometries using Hartree Fock and energies using all electron CISD with Davidson correction and DZDP basis set quality. [f] Ref 61 Streitwieser 1997, basis set: 6-31G*. [g] Ref 62 Dougherty *et al.* high pressure mass spectrometry. [h] Ref 63 From measurement of the rate coefficient at temperatures above $T = 300$ K using a flowing afterglow technique and a simplified modification of RRKM theory. [i] Ref 64 Larson and McMahon, using ion cyclotron resonance.

and underestimates $\Delta E^{\mathrm{T}S}$ significantly. Streitwiesers MP2 result of 7.7 kcal/mol seems erroneous, compared to the MP2 results of Botschwina (4.01 kcal/mol) and Deng *et al.* (3.5 kcal/mol). The overestimation of the CISD energy (8.7 kcal/mol) is probably due to a combination of an inaccurate (HF) geometry and a too small basis set (DZDP).

There are indications that the too low transition state energy by DFT–BP is systematic for structures with a symmetrical three-center four-electron bond, such as the σ–bond in Cl–C–Cl. For example, Gritsenko *et al.* [124] investigated the very similar

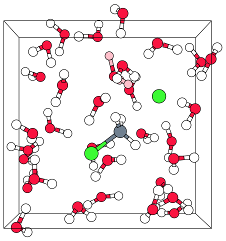

$[F - CH_3{-}F]^-$ transition state structure. They concluded that the delocalization of the exchange hole over the three atoms in combination with a very small non-dynamical correlation, is erroneously represented by the exchange part of the GGA density functional, which introduces a localized hole and thus a spurious non-dynamical correlation [124]. This is, of course, important to keep in mind as we proceed to the S_N2 reaction in water solution. Anticipating the results for the reaction in aqueous solution, we may expect that the transition state in the solvated case is underestimated by an amount in the order of 8 kcal/mol because of the similarity in the geometric and electronic structure of the reacting species. The accuracy of the solvation effects should, in principle, be in the order of 1 kcal/mol, as followed from the simulations in the previous sections.

Figure 3.4 plots the reaction energy profile, as well as the reaction enthalpy ΔH and the free energy ΔG. The latter two are calculated only between the reactant complex and the transition state because of the failure of the smooth change of vibrational contributions into translational and volume work contributions for further separated reactants. The total correction to the calculated energy ΔE_0 to obtain the enthalpy ΔH at a temperature of $T = 300$ K (see eqn 3.3) is very small for the ion–dipole complex. It amounts to less than 0.1 kcal/mol for the equilibrium geometry, and -0.9 kcal/mol for the transition state. This is in good agreement with the estimates by Vetter and Zülicke (0.1 kcal/mol and -0.5 kcal/mol, respectively). The formation of the ion–dipole complex from infinitely separated reactants involves a large negative entropy change, equal to $T\Delta S = -5.5$ kcal/mol. The entropy difference ($T\Delta S$) of the transition state with respect to the free reactants is -7.1 kcal/mol, which means that the intrinsic free energy reaction barrier is about 1.6 kcal/mol higher than the internal energy barrier.

3.3.4 S_N2 reaction in water

In this section, we will discuss the results of the constrained molecular dynamics simulations performed to study the $CH_3Cl + Cl^-$ reaction in a dilute aqueous solution of HCl. To obtain the free energy barrier ΔA, we calculated the mean force of constraint $\langle \partial H/\partial \xi \rangle_\xi$ at 5 points ($\xi = \{0.32, 0.35, 0.40, 0.45, 0.50\}$) along the reaction coordinate ξ (Eqn. 2). As a verification of the simulations, $\langle \partial H/\partial \xi \rangle_\xi$ was also calculated at three points at the product side of the reaction coordinate ($\xi = \{0.55, 0.60, 0.70\}$). Subsequently, two extra simulations were performed for the points $\xi = 0.27$ (because at $\xi = 0.32$ there was still too large an attraction between CH_3Cl and Cl^-, whereas for the separated reactants, the interaction between the reactants is expected approach to zero[†] and at $\xi = 0.43$ (where we expected an extremum in $\langle \partial H/\partial \xi \rangle_\xi$, after having fitted the first five points).

The results for the mean force of constraint are plotted in figure 3.5 (and listed in table 3.8). The dashed line is a cubic spline fitted to the calculated points. Integration of the mean force of constraint with respect to ξ (according to equation 3.7) results in the free energy barrier, shown by the solid line in the figure, yielding a barrier height of 22.2 kcal/mol. Taking into account the 8 kcal/mol error in the gas phase reaction, the free energy barrier of the reaction in aqueous solution would be 30.2 kcal/mol; an overestimation of about 3.6 kcal/mol compared to the experimental result of 26.6 kcal/mol

---

[†] note that in a very large (not periodic) box $\langle \partial H/\partial \xi \rangle_\xi$ will never reach zero

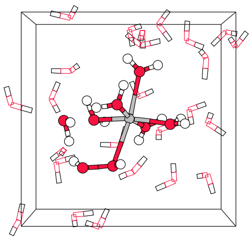

Figure 3.5: *The mean force of constraint* $\langle F \rangle_\xi$ *(dashed line; right-hand-side axis) and the Helmholtz free energy* ΔA *(solid line; left-hand-side axis) versus the reaction coordinate* ξ*. The crosses denote the values from subsequent constrained MD runs, starting with a reaction coordinate value of* $\xi = 0.270$*. The circles are from subsequent runs in the backward reaction coordinate direction, starting from the finished run with* $\xi = 0.55$*. The three asterisks denote the points at* $\xi = \{0.30, 0.40, 0.45\}$ *mirrored in (*ξ*=0.5,*F*=0) to indicate the hysteresis. See also text.*

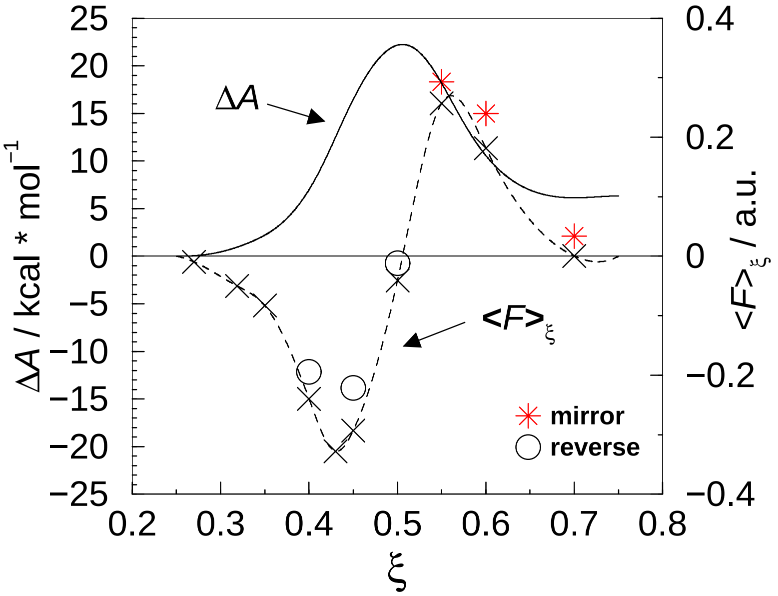

[66].

Because of the symmetry of the reaction the calculated energy profile should be symmetric. From the figure, it is obvious that the shape has a significant asymmetry. This asymmetry has been illustrated by asterisks in the figure. They have been drawn in figure 3.5 above the three points at the product side of the reaction ($\xi = \{0.55, 0.60, 0.70\}$) to picture the equivalent points at the reactant side (with the negative force) for comparison. Moreover, the mean force of constraint does not vanish at the transition state $\xi = 0.5$ as it should. The three product-side points as well as the point at the transition state apply to $[\mathrm{Cl} \cdots \mathrm{CH_3} \cdots \mathrm{Cl}]^-$ configurations with a driving force that is smaller toward the product-side (or larger toward the reactant-side) than was expected from the other points at the reactant-side. This can be characterized as hysteresis when forcing the reaction by the method of constraint. Most likely, this hysteresis is due to the surrounding water shell, which apparently adapts too slowly to the changing reactants configuration, when going from one simulation to the next by increasing ξ.

To test this explanation, we performed calculations for the reversing of the reaction. We performed the backward reaction for three points ($\xi = \{0.50, 0.45, 0.40\}$), where we

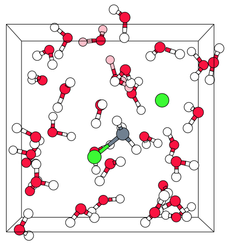

started from the constrained MD run at $\xi = 0.55$ and moved the constraint value slowly to the previous point on the reaction coordinate. Subsequently, we equilibrated for 2.5 ps, collected the force of constraint for 3 ps, and moved on to the next point, similar to the points of the forward reaction direction. The results are shown by the circles in figure 3.5. The hysteresis at the first point, $\xi = 0.50$, has disappeared since $\langle F(0.5)\rangle_\xi$ is zero (within the error in the force), as expected. Apparently, the solvent configuration is not pulling on either side of the reacting complex, at this point. For the other two points, we now find smaller absolute values for the mean force of constraint than we found in the forward reaction. This is consistent with the picture of a "memory effect" in the solvent, *i.e.* a too slow adaptation of the water configuration to the changed reaction coordinate.

A rough estimate of the systematic error on the free energy barrier due to the hysteresis can be made, by assuming that the deviation in the force will increase linearly from zero at the starting point of the separate reactants ($\xi \approx 0.25$) to the observed -0.041 a.u. at the transition state. Correcting the free energy profile for the corresponding overestimation (3.2 kcal/mol), gives a barrier height of 27 kcal/mol. The excellent agreement with experiment (26.6 kcal/mol), after the corrections for the DFT–GGA error in the gas phase transition state energy and the hysteresis in the constrained MD runs, must be a bit fortuitous, for the following reasons. First of all we have found the accuracy of the DFT–BP description of the energetics of the solvation to be of the order of 1 kcal/mol. Secondly, the experimental result refers to more dilute solution at neutral pH, with typically potassium used for the counter cation. In the present calculation, a proton acted as counter-cation, which can be expected to have some influence on the energetics of the reaction via its charge and solvation structure.

Next, we turn to the structural aspects of the reaction. In figure 3.6, we compare the radial distribution functions of the water atoms with respect to the leaving and attacking chloride ions, calculated for the transition state and for the more separated reactants ($\xi = 0.32$). From integration over the first peak of the distribution functions, the coordination numbers for the chloride ions were calculated and compiled in table 3.7 (for all simulated values of ξ).

To start with the separated reactants at $\xi = 0.32$, we note that the distribution functions $g_{\mathrm{Cl'-O}}$ and $g_{\mathrm{Cl'-H}}$ of the attacking chloride anion (dashed lines in the lower graphs) are very similar to the functions of pure HCl in water (dotted lines; see also figure 3.3). The distribution around the leaving chloride atom at $\xi = 0.32$ (upper two graphs) is in agreement with pure CH_3Cl in water (dotted lines), except for a small peak in $g_{\mathrm{Cl-H}}$ at $r = 2.3$ Å in the latter. The small peak in the pure CH_3Cl solution (case b) in section 3.2.4) can be attributed to one water molecule which is hydrogen bonded to the Cl of methylchloride. The main reason for the absence of this peak in $g_{\mathrm{Cl-H}}$ of the leaving Cl, must be the presence of the Cl^- anion, which has a strong influence on the solvent structure. The coordination numbers (in table 3.7) shows that the attacking chloride anion is solvated by about five water molecules, whereas the separate CH_3Cl does not show any attraction of water atoms. Note that $cn_{\mathrm{Cl'-H}}(\xi = 0.32) = 4.3$ confirms that this starting constrained simulation indeed does not fully resemble separated reactants as concluded in section 3.3.4, whereas the extra simulation of $\xi = 0.27$ shows coordination numbers of 5.4 and 6.3 in agreement with the values for the pure HCl in water (5.2 and 6.5, table 3.5).

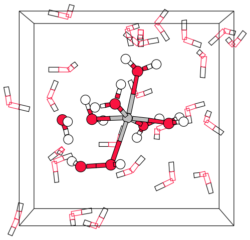

Table 3.7: *The coordination numbers of the water solvation shells around the attacking Cl′ and the leaving Cl, at different points on the reaction coordinate. The coordination numbers were calculated by integration over the peak in the radial distribution function (a hyphen indicates there was no such peak). Numbers between parentheses indicate that the peak was too broad for an accurate estimate.*

	Attacking chloride		Leaving chloride	
ξ	$cn_{\mathrm{Cl'-H}}$	$cn_{\mathrm{Cl'-O}}$	$cn_{\mathrm{Cl-H}}$	$cn_{\mathrm{Cl-O}}$
0.27	5.4	6.3	-	-
0.32	4.3	5.1	-	-
0.35	4.9	4.6	-	-
0.40	4.7	4.4	-	-
0.43	4.8	4.8	-	-
0.45	4.2	4.5	1.1	4.4
0.50	3.3	4.3	2.7	(4.8)
0.50*	2.9	(5.6)	3.0	(4.3)
0.55	2.2	(4.8)	4.0	5.0

* Coming back from $\xi = 0.55$, see text.

Next, we discuss the radial distribution functions for the transition state configurations (solid lines). These show a more equal solvation of the attacking and leaving chloride ions. However, the first peaks of the attacking chloride ion are still much more pronounced than the peaks arising from the first solvation shell around the leaving chloride. Also, the minimum at $r = 3.5$ Å is much deeper in $g_{\mathrm{Cl'-O}}$ than in $g_{\mathrm{Cl-O}}$. This asymmetry in the chloride solvation is reflected less strongly in the coordination numbers (table 3.7). The attacking chloride still has on average 3.3 hydrogens in the first shell, while the leaving chloride has only 2.7. The Cl–O coordination numbers cannot be determined accurately because the oxygen distribution function $g_{\mathrm{Cl-O}}$ of the leaving Cl does not show an unambiguous minimum. Still, from the hydrogen distribution, we can conclude that the attacking Cl is stronger solvated than the leaving Cl, at $\xi = 0.5$, which must be the grounds for the effective force of constraint at the transition state. Indeed, in the reversed reaction direction, where we found the expected $\langle F(0.5)\rangle_{\xi} = 0$, we also see a more symmetric hydrogen distribution (radial distribution functions not shown) and coordination number: 2.9 for the attacking Cl and 3.0 for the leaving Cl. Just before the transition state, the leaving chloride has only one hydrogen in the "first shell" ($cn_{\mathrm{Cl-H}}(\xi = 0.45) = 1.1$), whereas just after the transition state the attacking chloride still has two hydrogens ($cn_{\mathrm{Cl'-H}}(\xi = 0.55) = 2.2$). This difference leads to a larger value for the mean force of constraint at $\xi = 0.45$ in comparison with $\xi = 0.55$, and gives a

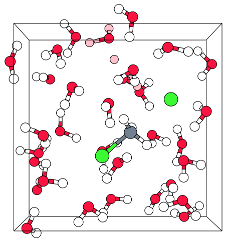

Figure 3.6: *Radial distribution of water around the leaving Cl atom (upper graphs) and attacking Cl′ atom (lower graphs) for two points on the reaction coordinate, namely $\xi = 0.5$ (the transition state: solid lines) and $\xi = 0.32$ (initial reactants: dashed lines). The graphs on the left-hand-side show the distribution of the water oxygens, and the right-hand-side graphs the distribution of the water hydrogens. For comparison, dotted lines are drawn in for the $g_{\mathrm{Cl-O}}$ and $g_{\mathrm{Cl-H}}$ of CH_3Cl in water (upper graphs) and HCl in water (lower graphs).*

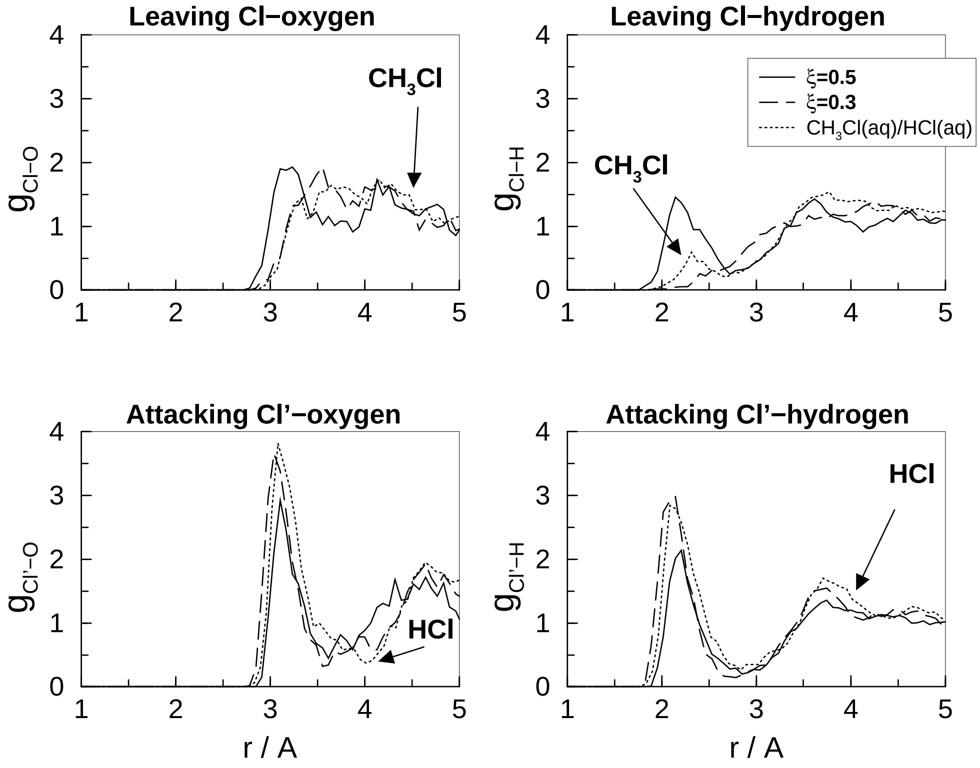

structural explanation for the observed hysteresis in the free energy profile of figure 3.5.

3.4 Discussion

The present results show that Car–Parrinello MD simulation is a powerful tool to assess solvent effects on a simple S_N2 reaction. Semi-quantitative results for the energetics and a detailed picture of the structural aspects of the reaction are obtained. However, the study also shows that at present time the calculations are not without limitations. The most important ones, the relatively small box size and the short trajectories that can be calculated, cannot easily be removed because they are related to the high computational expense. For example, the time necessary to calculate one point from figure 3.5 (say, 6 ps total time for equilibration and sampling) was about 11 days on 6 IBM-SP nodes

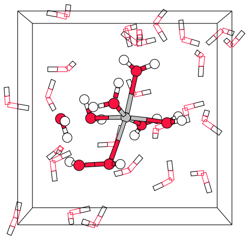

(power2sc processor) or 29 days on a cluster of 16 IBM RS6000 43P workstations.

The hysteresis found in the force of constraint is due to a memory effect in the solvent, which is directly related to the fact that the last configuration of every constrained AIMD run is used to construct the initial configuration for the simulation at the next point of the reaction coordinate, in combination with the limited time scale accessible to an AIMD simulation. Apparently, the rearrangements that have to be made by the solvent, to follow the change in the reaction coordinate from point to point, occur on a much longer time scale than the rotations and vibrations and diffusion of water molecules that are well described by our 10 ps molecular dynamics trajectories.

Simulating for longer times is the trivial solution to avoid memory effects. However, this could be as impractical as waiting for the reaction to occur spontaneously because there are indications that the adaptation of the aqueous solvent to the changing solute configurations is an activated process instead of a slowly diffusive process. In the 9 ps transition state simulation, for instance, a drift in the force of constraint would be expected, which should asymptotically decay towards zero, in the case of a slowly diffusively adapting solvation shell, but was not observed. Note also that, although sampling for extremely long times for each point ξ' will in principle remedy the hysteresis in the free energy profile, a too low barrier is found as these activated solvent adaptations are missing in the free energy profile. For comparison with the experimental rate constant, this is corrected by calculation of the pre-exponential factor, which includes the transmission coefficient κ, but the computational demand of this exercise increases dramatically with the amount of the underestimation of the free energy barrier (see further appendix 3.5). Secondly, we note that the force-field Monte Carlo simulations of the same S_N2 reaction in 250 water molecules by Chandrasekhar *et al.* [65], using the umbrella sampling technique, also shows a significant hysteresis. The calculated probability distribution $P(\xi = \xi_{TS})$ (figure 3.5 in ref 65) is not symmetric: the second peak at the reactant side next to the transition state is absent at the product side. This is also reflected in the radial distribution functions obtained from the MC simulation of the transition state.

It has become clear that certain necessary changes in the solvent as the reaction takes place are rare events on the typical AIMD time scales. One way to handle the problem of hysteresis is therefore to include the required solvent rearrangements into the reaction coordinate. Unfortunately, due to the large number of molecules involved and their complex rearrangements, finding a proper reaction coordinate is virtually impossible. The need to include solvent degrees of freedom into the reaction coordinate was also concluded recently by Geissler, Dellago and Chandler from their molecular simulations of the dissociation of NaCl in water [125]. In this work, they found additional free energy barriers in the solvent that have to be overcome as the reaction (*i.e.* the dissociation) occurs. For instance, the addition of a water molecule in the first solvation shell of Na^+ to bring the coordination from the initial five-fold to the final six-fold, required an amount of work equal to 1.7 k_BT ($\approx$1 kcal/mol)). During the S_N2 reaction in the present work, a Cl^- solvation shell has to lose two water molecules to reach the transition state, while at the same time the CH_3Cl chloride has to bond with three water molecules which have to be taken from the water network.

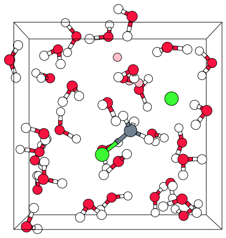

3.5 Conclusions

Using the Car–Parrinello method, we studied the solvation effects on the identity reaction between Cl^- and CH_3Cl in a dilute (1:32 mole ratio) aqueous solution of HCl. We compared the free energy profile of the reaction in the gas phase and in solution and analyzed the structure of the solution at different stages of the reaction. The free energy profile of the reaction in aqueous solution was obtained using the method of constrained molecular dynamics simulations in combination with thermodynamic integration. The calculated barrier yields 27 kcal/mol after application of certain corrections (see below). This corrected value is in good agreement with the experimental value of 26.6 kcal/mol.

There are two important error sources in these calculations. The DFT (Becke–Perdew functional) electronic structure calculations describe the solvent and the solvent–solute interactions, in particular the solvation of the Cl^- ion, the formation of the initial ion–dipole complex of Cl^- with CH_3Cl, and the solvation of the reaction system in the course of the reaction, with reasonable accuracy. However, although DFT–BP does exhibit an energy rise when going from the ion–dipole complex to the transition state, thus reproducing the well-known double well energy profile for the gas phase reaction, it underestimates the barrier height of ca. 13 kcal/mol by as much as 8 kcal/mol. This error, being related to an imbalance in the description of exchange and correlation in the transition state by present day generalized gradient approximations like Becke–Perdew, *cf.* ref 124, will persist in the transition state in solution. A correction of 8 kcal/mol has therefore been applied to the calculated barrier height. In the second place a "hysteresis", or inequivalence of forward and reverse reaction, has been found in the force of constraint profile. The hysteresis is due to a slow adaptation of the solvent to the reacting solutes and has the effect of pulling the reactants back toward the initial state when the constrained reaction coordinate is moved toward the product side. Apparently, the rearrangements that have to be made by the solvent occur on a much longer time scale than the rotations and vibrations and self-diffusion of water molecules that are well described by our 10 ps molecular dynamics trajectories. On the time scale of MD simulations, the rearrangements needed in the solvation shells of the reactants are rare events by themselves. Including solvent degrees of freedom in the reaction coordinate is in principle the way to handle this type of the rare events. [125]

The Car–Parrinello MD simulation of the reactants in a box with 32 water molecules is an important improvement on the numerous micro-solvation and dielectric continuum calculations. It is a great advantage that the varying solvation during the course of the reaction, due to the shift of negative charge from the attacking chloride initially to the leaving chloride finally, does not have to be described by parameterized model potentials that cannot be optimal for all occurring situations along the reaction coordinate. From the good agreement with experiment - after the corrections described above - we may infer that both the energetic and the entropic effects of the solvation on the free energy barrier are obtained to quite satisfactory accuracy with the AIMD simulation. Further improvements of this type of calculation can be envisaged, of both technical and more fundamental nature. At the technical side, we note that the limited size of the total system implies that approximations are made on the long range interactions in the solvent. Also the fixed volume has a small effect on the forces because the changing size of the reaction

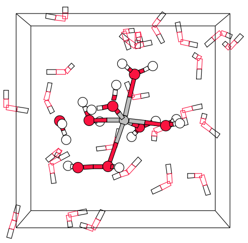

complex in solution affects the pressure on the system. The extension of the present type of calculation to larger systems will certainly be possible in the future due the rapid increase in available computing power. The most important deficiencies of the present work are of a more fundamental nature. The first is the underestimation of the transition state energy by the GGA (Becke–Perdew) functional. This will have to be remedied by the development of more accurate functionals, which, in view of computation time, should not rely on the incorporation of exact exchange. In the second place, it is desirable that the dynamics methods are improved in order to keep the necessary simulation times down to a manageable length. One possibility would be the development of methods to handle the slow adaptation of the solvent structure to the changing reaction coordinate by incorporating the necessary change in solvent structure in the reaction coordinate.

Acknowledgment

BE gratefully thanks W. K. den Otter for helpful discussions on the method of constrained MD. Support by the Prioriteitsprogramma Materialen - Computational Materials Science for BE, EJM is gratefully acknowledged. We thank the foundation NCF of the Netherlands Foundation for Scientific Research (NWO) for computer time. EJM acknowledges the ”Royal Netherlands Academy of Arts and Sciences” for financial support.

Appendix A: Force of constraint

The system can be constrained to a hyperplane $\xi(\mathbf{r}) = \xi'$ in phase space in a molecular simulation, by extending the Lagrangian with a term $\lambda \cdot (\xi(\mathbf{r}) - \xi')$, with $\mathbf{r}$ the atomic positions, ξ our reaction coordinate, and λ the Lagrange multiplier associated with the force on the holonomic constraint. Each atom i then feels a constraint force, equal to $F_i(\xi) = \lambda(d\xi/dr_i)$. It is well known that the use of constraints affects the phase space distribution (see *e.g.* ref 71). For a velocity-independent property p, the bias introduced by a constraint can be compensated using the relation

$$\langle p(\mathbf{r})\rangle^{\text{unconstr.}} = \frac{\langle Z^{-1/2} p(\mathbf{r})\rangle_\xi}{\langle Z^{-1/2}\rangle_\xi} \tag{3.5}$$

where the factor Z is defined by

$$Z = \sum_i \frac{1}{m_i}\left(\frac{\partial \xi}{\partial \mathbf{r}_i}\right)^2 \tag{3.6}$$

This was generalized recently for velocity dependent properties, such as the the mean force of constraint [17, 76]. In the formulation of reference 17 it reads:

$$F(\xi) = \frac{\langle \lambda_\xi Z^{-1/2}\rangle_\xi + \frac{1}{2} k_B T \langle Z_\xi^{-5/2} \sum_{i=1}^{N} \frac{1}{m_i} \nabla_i \xi \cdot \nabla_i Z\rangle_\xi}{\langle Z^{-1/2}\rangle_\xi} \tag{3.7}$$

where T is the temperature, k_B is Boltzmann's constant, and m_i is the mass of particle i.

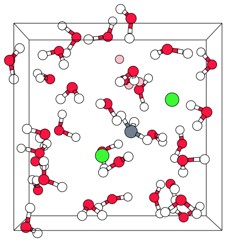

Table 3.8: *The average constraint force for the different reaction coordinate values ξ. The constraint force is shown once as the Lagrange parameter λ, once corrected according to equation 3.5 and once more with the full correction according to equation 3.7.*

ξ	λ	$\langle Z^{-1/2} \cdot \lambda \rangle_\xi / \langle Z^{-\frac{1}{2}} \rangle_\xi$	$F(\xi)$
0.27	-0.0091	-0.0098	-0.0095
0.32	-0.0494	-0.0498	-0.0496
0.35	-0.0815	-0.0831	-0.0830
0.40	-0.2384	-0.2396	-0.2394
0.43	-0.3268	-0.3277	-0.3276
0.45	-0.2929	-0.2931	-0.2930
0.50	-0.0408	-0.0408	-0.0408
0.55	0.2570	0.2572	0.2571
0.60	0.1955	0.1966	0.1964
0.70	0.0018	0.0004	0.0002

The second term in the numerator of equation 3.7 arises because the mean force of constraint depends on the velocities, through the kinetic term $\partial K / \partial \xi$ in the force of constraint (equation 1). In their work, they demonstrated the importance of the corrections for a constrained bending angle of a tri-atomic molecule and for a constrained dihedral angle in a tetra atomic molecule.

In table 3.8, we show the results for the mean force of constraint for our $\mathrm{S_N2}$ reaction using the constraint of equation 2, once as λ, once corrected according to equation 3.5 and once using equation 3.7. As the differences are very small, the bias on our system introduced by the constraint must by very small.

Appendix B: Reaction rate

To calculate the reaction rate of the $\mathrm{S_N2}$ reaction in aqueous solution, it is not correct to take the computed free energy difference ($\Delta A^\ddagger = 27$ kcal/mol) and plug it into the textbook relations

$$\frac{d[\mathrm{X}^-]}{dt} = \frac{d[\mathrm{CH_3Y}]}{dt} = -k_f[\mathrm{X}'^-][\mathrm{CH_3Y}] + k_b[\mathrm{Y}^-][\mathrm{CH_3X}] \tag{3.8}$$

$$k_f = \frac{k_B T}{h} e^{-\beta \Delta A^\ddagger} \tag{3.9}$$

for two reasons.

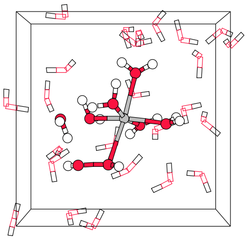

In the first place, is the exponential term, $e^{-\beta\Delta A^\ddagger}$ related to the Boltzmann probability $P(\xi^\ddagger)$ to find the reacting system in the transition state independent of the exact starting configuration in the reactant well. Thus, instead of taking $\Delta A^\ddagger = A(\xi = 0.5) - A(\xi = 0)$, the Boltzmann factor is obtained by integration over the reactant well of the free energy profile, using

$$P(\xi^\ddagger) = \frac{e^{-\beta A(0.5)}}{\int\limits_{-\infty}^{0.5} d\xi e^{-\beta A(\xi)}} \tag{3.10}$$

As the energy will increase rapidly as ξ decreases below zero (since it is associated with configurations in which none of the Cl's are chemically connected to the CH_3 part), it is not necessary to calculate the profile $A(\xi)$ up to $\xi \rightarrow \infty$. Also, we note that the profile is dependent on the size of the periodic supercell, simply because the available space, and therefore the entropy, of the system at a certain reactant state constraint value (say $\xi = 0$) increases with the box size. (Obviously, the probability to find the two reactants in the transition state is much smaller in an ocean of liquid than in a small box with a few tens of water molecules). Normalizing the Boltzmann factor with the concentration gives the correct result for the transition state theory rate for the second order rate coefficient.

In the second place, does the free energy in the exponential term of equation 3.9 include a correction for the fact that not in all occasions that the system reaches the transition state, it actually crosses the barrier to end up in the product well. Instead, the computed Boltzmann factor (equation 3.10) is an ensemble average that only gives the (transition state theory) upper limit of the rate constant k^{TST}, assuming that every time the barrier top is reached, the products are subsequently formed. Multiplying k^{TST} by the so-called transmission coefficient, κ, gives the true rate constant. The transmission coefficient is a time dependent function, which correlates the initial velocity of the system along the reaction coordinate, $\dot{\xi}$, on top of the barrier at time t with ξ at time $\tau = t + \Delta t$:

$$\kappa(\tau) = \frac{\left\langle \dot{\xi}(0)\delta(\xi(0) - \xi^\ddagger)\theta(\xi(\tau) - \xi^\ddagger)\right\rangle}{\left\langle \frac{1}{2}|\dot{\xi}(0)|\right\rangle} \tag{3.11}$$

For $\tau = 0$, the transmission coefficient $\kappa = 1$, but κ rapidly drops with increasing τ to a plateau value for τ much larger than the time scale of the barrier recrossings. This plateau value gives the desired correction to k^{TST}.

For a reaction in solution κ is related to the coupling λ between the reactants and the solvent, as schematically drawn in figure 3.7. At low reactant-solvent coupling values (aka Lindemann-Hinshelwood regime or energy diffusion regime), the energy obtained by the reactants from the solvent to reach the barrier top cannot be dumped rapidly back to the solvent environment after crossing the barrier. As a result, the reactant complex retains enough energy to cross the transition barrier back and forth until it finally loses the energy and the correlation between $\dot{\xi}(0)$ and the final value of ξ is low, hence a small transmission coefficient κ which is proportional to λ. At the other side (aka Kramers regime or spatial diffusion regime), the reactant complex is pushed back and forward by the fluctuation in the solvent environment, which also results in a small correlation and thus a small κ which is inversely proportional to λ. In between these two reactant-solvent coupling extremes κ has values closer to unity.

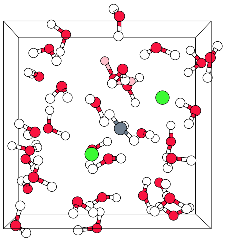

Figure 3.7: *Transmission coefficient κ as a function of the reactant-solvent coupling λ.*

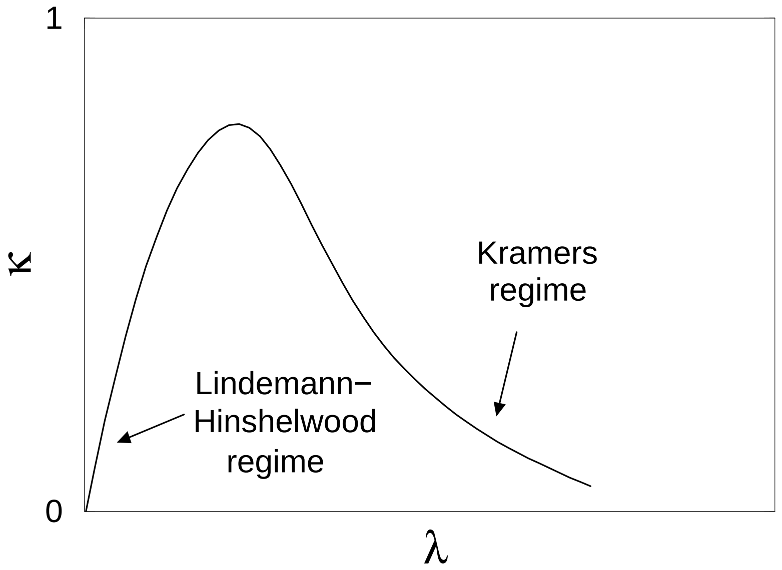

For the S_N2 reaction in water, we see that a large force pulls the $[Cl\cdots CH_3\cdots Cl]^-$ complex along the reaction coordinate in the either direction if the solvation of the two chloride groups becomes unbalanced (compare table 3.7 and figure 3.5). In order for the system to proceed to either side, one Cl has to gain solvent molecules in the solvation shell, whereas the other Cl has to expel H_2O molecules. Due to this very strong coupling between the solvent environment and the reaction complex, a low transmission coefficient is expected for the S_N2 reaction in water.

Appendix C: Coordination constraint as the reaction coordinate

During the constrained AIMD simulation at $\xi = 0.55$, a sudden jump in the force of constraint was observed, which is shown in the upper panel of figure 3.8 by the gray line and emphasized by the running average (black line). The jump indicates a fluctuation in the solvent environment around the $[Cl\cdots CH_3\cdots Cl]^-$ complex, which could be a stepwise relaxation of the lagging behind Cl solvation shells to the new constrained reaction coordinate value $\xi = 0.55$. Comparison of Cl coordination numbers and radial distribution functions before and after the sudden jump does not show significant modifications in the hydration, probably because the relevant solvent fluctuations are averaged out. We therefore computed a simple running function which counts all hydrogens around each Cl weighted by the square of the reciprocal Cl-H distance:

$$f_i(t) = \sum_j r^{-2}_{\mathrm{Cl_i-H_j}}(t) \qquad (3.12)$$

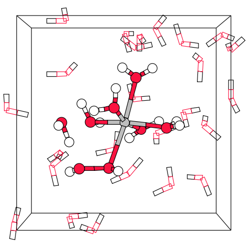

Figure 3.8: *Upper graph: the force of constraint shows a sudden jump at* $t \approx 26$ *in the AIMD run with* $\xi = 0.55$ *(gray line). Lower graph: the difference in amounts of solvation for the leaving and attacking Cl groups* $f_{\mathrm{Cl'}} - f_{\mathrm{Cl}}$, *as defined by equation 3.12, shows a very similar behaviour, which confirms the strong coupling between the reactants and the aqueous solution. The black lines are running averages.*

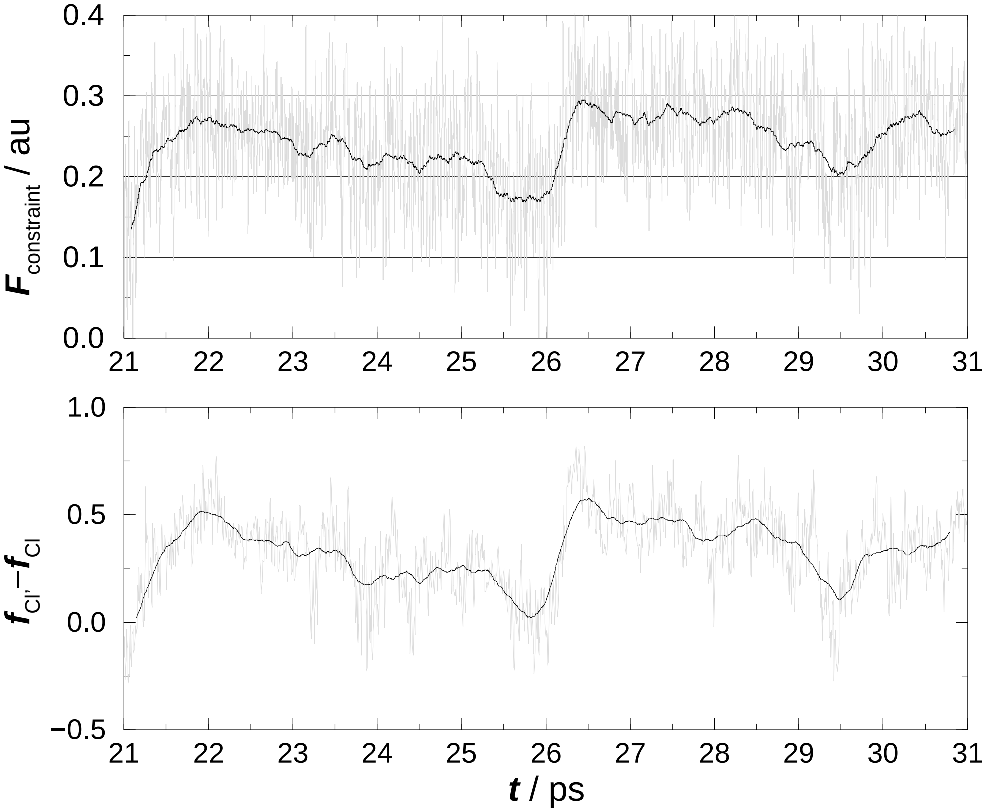

This function gives an indication of the number of water molecules in the neighborhood of a Cl and thus of the amount of Cl hydration. The difference of the amounts of hydration for both Cl's is plotted in the lower panel of figure 3.8, again with a running average in black. The figure indeed shows a strong correlation between the difference of Cl solvation and the force of constraint, confirming the expected strong reactant-solvent coupling (see also appendix 3.5).

Can we use this result to improve the reaction coordinate by including solvent degrees of freedom? Perhaps we can even control the S_N2 reaction in aqueous solution completely by gradually switching on the amount of hydration on the leaving Cl and simultaneously switching off the amount of hydration on the attacking Cl, using a constrained reaction coordinate of the form $f_{\mathrm{Cl'}} - f_{\mathrm{Cl}}$? Sprik proposed in 1998 such a coordination constraint using a fermi-dirac function of the solute-solvent distances to study the coordination in a lennard-jones argon liquid [126] and the (de-)protonation of H_2O in liquid water [127]. This approach and also his results indeed look very promising. However, we should note

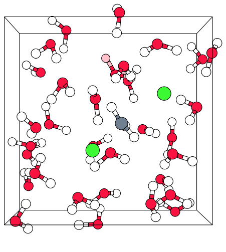

that a coordination constraint of this type does not fix the actual transition state of a process which involves a change in the coordination number. In other words, use of transition state theory will lead to a too low barrier so that one still has to perform the expensive compution of the transmission coefficient to compare with experiment.

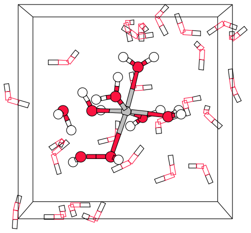

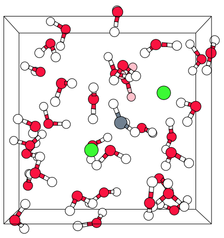

Chapter 4

Preparatory study of hydrated iron(II) and iron(III)

In the previous chapter, we have shown that the *ab initio* molecular dynamics (AIMD) simulation technique can provide us with detailed microscopic insight of elementary physical and chemical processes, such as the hydrophilic solvation of the chlorine ion and the hydrophobic solvation of methyl chloride, proton transfer through the aqueous solvent, and the prototype S_N2 reaction. The remaining chapters of this thesis are devoted to the mysterious and much debated field of Fenton chemistry. Fenton chemistry embodies a broad range of chemical reactions initiated by the application of the oxidative mixture of iron(II) ions and hydrogen peroxide, known as Fenton's reagent, named after H.J.H. Fenton, an (at that time) undergraduate at Christ's College in Cambridge, England, who reported in april 1876 a reaction between ferrous sulfate, hydrogen peroxide and tartaric acid in Chemical News. [128] More than a century later, the outstanding questions on the reaction mechanism and the active intermediates still remain, and obscure the wider appreciation of the Fenton chemistry in both industrial applications and in biological functions.

Many essential life processes, including photosynthesis, biosynthesis of the female hormone progestrone, and the metabolism of methanotrophs, involve multi-electron transformations catalyzed by iron containing metalloenzymes. In fact, iron is the most abundant transition metal ion in most terrestrial organisms. Hydrogen peroxide is a byproduct of aerobic metabolism and is implicated in cell death, aging, and a variety of pathologies [129, 130]. The toxic effects of H_2O_2 are attributed to DNA oxidation *via* Fenton-like reactions. Metalloenzymes such as heme-containing cytochrome P450 and nonheme methane monooxygenase, have inspired the development of biomimetic alkane hydroxylation catalysts [131, 132]. Current industrial applications of Fenton's reagent are found in catalyzed bleaching processes [133], pharmacology [134, 135], and advanced oxidation processes (AOPs), which mainly involve the destruction of organic pollutants in surface and groundwaters as well as in industrial wastewaters [136–139]. Moreover, Fenton chemistry was drawn to our attention by questions regarding the mechanism asked by the industry in the first place [140].

Our title study, *Chemistry in water*, thus continues with a very challenging system,

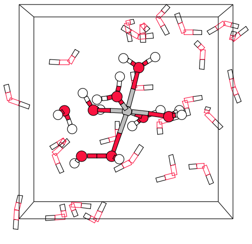

Figure 4.1: *Optimized ground-state structures of* $[\mathrm{Fe}^{\mathrm{III}}(H_2O)_5(H_2O_2)]^{3+}$ *(left-hand-side) and* $[\mathrm{Fe}^{\mathrm{II}}(H_2O)_5(H_2O_2)]^{2+}$ *(right-hand-side).*

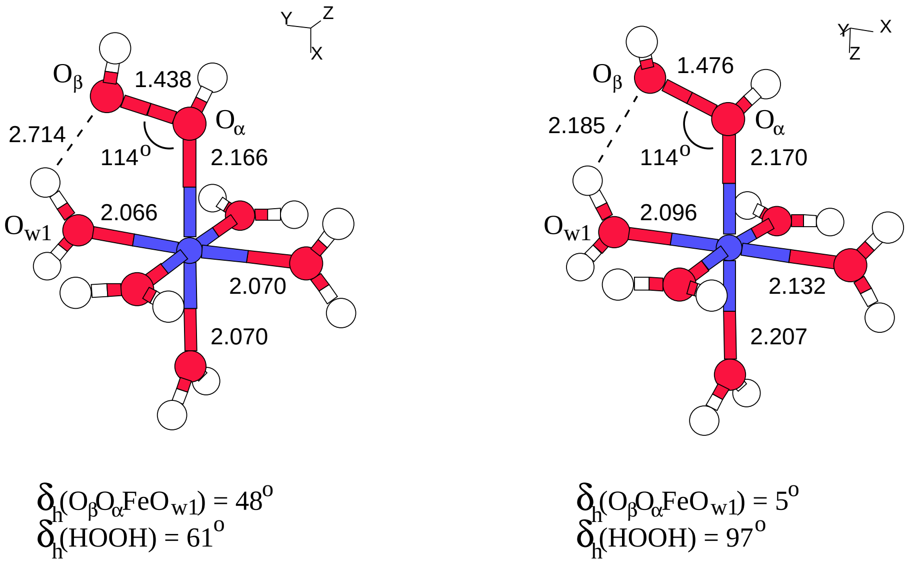

involving simultaneously the above mentioned physical and chemical processes, added to oxidation reactions catalyzed by the spin polarized transition metal, changing oxidation states of the metal ion and ligand exchange reactions. This complex involvement of Fenton chemistry should be seen as the ultimate test for the state-of-the-art AIMD technique. Microscopic insight of chemistry in water remains our main goal, but we also aim to solve the open questions on the active intermediate and the reaction mechanism of Fenton chemistry in water. We will furthermore investigate on the application of a number of techniques, including vibrational analysis, calculation of free energy, and transition path sampling, on Fenton's reagent and Fenton chemistry in water. This chapter will serve as an introduction, starting with a molecular orbital analysis of hydrogen peroxide and of the hexaaquairon and pentaaquaironhydrogen peroxide complexes. After that the AIMD simulations of iron(II) and iron(III) ions in water are discussed, and we end with the estimation of the acidity constant of hexaaquairon(III) in water.

4.1 Gas phase complexes

As we shall see later on, the chemical reactivity in aqueous solution of Fenton's reagent (Fe^{2+}/H_2O_2) differs totally from that of the so-called Fenton-like reagent (Fe^{3+}/H_2O_2), even though both iron(II) and iron(III) ions play an important role in Fenton chemistry and can form reactive intermediates with hydrogen peroxide, which are capable of oxidiz-

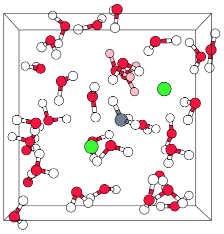

Figure 4.2: *$OH^{\cdot}$ radicals as building blocks*

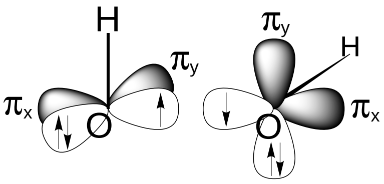

Figure 4.3: *From left to right: the highest four occupied molecular orbitals (2b, 3a, 4a and 3b) and the LUMO (4b), all of which can interact with the iron d-manifold, see also table 4.1.*

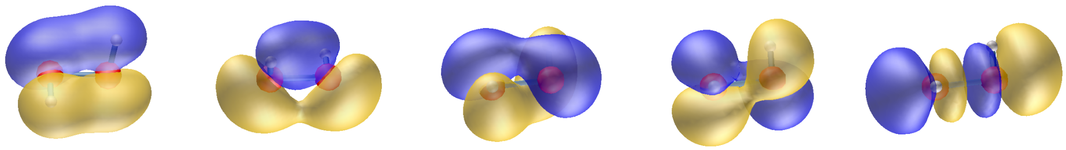

ing organic substrates. This difference in reactivity can be rationalized from the electronic structure of the pentaaqua iron hydrogen peroxide complexes. The computationally optimized structures are displayed in figure 4.1. However, we will first discuss the molecular orbital structure of the isolated reactants, hydrogen peroxide and hexaaqua iron(II) and iron(III), which also are the typical starting species for Fenton(like) chemistry in aqueous solution. The metal ligand interactions are well-understood from ligand field theory, and form therefore a means to verify our computations, as well as a reference to understand similar complexes with one or more water ligands replaced by other ligands, such as, in our case, hydrogen peroxide.

4.1.1 Hydrogen peroxide *in vacuo*

Since we are interested in the dissociation of hydrogen peroxide catalyzed by ferrous ion, we have computed first the geometry of H_2O_2 and the HO-OH bond dissociation energy in the vacuum. In particular, as is well known, we find that the H_2O_2 molecule is nonplanar with a twist angle of about 110° (point symmetry C_2). The nonplanarity of this molecule can be qualitatively understood by a molecular orbital analysis. [141] Since we are interested in the O-O bond cleavage, we take a slightly different route, using two $OH^{\cdot}$ radicals as building blocks (see scheme 4.2 and table 4.1). The $OH^{\cdot}$ radical has an unpaired electron in one of the π orbitals (π_x), and the O-O bond is basically an electron pair bond between these singly occupied orbitals. In order to avoid Pauli repulsion between the π_y lone pairs and between the O-H bond orbitals, rotation around the O-O bond axis over 90° (*cf.* scheme 4.2) brings these orbitals to zero or small overlap. Since there is also repulsion between a π_y lone pair and an O-H bond orbital, the dihedral H-O-O-H angle does not become exactly 90°, each O-H bond rotates a further 9°. Repulsion is

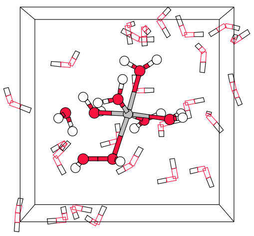

Table 4.1: *One-electron energies and percent composition of the lowest unoccupied and occupied molecular orbitals of* H_2O_2 *in terms of* $OH^{\cdot}$ *radical fragments. The point symmetry is* C_2. *We assume that in the fragment the O-H bond is oriented along the* z *axis and that the SOMO is the* π_x *orbital (see also scheme 4.2)*

Orbital	ϵ/[eV]	$OH^{\cdot}$ fragment orbitals
		occupied orbitals
1a	-27.99	91% 1σ, 8% π_x (bonding)
1b	-22.60	99% 1σ (antibonding)
2a	-13.39	54% 2σ, 34% π_x (bonding)
2b	-12.03	81% 2σ, 11% π_y, 6% π_x (antibonding)
3a	-10.39	48% π_x, 25% 2σ, 23% π_y (bonding)
4a	-7.54	73% π_y, 19% 2σ, 8% π_x (bonding)
3b	-6.65	89% π_y, 11% 2σ (antibonding)
		unoccupied orbitals
4b	-1.79	85% π_x, 8% 3σ (antibonding)
5a	-0.62	100% 3σ, (bonding)
5b	0.69	100% 3σ (antibonding)

also decreased by the O-H axes rotating 10° outwards, increasing the O-O-H angle to 100°. The shape of hydrogen peroxide can thus be understood straightforwardly from the σ bond ($p_\sigma + p_\sigma$) formed by the π_x orbitals along the O-O axis, slightly strained by the increase of the O-O-H angle to 100°. The HOMO-1 and HOMO of H_2O_2 correspond to the bonding and antibonding combinations of the doubly occupied π_y orbitals of the $OH^{\cdot}$ radicals, respectively, though a small mixing with other orbitals is present. The splitting between these two orbitals is small due to the small overlap between the π_y orbitals (see scheme 4.2). The bonding and antibonding combinations of the strongly overlapping π_x orbitals exhibit a much larger splitting. The antibonding combination is the lowest unoccupied molecular orbital (LUMO). The bonding combination, constituting the σ bond formed between the two π_x singly occupied orbitals of the $OH^{\cdot}$ radicals, enters mostly the 3a (HOMO-2) and 2a orbitals, see table 4.1. Its bonding character lowers it sufficiently to come close to, and mix with, the O-H bonding orbital 2σ. This mixing leads to lowering of the 2a (mostly 2σ) and raising of the 3a (mostly π_x). Notably the LUMO of H_2O_2, occupation of which will weaken the $O\cdots O$ bond, is 1 eV lower in energy than the LUMO of H_2O.

The computed energy needed to break the O-O bond in the isolated H_2O_2 molecule is 59.9 kcal/mol. The inclusion of the zero-point energy correction gives 54 kcal/mol, in reasonable agreement with the experimental value at 25°C of 51 kcal/mol. [142]

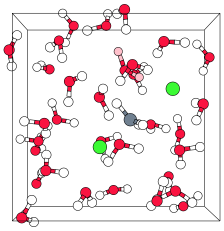

Figure 4.4: *Left-hand-side: sp lone pair orbital (HOMO-1) of water can form* σ*-bonding with the* $3d_{x^2-y^2}$ *and* $3d_{z^2}$ *metal orbitals. Right-hand-side: p lone pair orbital (HOMO) of water can form* π*-bonding with the* $3d_{xy}$*,* $3d_{xz}$*,* $3d_{yz}$ *metal orbitals.*

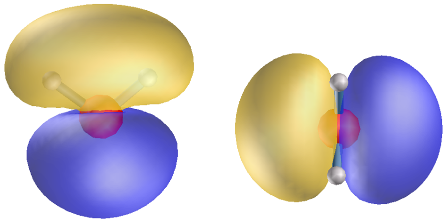

4.1.2 The $[\mathrm{Fe}^{\mathrm{III}}(\mathrm{H_2O})_6]^{3+}$ complex

We have optimized the hexaaqua iron(III) structure in the high-spin ($S = 2.5$) ground state. The octahedral coordination by the six water ligands together with the equal population of the five iron 3d orbitals with five electrons with parallel spins result in a classic example of the ligand field splitting into two e_g levels ($3d_{x^2-y^2}$, $3d_{z^2}$) and three t_{2g} levels ($3d_{xy}$, $3d_{xz}$, $3d_{yz}$). The Fe-O bond lengths are therefore all equal, namely R=2.068 Å. The metal-ligand interaction consists mainly from the plus charge–(induced-) dipole attraction, which is counterbalanced by the Pauli repulsion between the lone pairs of water and the filled orbitals on iron. The Mulliken population analysis shows that the water ligands each transfer 0.21 electron charge to iron(III). The main interacting orbitals localized on water are the highest occupied molecular orbital (HOMO) and the HOMO-1, shown in figure 4.4. The water HOMO consists of the p_π lone pair on oxygen and can overlap with the singly occupied $3d_{xy}$, $3d_{xz}$ and $3d_{yz}$ metal orbitals, giving rise to π-bonding. The HOMO-1 is the other, sp2 hybrid, oxygen lone pair, which can form σ-bonding with the $3d_{x^2-y^2}$ and $3d_{z^2}$ metal orbitals. Figure 4.5 shows the one-electron energy levels of the $[\mathrm{Fe}^{\mathrm{III}}(\mathrm{H_2O})_6]^{3+}$ complex separated into up-spin and down-spin levels. The five 3d metal orbitals together with the six σ-type and six π-type water orbitals mix to seventeen molecular orbitals (MOs), which are all filled with an electron for up-spin orbitals and only filled for the lower twelve for down-spin. The upper five down-spin orbitals are unoccupied. As there are more up-spin electrons, the up-spin levels are lower than their down-spin counterparts, due to the larger attractive exchange field working among the up-spin electrons. The large positive iron charge pulls the d-manifold down in energy, but the overlap repulsion with the ligand orbitals pushes it somewhat up again. The $3d_{x^2-y^2}$ and $3d_{z^2}$ (e_g) orbitals are directed towards the ligands and are therefore pushed up more than the $3d_{xy}$, $3d_{xz}$ and $3d_{yz}$ (t_{2g}) orbitals, which point along the diagonals in between the ligands. This energy difference, known as the ligand field e_g–t_{2g} splitting, $10D_q$, is most easily recognized in the five unoccupied down-spin levels. The upper two (e_g) levels are the antibonding combination of the $3d_{x^2-y^2}$ (75%) with the HOMO-1 of the ligands on the y-axis (13%) and on the x-axis (7%) and the antibonding combination of the $3d_{z^2}$ with the HOMO-1 of the ligands on the z-axis (13%) and on the x-axis (7%). The two bonding combinations are found at the bottom of the shown spectrum, with mostly σ_{lp} character; only the bonding combination of the six water HOMO-1 levels is lower in

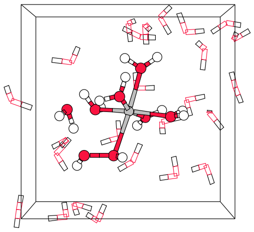

Figure 4.5: *One electron orbital energies and percent composition in the most important fragment orbital contributions for the* $[Fe^{III}(H_2O)_6]^{3+}$ *complex, in* D_{2h} *symmetry.*

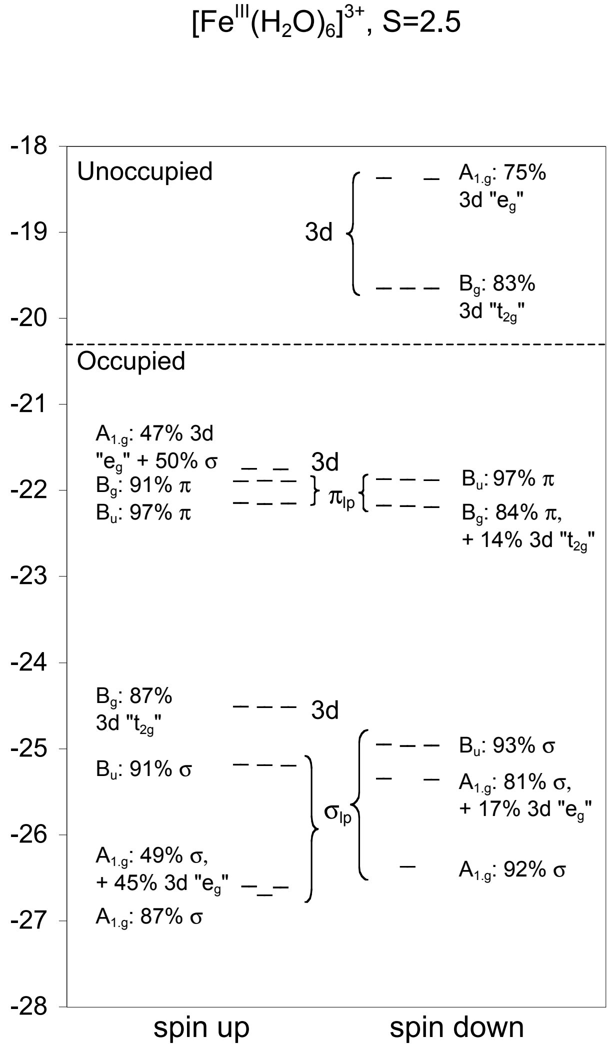

energy. The other three σ_{lp} levels are the non-bonding ungerade combinations of water pairs on the same axis, which do not mix with the (gerade shaped) 3d metal orbitals. They have almost pure σ_{lp} character; only a little metal 4P (3%) mixes in. The three unoccupied t_{2g} orbitals are the antibonding combinations of the metal $3d_{xz}$ (83%) with the HOMOs of the two ligands on the z-axis (15%), $3d_{xy}$ with the HOMOs of the two ligands on the x-axis and the $3d_{yz}$ with the HOMOs of the two ligands on the y-axis. Again we find the other three B_g bonding combinations lower in the spectrum, with mostly water π_{lp} character. This π-bonding sets the typical orientation of the water ligands to ensure maximum overlap. In between these bonding and antibonding combinations are again the three non-bonding ungerade combinations of pure π lone pairs from water ligands on the same axis. The same features apply for the (now all occupied) up-spin orbitals, but

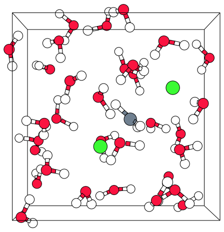

Figure 4.6: *One electron orbital energies and percent composition in the most important fragment orbital contributions for the [Fe^{II}(H_2O)$_6$]$^{2+}$ complex, in D_{2h} symmetry.*

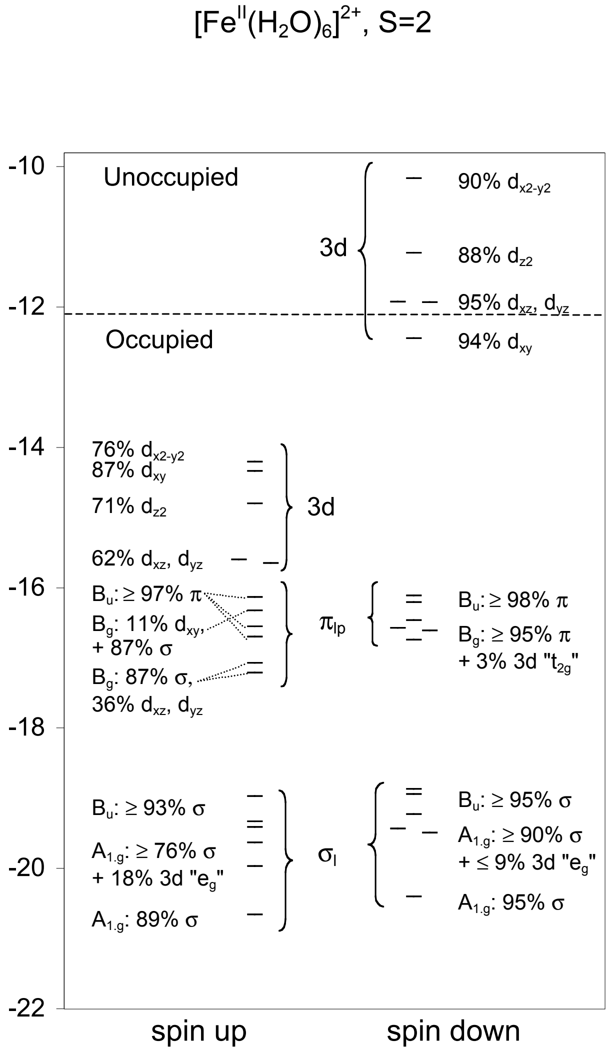

there are two differences which are the result of the down shift of the d-levels. A) the e_g metal levels become as low as the π_{lp} water levels causing a very large, almost 50%-50%, mixing. B) the t_{2g} metal levels shift even below the π water levels so that the three (lower) bonding MOs (from the B_g irreducible representation) are mainly 3d character and the upper three anti-bonding MOs (also B_g) become mainly water character.

4.1.3 The [$\mathbf{Fe^{II}(H_2O)_6}$]$^{2+}$ complex

This complex (in its high-spin, $S = 2$ ground state) differs from hexaaqua iron(III) by addition of one electron in the iron(III) complex's LUMO. Figure 4.5 shows that the LUMO is three-fold generate, so that we can make three energetically degenerate $S = 2$

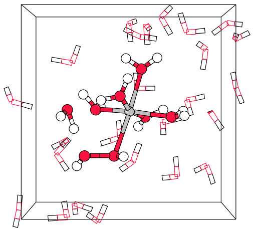

configurations for $[\mathrm{Fe^{II}(H_2O)_6}]^{2+}$ by populating one of them with an electron. Figure 4.6 shows the one-electron energy levels for the $\mathrm{d_{xy}^{\uparrow\downarrow} d_{xz}^{\uparrow} d_{yz}^{\uparrow} d_{x^2-y^2}^{\uparrow} d_{z^2}^{\uparrow}}$ configuration. The double occupation of $\mathrm{d_{xy}}$ breaks the "$\mathrm{t_{2g}}$" degeneracy. The down-spin $\mathrm{d_{xy}}$ is now populated, so it moves relatively downward due to exchange stabilization, but due to the extra Coulombic repulsion the up-spin $\mathrm{d_{xy}}$ rises with respect to $\mathrm{d_{xz}}$ and $\mathrm{d_{yz}}$. Also the "$\mathrm{e_{2g}}$" degeneracy is removed, because the $\mathrm{d_{x^2-y^2}}$ are more repelled by the down-spin $\mathrm{d_{xy}}$ electron, than the $\mathrm{d_{z^2}}$ orbital. Also the symmetry of the optimized geometry is affected. The population of the extra anti-bonding combination of $\mathrm{d_{xy}}$ with the π lone pairs of water ligands on the x-axis, elongates these two metal-ligand bonds to $R_{\mathrm{FeO}} = 2.22$ Å. The length of the other four bonds, in the yz-plane, is $R_{\mathrm{FeO}} = 2.12$ Å. The overall $\mathrm{Fe^{2+}}$-O bond elongation compared to $\mathrm{Fe^{3+}}$-O ($R_{\mathrm{FeO}} = 2.07$ Å) is of course the result of the reduced electrostatic (ion–(induced) dipole) attraction. The ligand-to-metal charge transfer is 0.11 electron per ligand; which is only half as much as for the iron(III) complex. The weakening of the metal-ligand bond is further illustrated by the first bond dissociation energy (FBDE) of one water ligand, which is 46 kcal/mol for $[\mathrm{Fe^{III}(H_2O)_6}]^{3+}$ and only 22 kcal/mol for $[\mathrm{Fe^{II}(H_2O)_6}]^{2+}$. The total orbital energy spectrum, but mostly the 3d, shifts upward with respect to that of $[\mathrm{Fe^{III}(H_2O)_6}]^{3+}$ due to the lower total charge. As a result, the up-spin anti-bonding combination of fragment orbitals is now mostly 3d character, and the bonding combination thus mostly π-lone pair character, in contrast with the up-spin MOs of the Fe(III) complex. Other differences with iron(III) are the increased mixing of the two up-spin $\mathrm{d_{xz}}$ and $\mathrm{d_{yz}}$ orbitals with the π-lone pairs, and the reduced mixing of the up-spin $\mathrm{d_{x^2-y^2}}$ and $\mathrm{d_{z^2}}$ with the σ-lone pairs.

4.1.4 The $[\mathrm{Fe^{III}(H_2O)_5(H_2O_2)}]^{3+}$ complex

We replaced the water ligand of the negative x-axis of the hexaaqua iron(III) complex by hydrogen peroxide. The geometry of this complex has been optimized in the high spin, $S = 2.5$, ground state, and is depicted in figure 4.1. The energies for the optimized $S = 0.5$ and $S = 1.5$ structures are higher in energy by 20.1 kcal/mol and 16.3 kcal/mol, respectively. $\mathrm{H_2O_2}$ binds, *via* its oxygen, end-on (η^1) to the iron(III) site, with a tilt angle of $\angle(\mathrm{FeOO}) = 114°$ and a dihedral angle of $\delta_h(\mathrm{OOFeO}) = 48°$ with respect to the water ligand on the negative z-axis. The HOOH dihedral angle has reduced to $\delta_h(\mathrm{HOOH}) = 61°$, from $\delta_h(\mathrm{HOOH}) = 110°$ in "free" hydrogen peroxide. The Fe-O bond length of $R(\mathrm{FeO}) = 2.17$ Å and FBDE of $\Delta E_{\mathrm{FBDE}} = 47$ kcal/mol are very similar to those of a water ligand of the hexaaqua complex (resp. 2.07 Å and 46 kcal/mol). Yet, the bonding of $\mathrm{H_2O_2}$ to iron(III) is quite different from that of a water ligand. Hydrogen peroxide has four occupied orbitals available which can donate charge to the partly empty iron 3d orbitals. These occupied orbitals together with the LUMO are shown in figure 4.3. The spectrum of the one-electron energy levels for the $[\mathrm{Fe^{III}(H_2O)_5(H_2O_2)}]^{3+}$ complex (shown in figure 4.7) is much more involved than the prototype octahedral splitting of hexaaqua iron(III), but now that we understand the latter we can readily scrutinize the MO structure of the hydrogen peroxide complex by comparing these two spectra.

On the down-spin side, we see again the five unoccupied levels with mainly iron 3d character, which we denote again with "e_g" and "t_{2g}"-like, although of course the octahedral symmetry is now broken. Hence, the "e_g" and "t_{2g}"-like MOs are no longer

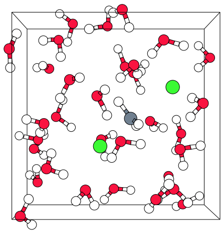

degenerate. The HOMO of the complex consists mostly of the doubly occupied HOMO of H_2O_2 (fragment orbital 4b). On the down-spin side we then find again the block of (5x) water π lone pairs augmented with the HOMO-1 (5a) of H_2O_2 and the block of (5x) water σ lone pairs plus the other two H_2O_2 MOs (4a and 3b). The upper three levels (numbered 40 to 42) of the π_{lp}/H_2O_2 block arise from non-bonding combinations of the ligands and the lower three levels (numbered 37 to 39) are the bonding combinations with mostly ligand character between the water π_{lp} MOs/ hydrogen peroxide HOMO-1 and the iron $3d_{\mathrm{xy}}$, $3d_{\mathrm{xz}}$ and $3d_{\mathrm{yz}}$ orbitals. In the energy range of the $\sigma_{\mathrm{lp}}/H_2O_2$ block, we find most of the HOMO-2 (bonding MO 4a) and the HOMO-3 (anti-bonding MO 3b) of hydrogen peroxide mixing to an anti-bonding combination and a bonding combination. The anti-bonding combination (no. 36) mixes in some water σ_{lp}, which rises therefore above the other two non-bonding combinations of σ_{lp} MOs (no. 34 and no. 35; compare also with the hexaaqua iron(III) spectrum in figure 4.5). The bonding combination of 4a and 3b mixes again with the bonding σ_{lp}/"e_g" combinations (resulting in 31-33), of which the lowest (no. 31) gets most of the H_2O_2 character. On the bottom (no. 30), we find again the bonding combination of the water σ lone pairs augmented with the H_2O_2 4a, similar to hexaaqua iron(III).

On the up-spin side, we see that the five orbitals with mainly iron 3d character (numbered 37-39 and 46-47) are separated by the π_{lp}/H_2O_2 block. This means that, similar to the hexaaqua iron(III) case, the bonding and antibonding combinations between metal "t_{2g}"-type orbitals and ligand MOs have interchanged character with respect to Fe^{2+} (see hereafter) due to the higher positive charge on the iron fragment, which lowers the 3d manifold with respect to the ligand fragment MOs. The two anti-bonding "e_g"-type combinations (no. 46 and no. 47) show a substantial mixing with the σ_{lp} and the HOMO-1 (5a) of H_2O_2. The three π-anti-bonding combinations (43-45) are followed by two non-bonding π combinations of the water ligand pair on the z-axis and the pair on the y-axis (no. 41 and no. 42). The lowest π/H_2O_2-block level (no. 40) is a H_2O_2 combination of the HOMO-1 and HOMO-2, which shows bonding with iron $3d_{\mathrm{x^2-y^2}}$ plus an anti-bonding contribution of the water σ_{lp} lone pair on the same axis. This MO is surprisingly σ shaped, in contrast to its down-spin counterpart (no. 37). The structure of the σ_{lp}/4a-3b block is similar to the down-spin side, although the HOMO-2 (4a) is even more distributed over other levels.

4.1.5 The $[Fe^{II}(H_2O)_5(H_2O_2)]^{2+}$ complex

The main difference between the geometry of the iron(II) hydrogen peroxide complex and the iron(III) hydrogen peroxide complex is the orientation of the H_2O_2 (see figure 4.1). After adding one electron to the previous complex, the hydrogen peroxide ligand has rotated towards an adjacent water ligand, so that the dihedral angle $\delta_h(O_\beta O_\alpha FeO_w)$ has become almost zero degrees. The distance between the hydrogen peroxide O_β and the water ligand hydrogen of $R_{\mathrm{OH}} = 2.19$ Å is close enough to form a weak internal hydrogen bond. However, comparison of the energies needed to remove a hydrogen (without relaxing the structure) from either side of this water ligand and the water ligand on the opposite side of iron(II), reveals that the extra stabilization of the hydrogen involved in the H-bond is in fact less than 2 kcal/mol; much less than the hydrogen bond in a water dimer, which

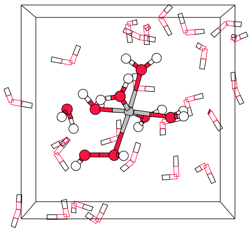

Figure 4.7: *One electron orbital energies and percent composition in the most important fragment orbital contributions for the* $[Fe^{III}(H_2O)_5(H_2O_2)]^{3+}$ *complex.*

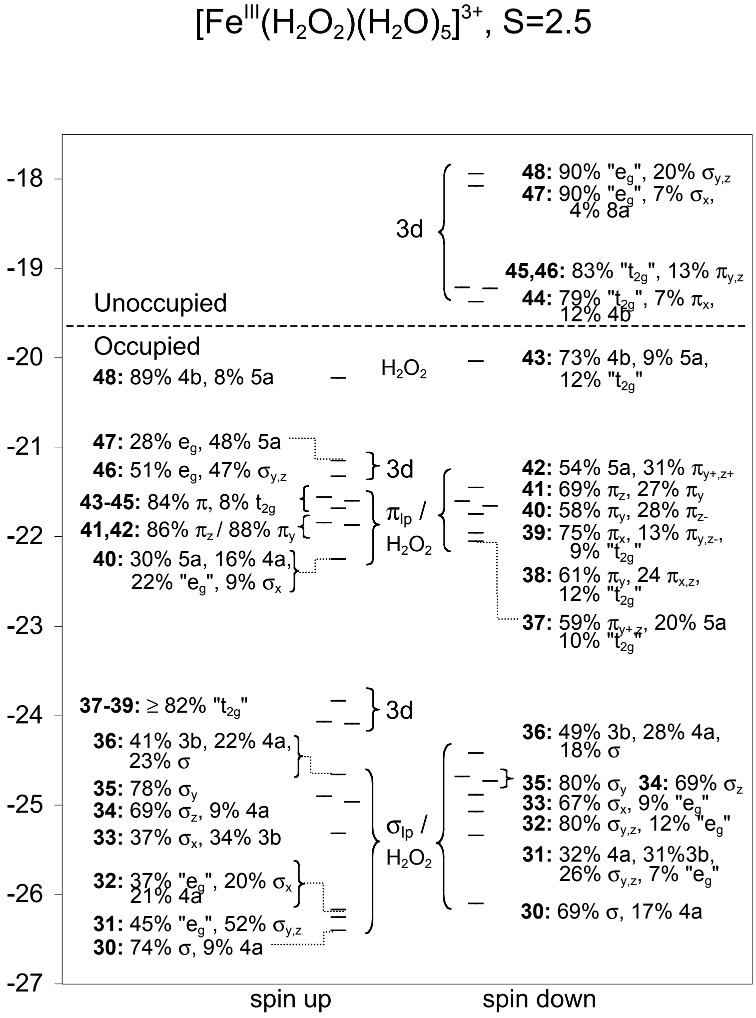

is 5 kcal/mol). The peroxide bond length of $R_{OO} = 1.476$ Å is only slightly longer than we found in the isolated hydrogen peroxide molecule ($R_{OO} = 1.468$ Å), whereas in iron(III) hydrogen peroxide we found a shortening to $R_{OO} = 1.438$ Å. The MO energies are shown in figure 4.8. Unlike making hexaaqua iron(II) from hexaaqua iron(III) by adding one electron, we now do not have to choose between three degenerate metal "t_2g" 3d orbitals to occupy one with a second electron, because the degeneracy is of course removed after replacing a water ligand for hydrogen peroxide. Instead the lowest 3d orbital is doubly occupied, which is the one that is least pushed up by anti-bonding water π-lone pairs (no. 44 in figure 4.7). This is d_{xz} in the complex orientation shown in figure 4.1. Similar changes to the MO picture as when going from $[Fe^{III}(H_2O)_6]^{3+}$ to $[Fe^{II}(H_2O)_6]^{2+}$, are observed when we move from the iron(III) hydrogen peroxide to the iron(II) hydrogen peroxide complex. For instance, the metal 3d manifold shifts again upward due to the

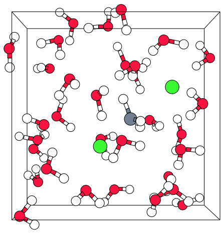

Figure 4.8: *One electron orbital energies and percent composition in the most important fragment orbital contributions for the [$Fe^{II}(H_2O)_5(H_2O_2)]^{2+}$ complex.*

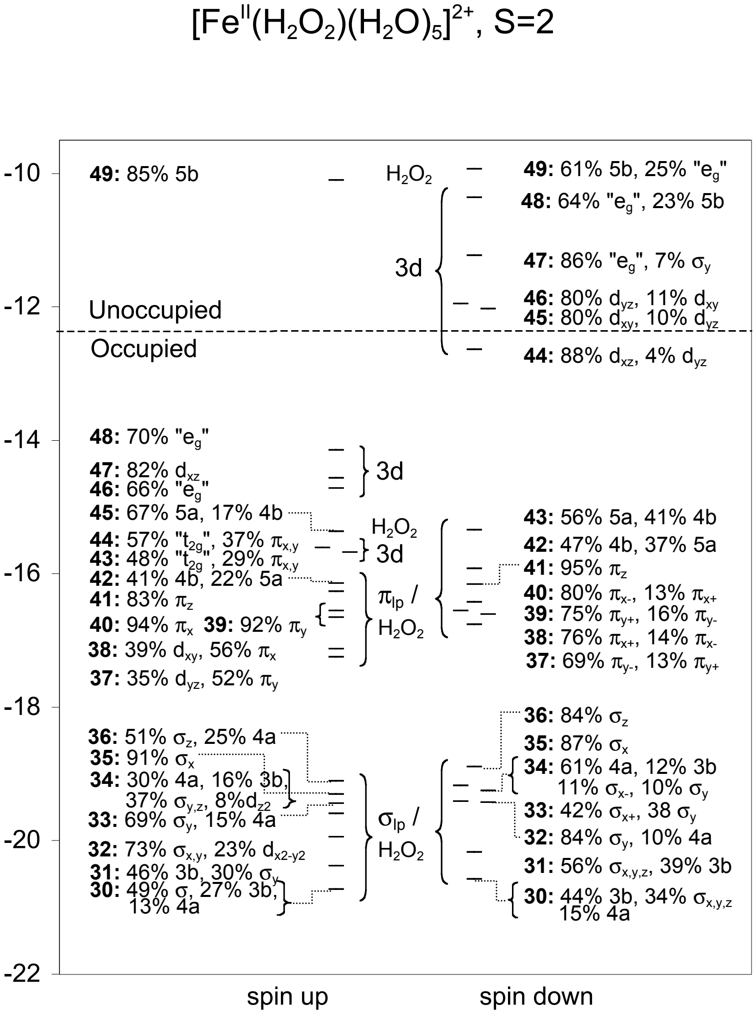

lower charge on iron(II) hydrogen peroxide, so that the up-spin π_{lp}-block is again below the 3d levels. An important difference with the iron(III) hydrogen peroxide complex is that the H_2O_2 HOMO (4b) is no longer the HOMO of the complex but mixes with the H_2O_2 HOMO-1 (5a) to a bonding and an anti-bonding combination (42 and 45 on the up-spin side and 42 and 43 on the down-spin side). Surprisingly, the lower (bonding) one is mostly (antibonding) HOMO character and stabilized with a little $3d_{z^2}$, whereas the higher one is mostly (bonding) HOMO-1 character in an anti-bonding combination with $3d_{yz}$. On the up-spin side, 4b also mixes with the "e_g" levels (13% in no. 48 and 7% in no. 45) and with a "t_{2g}" level (8% in no. 43). In the σ_{lp}-block we find again the 4a and 3b H_2O_2 orbitals combining and mixing with the σ_{lp} of water ligands and the iron $3d_{x^2-y^2}$ and $3d_{z^2}$. The main difference compared to iron(III) hydrogen peroxide is that now effectively most of the H_2O_2 HOMO-3 (3b) is found below the HOMO-2 (4a), which

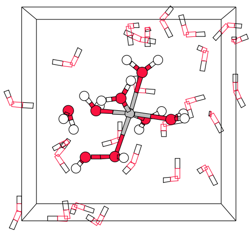

Figure 4.9: *Upper graph: two of the six Fe-O bond lengths* $R(\text{Fe-O}_{ligand})$ *as a function of time (one ligand leaves the coordination shell at* $t = 10$*ps). Middle graph: bond lengths of H-bonds donated to the leaving ligand oxygen; the initial H-bond (from* H_2O *no. 3) is replaced by hydrogens of two other solvent waters (no. 1 and 2) at* $t \approx 13$*ps. Lower graph: Potential energy (arbitrary zero).*

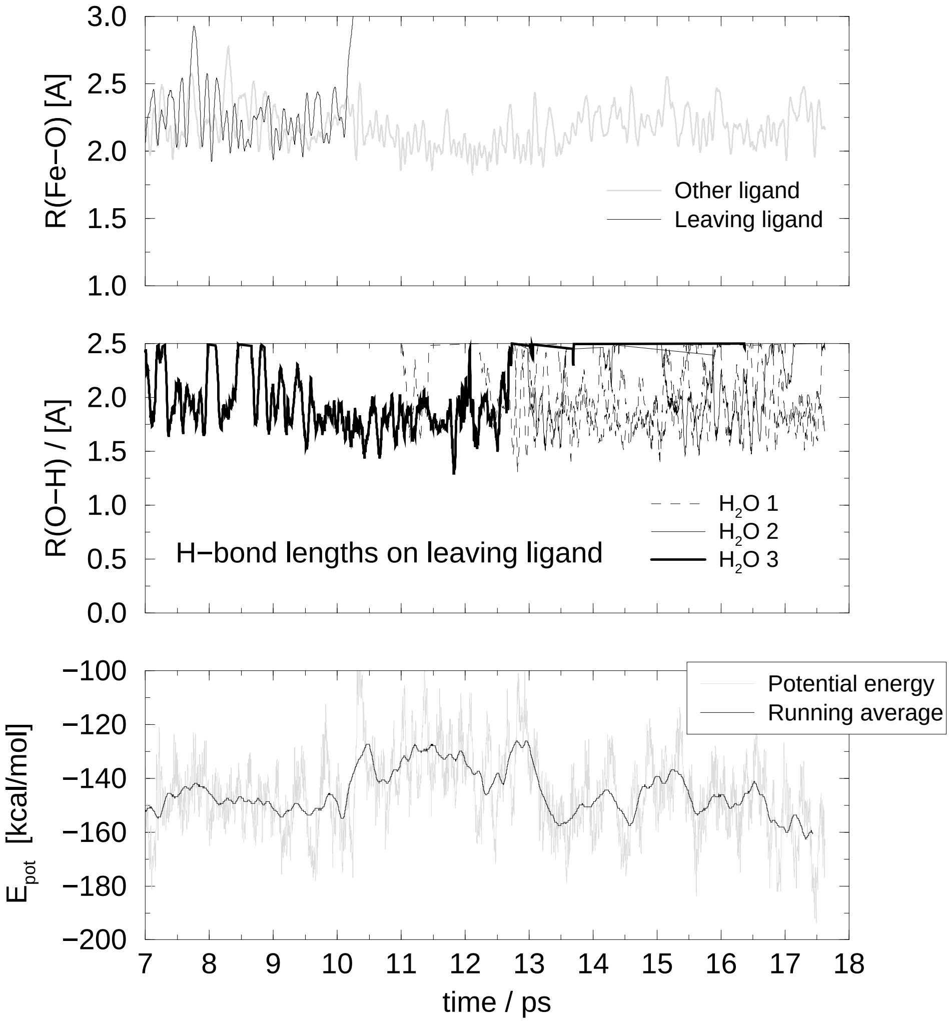

was reversed in the iron(III) hydrogen peroxide complex.

4.2 Fe^{2+} and Fe^{3+} ions in water

We have performed spin polarized Car-Parrinello MD simulations of Fe^{2+} ($S = 2$) and Fe^{3+} ($S = 2.5$) in aqueous solution. A cubic cell with an edge of $l_{\text{box}} = 9.865$ Å contained a single iron ion and 32 H_2O molecules and was subject to periodic boundary conditions to mimic an infinitely large solution. A Nosé thermostat with a period of 100 fs maintained

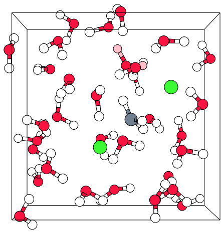

Figure 4.10: *Upper graph: radial distribution of water around* Fe^{2+} *in the initial hexaaqua complex (solid and dashed lines) in comparison to the subsequent pentaaqua complex (dotted lines). Lower graph: radial distribution of water surrounding other solvent water (solid lines) and water ligands (dashed lines).*

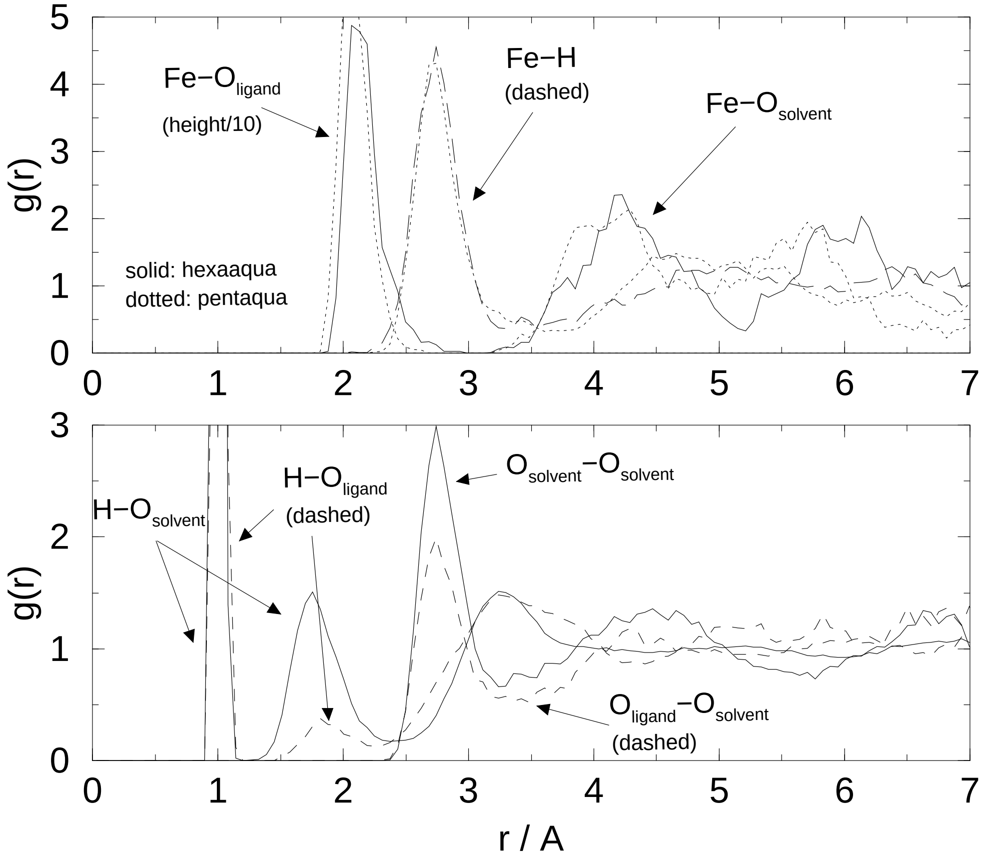

a temperature of 300 Kelvin. The positive charge of the systems was compensated by a uniformly distributed counter charge. Starting with Fe^{2+}(aq), we equilibrated the system for 6.5 ps, while applying six R(Fe-O) bond distance constraints to speed up the formation of the desired hexaaqua iron complex. The following 11 ps MD trajectory was used to gather statistics. After 3.2 ps a snapshot was taken, which was used to construct the Fe^{3+}(aq) system, by removing one electron and equilibrating for 2 ps more. Again 9 ps AIMD simulation were performed with this system to calculate physical properties.

The first 3.5 ps of the simulation of Fe^{2+}(aq), the hexaaqua iron(II) complex has the typical octahedral symmetry, with Fe-O bond distances fluctuating around 2.12 Å. After that, one of the water ligands moves rapidly away from the solvation shell into the bulk water, see upper graph in figure 4.9. The number of water ligands coordinating Fe^{2+} therefore decreases spontaneously from six to five, and stays five in the remaining 7.5 ps of the simulation. After 3 ps (at t = 13 ps), the solvent has donated two hydrogen

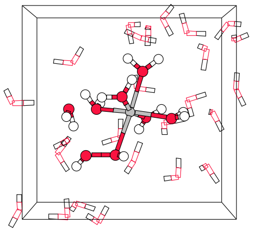

bonds to the leaving water ligand (illustrated by the middle graph in figure 4.9) and the complex structure has changed from the octahedral arrangement into a structure alternating between a square pyramid and a trigonal bipyramid. Hydrolysis of a water ligand of the iron(II) complex was not observed in our simulation, which is in agreement with the experimental acidity constant of $\mathrm{p}K_a = 9.5$. [143]

Figure 4.10 shows the radial distribution of water around the iron ion (upper graph) averaged over the first 3.5 ps (hexaaqua complex; solid and dashed lines) in comparison to the second part of the simulation (pentaaqua complex; dotted lines). The radial distribution functions for the (single) iron ion (upper graph) are noisy beyond a distance of 5 Å, due to the limited (3.5 ps) statistics. The differences between the functions for the 6-fold coordination versus the 5-fold coordination are quite small, and are mostly pronounced in the shift of the first Fe-O peak position, from $R = 2.12$Å ($\mathrm{Fe^{II}(H_2O)_6}$) to $R = 2.04$Å ($\mathrm{Fe^{II}(H_2O)_5}$). The experimental value for the $\mathrm{Fe^{2+}}$-O bond length is 2.1 Å (see table 4.2). The peaks, resulting from the water ligands, integrate nicely to 6 and 5 oxygens respectively. The second oxygen peak, indicating the second solvation shell, has a bit more noise. For the hexaaqua iron function, the Fe-O function has a maximum at R=4.2 Å followed by a minimum at R=5.2 Å and integrates to roughly 13 oxygens in the second solvation shell. The $\mathrm{Fe^{2+}}$-H radial distribution function has only one distinct peak at R=2.74 Å which gives a coordination number of 12.2 hydrogens, originating from the six water ligands.

The lower graph in figure 4.10 shows the radial distribution of the solvent O and H atoms around the oxygens of water ligands (dashed lines) and solvent molecules (solid lines) respectively. The distribution functions for the five-fold coordinated complex are not shown as they are very similar to the shown functions of the six-fold coordinated complex. The first H-O peak at $R = 1.0$ Å arising from the intermolecular OH bond of H_2O, is the same for ligand and solvent O atoms. Integration of the second OH peak at $R \approx 1.8$ Å arising from the intermolecular H-bonds between the solvent molecules, shows that solvent water O atoms accept on average 1.9 hydrogen bonds, which agrees very well with the 1.8 in pure water, published earlier [144]. For the water ligands, this peak is much smaller; on average, only 3 out of the six ligand O atoms accept a hydrogen bond from the water solvent. Also the first O-O peak, at $R \approx 2.7$ Å is smaller for the O atoms of the water ligands than for those of the solvent molecules. This peak integrates to a coordination number of $c_n = 3.7$ oxygens for solvent water O atoms, whereas each ligand oxygen finds only 2.6 solvent water oxygens in its first shell. The average oxygen-oxygen distance between ligand molecules and solvent waters is surprisingly the same as the one for solvent-solvent waters : R_{OO}=2.72 Å (also in pure water); in previous work we found in the gas-phase a much smaller distance for the O-O distance between a water molecule in a "second shell position" and the closest water ligand in the $\mathrm{[Fe^{II}(H_2O)_5]^{2+}}$-$H_2O$ complex. [145] Apparently, the strong interaction found in the gas phase complex is spread-out over more solvent molecules and therefore less apparent "per second shell molecule" in the complete solvent.

We now turn to the AIMD simulation of $\mathrm{Fe^{3+}}$ in water. Already in the equilibration phase, hydrolysis took place on one of the six water ligands, so that the simulation starts with an $\mathrm{[Fe^{III}(OH)(H_2O)_5]^{2+}}$ complex and a hydronium ion dissolved in water. After 2.3 ps, one of the water ligands moves away from the coordination shell of this 2+ complex

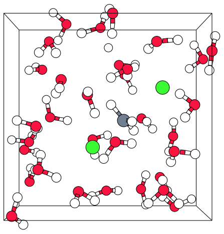

Table 4.2: *Results from the simulations of the Fe^{2+} ion and the Fe^{3+} ion in water compared to results from our simulation of $FeCl_2$ and from other simulations and experiment. R and Δ (Å) are the position of the maximum and the full width at half maximum respectively of a Gaussian fitted to the radial distribution peak. Θ is the average tilt angle (in degrees) of the ligand water molecules, defined as the angle between the Fe-O axis and the bisector of the water molecule.*

	$[Fe^{II}(H_2O)_6]^{2+}$					$[Fe^{III}(H_2O)_6]^{3+}$				
	R_{FeO}	Δ_{FeO}	R_{FeH}	Δ_{FeH}	Θ	R_{FeO}	Δ_{FeO}	R_{FeH}	Δ_{FeH}	Θ
PAW $n(H_2O)$=6	2.12		2.74		43	2.04	0.24	2.72	0.39	30
PAW $n(H_2O)$=5	2.04		2.70		32	1.97	0.28	2.68	0.41	28
PAW $FeCl_2$[a]	2.13	0.26	2.76	0.37	38	-	-	-	-	-
MD/SPC[b]	2.075		2.775		16					
Neutron diff.[c]	2.13	0.28	2.75	0.36	32	2.01	0.32	2.68	0.40	20
EXAFS[d]	2.10					1.98				

[a] Previously published, Ref. 146. [b] MD using a flexible "simple point charge" (SPC) model for water, Ref. 147. [c] Neutron diffraction on iron chloride in heavy water, Ref. 148. [d] EXAFS experiment Ref. 149.

into the solvent, similar to the iron(II) case (but we never observed this for 3+ complexes). Very occasionally the proton jumps back on the hydroxo ligand of the $[Fe^{III}(OH)(H_2O)_4]^{2+}$ complex. On the other hand, sometimes even a second hydrolysis is observed, *i.e.* donation of a second proton to the solvent, but this then only lasts a few femtoseconds. At 7 ps after the start of our simulation, a solvent water molecule enters the solvation shell and restores the hexaaqua complex (see also figure 4.11). This entering water molecule is not the same one that left 4.7 ps before, and also does it not enter at the same position as where the previous molecule left due to reorientation of the complex. After another 2.3 ps since the hexaaqua complex was restored, the simulation was stopped. In table 4.2, structural properties of the aqua iron(III) complex are compared with those obtained with other methods. The numbers on the first row are obtained from the radial distribution functions calculated from the last 2 ps of the simulation. The numbers on the second row show the averages over the pentaaqua iron(II) and iron(III) configurations. The small difference between the average Fe^{3+}-O and Fe^{3+}-H bond distances when going from the hexaaqua iron complex to the pentaaqua iron complex are very similar to the case of iron(II): R_{FeO} is reduced from 2.04 Å to 1.97 Å, and R_{FeH} is reduced from 2.72 Å to 2.68 Å. Again, these results are in good agreement with experiment.

In contrast with the generally accepted picture [150], we do not observe mainly the octahedrally coordinated hexaaquairon complexes for the iron(II) and iron(III) ions in aqueous solution, but in addition also five-fold coordinated pentaaquairon complexes. Recently, Pasquarello *et al.* found for the Cu(II) ion in aqueous solution solely the five-

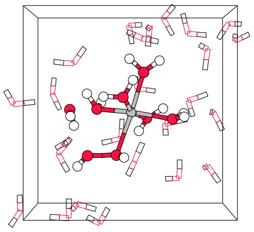

Figure 4.11: *Distances between iron(III) and three selected ligand oxygens during the AIMD simulation of* Fe^{3+} *in water. At about* $t = 18$ *ps, the hydroxo ligand with an average bond length of* $R_{FeO} = 1.87 \pm 0.05$ Å *obtains the proton from the solvent hydronium ion. At the same time another water ligand (dashed line) donates again a proton for about 1 ps. The water ligand that left after 2.3 ps is replaced by another solvent water 7 ps later (bold lines).*

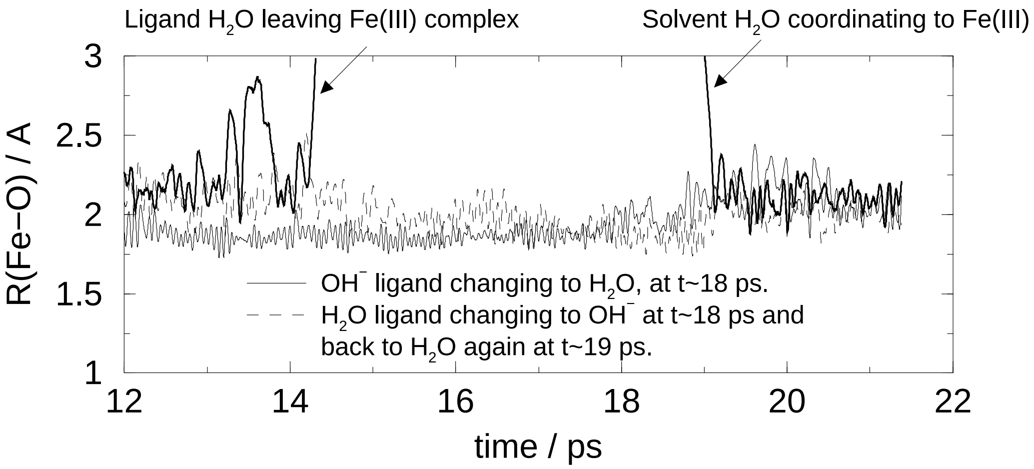

fold coordinated pentaaquacupper(II) complex [151], using neutron diffraction and Car-Parrinello molecular dynamics, breaking with of the consensus six-fold coordinated Jahn-Teller distorted octahedron picture [150]. Recent x-ray experiments have confirmed the fivefold coordinated Cu^{2+} aqua ion [152]. In our AIMD simulations, we find alternating five-fold and six-fold coordination for the hydrated iron ions. Unfortunately, present day computers do not yet allow for long enough AIMD simulations to give an estimate for the equilibrium constant between the two complexes or for the ligand exchange rate. NMR experiments have shown water ligand residence times of $3.1 \cdot 10^{-7}$ s and $6 \cdot 10^{-3}$ s for hexaaqua iron(II) and iron(III) [150], respectively, which is nevertheless much longer than we observe in our simulations. We have also evaluated the first bond dissociation energies (*i.e.* the energy to remove one ligand) for the hexaaqua iron structures *in vacuo*. We find a value of 22.1 kcal/mol for the $S = 2$ $[Fe^{II}(H_2O)_6]^{2+}$ complex and 45.7 kcal/mol for the $S = 5/2$ $[Fe^{III}(H_2O)_6]^{3+}$ complex. Clearly, the aqueous solution strongly stabilizes the dissociated complexes. The facile expulsion of a water ligand by the hexaaquairon complexes in aqueous solution should come as no surprise, as the creation of vacant coordination sites on the metal ion are required to explain the catalytic activity of solvated iron complexes. However, the NMR residence times indicate that the ligand exchange rate is overestimated by AIMD. This might be due to an underestimation of the ligand exchange energy barrier by DFT using the Becke-Perdew exchange-correlation functional, as the accuracy of binding energies was previously found to be in the order of 1 kcal/mol [144]. Also, the omission of explicit counter ions and the relatively small box size could have an effect on the exchange rate and also on the balance of fivefold versus sixfold coordination.

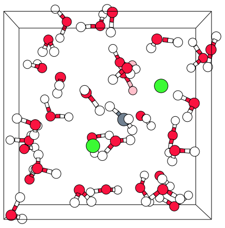

Nevertheless, we suggest that a re-examination of the fitting models of previous spectroscopic data as well as new (more accurate) measurements on iron ions in aqueous solution could be worthwhile, as already was shown for the Cu(II) ion in water, recently [151].

4.3 Estimation of the pK_a of hexaaqua iron(III) in aqueous solution

From the observed dynamic equilibrium between hexaaquairon(III) and the conjugate base plus hydronium ion, see equation 4.1,

$$\left[\mathrm{Fe^{III}(H_2O)_6}\right]^{3+} + \mathrm{H_2O} \quad \longleftrightarrow \quad \left[\mathrm{Fe^{III}(H_2O)_5(OH)}\right]^{2+} + \mathrm{H_3O^+} \tag{4.1}$$

we can make an estimate of the acidity constant pK_a for this reaction, by accumulating the relative abundance of the hydronium ion, x, in our system.

$$\mathrm{p}K_a = -\log\left(\frac{\left[\left[\mathrm{Fe^{III}(H_2O)_5(OH)}\right]^{2+}\right]\cdot\left[\mathrm{H_3O^+}\right]}{\left[[\mathrm{Fe^{III}(H_2O)_6}]^{3+}\right]}\right) = -\log\left(\frac{x^2\,[\mathrm{HB}]_0}{1-x}\right) \tag{4.2}$$

Here $[\mathrm{HB}]_0$ is the starting concentration of the acid ($[\mathrm{Fe^{III}(H_2O)_6}]^{3+}$) (before hydrolysis has taken place), divided by the activity of H_2O (which is approximately one). The OH distances R_{OH} in each water ligand were taken for the order parameter to distinguish between whether the system finds itself on the left-hand-side or the right-hand-side of equation 4.1. That is, if one of the twelve R_{OH} in the hexaaqua iron(II) complex was longer than an arbitrarily chosen criterion (say $R_{\mathrm{OH}}^{\max}$=1.3 Å), obviously hydrolysis of a ligand has taken place and a hydronium ion is formed in the solvent. The last two picoseconds of the simulation, in which the hexaaqua iron(III) complex is recovered, is used for the estimate of pK_a. Unfortunately, we find that the resulting pK_a depends on our choice for $R_{\mathrm{OH}}^{\max}$, which is shown in table 4.3. If we take our criterion to be equal to $R_{\mathrm{OH}}^{\max}$=1.3, which was also used by Tuckerman *et al* [52,53] to distinguish between different types of hydronium complexes in water, we find a too low value of pK_a=0.628 compared to the experimental number of 2.2. Taking $R_{\mathrm{OH}}^{\max}$=1.5, we discard many configurations from x which belong to situations where the hydronium ion is not yet completely free from the complex, but instead the proton is jumping back and forth between the aqua ligand and the solvent water molecule. The resulting pK_a=1.47 is in reasonable agreement with experiment. Much better than for instance is obtained with static DFT calculation on large aqua iron clusters in a dielectric continuum, which gave an acidity constant of pK_a=-4.0 [153].

4.4 Concluding remarks

We have rationalized the structure of hydrogen peroxide by the buildup of the molecular orbitals from the $\mathrm{OH^{\cdot}}$ radical fragments and we have performed the orbital analysis for the hexaaquairon(II) and hexaaquairon(III) complexes as well as for the two pentaaquironhydrogen peroxide complexes. We have also performed *ab initio* (DFT) molecular dynamics

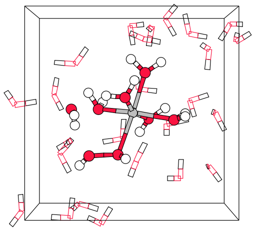

Table 4.3: *Estimates for the acidity constant* pK_a *for the first hydrolysis reaction of hexaaqua iron(III) in water from the AIMD simulation, depending on the order parameter* $R_{\mathrm{OH}}^{\mathrm{max}}$ *(above the dotted line), compared with other work (below the dotted line).*

Method	x	K_a	$\mathrm{p}K_a$
$R_{\mathrm{OH}}^{\mathrm{max}}$=1.2	0.512	0.927	0.033
$R_{\mathrm{OH}}^{\mathrm{max}}$=1.3	0.307	0.235	0.628
$R_{\mathrm{OH}}^{\mathrm{max}}$=1.5	0.130	0.034	1.47
....	....	....	....
DFT-B3LYP[a]		10^4	-4.00
experiment[b]		$6{\cdot}10^{-3}$	2.2

[a] Static DFT calculation of $\mathrm{Fe(H_2O)}_{18}^{3+}$ cluster in dielectric continuum [153]. [b] Ref. 154

simulations of the iron(II) ion in water and the iron(III) ion in water. The intramolecular bond distances for the hexaaquairon complexes are in good agreement with those from experiment. In our simulations, the water ligands exchange relatively easily with the solvent compared to experiment. The hexaaquairon(III) complex was found to acidic in contrast to hexaaquairon(II). The $\mathrm{p}K_a$ value of hexaaquairon(III) has been estimated to be 1.47, in reasonable agreement with the experimental number of 2.2.

Chapter 5

A Car-Parrinello study of the formation of oxidizing intermediates from Fenton's reagent in aqueous solution*

This chapter demonstrates the spontaneous formation of the much contested ferryl ion, $Fe^{IV}O^{2+}$, in an aqueous solution of iron(II) and hydrogen peroxide by means of first principles molecular dynamics simulations. Starting from hydrogen peroxide coordinated to pentaaqua iron(II) in water, we show that the oxygen-oxygen bond breaks spontaneously to form $[(H_2O)_5Fe^{III}OH]^{2+}$ and a very short living $OH^{\cdot}$ radical. This radical abstracts immediately a hydrogen from a water ligand to form $[(H_2O)_4Fe^{IV}(OH)_2]^{2+}$ and a water molecule. The hydrated ferryl ion $[(H_2O)_5Fe^{IV}O]^{2+}$ is formed in a second step by proton donation from one OH ligand to the solvent. Starting from separated hydrogen peroxide and pentaaqua iron(II) in water, we find a reactive pathway in which the ferryl ion is formed in a more direct way. As soon as H_2O_2 enters the iron(II) coordination shell, the oxygen-oxygen bond breaks and again an OH ligand and a short living $OH^{\cdot}$ radical is formed. The radical abstracts the hydrogen from the OH ligand to form again the ferryl ion.

5.1 Introduction

The proposed reaction mechanisms for the oxidation of organic substrates with the Fenton reagent [155] (a mixture of ferrous ions and hydrogen peroxide) can roughly be divided into two groups. The first group regards Fenton chemistry as the production of free hydroxyl radicals by the metal catalyzed decomposition of the peroxide [156]

$$Fe^{2+} + H_2O_2 \rightarrow Fe^{3+} + OH^- + OH^{\cdot} \tag{5.1}$$

The other mechanisms involve the formation of a highly reactive iron-oxo complex such as the ferryl ion ($[Fe^{IV}O]^{2+}$) as the oxidative intermediate. [157] The reactions are of indus-

---

*B. Ensing, F. Buda, P. E. Blöchl, and E. J. Baerends, *Phys. Chem. Chem. Phys.* **4**, 3619 (2002). B. Ensing, F. Buda, P. E. Blöchl, and E. J. Baerends, *Angew. Chem. Int. Edit.* **40**, 2893 (2001)

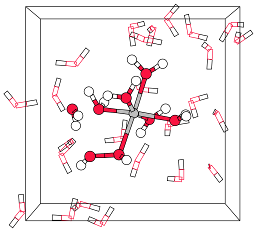

trial interest for their applications in waste water treatment and paper bleaching, but also in biological processes are their oxygen activation abilities recognized. Recently, much attention has been given to iron containing biological molecules that efficiently catalyze the oxidation of organic substrates, such as the antitumor drug bleomycin [158], cytochrome oxydase [159–162] and methane monooxygenases [163, 164]. Biomimetically designed ligand environments of iron complexes [131, 132] are studied to optimize industrial catalysts, but also other chelated [165, 166] and un-chelated [136, 139, 167] iron(II)/H_2O_2 complex in aqueous solution are studied as well as oxidations by bare iron-oxo species in the gas phase [168–170] in order to reveal the reaction mechanisms. Despite the numerous studies over more than 60 years, the controversy remains as there have not yet been definitive experiments to distinguish between the proposed alternatives. The main experimental difficulty, the extremely short life times of the reaction intermediates, is not a problem for computer simulation methods. A second difficulty is the sensitivity of Fenton chemistry to the reaction conditions, such as the pH, the metal ligands (chelating agents), and the nature of organic substrates, which complicate the development of a microscopic model. We have therefore first restricted ourselves in a previous study to the mechanism of the basic reaction between hydrated Fe(II) and hydrogen peroxide *in vacuo* [145]. Subsequently, the influence of other parameters on the mechanism will be the subject of study, starting with the solvent effect of aqueous solution in the present study. A preliminary account has appeared in ref. 171.

In the gas-phase study, we have analyzed the reaction of H_2O_2 with Fe^{2+} from the point of view of the energetics and the electronic and geometric structure using Density Functional Theory (DFT) calculations. As the primary step in the proposed models usually is the coordination of the hydrogen peroxide to iron,

$$L_6Fe^{II} + H_2O_2 \leftrightarrow L_5Fe^{II}H_2O_2 + L \tag{5.2}$$

we started from a configuration of H_2O_2 coordinated to a pentaaqua iron(II) complex. It turned out that the complexed hydrogen peroxide easily dissociates but the formation of free $OH^{\cdot}$ radicals is from an energetic point of view very unlikely. Instead, the formation of the ferryl ion ($[(H_2O)_5Fe^{IV}{=}O]^{2+}$) plus water is exothermic by $\Delta E_0 = 28$ kcal/mol. [145]

In practice however, these reactions take place in aqueous solution and the solvent effects are expected to be an important factor in the balance between the competing reactions. Already in our gas phase study we have observed that adding a single water molecule could facilitate the formation of the ferryl ion from the Fenton reagent by lowering the reaction barrier of the proton transfer process. In the present study, we introduce the effects of a complete water solution environment and report the oxidizing intermediates formed in the reaction of Fe^{2+} and hydrogen peroxide in water at T=300K predicted by computer simulation. To be able to model correctly the active role of the solvent water molecules in the Fenton reaction, the method of choice for this study is the Car–Parrinello (CP) method. [49] The CP method applies classical molecular dynamics (MD), computing the inter- and intramolecular forces from the electronic structure determined quantum mechanically with Density Functional Theory (DFT) in an efficient way. The CP method is therefore regarded as an *ab initio* (DFT) molecular dynamics (AIMD) method. This method has proven to be a very valuable tool to study at a microscopic

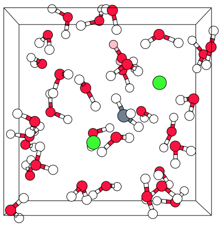

scale structure and dynamics of water [50, 51], (metal–) ions in water [52, 53, 117, 172] and simple chemical reactions in aqueous solution. [54, 55, 144] The full strength of AIMD becomes apparent in the simulation of bond breaking and making as *e.g.* a proton or $OH^{\cdot}$ radical jumps through an aqueous solution; something that is practically impossible to model with classical force fields.

This paper is structured as follows: in the next section (section 5.2), we start with the computational details. Then, in order to asses the accuracy of the Car-Parrinello method in the description of the solvent structure around an iron complex, we compare structural properties of $FeCl_2$ in water with experimental data (section 5.2.1). The presentation of our results (section 5.3) begins with static DFT calculations of the energetics for the elementary reactions to produce the $OH^{\cdot}$ radical and the ferryl ion with the Fenton reagent *in vacuo*, in section 5.3.1. Our main results, the reaction mechanisms of iron(II) and H_2O_2 in aqueous solution at room temperature, are presented in sections 5.3.2, 5.3.3 and 5.3.4. We first show the spontaneous formation of iron(IV)oxo species in an AIMD simulation when we start from H_2O_2 coordinated to pentaaqua iron(II), via an iron(IV) dihydroxo intermediate, with and without solvent molecules playing an active role in the mechanism (sections 5.3.2 and 5.3.3, respectively). In section 5.3.4, we also include the coordination process, by starting from separated reactants in water. A summary and conclusions are given in section 5.4.

5.2 Methodology

All electronic structure calculations were performed using the density functional theory (DFT) method (see *e.g.* ref. 46). We used the Becke-88 gradient corrected exchange functional [67] and the Perdew-86 gradient corrected correlation functional. [38] The *ab initio* (DFT) molecular dynamics calculations of the systems including the solvent environment were done with the Car-Parrinello (CP) method [49] as implemented in the CP-PAW code developed by Blöchl [24]. The one-electron valence wave functions were expanded in an augmented plane wave basis up to a kinetic energy cutoff of 30 Ry. The frozen core approximation was applied for the 1s electrons of O, and up to 3p for Fe. For the augmentation for H and O, one projector function per angular-momentum quantum number was used for *s*- and *p*-angular momenta. For Fe, one projector function was used for *s* and *p* and two for *d*-angular momenta. The characteristic feature of the Car-Parrinello approach is that the electronic wave function, *i.e.* the coefficients of the plane wave basis set expansion, are dynamically optimized to be consistent with the changing positions of the atomic nuclei. The mass for the wave function coefficient dynamics was μ_e=1000 a.u., which limits the MD timestep to $\delta t = 0.19$ fs. To maintain a constant temperature of $T = 300$K, a Nosé thermostat [69] was applied with a period of 100 femto-second. Periodic boundary conditions were applied to the cubic systems containing one iron ion, one hydrogen peroxide molecule and 31 water molecules. The size of the cubic box was 9.900 Å. The positive charge of the systems was compensated by a uniformly distributed counter charge.

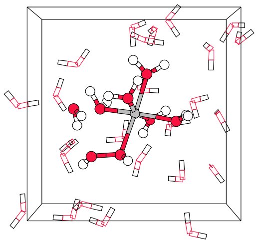

5.2.1 Fe^{2+} + 2 Cl^- in water

In this subsection, we will present the results of a short AIMD simulation of iron(II)chloride in water and compare with experimental results to assess the accuracy of the DFT approach and its implementation in the CP-PAW code, with respect to the description of high-spin iron in water. The main reason for using this system for reference calculations is that there are experimental data available for iron(II)chloride (aq) and at similar high concentration as in our simulation.

The system was constructed from an older simulation of Fe^{2+} (high–spin) in a cubic box with 32 water molecules and a uniformly distributed counter charge. Two chloride anions were added to this box and the box was scaled up to an edge of l_{box}=9.9684 Å. The formal concentration of $FeCl_2$ is 1.7 mol·l^{-1}. The total charge of the box is zero and the total spin equals $S = 2$. A temperature of T=300K was maintained during the 6.35 ps AIMD simulation. The first 2.5 ps were used for equilibrating the system and the following 3.85 ps trajectory was used for analysis.

Figure 5.1 shows the radial distribution of water hydrogens and oxygens around the iron(II) cation (upper graph) and the two chloride anions (lower graph). The first peak in the Fe-O curve is centered at $r = 2.134$ Å and originates from the 6 water ligand oxygens in the coordination shell of Fe^{II}. None of these six ligands exchange with solvent molecules during our short simulation, which follows from the zero value of $g_{\text{Fe}-\text{O}}$ at $r = 3.2$ Å. The peak position and the width at half height Δ_{FeO} agree very well with the neutron diffraction data of a 1 molal iron chloride solution, shown in table 5.1. The little shoulders at the right hand side of the peak are probably due to the sharing of water molecules by iron and one of the chloride anions. Also Fe-O bond elongations due to Jahn-Teller distortions in the high-spin hexaaqua iron(II) complex could explain these little shoulders, but in that case simultaneous Fe-O bond elongations are expected for a pair of opposite water ligands. We did not find any evidence for such a correlation. The second peak arising from water molecules in the second iron shell is centered at 4.26 Å, which is slightly less than the 4.30-4.51 Å, obtained with x-ray diffraction [150]. Integration of the peak up to the shallow minimum at $r = 4.77$ Å gives 10.5 for the number of water molecules in the second solvation shell of iron. Note however, that the limited statistics of the short AIMD trajectory causes noise in this curve and in the location of the (relatively subtle) minimum which serves as the upper integration limit. Integration of a Gaussian fitted to this Fe^{II}-O peak gives a larger number of 11.67 water molecules. Integration of the first peak of the O_{ligand}-O_{solvent} radial distribution function (data not shown) results in 1.78 second shell water molecules per water ligand, *i.e.* 10.7 molecules in the second solvation shell of iron. The experimental number of 12 from X-ray diffraction of a frozen 55.5 $H_2O/FeCl_2$ molar ratio solution is not very accurate, which follows from the deviation of least-squares fitted model of these authors to their measured data for distances larger than 4 Å. [173] The position and shape of the first Fe^{II}-H correlation peak arising from the 12 water ligand hydrogens agrees very well with neutron diffraction data (table 5.1). Although the minimum at $r = 3.5$ Å does not go to zero, no hydrolysis of the hexaaqua iron complex is observed during the simulation. The abundancy of hydrogen at a distance of $r = 3.5$ Å from the iron ion must therefore come from second shell water molecules.

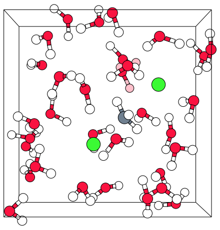

Table 5.1: *Structural properties of $FeCl_2$ in water compared to experiment. R and Δ are the position of the maximum and the full width at half maximum respectively of a Gaussian fitted to the radial distribution peak. n is the coordination number derived from integration over the peak. Θ is the average tilt angle of the ligand water molecules, defined as the angle between the Fe-O axis and the bisector of the water molecule.*

	R_{FeO}(Å)	Δ_{FeO}(Å)	n_{FeO}	R_{FeH}(Å)	Δ_{FeH}(Å)	n_{FeH}	Θ(°)
AIMD	2.134	0.263	6.0	2.762	0.371	12.1	38 ± 18
Neutron diff.[a]	2.13	0.28	6.0	2.75	0.36	12.1	32 ± 15

[a] 1 molal iron(II) chloride in acidic heavy water solution. [148]

The lower graph shows the distribution of water molecules around the chloride anions. The first peaks of g_{ClH} and g_{ClO} originating from the first Cl^- solvation shell are very similar to the ones from the radial distribution functions of HCl in water, published earlier [144]. The positions of the peak maxima $r_{\mathrm{ClH}} = 2.1$ Å and $r_{\mathrm{ClO}} = 3.1$ Å are identical. The main difference is that the present peaks are slightly less pronounced, *i.e.* they have a somewhat lower maximum and less deep minimum following the peak. Also the comparison with the neutron diffraction results on a 2 molal $NiCl_2$ solution is quite satisfactory ($r_{\mathrm{ClH}} = 2.28$ Å and $r_{\mathrm{ClO}} = 3.1$ Å, respectively) [174], although the Cl-H peak is shifted a little to the right-hand-side and is also a little broader in the experiment, resulting in a coordination number of 6.4 for Cl^- in $NiCl_2$(aq). Integration over the $g_{\mathrm{Cl-H}}$ peak up to $r = 2.70$ Å result in a coordination number of $n_c = 4.9$, slightly lower than the 5.2 found for the hydrochloric acid simulation. [144] This difference as well as the lack of the pronounced second shell structure in the present graphs, contrary to the HCl(aq) distribution, is the result of the higher concentration of structure making ions in the $FeCl_2$ (aq) simulation compared to the HCl(aq) one (the latter system contained 1 proton and 1 Cl^- per 32 H_2O). The presence of the hexaaqua iron moiety and the other Cl^- anion in the neighborhood do not allow the first chloride to build the hydration structure beyond the first solvation shell in the same way as in a more dilute Cl^- solution. On average, one (1.2) of the water molecules in the first solvation shell of Cl^-, belongs to the hexaaqua iron complex. The iron(II) chloride distances vary between 3.5 and 6.5 Å, and the Cl-Cl distance varies between 5 and 8 Å. Note that the maximum distance two particles can separate in the periodic box is 8.63 Å.

One final structural property we mention is the orientation of the six ligand water molecules, defined as the average angle between the Fe-O axis and the bisector of the water molecule, Θ. This tilt angle fluctuates around 38 degrees with a standard deviation of 18 degrees, which is again close to the experimental number of 32° ± 15°.

We conclude that AIMD with the BP functional and with the 30 Ry cutoff plane wave basis set is very well capable to describe the nearest solvent structure of high-spin iron(II).

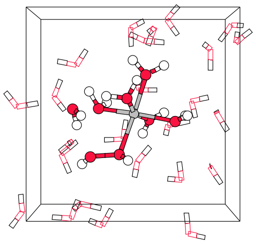

Figure 5.1: *Radial distribution of water around Fe^{2+} (upper graph) and Cl^- (lower graph) in $FeCl_2$ (aq).*

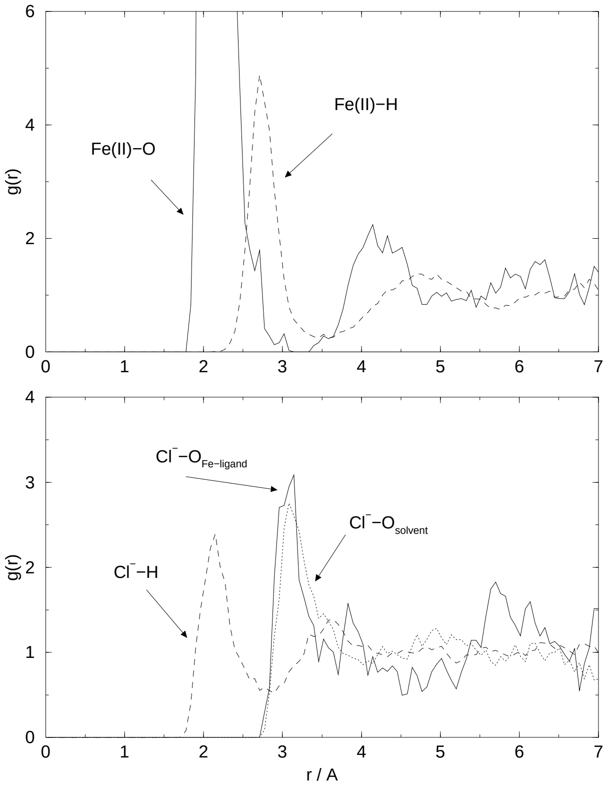

5.3 Results

5.3.1 Energetics of $OH^{\cdot}$ versus Fe(IV)O formation *in vacuo*

The energetics of the elementary reactions *in vacuo*, were calculated, using the Slater type orbital based ADF package. [70] The same exchange-correlation functional was used for the static DFT calculations as in the *ab initio* (DFT) molecular dynamics calculations. [38,67] The Kohn-Sham orbitals were expanded in a large even-tempered all-electron Slater-type basis set containing: 4 s, 2 p, and 1 d functions for hydrogen; 6 s, 4 p, 2 d, and 1 f functions for oxygen; and 11 s, 7 p, 5 d, and 1 f functions for iron [175]. The results are compiled in table 5.2. Some of these data are already given in ref. 145; small differences between table 5.2 and ref. 145 are due to the better basis set used for the present results in the table.

We see that it costs 60 kcal/mol to dissociate hydrogen peroxide into two hydroxyl radicals in the gas phase. The inclusion of the zero-point energy correction gives 54 kcal/mol, in reasonable agreement with the experimental value at 25°C of 51.2 kcal/mol. [142] The iron catalyzed production of a hydroxyl radical and a hydroxo ligand starting from a pentaaqua iron(II) hydrogen peroxide complex costs 21 kcal/mol. The reduction by 39 kcal/mol is obtained from the much stronger Fe^{III}-OH^- bond compared to the

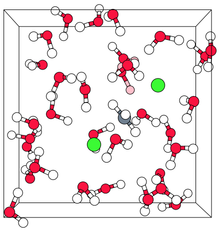

Table 5.2: *Bond dissociation energies and rearrangement energies in kcal/mol for isolated ("gas phase") complexes, calculated with the Amsterdam Density Functional program (ADF) using the Becke-Perdew exchange correlation functional. No zero point energy corrections were applied.*

	Gas phase reaction			ΔE
A	H_2O_2	$\rightarrow$	$2\ OH^{\cdot}$	59.9
B	$[(H_2O)_6Fe^{II}]^{2+}$	$\rightarrow$	$[(H_2O)_5Fe^{II}]^{2+} + H_2O$	22.1
C	$[(H_2O)_5Fe^{II}(H_2O_2)]^{2+}$	$\rightarrow$	$[(H_2O)_5Fe^{II}]^{2+} + H_2O_2$	22.8
D	$[(H_2O)_5Fe^{III}(OH)]^{2+}$	$\rightarrow$	$[(H_2O)_5Fe^{II}]^{2+} + OH^{\cdot}$	61.9
E	$[(H_2O)_5Fe^{II}(H_2O_2)]^{2+}$	$\rightarrow$	$[(H_2O)_5Fe^{III}(OH)]^{2+} + OH^{\cdot}$	20.7
F	$[(H_2O)_5Fe^{II}(H_2O_2)]^{2+}$	$\rightarrow$	$[(H_2O)_4Fe^{IV}(OH)_2\text{–}H_2O]^{2+}$	-29.3
G	$[(H_2O)_5Fe^{II}(H_2O_2)]^{2+}$	$\rightarrow$	$[(H_2O)_4Fe^{IV}(OH)_2]^{2+} + H_2O$	-1.3
H	$[(H_2O)_4Fe^{IV}(OH)_2\text{–}H_2O]^{2+}$	$\rightarrow$	$[(H_2O)_5Fe^{IV}O\text{–}H_2O]^{2+}$	-4.5
I	$[(H_2O)_4Fe^{IV}(OH)_2]^{2+}$	$\rightarrow$	$[(H_2O)_5Fe^{IV}O]^{2+}$	-6.7

Fe^{II}-H_2O_2 bond: E≈A+C-D in the table. Still, free $OH^{\cdot}$ radical formation in the gas phase remains very unfavorable. However, the remaining 21 kcal/mol can be overcome by formation of a second Fe-OH^- bond if the oxygen-oxygen cleavage is accompanied by hydrogen abstraction from an adjacent water ligand (see also figure 5.2) by the β–oxygen to form dihydroxo tetraaqua iron(IV) and water. This step is exothermic by 29 kcal/mol with a small reaction barrier of 6 kcal/mol (reaction F in the table). The pentaaqua iron(IV) oxo complex (ferryl ion) is then easily produced from the dihydroxo complex in a second exothermic step, via an internal proton transfer reaction (reaction H in the table). The water molecule produced in the first step is strongly bonded to the complex via the hydrogen of an OH^- ligand. By abstracting the hydrogen of this OH^- ligand and passing on another hydrogen to the second OH^- ligand, this water molecule facilitates step two and keeps the barrier for this transformation as low as 3.5 kcal/mol. Without the water molecule, the barrier for the second step is 18 kcal/mol. The total reaction energy for the formation of the ferryl ion from the pentaaqua iron(II)hydrogen peroxide is -34 kcal/mol (F + H in the table).

These energies show that the ferryl ion is the more likely candidate for the oxidating species in Fenton chemistry instead of the $OH^{\cdot}$ radical. The gas phase study [145] has also strongly indicated that solvent effects are important for the energetics, a striking example being the lowering of the barrier of the second step by inclusion of one water molecule in a "second solvation shell" position. Not only the reaction barriers will be modified by solvent effects but also the overall energetics. For instance, a large part of the 34 kcal/mol exothermicity of the ferryl ion formation in the gas phase originates from

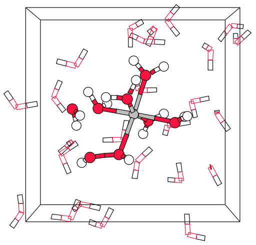

Figure 5.2: *Scheme of five-membered ring in the* $[(H_2O)_5Fe^{II}H_2O_2]^{2+}$ *complex. Geometry optimized with ADF DFT-BP using the large STO basis set mentioned in section 5.2.*

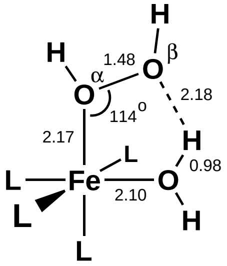

the very strongly bound "second solvation shell" water molecule produced in the first step (reaction F). This interaction energy is in the order of 28 kcal/mol (compare *e.g.* reaction F and G), which is much larger than for a typical hydrogen bond (this has been elucidated in ref. 145). In aqueous solution, this second solvation shell position would already be taken by a solvent molecule, so that the overall reaction energetics for the ferryl ion formation in solution is more likely to be in the order of -8 kcal/mol (G + I in the table). Of course, we also have to keep in mind that the solvation of the reactant (pentaaqua iron(II) hydrogen peroxide) cannot be expected to be the same as the solvation of the products (either $[(H_2O)_5Fe^{IV}O)]^{2+}$ and H_2O or $[(H_2O)_5Fe^{III}OH)]^{2+}$ and $OH^{\cdot}$), so that the reaction energies for reactions E, G and I will be modified in aqueous solution. Solvent effects can therefore make the preference for the ferryl ion formation over the free $OH^{\cdot}$ radical mechanism less prominent, or even make the two mechanisms competitive, in contrast to the gas phase Fenton chemistry. Whether this is the case, is the topic of the present study.

5.3.2 Starting from hydrogen peroxide coordinated to Fe^{II}

The system of H_2O_2 coordinated to Fe^{2+} in water was created from a previous CP-PAW MD run of Fe^{2+} (high spin) in a periodic cubic unit cell with 32 water molecules, by replacing one of the six water ligands by hydrogen peroxide. A short MD run of 1.16 ps. averaged out the short memory of any unphysical forces or velocities arising from the construction of the system. The pentaaqua iron(II) hydrogen peroxide complex was found to be a local minumum on the potential energy surface in the gas phase [145] and has also been proposed as a stable intermediate in aqueous solution [167, 176]. As we however found that the barrier for oxygen-oxygen lysis in water is very small, we fixed the hydrogen peroxide oxygen-oxygen distance at $R(OO) = 1.50$ Å and the Fe-H_2O_2 distance at $R(FeO) = 2.124$ Å, during this period of system equilibration, to prevent the premature breakup of the complex by the unrelaxed environment. Also the five iron-water ligand distances $R(FeO)$ were constrained the first 0.65 ps to their value at the first time step ($R(FeO) \approx 2.2$ Å).

After the equilibration, the MD simulation was continued (without any bond con-

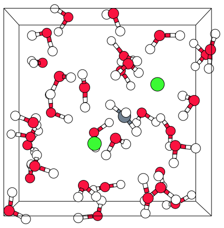

Figure 5.3: *Five snapshots of the first reaction step, starting 2 fs after the moment that the* R(OO) *and* R(FeO) *constraints of* H_2O_2 *coordinated to* $[Fe(H_2O)_5]^{2+}$ *were released* ($t = 0$)*. The hydrogen peroxide coordinated to the pentaaqua iron complex is drawn in the center of the unit cell with one of its periodic images drawn above. The two solvent waters that are involved in the reaction are also shown, but for simplicity, the other solvent water molecules are left out. See also text.*

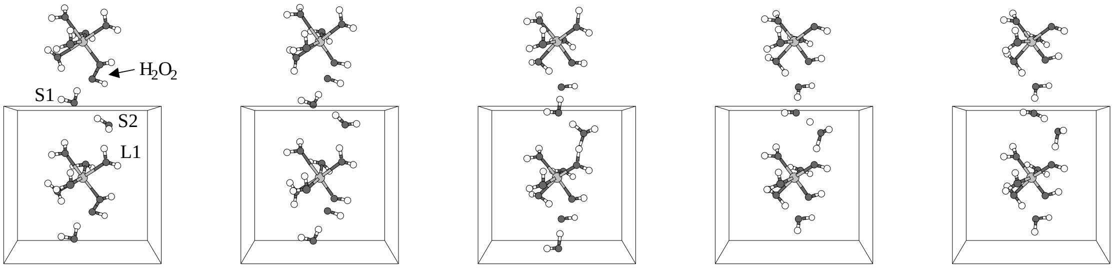

t=2 fs t=41 fs t=126 fs t=137 fs t=144 fs

straints) and the evolution of the coordinated Fenton reagent in water was followed for 10.2 ps. Figure 5.3 shows five snapshots of the $[(H_2O)_5Fe^{II}(H_2O_2)]^{2+}$ complex in the cubic unit cell at subsequent times during the first part of the simulation. Two of the solvent molecules have also been drawn, since they take part in the reaction to be described below; all other solvent molecules have been left out for clarity. The cubic unit cell is surrounded at all sides by its periodic repetitions, which provides a representation of the infinite solvent environment. In order to aid the discussion, we have drawn in figure 5.3 one periodic repetition of the complex and one water molecule in the cell above the central unit cell. Note that this water molecule is the periodic repetition of the water molecule drawn close to the bottom of the central unit cell. It is interesting to observe that in the first panel the orientations of the H_2O_2 ligand at the top iron complex, the water at the bottom in the top cell (indicated with “S1”), and the water in the upper part of the central cell (“S2”) together with a water ligand at the Fe in the central cell (“L1”) are close to creating an H-bond wire. This H-bond wire is fully established in the second panel by slight reorientations of the water molecules.

Almost immediately after the bond constraints were released at t=0 fs, the peroxide dissociates into a hydroxo group coordinated to iron and an $OH^{\cdot}$ radical which attacks a solvent water molecule that was hydrogen bonded to the hydrogen peroxide β-oxygen (see snapshots 1 and 2 in figure 5.3). Snapshots 2 and 3 show this solvent water molecule (the water molecule in the lower part of the central unit cell, as well as its periodic image drawn in the top cell) moving to the cell boundary, and in panel 4 actually crossing the boundary (at least an OH moiety). This OH moiety leaves the central unit cell across the bottom plane, but of course the periodic image OH in the top cell leaves the top cell and enters the central unit cell across the top plane of the central cell. The H of this H_2O is abstracted by the $OH^{\cdot}$ radical coming from the coordinated H_2O_2. The intertesting point

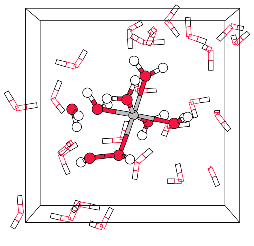

(see snapshots 4 and 5) is that the $OH^{\cdot}$ radical through a chain of H abstractions, running along the preestablished H-bond wire, actually abstracts a H from a water ligand of the neigbouring Fe complex. Closer inspection shows that the radical passage is not a typical chain reaction but rather a concerted process: snapshot 3 reveals that the "chain" starts simultaneously at both ends and is terminated in the middle (snapshot 4 and 5).

$$\Big[(H_2O)_5Fe^{II}H_2O_2\Big]^{2+} \rightarrow \Big[(H_2O)_4Fe^{IV}(OH)_2\Big]^{2+} + H_2O \tag{5.3}$$

The formation of the tetraaqua iron(IV) dihydroxo complex as the first step in the H_2O_2 dissociation (eq. 5.3) agrees with the energetic requirements derived from the gas phase calculations, see section 5.3.1. Of course, the concerted radical passage could not be observed without explicit inclusion of the aqueous solvent environment. The use of periodic boundary conditions is a means to simulate the "infinite" solvent environment with finite computational resources. It is, however, from this simulation easy to see what the possibilities are in a very large cell, or in a system without periodicity. We have established that O-O dissociation in a coordinated H_2O_2, leading to one Fe-OH bond and an $OH^{\cdot}$ radical, is only energetically possible if an additional Fe-OH bond is formed. This implies that the concerted radical path has to terminate at a water ligand. This leaves the following possibilities: a) if the pentaaqua iron(II) hydrogen peroxide complex would be in the neighborhood of a hexaaqua iron(II) complex, the $OH^{\cdot}$ passage might be, via two or three solvent waters, to a water ligand of the hexaaqua iron(II), with two mono-hydroxo pentaaqua iron(III) complexes as the result; b) with only one pentaaqua iron(II) hydrogen peroxide complex in such a system, the radical passage can go via a few solvent waters and end up with hydrogen abstraction from one of the water ligands of this same iron complex, resulting in the dihydroxo complex. This is the likely reaction pathway in a typical experimental situation where the iron catalyst is present in a low concentration. Indeed, in preliminary simulations we are performing to study the possibility of H abstraction from organic substrates, we have encountered reaction pathways in which the H abstraction took place from H_2O coordinated to the same Fe center (see figure 5.4).

We observed that the formed iron(IV)dihydroxo complex is in equilibrium with its conjugate base by proton donation to the solvent (eq 5.4).

$$\Big[(H_2O)_4Fe^{IV}(OH)_2\Big]^{2+} + H_2O \leftrightarrow \Big[(H_2O)_3Fe^{IV}(OH)_3\Big]^{+} + H_3O^{+} \tag{5.4}$$

The apparent acidity of the Fe^{IV} complex obviously can only be seen in a simulation including the solvent. The donated proton is passed on in the solvent to end up again on a hydroxo ligand, which of course does not have to be the same ligand that donated the proton to the solvent initially. Then, hydrolysis of this newly formed or another water ligand may take place, and so forth. As a result of this dynamic equilibrium, the hydroxo ligands are transformed into water ligands and *vice versa*. Eventually at a time when the system happens to find itself on the left-hand-side of equation 5.4 (in our simulation, 1.7 ps after the formation of the dihydroxo iron(IV) complex, eq. 5.3), a proton is donated by a hydroxo ligand instead of a water ligand and the iron-oxo complex is formed in our simulation.

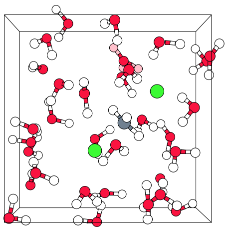

Figure 5.4: *Snapshot of an AIMD simulation of the oxidation reaction of pentaaquairon(II) hydrogen peroxide and methane in water (for simplicity, the solvent water molecules are left out). After* O^{α}*-*O^{β} *lysis, the* $O^{\beta}H^{\cdot}$ *radical immediately "grabs" the H of an adjacent water ligand, to form a water molecule and tetraaqua dihydroxo iron(IV).*

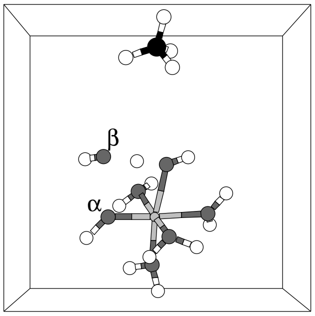

$$\left[(\mathrm{H_2O})_4\mathrm{Fe^{IV}(OH)_2}\right]^{2+} + \mathrm{H_2O} \rightarrow \left[(\mathrm{H_2O})_4\mathrm{Fe^{IV}O(OH)}\right]^{+} + \mathrm{H_3O^+} \tag{5.5}$$

Such proton donation by a hydroxo ligand has been reported before for *e.g.* the mechanism for oxo-hydroxo tautomerism observed by high-valent iron porphyrins with an oxo and hydroxo group as axial ligands in aqueous solution. [177] After another two pico-seconds, one of the water ligands leaves the first solvation shell [178], and the formed $\left[(\mathrm{H_2O})_3\mathrm{Fe^{IV}O(OH)}\right]^{+}$ complex undergoes no more spontaneous chemical changes in the next 6 pico-seconds.

The reported reaction pathway took place spontaneously, once we had constructed the initial reactants configuration. The observed reactions occur apparently without a significant reaction barrier, which puts doubt on the assumption in certain kinetic models [167, 176] that there exists a steady state of the concentration of complexed $[\mathrm{Fe^{II}}$–$\mathrm{H_2O_2}]^{2+}$. In agreement with the energetics obtained in gas phase calculations, we confirm the formation of the iron(IV)-oxo complex from the Fenton reagent, but in view of the "radical passage" mechanism of the first step (figure 5.3), the question may be raised whether $\mathrm{OH}^{\cdot}$ radicals can be excluded as possible reactive intermediates. In the gas phase, we find that reaction 5.6

$$\left[(\mathrm{H_2O})_5\mathrm{Fe^{II}H_2O_2}\right]^{2+} \rightarrow \left[(\mathrm{H_2O})_5\mathrm{Fe^{III}(OH)}\right]^{2+} + \mathrm{HO}^{\cdot} \tag{5.6}$$

is endothermic by 21 kcal/mol (table 5.2). The $\mathrm{OH}^{\cdot}$ formation followed by transfer away from the complex into the solvent, where it might react further with an organic substrate,

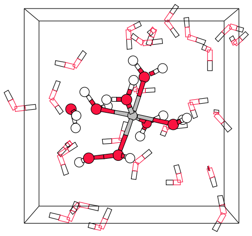

is therefore not likely. Instead, the radical is quenched, according to the pathway in figure 5.3, through a short, energetically favorable, transfer along a hydrogen-bond wire through the solvent to a complex (either the initial one or a neighboring complex) where the necessary energy is gained by formation of a second OH ligand. Only in case of a high organic substrate concentration, *i.e.* a high chance of finding an organic molecule in the neighborhood of the iron complex where the hydrogen peroxide is coordinated, can we expect the $OH^{\cdot}$ radical to have a significant contribution in the oxidation reactions, because the radical transfer could find a path along an H-bond wire to an organic substrate molecule if the latter is close enough. In all other cases, the ferryl ion is expected to be the active intermediate formed by the Fe^{II} and hydrogen peroxide in water.

The quenching of the $OH^{\cdot}$ radical by hydrogen abstraction from a H_2O ligand explains a notorious problem in the application of the Fenton reagent, namely the degradation of the chelating agents (see *e.g.* refs. 176, 179, 180). Chelating agents are bulky ligand complexes, applied to increase the solubility of the iron catalyst. However, in practice the ligands degrade during the reaction, reducing the number of catalytic cycles per metal complex. The degradation can now be understood as the scavenging process by the very short-lived $OH^{\cdot}$ radical, which is initially formed in the H_2O_2 oxygen-oxygen cleavage.

5.3.3 Internal H-bond in Fe^{II}-H_2O_2 complex

The isolated $\left[(H_2O)_5Fe^{II}(H_2O_2)\right]^{2+}$ complex is internally stabilized by a hydrogen bond between the β-oxygen of the peroxide and an adjacent water ligand, see figure 5.2. The produced $OH^{\cdot}$ radical is in the gas phase immediately quenched by H abstraction from that water ligand. [145] To investigate this shortest possible $OH^{\cdot}$ radical transfer without any intervening solvent molecules we started a second AIMD simulation, from the last configuration of the equilibration run of the previous simulation and induced this hydrogen bond by constraining the distance from the H_2O_2 β-oxygen to an H of an adjacent H_2O ligand to the value of $R_{OH} = 2.06$ Å from ref 145. The Fe-O bond constraints were released after 1.5 ps. and the remaining peroxide R_{OO} bond and the induced hydrogen bond were released after 1.93 ps. Also in this simulation the peroxide dissociates almost immediately. The hydroxyl radical remains hydrogen bonded to the water ligand for 300 femto-seconds and then abstracts the hydrogen (as in the gas phase computation) to form a water molecule and again the iron(IV)dihydroxo complex. The simulation was continued for 6 pico-seconds more in which occasionally a proton was donated by a H_2O ligand to the solvent and *vice versa* (equation 5.4) but this time no iron(IV)-oxo complex was formed. Also exchange of one of the water ligands with a solvent molecule was observed once in this simulation, but no migration of a ligand to the second coordination sphere. [178]

The spontaneous formation of the internal hydrogen bond in the pentaaqua hydrogen peroxide complex is not expected to be as likely in the solvent as it is in the isolated situation, because the hydrogen peroxide ligand can form hydrogen bonds with solvent waters instead of forming the five membered ring (see figure 5.2) via the adjacent water ligand. However, the reaction path via the internal hydrogen bond illustrates a special case of the $OH^{\cdot}$ radical quenching, by transformation of a water ligand into an hydroxo ligand, namely a path without any solvent molecules involved.

We observe that the iron(IV)(*di-/tri-*)hydroxo complex, which in the first simulation

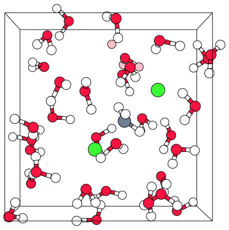

transformed to the iron(IV)-oxo moiety soon after the first step, does not do so in the present simulation. The reason for this spread in the lifetime of the hydroxo complex can be understood if we assume that reaction 5.5 is only likely to occur if the system finds itself on the left-hand-side of reaction 5.4, *i.e.* from the dihydroxide. The complex should not already have donated a proton from a water ligand to the solvent to form the trihydroxide. This assumption is endorsed by the reaction energy $\Delta E = 65$ kcal/mol of gas phase reaction 5.7,

$$\left[(H_2O)_3Fe^{IV}(OH)_3\right]^+ + H_2O \rightarrow \left[(H_2O)_3Fe^{IV}O(OH)_2\right] + H_3O^+ \tag{5.7}$$

Although this number is of course modified in aqueous solution due to the solvent effects, it is clear that a second hydrolysis after one of the water ligands has already been hydrolyzed is energetically very unfavorable. If hydrolysis of a water ligand has already taken place, it can take some time before the proton traversing through the solvent ends up on the complex again, providing a new possibility for reaction 5.5 to occur in which the iron oxo is formed. At high pH the equilibrium of reaction 5.4 will move to the trihydroxo complex side, which provides us with an explanation for the reduced reactivity of the aqueous Fenton reagent at pH > 5. [176] Note however, that the main reason to employ non–chelated Fenton chemistry at pH as low as 2-3 is the very low solubility of iron at higher pH.

5.3.4 H_2O_2 coordinating to and reacting with Fe^{2+}

Transition metal catalyzed reactions are often assumed to start with coordination of a reactant to the transition metal ion by a ligand substitution reaction. If the substitution reaction is dissociative, a vacant coordination site is first created, which is frequently induced by thermal or photochemical means. The relative probability of a dissociative mechanism for the substitution of a H_2O ligand for H_2O_2 in the Fenton reaction is not known. However, rather than starting from the coordinated H_2O_2 as in section 5.3.2, we wish to investigate in the present section whether formation of an iron oxo species is also probable when we start from a vacant coordination site to which the hydrogen peroxide will coordinate in the first step of the reaction. The energetic requirements will be essentially different since the 23 kcal/mol bond energy of H_2O_2 to pentaaquairon(II) will become available in this first step. So in this section we present the results of the AIMD simulation of a reaction pathway for the reaction of hydrogen peroxide with an aqua iron(II) complex containing a vacant coordination site. Waiting for the spontaneous diffusion of H_2O_2 to the vacant iron site could take a very long time in an AIMD simulation, simply because the reactants are as likely to separate as to approach each other and secondly because the vacant iron site is more likely to be occupied by one of the solvent water molecules than by the single H_2O_2. To increase the probability of observing a reactive encounter we need a favorable set of momenta for the reactants and the solvating water molecules to start with. In the following we will describe the method we used to obtain such a set of momenta for a configuration of separated reactants in water followed by the simulation of the reactive pathway.

We started an AIMD simulation of the pentaaqua iron(II) hydrogen peroxide complex in water, similar to the approach in the previous section. As we now know, this complex

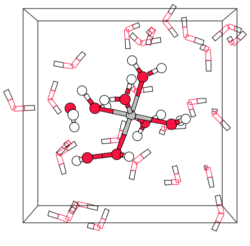

is unstable against the iron(IV) dihydroxo complex, so we constrained the H_2O_2 oxygen-oxygen bond distance to $R_{\mathrm{OO}} = 1.5$ Å to prevent the dissociation to occur. After an equilibration time of 5 ps, we perturbed the system to force the H_2O_2 ligand to leave the complex and diffuse into the solvent. There are several possibilities to make a ligand dissociate from the complex, such as adding a potential or changing the velocities of the iron complex and the H_2O_2 into opposite directions. We, however, chose to shorten the Fe-O bond distances for the five water ligands, which causes the complex to expel the hydrogen peroxide ligand. In figure 5.5, we show the evolution of the two Fe-O (of $\mathrm{Fe^{II}}$–H_2O_2) distances in the upper graph, starting with the last two ps of the equilibration phase. The lower graph shows the constrained O-O bond distance and the HO^{β} distance, with β denoting the hydrogen peroxide oxygen which is not bonded to iron (and α denoting the other oxygen). The shorter $\mathrm{Fe\text{-}O}^{\alpha}$ distance fluctuates around 2.11 Å which is slightly shorter than the average water ligand Fe-O binding of 2.17 Å in this complex. We already expected similar bonding properties for the H_2O_2 and H_2O ligands from the first bond dissociation energies in the gas phase complexes (see table 5.2) being almost equal. The hydrogen peroxide ligand is well solvated by water molecules. Both hydrogens form hydrogen bonds to solvent water molecules and also the oxygen O^{β} accepts on average 1 to 2 hydrogen bonds from solvent molecules.

At $t = 5.1$ ps, we constrained the Fe-O distances of the five water ligands at their actual value and shortened the bond length in the following 100 steps (ca. 19.4 fs) to $R = 1.8$ Å. The result is that the H_2O_2 ligand is expelled from the iron(II) coordination shell and moved into the solvent, which is shown by the upper graph in figure 5.5. The dotted lines starting at $t = 5.1$ ps show an unsuccessful attempt, where we shortened the five iron water ligands distances to only $R = 2.0$ Å. The solid and dashed lines, however, show the successfully enforced dissociation, where especially $R_{\mathrm{Fe-O}^{\alpha}}$ increases rapidly, within 600 fs, to a distance of 5.4 Å. The other oxygen, O^{β} is hydrogen bonded to 2 solvent water molecules and also the hydrogen bonded to O^{β} forms a hydrogen bond to a solvent water, which makes this part of H_2O_2 more difficult to move and causes the H_2O_2 to rotate during the separation, bringing O^{α} further away from Fe than O^{β}. At $t = 5.7$ ps, we now have a configuration of separated reactants in water, with a set of momenta that will lead to further separation. This configuration we take as the starting point for our reaction pathway and we reverse all atomic velocities to obtain a set of momenta that will lead to approaching reactants. Also, the velocities of the fictitious plane wave coefficient dynamics are reversed as well as the velocity of the Nosé thermostat variable. We remove the H_2O_2 oxygen-oxygen bond distance constraint to allow dissociation to occur and also the five iron water ligand bond distance constraints are removed. From this point we start the simulation of the reaction pathway.

The Verlet algorithm used for the integration of the equations of motion is time reversible so that the system initially tracks back onto the "forward" trajectory of the separating reactants, when the velocities are reversed. This can be seen from the symmetry of the $R_{\mathrm{Fe-O}}$ plots in the upper graph (figure 5.5) close to the mirror line at $t = 5.703$ ps. However, due to the removal of the bond distance constraints, the reversed trajectory diverges rapidly from the forward path, as should be expected from the well-known Lyapunov instability of MD trajectories towards small differences in the initial conditions. In fact, the trajectory followed by the approaching reactants is so much different from

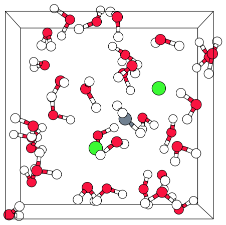

Figure 5.5: *Upper graph: The two Fe-O (H_2O_2 oxygens) distances as a function of time, starting from the last part of the equilibration phase (coordinated Fe-H_2O_2 complex). At t=5.1 ps H_2O_2 is pulled away from Fe^{II}. At t=5.7 ps the velocities are reversed. Lower graph: The O-O distance is initially fixed until t=5.7 ps. At t=6.5 ps O-O bond cleavage takes place. The OH ligand bond is broken at t=6.85 ps, when the $OH^{\cdot}$ radical grabs its hydrogen.*

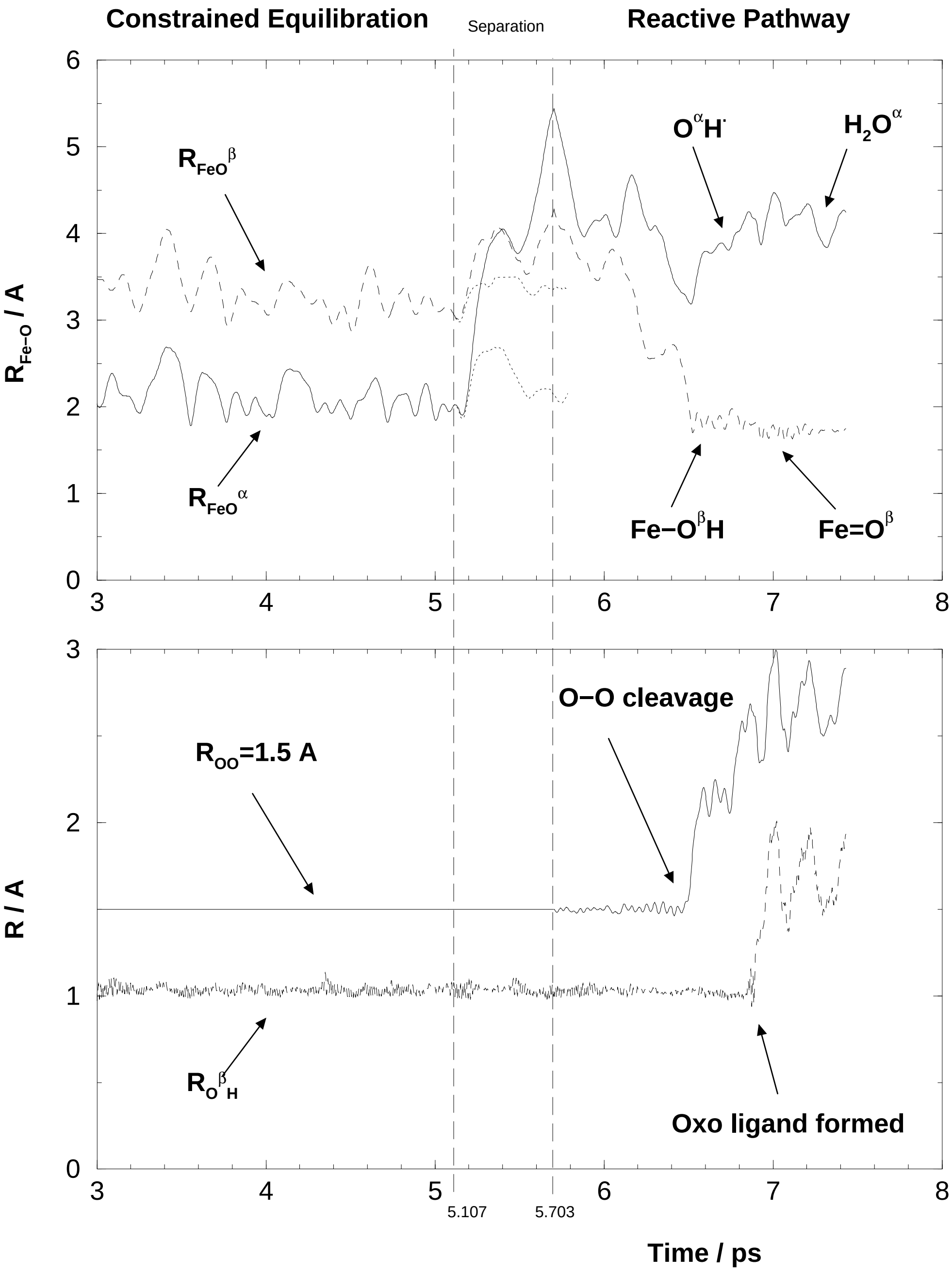

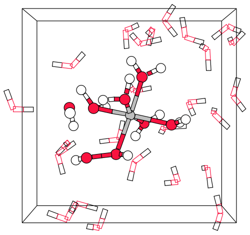

the trajectory followed by the separating reactants that now the other H_2O_2 oxygen O^{β} forms a bond with the iron(II) complex at $t = 6.5$ ps, *i.e.* 0.8 ps after the velocities were reversed. Almost immediately after the Fe-O^{β} bond is formed the H_2O_2 dissociates, which can be seen from the increasing $R_{\mathrm{Fe-O}^{\alpha}}$ and $R_{\mathrm{O-O}}$ after $t = 6.5$ ps in figure 5.5. The first three pictures in figure 5.6 show snapshots of the system (with omission of all solvent water molecules, except one, for clarity) during this coordination process. Note that the incoming hydrogen peroxide, in the lower part of the unit cell in panel 1, to the right, enters the vacant coordination site of the pentaaqua Fe(II) complex in panel 2. Apparently, the incoming hydrogen peroxide does not equilibrate in the local minimum representing the iron hydrogen peroxide complex, but instead it dissociates as soon as the iron oxygen distance reaches the short value of 2.1 Å forming the (formally) Fe^{3+}-OH^{-} complex and a hydroxyl radical. The much shorter average iron hydroxo ligand bond length of $R_{\mathrm{Fe-O}^{\beta}} = 1.84$ Å and the higher frequency compared to the Fe-O bond of a H_2O_2 or H_2O ligand confirm that indeed the $O^{\beta}H^{\cdot}$ brought the iron to the higher oxidation state of +3, increasing the bond strength by the extra electrostatic attraction. About 350 fs after the $O^{\alpha}H^{\cdot}$ radical is formed, it is attracted by the hydrogen of the $O^{\beta}H^{-}$ hydroxo ligand, which is abstracted about 50 fs later to form a water molecule and the ferryl ion moiety. The average $Fe^{4+}{=}O^{2-}$ bond length of 1.72 Å is even shorter than the iron-oxygen bond in the Fe^{3+}-OH^{-} complex (see again figure 5.5) and also the frequency increases with 100-200 cm^{-1} to roughly 700 cm^{-1} (the statistics do not allow for an accurate number for the frequency). Again, we have found the spontaneous formation of the ferryl ion.

One of the side effects of the increasing oxidation state of the iron complex, going from 2+ to 4+ during the reactive pathway, is that the acidity of the complex increases. We have already seen this phenomenon in the simulation described in the previous section. Again, as shown in the last three snapshots in figure 5.6, hydrolysis of one water ligand takes place at a time somewhere between the moment that the Fe^{III} complex was formed and the momemt that Fe^{IV} was formed. So also in this reactive pathway we end up with the $[(H_2O)_4Fe(IV)(OH)(O)]^{+}$ complex and an extra proton in the solvent.

Although the same iron(IV)oxo complex is formed as in the previous simulations starting from the equilibrated pentaaqua iron(II) hydrogen peroxide complex, there is a difference in the mechanism. In the previous sections, we have seen the formation of the dihydroxo iron(IV) complex as the initial step, as was also predicted by our gas phase study. The iron(IV)oxo complex (ferryl ion) can then be formed in a second step by hydrolysis of an hydroxo ligand (as demonstrated by our first simulation, section 5.3.2). Instead, in the present simulation starting from separated reactants, the ferryl ion is formed via a more direct mechanism. The $OH^{\cdot}$ radical does not find a fast terminating route along an H-bond wire to a water ligand to form a dihydroxo complex, but stays in the neighborhood of the formed OH^{-} ligand and then finds a quenching pathway by abstracting its hydrogen after roughly 0.3 ps. Apparently, in this case, a pathway to quench the radical in concertation with the O-O bond cleavage and make the process exothermic is not necessary. Indeed, in the present simulation, the energy balance is different. Starting from coordinated H_2O_2 (section 5.3.2) the energy needed for the $OH^{\cdot}$ formation is equal to the energy needed to dissociate the oxygen-oxygen bond of H_2O_2 (A in table 5.2) minus the energy gain of replacing the Fe^{II}–H_2O_2 bond with the much stronger Fe^{III}-OH bond (C-D). Starting with a vacant coordination site and H_2O_2 in solvation (the present

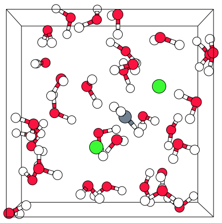

Figure 5.6: *Six snapshots of the reaction path, starting with the configuration where the velocities were reversed. In this reactive trajectory, the hydrogen peroxide coordinates at the vacant* Fe^{II} *site after 0.7 ps. The O-O bond dissociates and the* $OH^{\cdot}$ *radical wanders off (frame 3 and 4). Then in a second step the* $OH^{\cdot}$ *radical takes the hydroxo group hydrogen forming a water molecule and the ferryl complex. One solvent molecule that accepts a ligand proton is also shown, but for simplicity, the other solvent water molecules are left out. See also text.*

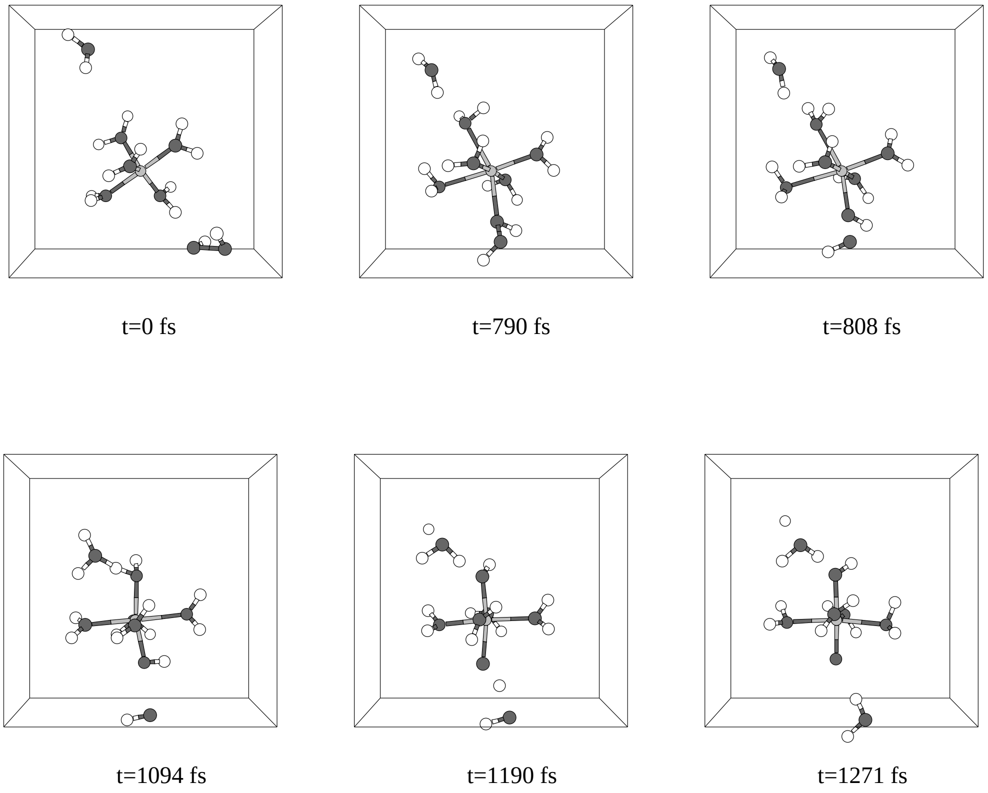

t=0 fs

t=790 fs

t=808 fs

t=1094 fs

t=1190 fs

t=1271 fs

simulation) leaves us with an extra 23 kcal/mol (neglecting the solvent effects), which is enough to form the $OH^{\cdot}$ radical without the need of a fast transfer to an exothermic termination.

The reactive pathways presented in this work illustrate possible microscopic routes via which the chemical reactions could take place. In a next study, will test how realistic the last pathway, illustrating coordination and reaction of H_2O_2 with iron(II), is, by initiating many new reactive trajectories from this last pathway using the method of transition path sampling.

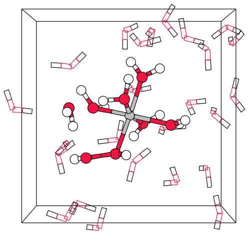

5.4 Summary and conclusions

We have performed Car–Parrinello molecular dynamics to identify the oxidative species of the Fenton reagent in water. Starting from different initial conditions, we observed in two molecular dynamics simulations, the spontaneous formation of the contested ferryl ion, which confirms the model first proposed by Bray and Gorin, and agrees with the overall energetics obtained for the reactants *in vacuo*.

Starting from the pentaaqua iron(II) hydrogen peroxide complex in aqueous solution, the oxygen-oxygen bond of the H_2O_2 ligand cleaves almost immediately to form a pentaaqua iron(III) hydroxo complex and an $OH^{\cdot}$ radical. The $OH^{\cdot}$ radical immediately abstracts either directly, or via one or two solvent water molecules, a hydrogen of a water ligand to form tetraaqua dihydroxo iron(IV) and a water molecule. This is in agreement with the formation of the $OH^{\cdot}$ radical being energetically unfavorable. So, the oxygen-oxygen dissociation is made energetically possible, because a fast transfer along an H-bond wire through the solvent to a low energy end product is found by the $OH^{\cdot}$. The dihydroxo iron(IV) ion was found to be a meta–stable complex which in our first simulation transformed into the ferryl ion, again in agreement with the relative energies in the gas phase.

Starting from artificially separated reactants (*i.e.* the hydrogen peroxide and the pentaaqua iron(II) complex with a vacant coordination site), we simulated another possible reactive pathway. We found the coordination process to be followed by spontaneous reaction to again the ferryl ion and a water molecule. In this pathway, the meta–stable intermediate of coordinated Fe^{II}-H_2O_2 as proposed in the literature was not formed, but instead immediate dissociation of the oxygen-oxygen bond took place, as soon as the reactants were close enough to each other. In contrast with the two step mechanism found earlier via a dihydroxo iron(IV) intermediate, more direct formation of the iron(IV) oxo ion took place via hydrogen abstraction by $OH^{\cdot}$ from Fe^{III}-OH^{-}, soon after the oxygen-oxygen cleavage. In this mechanism the energy needed to form the $OH^{\cdot}$ radical can be accounted for by the energy gain of the Fe^{II}-H_2O_2 bond formation.

Our simulations disfavor but do not rule out completely the Haber and Weiss $OH^{\cdot}$ radical mechanism (which is, especially in biochemistry, often taken as synonymous to Fenton chemistry). In the initial step of the iron catalyzed hydrogen peroxide dissociation, always first a very short-lived $OH^{\cdot}$ radical appears, and the L-Fe^{III}-OH^{-} complex. However, this radical has no independent existence, it abstracts a hydrogen either immediately or in a short transfer via one or two solvent molecules from a water ligand to form a dihydroxo iron(IV) complex, or even directly from the OH ligand to form the ferryl ion; in both cases neutralizing itself to a water molecule. Also when other ligands than water molecules are used, such as chelating agents, the radical may scavenge these ligands. The degradation of chelating agents, limiting the number of catalytic cycles one complex can undergo, is a notorious phenomenon in Fenton chemistry.

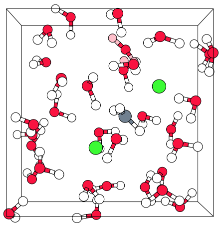

Acknowledgement

We acknowledge gratefully the helpful discussions with Michiel Gribnau from Unilever in Vlaardingen and the support by the Prioriteits Programma Materialen - Computational Materials Science (PPM-CMS). We thank the foundation NCF of the Netherlands Foundation of Scientific Research (NWO) for computer time.

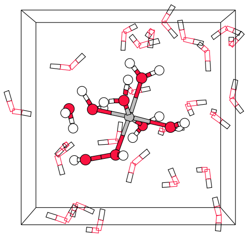

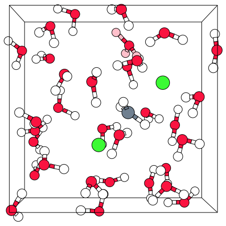

Chapter 6

Fenton-like chemistry in water: oxidation catalysis by Fe(III) and H_2O_2*

The formation of active intermediates from the Fenton-like reagent (a mixture of iron(III) ions and hydrogen peroxide) in aqueous solution has been investigated using static DFT calculations and Car-Parrinello molecular dynamics simulations. We show the spontaneous formation of the iron(III)hydroperoxo intermediate in a first step. The Fenton-like reaction thus proceeds very differently compared to Fenton's reagent (*i.e.* the Fe^{II}/H_2O_2 mixture), for which we have recently shown that the first step is the spontaneous O-O lysis of hydrogen peroxide when coordinated to iron(II) in water. For the second step in the reaction mechanism of the Fenton-like reagent, we compare the possibilities of homolysis and heterolysis of the O-O bond and the Fe-O bond of the produced $[(H_2O)_5Fe^{III}OOH]^{2+}$ intermediate. We find that concomitant hydrolysis of the reacting species plays a crucial role and, taking this into account, that O-O homolysis ($[(H_2O)_4(OH)Fe^{III}OOH]^+ \rightarrow [(H_2O)_4(OH)Fe^{IV}O]^+ + OH^{\cdot}$) *in vacuo* is most favorable with $\Delta E^{\ddagger}_{0\mathrm{k}} = 26$ kcal/mol. However, also the proper inclusion of the solvent effects is important. We have therefore calculated the free energy barrier for the O-O homolysis of the iron(III)hydroperoxo intermediate in aqueous solution at $T = 300$ K, using the method of constrained molecular dynamics and thermodynamic integration, resulting in $\Delta A^{\ddagger}_{300\mathrm{k}} = 21$ kcal/mol. Analysis of the vibrational spectra of the high-spin ($S = 5/2$) and the low-spin ($S = 1/2$) Fe(III)OOH intermediate confirms the in the literature suggested effect of the spin-state on the Fe-O and O-O bond strengths. In fact, we predict that with ligands inducing a low-spin iron(III)hydroperoxo intermediate, the barrier for the O-O homolysis will be even significantly lower.

---

[*] B. Ensing, F. Buda, and E. J. Baerends, *submitted to J. Phys. Chem. A*

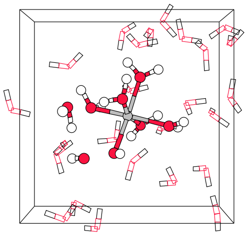

6.1 Introduction

The activation of oxygen by transition metal oxides is of fundamental importance in organic synthesis, catalysis and biochemistry. Efficient catalysts are found in nature for the hydroxylation and oxidation of organic molecules. Examples are cytochrome P450, methane monooxygenase (MMO), and the antitumor drug bleomycin (BLC), all of which have low-valent iron ions as the active centers that can be turned into highly reactive high-valent iron-oxo, iron-peroxo or iron-hydroperoxo complexes. Also Fenton's reagent, a mixture of iron(II) ions and hydrogen peroxide, is widely applied to oxidize organic substrates. Although H.J.H. Fenton himself used the unchelated Fe^{2+}/H_2O_2 mixture in acidic aqueous solution when he first recorded the oxidative potential of this mixture in 1876 [128, 155], many modifications have since then been applied in order to alter the reactivity, to enhance the solubility in other solvents, to increase the pH range, and to avoid precipitation of the metal catalyst. This has led to a great variety of ligated iron(II) complexes in combination with H_2O_2 (or HOCl), or even with different transition metals, such as Mn(II) or Fe(III) which are all often referred to as *Fenton's reagent*. To distinguish between the iron(II) and iron(III) combinations, we will however follow the convention of using *Fenton-like reagent* for the Fe^{3+}/H_2O_2 mixture and restrict the use of *Fenton's reagent* to denote the Fe^{2+}/H_2O_2 mixture. The Fenton-like reagent is also capable of oxidizing organic substrates, but it is somewhat less reactive than Fenton's reagent. As iron(III) can be produced in applications of Fenton's reagent, Fenton chemistry and Fenton-like chemistry often occur simultaneously. Interestingly, Fenton and Fenton-like chemistry are generally believed to proceed via similar mechanisms as oxidation reactions with the aforementioned complex and bulky enzymes.

Until recently, Fenton chemistry was still far from being fully understood. Numerous reaction mechanisms have been proposed based on different active intermediates such as $OH^\cdot$ and $OOH^\cdot$ radicals and the earlier mentioned high-valent iron species. Haber and Weiss' $OH^\cdot$ radical mechanism [156] is probably the most popular candidate for the Fenton reaction:

$$Fe^{2+} + H_2O_2 \rightarrow Fe^{3+} + OH^- + OH^\cdot \tag{6.1}$$

followed by the alternative mechanism first suggested by Bray and Gorin [157], in which the ferryl ion, $[Fe^{IV}O]^{2+}$, is supposed to be the active intermediate:

$$Fe^{2+} + H_2O_2 \rightarrow [Fe^{IV}O]^{2+} + H_2O \tag{6.2}$$

In both mechanisms, the hydrogen peroxide O-O lysis forms the essential step. We have recently performed static density functional theory (DFT) calculations to study the active species produced by the hydrated Fenton's reagent $[Fe^{II}(H_2O)_5\ (H_2O_2)]^{2+}$ *in vacuo* [145] as well as *ab initio* (DFT) molecular dynamics (AIMD) simulations of Fe^{2+} and H_2O_2 in aqueous solution [146, 171]. In this work, we showed that the ferryl ion is easily formed when hydrogen peroxide coordinates to an iron(II) ion in water, which confirms the reaction mechanism first proposed by Bray and Gorin (reaction 6.2). Moreover, formation of the ferryl ion from the hydrated Fenton's reagent *in vacuo* was found to be energetically favored over the formation of free hydroxyl radicals (reaction 6.2).

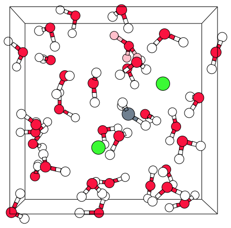

For the Fenton-like reagents it is believed that initially no O-O bond breaking takes place, but instead an iron(III)hydroperoxo intermediate is formed as the first step *via* hydrolysis:

$$Fe^{3+} + H_2O_2 \rightarrow [Fe^{III}OOH]^{2+} + H^+ \tag{6.3}$$

This intermediate might be able to react with organic substrates or break up in smaller active species in a second step. The iron(III)hydroperoxo may *e.g.* homolyze at the Fe-O bond [132, 181, 182]

$$[Fe^{III}OOH]^{2+} \rightarrow Fe^{2+} + OOH^{\cdot} \tag{6.4}$$

generating iron(II) and producing the reactive $OOH^{\cdot}$ radical, or at the O-O bond producing the ferryl ion and an $OH^{\cdot}$ radical [132, 158]:

$$[Fe^{III}OOH]^{2+} \rightarrow [Fe^{IV}O]^{2+} + OH^{\cdot} \tag{6.5}$$

Alternatively, O-O bond heterolysis could take place, producing the highly reactive Fe^{V} species [132, 183]:

$$[Fe^{III}OOH]^{2+} \rightarrow [Fe^{V}O]^{3+} + OH^{-} \tag{6.6}$$

Probably many of the proposed mechanisms compete with each other depending on the reaction conditions, such as the metal ligands, the solvent, the pH and the organic substrate to be oxidized. This is of course one of the reasons why Fenton-like chemistry still holds secrets. Another important reason is the very elusive nature of the active species, which live too short to have been definitively observed yet in experiments. Obviously, that is not a problem for computer simulations.

In the present work, we will investigate the active species for the Fenton-like chemistry, and we will focus on the differences between iron(II) and iron(III) in activating hydrogen peroxide. To simulate the generation, evolution and termination of reactive intermediates such as hydroxyl radicals we need an accurate description of the aqueous environment. The method of choice is *ab initio* (DFT) Molecular Dynamics method (AIMD), using the Car-Parrinello technique, which has already proven to be a very useful tool for our type of systems. [52, 144, 171, 184] Density functional theory (DFT) has already proven to be very useful for the unraveling of the activation mechanisms of MMO [163, 164, 185–188] and P450 [159–161, 189, 190] and the oxidation of methane and benzene with the bare ferryl ion ($Fe^{IV}{=}O$) [168, 170, 191–195].

The paper is organized as follows. First, we briefly summarize the computational details in section 6.2. In section 6.3, we present our results, starting with the static DFT calculations of the energetics of the proposed elementary Fenton and Fenton-like reactions of the hydrated iron hydrogen peroxide complexes *in vacuo*. Clearly, the different nature of the Fe(III)/H_2O_2 reagent compared to the Fe(II)/H_2O_2 reagent is revealed, showing that $OH^{\cdot}$ radical or ferryl ion formation *via* O-O lysis as the first mechanistic step is energetically very unfavorable and instead hydrolysis (eq 6.3) is indeed predicted to be the most likely initial step. However, realistic modeling of the hydrolysis, *i.e.* simulating the donation of H^+ by the iron(III) complex to the aqueous solution, requires the explicit inclusion of the solvent molecules. This is done in subsection 6.3.2 by first presenting

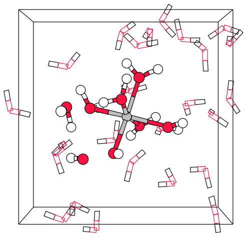

three illustrative AIMD simulations of the reaction between Fe^{III} and H_2O_2 in water, which show the spontaneous formation of the iron(III)hydroperoxo species, followed by the characterization of Fe(III)OOH(aq). We have computed the vibrational spectra for the iron(III)hydroperoxo species in both the high-spin ($S = 5/2$) state and the low-spin ($S = 1/2$) state, and have compared to experimental Raman spectra. As the second step in the Fenton-like mechanism, the O-O homolysis of the iron(III)hydroperoxo species, producing the ferryl ion and a hydroxyl radical, is predicted by our static DFT calculations *in vacuo*. The free energy barrier for this step was computed in aqueous solution using the method of constrained molecular dynamics and thermodynamic integration, the results of which are presented in subsection 6.3.3. The paper ends with conclusions in section 6.4.

6.2 Computational Details

The electronic structure calculations, to compute the energies, geometry optimizations and frequencies of the molecules and hydrated iron complexes *in vacuo*, were performed at the DFT level of theory (see *e.g.* ref. 46), as implemented in the Amsterdam Density Functional package ADF [70]. We used the Becke-88 gradient corrected exchange functional [67] and the Perdew-86 gradient corrected correlation functional [38]. The Kohn-Sham orbitals were expanded in a large even-tempered all-electron Slater-type basis set containing: 4 *s*, 2 *p*, and 1 *d* functions for hydrogen; 6 *s*, 4 *p*, 2 *d*, and 1 *f* functions for oxygen; and 11 *s*, 7 *p*, 5 *d*, and 1 *f* functions for iron [175]. The *ab initio* (DFT) molecular dynamics calculations of the systems including the solvent environment were done with the Car-Parrinello (CP) method [49] as implemented in the CP-PAW code developed by Blöchl [24]. The one-electron valence wave functions were expanded in an augmented plane wave basis up to a kinetic energy cutoff of 30 Ry. The frozen core approximation was applied for the 1*s* electrons of O, and up to 3*p* for Fe. For the augmentation for H and O, one projector function per angular-momentum quantum number was used for *s*- and *p*-angular momenta. For Fe, one projector function was used for *s* and *p* and two for *d*-angular momenta. The characteristic feature of the Car-Parrinello approach is that the electronic wave function, *i.e.* the coefficients of the plane wave basis set expansion, are dynamically optimized to be consistent with the changing positions of the atomic nuclei. The mass for the wave function coefficient dynamics was μ_e=1000 a.u., which limits the MD time step to $\delta t = 0.19$ fs. To maintain a constant temperature of $T = 300$K a Nosé thermostat [69] was applied with a period of 100 femto-second. Periodic boundary conditions were applied to the cubic systems containing one iron ion, one hydrogen peroxide molecule and 31 water molecules. The size of the cubic box was 9.900 Å. The positive charge of the systems was compensated by a uniformly distributed counter charge.

6.3 Results

We assume, as is usually done, that the initial step in Fenton and Fenton-like chemistry is the nucleophilic addition of hydrogen peroxide to the iron complex by exchanging with a water ligand in the hydration shell [196]. In the next section (6.3.1), we discuss the energetics of various reactions starting from the $[Fe^{II}(H_2O)_5(H_2O_2)]^{2+}$ and the

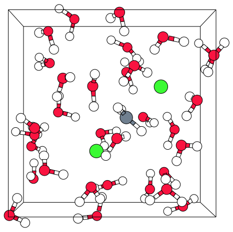

Figure 6.1: *Optimized ground-state structures of* $[Fe^{III}(H_2O)_5(H_2O_2)]^{3+}$ *(left-hand-side) and* $[Fe^{II}(H_2O)_5(H_2O_2)]^{2+}$ *(right-hand-side).*

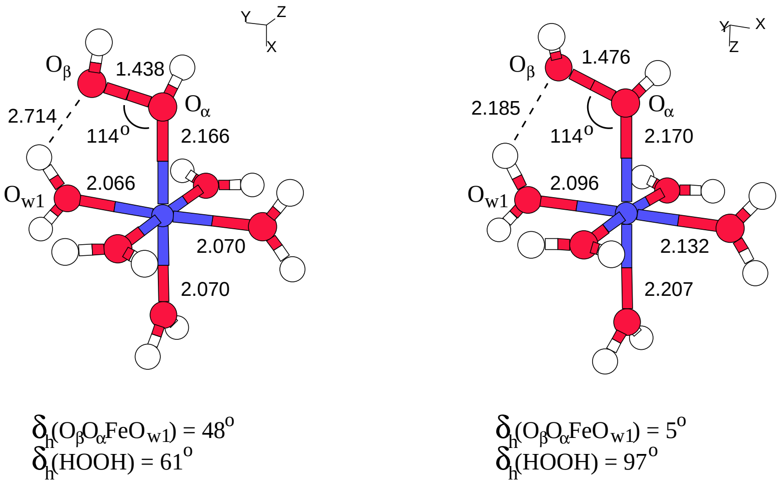

$[Fe^{III}(H_2O)_5(H_2O_2)]^{3+}$ complexes in order to investigate the thermodynamic possibilities and impossibilities. Figure 6.1 shows the geometry optimized structures of these two complexes *in vacuo*. Later on, in section 6.3.2, we will show an illustrative pathway of the reaction of H_2O_2 with Fe^{3+} in water, which includes the coordination process.

6.3.1 Elementary Fenton and Fenton-like reactions *in vacuo*

We have computed the reaction energies of the elementary Fenton and Fenton-like reactions of the hydrated iron complexes *in vacuo*, among which the ones mentioned in the introduction (equations 6.1-6.6), and compiled the results in table 6.1. The first two columns of numbers on the left-hand-side show the reaction energies in kcal/mol with an iron(II) complex and an iron(III) complex as the reactant, respectively. Hydrated metal ions can be acidic, the acidity increasing with increasing oxidation state of the metal ion. For example, the acidity constant of $[Fe^{III}(H_2O)_6]^{3+}$ equals $pKa = 2.2$ [154], so that in aqueous solution hydrolysis easily takes place to form the iron(III)hydroxo complex $[Fe^{III}(H_2O)_5(OH)]^{2+}$ and a free hydronium ion. As we shall see, the lowering of the total charge on the metal complex from 3+ to 2+ has a significant effect on the reactivity. The reaction energies of the present elementary reactions starting from such an iron(III)hydroxo complex are given in the last column of table 6.1. Deprotonation of an iron(II) complex is less likely. The acidity constant of hexaaquairon(II) is $pKa = 9.5$ [143], so that the $[Fe^{II}(H_2O)_5(OH)]^{+}$ complex forms an improbable starting species.

Starting from hexaaquairon complexes, we see after comparing reactions A and B, that the ligand exchange of a water ligand by hydrogen peroxide is almost thermoneutral, but that the water (and H_2O_2) ligands are much stronger bonded to the 3+ charged iron(III)

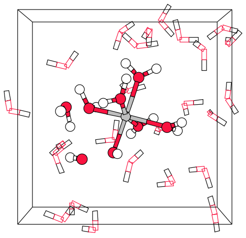

Table 6.1: *Comparison of DFT-BP reaction energies (kcal/mol) starting with either an iron(II) complex (n=2) or an iron(III) complex (n=3). The last column shows the reaction energy starting with iron(III) (n=3), but with one water ligand replaced by an hydroxo ligand, so that the complex has the same total charge as the iron(II) complex.*

Gas phase reaction		Fe(II)	Fe(III)	Fe(III)OH$^-$
A	$Fe^{n+}(H_2O)_6 \rightarrow Fe^{n+}(H_2O)_5 + H_2O$	22.1	45.7	24.7
B	$Fe^{n+}(H_2O)_5(H_2O_2) \rightarrow Fe^{n+}(H_2O)_5 + H_2O_2$	22.8	46.4	25.4
C	$Fe^{n+}(H_2O)_5(H_2O_2) \rightarrow Fe^{(n+1)+}(H_2O)_5(OH^-) + HO^{\cdot}$	20.7	60.8	38.5
D	$Fe^{n+}(H_2O)_5(H_2O_2) \rightarrow Fe^{(n+2)+}(H_2O)_5(O^{2-}) + H_2O$	-8.0	56.9	9.6
E	$Fe^{3+}(H_2O)_5(H_2O_2) + H_2O \rightarrow Fe^{3+}(H_2O)_5(OOH^-) + H_3O^+$		-156	
F	$Fe^{3+}(H_2O)_5(H_2O_2) + H_2O \rightarrow Fe^{3+}(H_2O)_4(OH^-)(H_2O_2) + H_3O^+$		-145	
G	$Fe^{3+}(H_2O)_5(OOH^-) \rightarrow Fe^{2+}(H_2O)_5 + HOO^{\cdot}$		36.8	40.6
H	$Fe^{3+}(H_2O)_5(OOH^-) \rightarrow Fe^{3+}(H_2O)_5 + HOO^-$		417	281.
I	$Fe^{3+}(H_2O)_5(OOH^-) \rightarrow Fe^{4+}(H_2O)_5(O^{2-}) + HO^{\cdot}$		42.6	26.1
J	$Fe^{3+}(H_2O)_5(OOH^-) \rightarrow Fe^{5+}(H_2O)_5(O^{2-}) + HO^-$		444.	281.

complexes than to the 2+ charged iron(II) and iron(III)hydroxo complexes (by more than 20 kcal/mol). The production of a free hydroxyl radical, starting from hydrogen peroxide coordinated to iron(II) (as in the Haber and Weiss mechanism, reaction 6.1) costs 20.7 kcal/mol (reaction C in the table), a reduction of 39.2 kcal/mol with respect to the dissociation of free hydrogen peroxide into two hydroxyl radicals ($\Delta E = 59.9$ kcal/mol at the same level of theory and 54 kcal/mol including the zero point energy, in reasonable agreement with the experimental value at 25°C of 51.2 kcal/mol). For hydrogen peroxide coordinated to pentaaquairon(III) on the other hand, does the O–O dissociation and free $OH^{\cdot}$ radical formation not lead to a reduction compared to free H_2O_2 dissociation, but is even slightly more endothermic (by 1 kcal/mol). The $OH^{\cdot}$ radical produced in reaction C can also abstract the hydrogen from the produced hydroxo ligand to form the ferryl ion ($[Fe^{IV}(H_2O)_5O]^{2+}$) and a water molecule, following the Bray and Gorin mechanism (reaction 6.2) when starting from $[Fe^{II}(H_2O)_5(H_2O_2)]^{2+}$ or the $[Fe^{V}(H_2O)_5O]^{3+}$ species and H_2O when starting from $[Fe^{III}(H_2O)_5(H_2O_2)]^{3+}$ (reaction D in the table). In the first case, the overall reaction is exothermic by 8 kcal/mol, but starting with iron(III), the formation

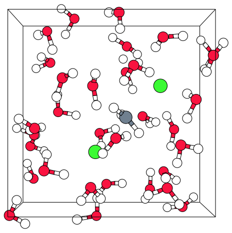

of the oxo species is again energetically very unfavorable ($\Delta E = 56.9$ kcal/mol). These numbers clearly show, in the first place, that the highly reactive OH$^{\cdot}$ radical and high-valent iron oxo species are much more easily formed from Fenton's reagent (Fe^{2+}/H_2O_2) than from the Fenton-like reagent (Fe^{3+}/H_2O_2), confirming the experimentally observed difference in oxidative reactivity between the two reagents. In the second place, reactions C and D indicate that the ferryl ion is a much more likely candidate for the active species in Fenton chemistry than the free OH$^{\cdot}$ radical. In refs 145,146,171,197, we have discussed the Fenton reagent more extensively, and we have shown that in the two-step process that leads to formation of the ferryl ion, the highest of the two transition states is only 6 kcal/mol. We have also investigated the reactivity of the ferryl ion towards organic substrates by simulating the oxidation of methane to methanol by the ferryl ion [198]. We will now continue to focus solely on the Fenton-like reagent.

The formation of the iron(III)hydroperoxo species from iron(III)hydrogen–peroxide in aqueous solution (reaction 6.3), which is believed to be the initial step in Fenton-like chemistry (reaction E in table 6.1), is poorly modeled *in vacuo*. The absolute reaction energies of such charge separation reactions are typically highly overestimated, due to the omission of the screening of the solvent and the energies of solvation. The hydrolysis of hexaaquairon(III) for instance, forming pentaaqua hydroxo iron(III) by donating a proton to a water molecule *in vacuo*, results in an energy gain of 145 kcal/mol, whereas the experimental acidity constant of $\mathrm{p}Ka = 2.2$ indicates an (free) energy loss of 3 kcal/mol. However, we can nevertheless compare the reaction energies of charge separation processes for which the solvent effects are expected to be similar. Hydrolysis of coordinated H_2O in pentaaquairon(III)hydrogen–peroxide (reaction F in table 6.1), for example, is not expected to be much different from the hydrolysis of hexaaquairon(III), and the reaction energies *in vacuo* are indeed in both cases found to be -145 kcal/mol. Now, we can compare reaction E and F, assuming no large differences in energies of solvation for the products, and conclude that the formation of the iron(III)hydroperoxo species in aqueous solution indeed is a likely initial step in Fenton-like chemistry, and that the hydrolysis of the H_2O_2 ligand is probably even favored over the hydrolysis of a H_2O ligand. Nevertheless, we want to stress that the proper inclusion of the solvent effects is required to accurately model this first step in Fenton-like chemistry.

Reactions G till J in the table are possible reactions of a second step, in which the iron(III)hydroperoxo species forms very reactive particles such as radicals and high-valent iron oxo species. We see that the unscreened charge separation processes of Fe-O bond or O-O bond heterolysis (reactions H and J, respectively) again results in very high values for the reaction energies *in vacuo* (this time uphill), which makes it impossible to compare these reactions with the homolysis equivalents (reactions G and I, respectively), although we doubt that inclusion of the solvent screening and solvation energies will bring the reaction energies of reaction H and J in aqueous solution below 50 kcal/mol. The energies for the homolysis of the Fe-O or O-O bond of 36.8 kcal/mol and 42.6 kcal/mol are also rather high. An important difference between the two reactions is that, although they both produce highly reactive radicals, in the Fe-O homolysis (G) the formal oxidation state of iron is lowered, whereas in the O-O homolysis (I) the formal oxidation state of iron increases. As the acidity of hydrated metal ions increases with the oxidation state of the metal (see before), hydrolysis of the metal complex works in opposite directions

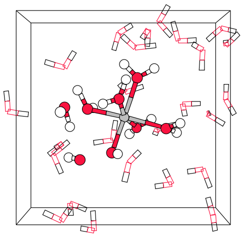

for the two homolysis reactions. Taking the hydrolysis effect into account results in O-O homolysis forming the most probable second step in Fenton-like chemistry, with a reaction energy of 26.1 kcal/mol *in vacuo*, comparable to the initial ligand expulsion step, reaction A (see the third column of table 6.1 for the reaction energies when first hydrolysis of an H_2O ligand has occurred). As in this reaction both $OH^{\cdot}$ radicals and ferryl ions are formed, it is particularly interesting to study this O-O homolysis in more detail with inclusion of the water environment. In section 6.3.3, we will compute the free energy barrier for the O-O homolysis reaction in aqueous solution, and will then consider the role of (simultaneous) hydrolysis of a H_2O ligand in more detail.

Summarizing, the static DFT calculations show that for iron(III)hydrogen–peroxide the direct formation of the $OH^{\cdot}$ radical (C) or the high-valent iron oxo species(D) is energetically much less favorable than for iron(II)hydrogen–peroxide. Secondly, the acidity of iron(III) complexes is expected to play an important role as the hydrolysis of a water ligand lowers the reaction energies dramatically, particularly in the case of the iron(V)oxo complex formation (D). In the third place, hydrolysis of the H_2O_2 ligand of $[Fe^{III}(H_2O)_5(H_2O_2)]^{3+}$, producing the iron(III)hydroperoxo species (E) is energetically favored over hydrolysis of a water ligand (F). In the next section, we will show that in aqueous solution indeed the hydrolysis of the H_2O_2 ligand (E) forms the initial step in the Fenton-like chemistry, so that for the next step the transformation of the iron(III)hydroperoxo species becomes important. Fourth, possible second-step transformations are the homolysis of the Fe-O bond (G) and the O-O bond (I) of which the latter becomes particularly interesting when a second hydrolysis (of a water ligand) takes place. We will investigate the O-O bond homolysis and the simultaneous second hydrolysis in aqueous solution in section 6.3.3.

6.3.2 The first reaction step in Fenton-like chemistry in water: formation and characterization of the iron(III) hydroperoxo species

a) Formation. In this section, we will describe the results of our study of the most likely intermediate formed in a mixture of iron(III) ions and hydrogen peroxide in water. We will follow the same approach as in our previous work [146] on the active intermediate formed from iron(II) and hydrogen peroxide, which makes it easy to compare the reactions with each other. In this previous work on Fenton's reagent, we showed two illustrative pathways of the reaction between Fe^{2+} and H_2O_2 in water producing the high-valent iron-oxo species $[Fe^{IV}O]^{2+}$. The ferryl ion formation occurred either in two steps, via an iron(IV) dihydroxo intermediate ($[Fe^{IV}(OH)_2]^{2+}$), if we started from a $[Fe^{II}(H_2O_2)]^{2+}$ complex, or via a more direct "rebound" mechanism if we started from separated Fe^{2+} and H_2O_2, thus including the coordination process of H_2O_2 to an empty iron(II) site. The $[Fe^{II}(H_2O_2)]^{2+}$ complex was not found to be a stable intermediate in aqueous solution, unlike $[(H_2O)_5Fe^{II}(H_2O_2)]^{2+}$ *in vacuo*.

For the present reaction of hydrogen peroxide with iron(III), we performed a Car-Parrinello MD simulation of H_2O_2 coordinated to Fe^{3+}, surrounded by 31 water molecules in a cubic box with periodic boundary conditions. We used a snapshot from the study

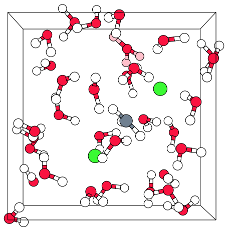

of the $[\mathrm{Fe^{II}(H_2O_2)}]^{2+}$ complex in water for the initial configuration, and removed in that configuration one spin-down electron from the system. The total spin was thus $S = 5/2$, and the total charge equaled 3+, which was counterbalanced by a uniformly distributed 3– charge. We relaxed the system to the new situation, by an MD run of 3.5 ps. During this time of equilibration, bond constraints were applied to the Fe-O and O-O bonds, fixing these bond lengths to their equilibrium distances, in order to prevent a premature breakup of the complex by the unrelaxed environment. Next, we removed the constraints and followed the evolution of the $[\mathrm{Fe^{III}(H_2O_2)}]^{3+}$ complex in water for 5 ps.

Already in the equilibration phase, hydrolysis had taken place on the α–oxygen of the ligated hydrogen peroxide (α denotes the oxygen connected to iron), donating the proton to the water solvent:

$$\Big[\mathrm{(H_2O)_5Fe^{III}(H_2O_2)}\Big]^{3+} + \mathrm{H_2O} \rightarrow \Big[\mathrm{(H_2O)_5Fe^{III}(OOH)}\Big]^{2+} + \mathrm{H_3O^+} \tag{6.7}$$

Our simulation thus started with an iron(III)hydroperoxo complex and a hydronium ion in water, and no further spontaneous transformation took place during the 5 ps of molecular dynamics. The oxygen-oxygen bond did not break but instead fluctuated around an average bond length of $R_{\mathrm{OO}} = 1.466$ Å, contrary to the oxygen-oxygen bond of hydrogen peroxide coordinated to iron(II) which was found to cleave spontaneously in aqueous solution. Also was the aqueous proton not seen to jump back on the hydroperoxo ligand during our simulation, as with the dynamic equilibria we have for instance seen for hydrolysis of aqua ligands of hexaaquairon(III) (see before) and the $[\mathrm{(H_2O)_4Fe^{IV}(OH)_2}]^{2+}$ complex. [171] The OH bond length fluctuations of the aqua ligands were significantly larger than the ones in hexaaquairon(II), with maxima of $R_{\mathrm{OH}}^{\max} = 1.4$ Å ($R_{\mathrm{OH}}^{\max} = 1.1$ Å in hexaaquairon(II)), almost donating a proton to the solvent, but never dissociating completely. This indicates that the acidity of $[\mathrm{(H_2O)_5Fe^{III}(OOH)}]^{2+}$ is in between that of hexaaquairon(II) and hexaaquairon(III).

To make sure that the hydroperoxo ligand formation (during the equilibration phase) was not the result of non-equilibrium solvent effects, we started a second MD simulation from a configuration of the equilibration phase at a time just before the hydrogen peroxide hydrolysis took place. This time, we constrained the O^{α}-H bond length to prevent hydrolysis during a 1.2 ps equilibration run, after which we removed the constraint and again followed the evolution of the system. Although during most of the equilibration time now an aqua ligand donated a proton to the solvent (reaction equation 6.8),

$$\Big[\mathrm{(H_2O)_5Fe^{III}(H_2O_2)}\Big]^{3+} + \mathrm{H_2O} \leftrightarrow \Big[\mathrm{(H_2O)_4Fe^{III}(OH)(H_2O_2)}\Big]^{2+} + \mathrm{H_3O^+} \tag{6.8}$$

this proton is united with the hydroxo ligand again at the end of the equilibration so that indeed we started with a $[\mathrm{(H_2O)_5Fe^{III}(H_2O_2)}]^{3+}$ complex in water. After 0.2 ps, again hydrolysis of the coordinated hydrogen peroxide takes place so that the $\mathrm{Fe^{III}OOH}$ moiety is formed which again remains stable for the next 1.75 ps, after which we stopped the computation. Clearly, this second simulation shows that the $\mathrm{H_2O_2}$ ligand hydrolysis was not an effect of the unrelaxed environment (which was not clear from the first simulation). And secondly, the higher stability of the O-O bond compared to the iron(II)hydrogen–peroxide case is not a result of the $\mathrm{H_2O_2}$ hydrolysis, since no O-O lysis occurred spontaneously when only the O^{α}-H bond length was constrained.

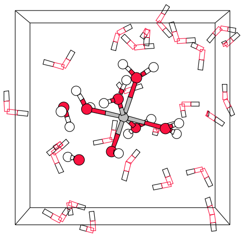

Figure 6.2: *The Fe-*O^{α}*, Fe-*O^{β}*,* O^{α}*-*O^{β} *and* O^{α}*-H distances as a function of time during the AIMD simulation of* H_2O_2 *and* Fe^{3+} *in water, starting from the last part of the equilibration phase (coordinated Fe-*H_2O_2 *complex). After* $t = 3.32$ *ps, Fe-*O^{α} *increases as* H_2O_2 *leaves the coordination shell. At a separation of more than 3 Å, all velocities are reversed and simulation shows the process of coordination of hydrogen peroxide occurring almost simultaneous with the hydrolysis forming the iron(III)hydroperoxo moiety.*

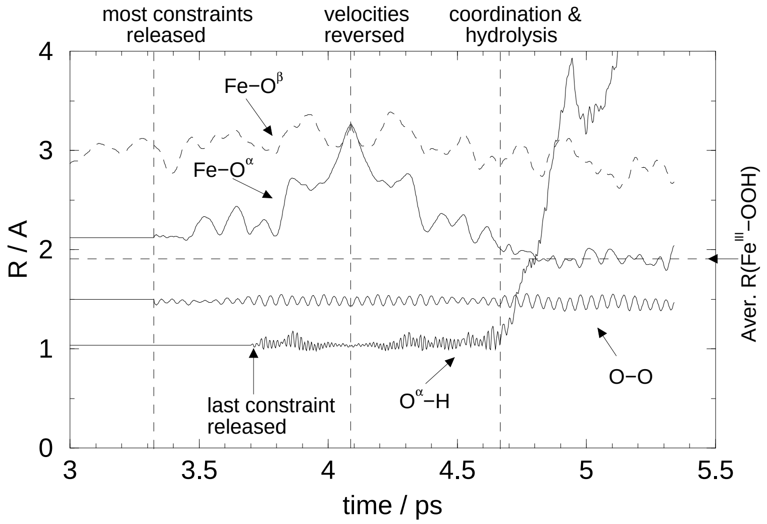

Finally, we performed a last AIMD simulation in which we also wanted to include the formation of a coordination bond of hydrogen peroxide to a vacant coordination site of iron(III). Starting with a random configuration in which the solvated reactants are separated from each other a certain distance is however very unpractical, because the probability of a spontaneous coordination is too small to make an observation likely in the relatively short time of a typical AIMD simulation. We therefore applied a simple device, which had worked already very well for the iron(II)/H_2O_2 system. [146] We carried out a constrained AIMD simulation of hydrogen peroxide coordinated to iron(III) in water. The O-O bond, the Fe-O^{α} bond and the O^{α}-H bond were fixed to their equilibrium distances and also a bond constraint was applied to the distance between the peroxide's O^{β} and the hydrogen of an adjacent water ligand, fixing this distance to $R_{\mathrm{OH}} = 2.0$ Å. The small strain induced in the five-membered ring which is closed by the R_{OH} constraint (see also figure 6.1) was enough to pull hydrogen peroxide from the aquairon complex when we released all constraints, except the O^{α}-H bond constraint. This process is illustrated in figure 6.2, showing the distances Fe-O^{α}, Fe-O^{β}, O^{α}-O^{β} and O^{α}-H as a function of time, starting just before the moment we released these bond constraints.
After release of all constraints except the O^{α}-H bond constraint, at $t = 3.32$ ps, the Fe-O^{α} bond starts to break, which is visible in figure 6.2 as the appearance of oscillations with increasing amplitude of $R_{\mathrm{Fe-O^{\alpha}}}$, and at $t > 3.9$ ps, Fe and O^{α} clearly separate. During the dissociation process, at $t = 3.72$ ps, we also released the O^{α}H bond constraint. At

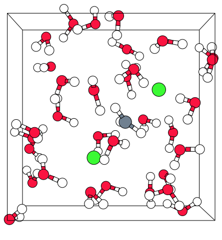

Figure 6.3: *Frequency spectra of the $Fe^{III}OOH$ species in water in the electronic high-spin state $S = 5/2$ (upper half) and in the low spin state $S = 1/2$ (lower half).*

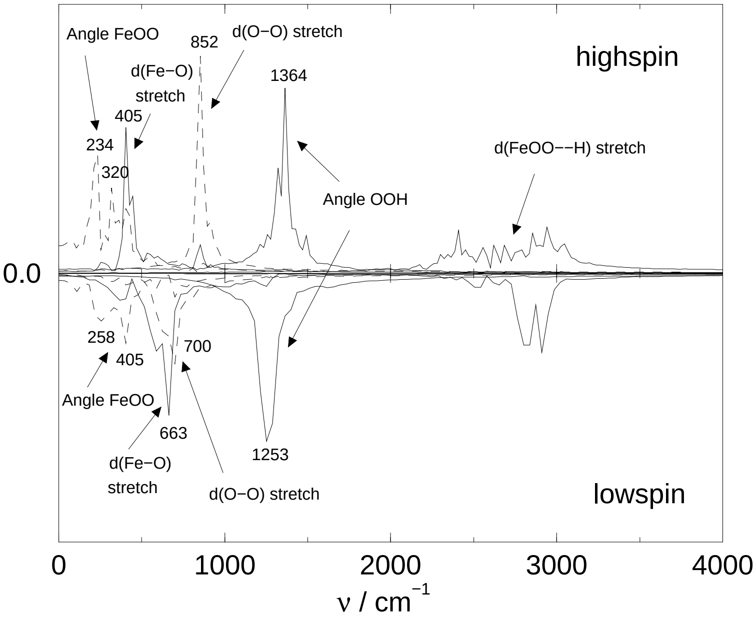

time $t \approx 4.1$ ps, we now have a situation where the Fe-O$^\alpha$ distance has increased to more than 3 Å *i.e.* the iron aqua complex and H_2O_2 are separated from each other by at least 3 Å, with velocities that will lead to further separation. At this point, we reverse all the velocities (including those of the electronic wave function degrees of freedom and the Nosé thermostat variable) so that the reactants will now approach each other in the same way as they separated. The difference of course is that the O$^\alpha$-H is now free to dissociate. In figure 6.2, we indeed see that as soon as hydrogen peroxide coordinates to the Fe^{3+} ion, the O$^\alpha$-H bond breaks, the proton moves into the solvent and the iron(III)hydroperoxo complex is being formed.

These illustrative pathways, confirm our inference from the calculation in vacuum (table 6.1), that formation of the Fe(III)(OOH) species is a likely candidate for the initial step in the Fenton-like reaction, in agreement with experiment, and secondly, that the oxygen-oxygen bond does not break so easily as in hydrogen peroxide coordinated to iron(II), which ultimately led to the ferryl ion as the most likely active intermediate in the Fe(II) catalysis. Moreover, formation of $[Fe^{III}(H_2O)_5(OOH)]^{2+}$ seems much more likely than formation of $[Fe^{III}(H_2O)_4(OH)(H_2O_2)]^{2+}$, in agreement with table 6.1. This implies that as the second step of the Fenton-like reaction we should investigate the subsequent transformation of Fe(III)(OOH). This will be done in subsection 6.3.3. However, we will first investigate further the iron(III)hydroperoxo complex itself, making a connection with the experimental characterization of this moiety by vibrational spectroscopy of this metal-ligand system in various solvents and with different ligand environments.

b) Characterization: Fe(III)-OOH vibrations. Spectroscopic experiments have

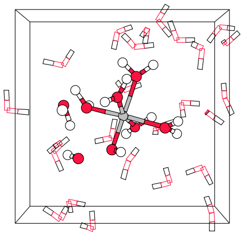

indicated that the spin-state of Fe(III)OOH complexes has a strong effect on the Fe-O and the O-O bond strengths [199, 200]. Resonance Raman spectroscopy on low-spin iron(III) hydroperoxo complexes with large ligands such as N4Py (N,N-bis-(2-pyridylmethyl)-N-bis(2-pyridyl)methylamine) [201], TPA (tris-(2-pyridylmethyl)-amine) [200] and TPEN (N,N,N',N'-tetrakis-(2-pyridylmethyl)-ethane-1,2-diamine) [202] show O-O bond vibrations with frequencies between 789-801 cm^{-1} and Fe-O bond vibrations between 617-632 cm^{-1}. High-spin complexes show stronger O-O bonds ($\nu_{\mathrm{O-O}} > 844\ \mathrm{cm}^{-1}$) and weaker Fe-O bonds ($\nu_{\mathrm{Fe-O}} < 503\ \mathrm{cm}^{-1}$). The spin-state is normally dictated by the ligand field splitting $10Dq$ caused by the ligands, but in our computer experiments we can simply fix the number of spin-up and spin-down electrons. We have thus calculated the Fe(III)OOH frequencies of the complex in water at $T = 300$ K for both spin states. This was done by performing an AIMD simulation for each spin-state starting from the last frame of the first simulation of Fe(III)OOH (see previous section). The hydronium ion in the solvent was replaced with a water molecule to avoid the influence it could have on the vibrations of the complex. We calculated a 2.5 ps AIMD trajectory, from which the last 1.5 ps was used to calculate the velocity autocorrelation of specific vibrations, such as the oxygen-oxygen bond stretching $d_{\mathrm{OO}}(t)$. The Fourier transformation of these velocity autocorrelation functions gives the vibration spectra shown in figure 6.3. The peaks shown in figure 6.3 are rather broad which is partly due to the relatively short simulation time (limited statistics). Nevertheless, the statistics are sufficient to clearly resolve the large differences between the low-spin and the high-spin spectra.

The OH stretch vibration in the hydroperoxo ligand gives rise to a broad region of peaks around 2500-3000 cm^{-1} in the $S = 5/2$ state, whereas these peaks are more localized in the low-spin state. In the simulation (and also in experiments [206]), the OH stretch frequency decreases when the hydrogen forms a hydrogen bond with a solvent water molecule. The shorter (stronger) the hydrogen bond, the lower the OH frequency. The average hydrogen bond length between the hydroperoxo hydrogen and the nearest solvent oxygen is 0.08 Å shorter in the high-spin state than in the low-spin state, while the average OH bond length in the hydroperoxo ligand is 0.01 Å longer. This could be an indication that the hydroperoxo ligand is more easily deprotonated in high-spin complexes, giving rise to the peroxo ligand, than in low-spin complexes.

The O-O stretch vibration decreases from 852 cm^{-1} to 700 cm^{-1} when going from the high-spin state to the low-spin state and the Fe-O stretch vibration increases from 405 cm^{-1} to 663 cm^{-1}, in agreement with the trend found with Raman spectroscopy for different complexes. For comparison, we have also optimized the geometry for the $[\mathrm{Fe^{III}(H_2O)_5(OOH)}]^{2+}$ complex *in vacuo* for the $S = 1/2$ state and the $S = 5/2$ state, and calculated the vibrational frequencies in the harmonic approximation. The results are shown in table 6.2, together with a compilation of values for the O-O and Fe-O stretch vibrations obtained using Raman spectroscopy on several low-spin and high-spin complexes. The O-O stretch vibration is significantly lower in the solvent than in the gas phase complex. This decrease, indicating a weakening of the O-O bond in aqueous solution, is due to the interaction of solvent water molecules with the hydroperoxo group. Not only the hydrogen, but also both oxygens are involved in hydrogen bonds with the solvent. Integration of the radial distribution functions (data not shown) obtained from the first 5 ps simulation of high-spin Fe(III)OOH in water (see previous paragraph) gives

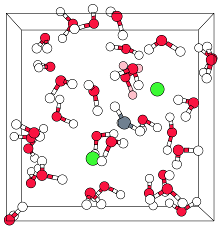

Table 6.2: *Fe(III)OOH vibrations calculated for the hydrated complex in vacuo and in aqueous solution compared to experimental Raman frequencies of low-spin complexes (upper part) and high-spin complexes (lower part).*

	∠FeOO	*d*FeO	*d*OO	∠OOH	*d*OH
	low-spin calculations				
$(H_2O)_5Fe^{III}OOH$ (g) [a]	253, 326	626	810	1291	3544
$(H_2O)_5Fe^{III}OOH$ (aq) [b]	258, 405	663	700	1253	2500-3000
	–experiment–				
$[(N4Py)Fe(OOH)]^{2+}$ [c]		632	790		
$[(TPA)Fe(OOH)]^{2+}$ [c]		626	789		
$[(TPEN)Fe(OOH)]^{2+}$ [d]		617	796		
$[(trispicen)Fe(OOH)]^{2+}$ [d]		625	801		
$[(trispicMeen)Fe(OOH)]^{2+}$ [d]		617	796		
	high-spin calculations				
$(H_2O)_5Fe^{III}OOH$ (g) [a]	180, 209	445	980	1366	3514
$(H_2O)_5Fe^{III}OOH$ (aq) [b]	234, 320	405	852	1364	2000-3000
	–experiment–				
$[(TPEN)Fe(\text{-}\eta^2\text{-}OO)]^{2+}$ [d]		468	821		
$[(trispicMeen)Fe(\text{-}\eta^2\text{-}OO)]^{2+}$ [d]		468	820		
$[Fe(EDTA)(\text{-}\eta^2\text{-}OO)]^{3-}$ [e]		459	816		
$[Fe(EDTA)(\text{-}\eta^2\text{-}OO)]^{3-}$ [f]		472	824		
Oxyhemerythrin($\text{-}\eta^1$-OOH) [g]		503	844		

[a] This work: static DFT. [b] This work: AIMD including aqueous solution. [c] Ref 200. [d] Ref 199. [e] In frozen solution, Ref 203. [f] In liquid solution at room temperature, Ref 204. [g] Ref 205.

an average of 1.6 solvent hydrogens within a 2.3 Å radius of O^β and 0.8 (other) solvent hydrogens within a 2.3 Å radius of O^α. Surprisingly, the static DFT results *in vacuo* for the low-spin O-O and Fe-O vibrations compare better with the experimental results than the ones obtained from the dynamics in aqueous solution at $T = 300$ K. This could be due to (again) the aqueous solvent interactions with the hydroperoxo ligand in the simulation, whereas the Raman spectroscopy studies using the hydrophobic pyridine based ligands as N4Py, TPA, TPEN, trispicen and trispicMeen typically took place in solvents such as acetone and acetonitrile. Another factor is of course the ligand field on the aqua ligated iron in the simulation, which is quite different from the ligand fields on iron complexed by these large nitrogen multidentate ligands used in the experiments. Comparison of our high-spin results with the only η^1-OOH complex listed, namely oxyhemerythrin in aqueous solution, indicates that both factors could play a role: the Raman O-O stretch vibration agrees now much better with the AIMD result as in both results the solvent

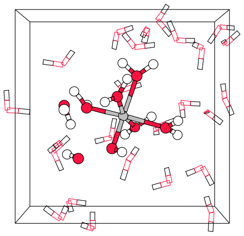

used is water which interacts with the hydroperoxo ligand, and secondly, the Fe-O stretch vibrations are still a bit off due to the different ligand field (note that oxyhemerythrin is a diiron species: L-Fe(III)-O-Fe(III)-OOH).

Concluding, we find that indeed the spin-state is an important factor for the O-O bond and Fe-O bond strengths in Fe(III)OOH complexes. The ligands (chelating agents) used in Fenton-like chemistry are therefore expected to directly influence the chemistry, because ligands inducing a large ligand field give rise to low-spin Fe(III)OOH complexes with stronger Fe-O bonds and weaker O-O bonds compared to the Fe-O and O-O bonds in the high-spin complexes which occur with ligands inducing a small ligand field. For the suggested second-step reactions following the initial Fe(III)OOH formation (reactions 6.4 till 6.6), the low-spin complexes thus promote the steps involving O-O lysis but make the steps involving Fe-O bond breaking even more unfavorable.

6.3.3 The second step in Fenton-like chemistry in water: calculation of the free energy barrier of O-O homolysis of Fe(III)OOH

One of the proposed second reaction steps in the oxidation catalysis by the Fenton-like reagent involves homolysis of the oxygen-oxygen bond of the iron(III)hydro-peroxo species, producing an $OH^{\cdot}$ radical and the ferryl ion (reaction 6.5). We have studied this reaction in detail, since it has emerged from our static DFT calculations as one of the most likely second reaction steps, in particular when the hydrolysis of a water ligand is simultaneously taken into account.

We have performed constrained AIMD simulations to calculate the free energy profile for the oxygen-oxygen bond homolysis reaction of the $[Fe^{III}(H_2O)_5OOH]^{2+}$ complex into an iron(IV)oxo species and an $OH^{\cdot}$ radical in water. The oxygen-oxygen bond length R_{OO} was taken as the constrained reaction coordinate, which seems intuitively a good choice that includes the most important contribution to the intrinsic reaction coordinate. The main drawback of this choice is however that it does not prevent unwanted side reactions such as the abstraction of solvent molecule hydrogens by the $OH^{\cdot}$ radical produced. For large values of the constrained reaction coordinate R_{OO}, the $OH^{\cdot}$ radical can abstract a solvent hydrogen forming H_2O, while an $OH^{\cdot}$ species "jumps" through the solvent by a chain reaction. The sampled force of constraint, associated with the force necessary to keep a H_2O molecule (instead of the $OH^{\cdot}$) constrained to the oxygen of the iron complex, will then be of course meaningless. We will therefore take the same approach as was done in the work by Trout and Parrinello, who studied the dissociation of H_2O in water in H^+ and OH^- with the same technique, [207] and only calculated the profile up to (or at least very close to) the transition state. Since the subsequent reaction of the $OH^{\cdot}$ "jumping" into the solvent is thermoneutral, the free energy profile of the homolysis is not expected to decrease by more than a few kcal/mol beyond the transition state (due to the increasing entropy of the leaving $OH^{\cdot}$ radical and the solvation of the oxo site). Moreover, the transition state energy is the more important parameter to determine whether the oxygen-oxygen homolysis is indeed a probable mechanism.

Eight constrained AIMD runs were performed with constrained oxygen-oxygen bond

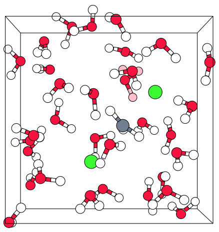

Figure 6.4: *The mean force of constraint $\langle F \rangle_R$ (dashed line; right-hand-side axis) and the Helmholtz free energy ΔA (solid line; left-hand-side axis) versus the oxygen-oxygen distance R_{OO}. The crosses denote the values from constrained MD runs sampled during 2 picoseconds and the circles denote the average constraint force during 1.3 ps, up to the moment that the $OH^{\cdot}$ radical abstracts a hydrogen from a nearby solvent molecule. The dotted lines give the energies of the hydrated complex in vacuo, calculated with the ADF program (triangles) and with the PAW program (squares). The limits of infinitely far separated products (reaction I in table 6.1) are indicated by vertical dashed lines.*

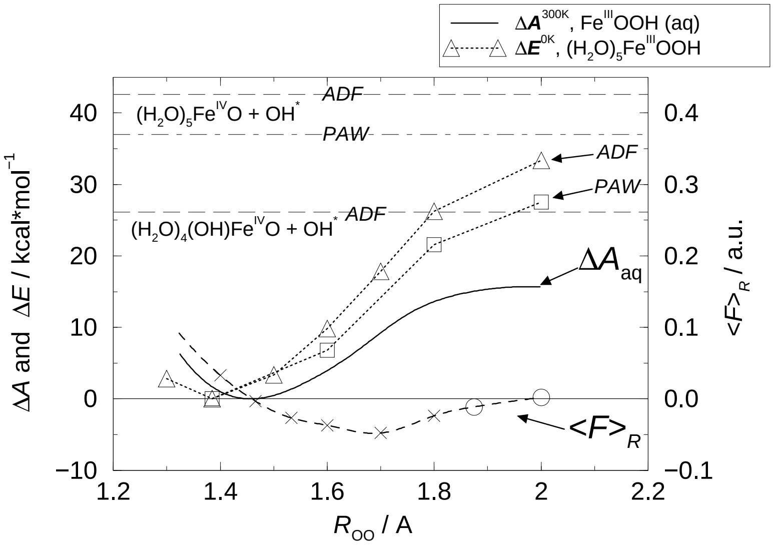

lengths varying from $R_{\mathrm{OO}} = 1.4 - 2.0$ Å. The initial configuration of each constrained simulation was taken from the last frame of the first simulation of hydroperoxo iron(III) in water, including the hydronium ion (see section 6.3.2). For each system, a short AIMD simulation was started to bring R_{OO} to the desired value in 2000 steps. Then equilibration of each system took place for 2 picoseconds, after which the force of constraint was accumulated for another 2 picoseconds. The obtained values for the mean force of constraint are denoted by crosses and circles in figure 6.4 and fitted with a quadratic spline. Integration of the mean force of constraint gives the Helmholtz free energy profile $\Delta A(R_{\mathrm{OO}})$, where we take the minimum at $R = 1.46$ Å for the offset of the energy scale (solid line). The circles indicate those constrained simulations during which the $O^{\beta}H^{\cdot}$ radical abstracts a hydrogen and transforms into a water molecule. Indeed, this occurs for the R_{OO} values close to the transition state, for which the $O^{\beta}H$ part has acquired enough radical character to abstract a hydrogen when a nearby solvent molecule moves into a suitable position. In both cases (at $R_{\mathrm{OO}} = 1.875$ Å and at $R_{\mathrm{OO}} = 2.000$ Å), the hydrogen abstraction occurs after about 1.3 ps simulation. The values for the mean force of constraint denoted by the circles are the averages over these 1.3 ps. After the H abstraction by $O^{\beta}H^{\cdot}$, the force of constraint goes to zero, or becomes even slightly positive

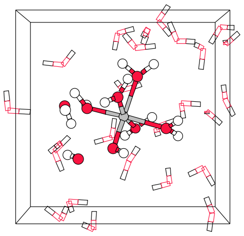

(repulsive) because the produced water molecule is repelled by the oxo ligand at the short constrained oxygen-oxygen distance, rather than attracted like the $OH^{\cdot}$ radical shortly before. For the O-O distance of $R_{\mathrm{OO}} = 2.000$ Å, the average force of constraint (over the 1.3 ps before the H abstraction) is almost equal to zero, which indicates that this O-O distance is indeed very close to the transition state.

The free energy reaction barrier for the homolysis reaction in water is found to be $\Delta A^{\ddagger} = 15.7$ kcal/mol, which is low compared to the $\Delta E = 42.6$ kcal/mol (ground-state) energy change found for the reaction *in vacuo*, or even the $\Delta E = 26.1$ kcal/mol for the hydrolyzed complexes *in vacuo* (reaction I in table 6.1). We have also plotted twice the contour for the reaction energy $\Delta E^{0\mathrm{K}}$ of the homolysis of the $[\mathrm{Fe^{III}(H_2O)_5OOH}]^{2+}$ complex *in vacuo* (triangles connected by a dotted line, and the value for infinite product separation indicated by the vertical dashed line); once computed with the ADF program and once computed with the PAW program. Unfortunately, we find an increasing underestimation of the energy profile with increasing R_{OO}, calculated with PAW compared to the highly accurate (all-electron, large basis set) ADF results, with a maximum difference of 5.6 kcal/mol at $R_{\mathrm{OO}} = 2.0$ Å and at infinite separation. The error does not seem to be due to the plane-wave cutoff of 30 Ry (it is only reduced by 0.5 kcal/mol when going to 50 Ry) and can be attributed to the partial waves for the inner region of the valence electrons and the projector functions for the iron atom used in the PAW calculations. Although bond energies in iron(III) and iron(IV) complexes computed with PAW agree within 2 kcal/mol with those using ADF, we have found after extensive tests that the stability of the (formally) $\mathrm{Fe^{4+}}$ configuration is overestimated by 5-6 kcal/mol with respect to the (formally) $\mathrm{Fe^{3+}}$ configuration. This indicates that also the free energy barrier of the homolysis in aqueous solution has to be corrected for this error so that the true value becomes $\Delta A^{\ddagger} \approx 21$ kcal/mol. Solvent effects thus strongly reduce the transition state barrier for the O-O homolysis reaction in water. The main contribution to this effect is expected to originate from the larger absolute energy of solvation for the separating transition state complex ($\mathrm{Fe^{IV}{=}O \cdots OH^{\cdot}}$) in comparison with the reactant molecule, $\mathrm{Fe^{III}OOH}$. (Note that often reaction barriers are increased in aqueous solution, because the sum of the absolute energies of solvation for two reacting molecules is typically larger than that for the single transition state complex.)

The upper graph in figure 6.5 illustrates the transformation of the $\mathrm{Fe^{III}}$–$\mathrm{OOH^-}$ bond into an $\mathrm{Fe^{IV}{=}O^{2-}}$ bond by showing the average Fe-O^{α} distance as a function of the reaction coordinate. The two dashed lines indicate the average R_{FeO} for the pentaaqua-iron(III)hydroperoxo complex in water (obtained from the first 5 ps simulation described in section 6.3.2), equal to 1.922 Å and the average R_{FeO} for the ferryl ion in water equal to 1.680 Å. This latter number was obtained from the $[\mathrm{Fe^{IV}O(OH)}]^{+}$ moiety produced in the reaction between $\mathrm{Fe^{II}}$ and $\mathrm{H_2O_2}$ in water (*cf.* ref 146), in which indeed a water ligand hydrolyzed to form the $\mathrm{OH^-}$ ligand as suggested in section 6.3.1. This apparent increased acidity of the iron(IV) species compared to that of iron(III) is discussed below. Proceeding with the Fe-O distance, we see that R_{FeO} decreases rapidly when the oxygen-oxygen separation becomes larger than 1.7 Å, which indicates the changing character of the metal and the bonds. At the reaction coordinate value of $R_{\mathrm{OO}} = 2.0$ Å, the average R_{FeO} (over the 1.3 ps simulation before the $\mathrm{O^{\beta}H^{\cdot}}$ radical abstracts a solvent hydrogen) has decreased practically to the average value of free $[\mathrm{Fe^{IV}O(OH)}]^{+}$, which indicates that

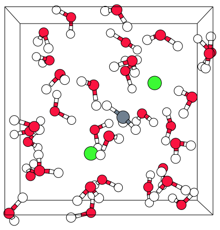

Figure 6.5: *Left-hand-side graph: average Fe-Oα bond length as a function of the constrained reaction coordinate R_{OO}. Two dashed lines indicate the average values for reactant and product iron complexes in solution, respectively. Open circles denote the average R_{FeO} after the product $O^{\beta}H^{\cdot}$ transformed into H_2O by H-abstraction from an adjacent solvent molecule. Right-hand-side graph: average number of hydronium ions as a function of the reaction coordinate.*

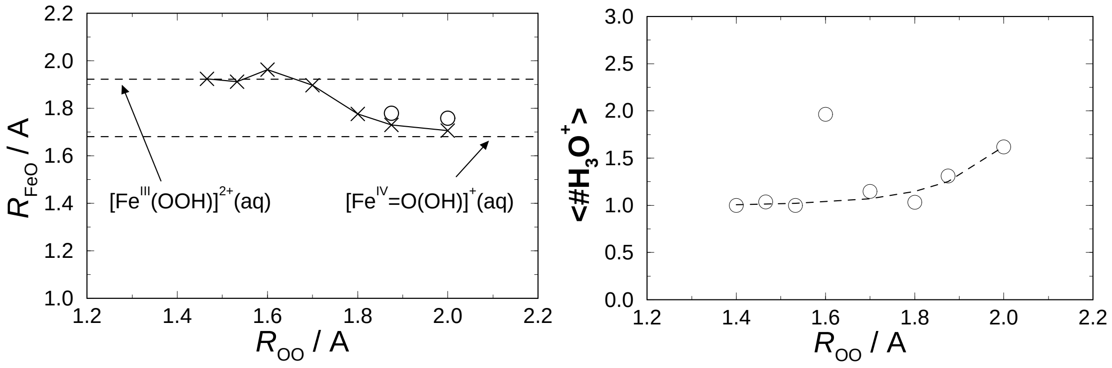

at $R_{\mathrm{OO}} = 2.0$ Å the reaction is close to completion. The open circles in figure 6.5 denote the averages over the simulation part after the $\mathrm{O}^{\beta}\mathrm{H}^{\cdot}$ radical transformed into $\mathrm{H_2O}^{\beta}$ by H-abstraction from an adjacent solvent molecule. At $R_{\mathrm{OO}} = 1.6$ Å, the average R_{FeO} is a little larger than expected from the trend. This is the result of proton donation from the iron complex (*i.e.* hydrolysis) to the aqueous solvent during the constrained simulation at this reaction coordinate value, which we will explain below.

As mentioned before, we expect hydrolysis of water ligands to lower the reaction energy of the oxygen-oxygen homolysis (see the change from 42.6 to 26.1 kcal/mol for reaction I in table 6.1), and secondly we expect hydrolysis to become more frequent for iron(IV) (product) compared to iron(III) (reactant). In our short constrained dynamics simulations of the enforced O^{α}–O^{β} homolysis in aqueous solution, we can indeed observe these trends by plotting the average number of hydronium ions in the solvent versus the reaction coordinate R_{OO} (see circles in the lower graph in figure 6.5 and the dotted lines to guide the eye). The water ligand O-H distances R_{OH} were taken as the order parameters: all 10 $R_{\mathrm{OH}} < 1.3$ Å means that no hydrolysis has taken place. At the reactant side (small R_{OO}), hydrolysis is rarely observed during the 2 ps simulations and only the one hydronium ion which we started with (originating from the hydrogen peroxide when it reacted with iron(III), see previous sections) brings the average number to 1 $\mathrm{H_3O^+}$. Going towards higher R_{OO} values, the oxidation state of the iron ion goes to four and the complex is seen to become more acidic, confirming the second trend mentioned. At $R_{\mathrm{OO}} = 2$ Å, 62 % of the time a (second) proton was donated to the solvent by the complex (in the 1.3 ps before H abstraction by the leaving $\mathrm{O}^{\beta}\mathrm{H}^{\cdot}$ from a solvent water), which justifies the previous comparison of R_{FeO} with that of the hydrolyzed ferryl ion ($[\mathrm{Fe^{IV}O(OH)}]^+$) in the upper graph. At $R_{\mathrm{OO}} = 1.6$ Å, the average number of 1.96 hydronium ions seems out of order in this trend. In the simulations, we see that for this run the two hydronium ions are

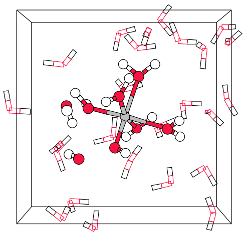

most of the time jumping freely around in the solvent. In the other runs however, we find that most of the time one of the protons jumps back and forth between the ligand and a solvent water molecule and thus remains in the neighborhood of the complex. Apparently we can separate the ligand hydrolysis into two stages which show resemblance with the dynamics of free hydronium ion transfer in water (*cf.* ref. 53), namely: 1) a fast process which involves the sharing of the proton by a ligand and a solvent molecule (or two solvent waters for the free hydronium ion, with a frequency $\nu \approx 5$ ps^{-1}) and 2) a much slower process, which is connected to the actual stepwise diffusion of the hydronium ion through the solvent. The latter process concerns changes in the second coordination shell hydrogen bond network which in water was found to have a frequency of about 0.5 ps^{-1}. [53] Obviously, our 2 ps AIMD simulations are too short to capture good statistics of the slow process, so that in each simulation we either see the excess proton being shared by two water molecules in the solvent (namely in the run with $R_{\mathrm{OO}} = 1.6$ Å,) or it is being shared by a ligand and a solvent molecule (as in all other runs). Fortunately, already from the distribution in the fast jumping process we obtain information on the acidity (*i.e.* the ability to donate a proton to the aqueous environment) of the iron complex, as shown in figure 6.5, but for comparison with experimental pK_a values we need to include also the slower hydronium ion transport. The run with $R_{\mathrm{OO}} = 1.6$ Å confirms the first trend mentioned in this paragraph: replacement of a water ligand by a hydroxo ligand facilitates the oxygen-oxygen homolysis. In our constrained MD exercise this is seen by the lower absolute constraint force resulting in a dent in the mean constraint force profile in figure 6.4 and also in the R_{FeO} profile in figure 6.5. If we could afford better statistics by performing much longer simulations, in principle the two states (pentaaqua versus hydrolyzed tetraaqua hydroxo complex) would be sampled with correct weights, giving the correct mean force of constraint and free energy profile. In our result however, we find for all runs except the one with $R_{\mathrm{OO}} = 1.6$ Å mostly the pentaaqua complex, so that we should take into account an overestimation of a few kcal/mol for the free energy barrier. Moreover, if we would be interested in calculating the reaction rate of the O-O homolysis reaction in water we should either control the hydrolysis process by including it in the reaction coordinate or we should expect a large deviation from the transition state theory reaction rate, and therefore perform the cumbersome computation of the transmission coefficient in the pre-exponential factor. We can nevertheless conclude that our estimation of the free energy barrier of the O-O homolysis of the iron(III)hydroperoxo intermediate in aqueous solution indicates that this formation of a ferryl ion and the $\mathrm{OH}^{\cdot}$ radical is a likely second step in Fenton-like chemistry. And secondly, the simulations confirm the hypothesis that water ligand hydrolysis plays an important role in the process.

6.4 Conclusions

We have performed static DFT calculations on the hydrated Fenton-like reagent *in vacuo*, $[\mathrm{Fe^{III}(H_2O)_5(H_2O_2)}]^{3+}$, and *ab initio* (DFT) molecular dynamics simulations of the Fenton-like reagent in aqueous solution, $\mathrm{Fe^{3+}/H_2O_2(aq)}$, to determine and characterize the active intermediates. The static DFT calculations on the hydrated iron(III) complexes *in vacuo* showed that the direct formation of active intermediates, such as the $\mathrm{OH}^{\cdot}$ radical or a

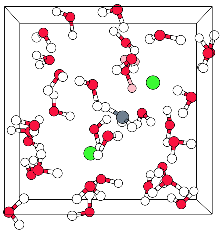

high-valent iron oxo species ($[\mathrm{Fe^{V}O}]^{3+}$) are endothermic by as much as 61 and 57 kcal/mol, respectively. This is in agreement with the experimentally observed much lower reactivity of the Fenton-like reagent compared to Fenton's reagent ($\mathrm{Fe^{II}/H_2O_2}$), for which we found that the formation of the highly reactive ferryl ion ($[\mathrm{Fe^{IV}O}]^{2+}$) is exothermic by 8 kcal/mol *in vacuo*.

The question how the Fenton-like reagent can still be active, and what the important reaction intermediates are, has been answered by *ab initio* (DFT) molecular dynamics simulations of the Fenton-like reagent in aqueous solution. The solvent effects prove to play a crucial role in the two reaction steps that lead from the H_2O_2 coordination in a $[(\mathrm{H_2O})_5\mathrm{Fe^{III}}(\mathrm{H_2O_2})]^{3+}$ complex to both $\mathrm{OH}^{\cdot}$ radicals and ferryl ions, $[\mathrm{Fe^{IV}O}]^{2+}$ as active oxidative species. The first step is donation of the α-proton of coordinated hydrogen peroxide to the solvent, as already suggested by the calculations *in vacuo* and confirmed by the AIMD simulations. The second step is suggested by our static DFT calculations to be O–O bond homolysis, producing the ferryl ion and a hydroxyl radical. This reaction step is uphill by 43 kcal/mol *in vacuo*, which is reduced to 26.1 kcal/mol upon hydrolysis of a water ligand. The AIMD simulations indicate that the solvent effects lower the barrier for O–O bond homolysis in $[(\mathrm{H_2O})_5\mathrm{Fe^{III}}(\mathrm{OOH})]^{2+}$ significantly, to a free energy barrier at $T = 300$ K in aqueous solution of approximately $\Delta A^{\ddagger} = 21$ kcal/mol, with concomitant hydrolysis of a water ligand. The important iron(III)hydroperoxo(aq) intermediate has been investigated by comparing calculated vibrational properties with experimental data. Comparison of the calculated vibrations of the low-spin Fe(III)OOH confirms the influence of the spin-state of iron on the Fe–O and O–O bond strength, proposed in the literature. As the O-O bond strength is decreased and the Fe–O bond strength is increased in the low-spin Fe(III)OOH compared to the high-spin Fe(III)OOH, we expect the reaction free energy barrier for the O–O homolysis to be significantly lower for low-spin complexes.

Acknowledgements

We acknowledge gratefully the helpful discussions with Michiel Gribnau from Unilever in Vlaardingen and the support by the Prioriteits Programma Materialen - Computational Materials Science (PPM-CMS). We thank the foundation NCF of the Netherlands Foundation of Scientific Research (NWO) for computer time.

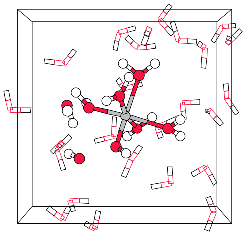

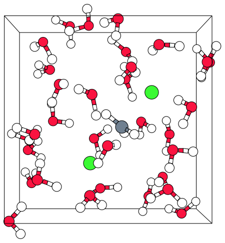

Chapter 7

Reaction path sampling of the reaction between iron(II) and hydrogen peroxide in aqueous solution*

Previously, we have studied the coordination and dissociation of hydrogen peroxide with iron(II) in aqueous solution by Car–Parrinello molecular dynamics at room temperature. We presented a few illustrative reaction events, in which the ferryl ion ($[Fe(IV)O]^{2+}$) was formed either by a rebound mechanism or by a two-step mechanism via an iron(IV)dihydroxo intermediate, depending on the starting configuration, which was from either separated reactants or H_2O_2 already coordinated to the Fe^{2+} ion, respectively. In the present work, we test if the illustrative reaction events are indeed representative ones. This is done by generating two sequences of 10 reactive pathways each, using the transition path sampling technique, taking as the initial trajectory the previous reactive pathway which followed the rebound mechanism. Along the generated sequence of reaction pathways, we observed (a) decreasing lifetimes of the intermediate $OH^{\cdot}$ radical, and (b) a change in the reaction mechanism towards the two-step mechanism in which (c) the H-bonded wire through the solvent, along which the $OH^{\cdot}$ radical jumps towards termination, becomes as short as a single H_2O molecule. These trends are rationalized from the point of view that the solvent is not relaxed around the separated reactants in the initial pathway, due to the artificial constraints imposed on the system in order to create a reaction event. During the transition path sampling, the solvent environment relaxes and incorporates H_2O_2 in its hydrogen bonded network. This leads to fast $OH^{\cdot}$ radical transfer and termination along the established H-bond wires in the solvent, which is in favor of the two-step mechanism.

---

*B. Ensing and E. J. Baerends, *J. Phys. Chem. A* **106**, 7902 (2002)

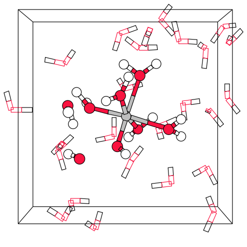

7.1 Introduction

Although the strength of molecular dynamics (MD) simulations lies in its use as a statistical tool to compute physical properties as ensemble averages, it is also used to simulate and analyze only single (or very few) illustrative events, for instance to show the possibility of certain chemical reaction pathways (see for some diverse examples refs. 193, 208–211). Chemical reactions are commonly activated processes, *i.e.* the reactants have to pass a free energy barrier (transition state) before transforming into the products. If this reaction barrier is high compared to the thermal energy of the system, the probability becomes very small to find the reactants in the transition state and thus observe a reaction event on the timescale of the thermal molecular vibrations. In molecular dynamics simulations, which is a good technique to sample the thermal molecular vibrations, the chemical reaction is then a rare event. To simulate a reactive pathway, one therefore has to manipulate the system and enforce a reactive encounter by using for instance a geometric constraint or umbrella potential or by introducing kinetic energy in some translational, rotational or vibrational mode. Obviously, this manipulation makes the dynamics of the illustrative reaction pathway less realistic. Whether the found pathway is indeed a representative one can be tested using the technique to generate new pathways from earlier found pathways known as the transition path sampling method developed by Bolhuis, Dellago and Chandler [212, 213]. This amounts to making small random changes to the atomic momenta of a randomly chosen configuration along an existing pathway and integrating the equations of motion backwards and forwards in time from this new point in phase space. If this leads again from reactants to products, it is accepted as a new pathway, which can then again be used to generate new pathways, and so forth.

We have recently studied the dissociation of hydrogen peroxide by iron(II) ions in aqueous solution, using *ab initio* (DFT) molecular dynamics simulations (AIMD) [146, 171]. The mixture of Fe^{2+} and H_2O_2, also known as Fenton's reagent [155], is known to oxidize organic substrates either via $OH^{\cdot}$ radicals [156] or via a high-valent iron oxo species [157] (ferryl ion) as the reactive intermediate. In this previous work, we have generated reactive pathways of the reaction between iron(II) and hydrogen peroxide, starting from two different initial conditions: a) starting from hydrogen peroxide coordinated to pentaaqua iron(II) in water, we found a pathway which resulted in the formation of a dihydroxo iron(IV) moiety, which transformed into the ferryl ion in a second step a short time (3 ps) later; b) starting from hydrogen peroxide and pentaaqua iron(II) separated from each other an arbitrary distance (≈ 4 Å), we found a pathway which lead to the ferryl ion via a more direct rebound mechanism. In both cases, we used bond distance constraints in the initial MD steps to prepare a configuration that would lead to a reactive pathway. Unfortunately, the resulting pathways are likely to contain a memory of the preparation using the unphysical constraints.

In this work, we will apply the transition path sampling technique to generate new reaction paths from the earlier found pathway of the hydrogen peroxide coordinating to and reacting with pentaaqua iron(II) in water. In principle, transition path sampling can be (and, in classical MD, has been) used to generate thousands of reaction paths, in which case again the statistical strength of MD is put to good use and quantities such as the reaction rate and rates of energy dissipation can be obtained. Unfortunately at the

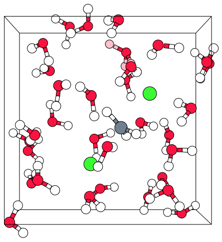

present time, the computational cost of *ab initio* molecular dynamics, which is needed to accurately describe the bond-breaking and making and the changing oxidation state of iron during the course of our reaction in water, does not allow for the simulation of more than a few tens of reaction pathways for systems as large as ours (see for another example ref. 184). This should however be enough to obtain reaction paths which have lost the memory of our initial artificial system preparation and show that either or both of the earlier found pathways are indeed realistic illustrative reaction paths or perhaps even reveal a new, third, reaction mechanism.

This article is structured as follows. We will first give a short recapitulation of our previous results on the Fenton reaction and our starting reaction pathway. Then, we briefly summarize the computational details of our Car-Parrinello MD simulations in section 7.3, followed by an introduction of the transition path sampling technique in section 7.4. The results are presented in section 7.5, starting with the estimation of the transition state of the initial path, following a new procedure. After that, the results of the pathway relaxation are presented in section 7.5-7.5.2. These results, interestingly showing a change in the reaction mechanism, and in fact confirming previous predictions, are rationalized in the discussion part (section 7.6), which is followed by the conclusions.

7.2 Initial reaction path

Fenton's reagent, used for oxidation of organic substrates, consists of an aqueous ferrous ion solution which catalyzes oxidation with hydrogen peroxide. The active species is believed to be either the $OH^{\cdot}$ radical produced via reaction equation 7.1 [156],

$$\begin{aligned} \mathrm{Fe}^{2+} + \mathrm{H_2O_2} &\rightarrow \mathrm{Fe}^{3+} + \mathrm{OH}^{-} + \mathrm{OH}^{\cdot} && (7.1) \\ \mathrm{Fe}^{2+} + \mathrm{H_2O_2} &\rightarrow \mathrm{FeO}^{2+} + \mathrm{H_2O} && (7.2) \end{aligned}$$

or the ferryl ion (*i.e.* iron(IV)oxo ion) via reaction equation 7.2 [157]. Static DFT calculations of hydrogen peroxide coordinated to pentaaquairon(II) *in vacuo* show that the oxygen-oxygen dissociation producing the $OH^{\cdot}$ radical according to reaction 7.1 is endothermic by 21 kcal/mol [145, 146]. This is in fact a reduction of 39 kcal/mol compared to the dissociation of isolated H_2O_2 into two $OH^{\cdot}$ radicals. The formation of pentaaqua-iron(IV)oxo and a water molecule according to reaction 7.2 was proposed to proceed via a dihydroxoiron(IV) intermediate (reaction equation 7.3)

$$\begin{aligned} \left[\mathrm{Fe^{II}(H_2O)_5(H_2O_2)}\right]^{2+} &\rightarrow \left[\mathrm{Fe^{IV}(H_2O)_4(OH)_2}\right]^{2+} + \mathrm{H_2O} \\ \left[\mathrm{Fe^{IV}(H_2O)_4(OH)_2}\right]^{2+} &\rightarrow \left[\mathrm{Fe^{IV}(H_2O)_5(O)}\right]^{2+} && (7.3) \end{aligned}$$

and was found to be overall exothermic by 8 kcal/mol. The ferryl ion is 7 kcal/mol lower in energy than its dihydroxo isomer.

Usually, Fenton chemistry takes place in aqueous solution and the solvent effects are expected to play an important role in the reaction mechanisms. The static DFT calculations, for example, pointed out that solvent water molecules can act as bridges in the hydrogen transfer occurring in the second step of reaction 7.3 and of course also the $OH^{\cdot}$ radical can jump via solvent water molecules, opening new pathways. The reaction free

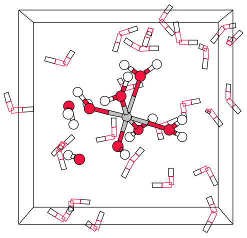

energy profile of a chemical reaction in aqueous solution can in principle be estimated with *ab initio* molecular dynamics using an umbrella potential or a geometric constraint (see *e.g.* refs. 54, 55, 144) if a good estimate of the transition state and an appropriate reaction coordinate are known. These are however not known *a priori* for our system. To obtain some idea of the possible molecular reaction mechanisms in water, we performed illustrative reaction pathways of the reaction between iron(II) and hydrogen peroxide in water. [146, 171] One of the pathways shows a new mechanism, and this pathway will be the initial path for the generation of new pathways in the present study.

Figure 7.1 shows characteristics of the pathway of ref. 146 that will be used as the initial pathway for the transition path sampling, we will carry out in the present work. The relevant geometric parameters (the FeO^{α} and FeO^{β} distances in the upper graph and the hydrogen peroxide $O^{\alpha}O^{\beta}$ and $O^{\alpha}H$ distances in the lower graphs, O^{α} and O^{β} being the H_2O_2 oxygens with O^{α} the one that becomes connected to iron in the reactive pathway) are shown as a function of time for this pathway. The actual reaction pathway starts at a time $t = 5.7$ ps denoted by one of the vertical dashed lines. Everything before that time, we will regard as the preparation for this pathway. The first 5 picoseconds are merely equilibration of the system, which consists of hydrogen peroxide coordinated to pentaaqua iron(II) and 26 solvent water molecules. The cubic unit cell was subject to periodic boundary conditions and a Nosé thermostat maintained an average temperature of $T = 300$ K. To avoid a premature breakup of the complex, the H_2O_2 oxygen-oxygen bond distance was constrained to 1.5 Å. At $t = 5.1$ ps, indicated by the first vertical dashed line, we constrained the five FeO bond distances between the iron ion and the water ligands and decreased them from the average $R_{\rm OO} = 2.1$ Å to $R_{\rm OO} = 1.8$ Å in 100 AIMD steps, which forces the sixth ligand, H_2O_2, out of the coordination shell. At $t = 5.7$ ps, we have arrived at a configuration with pentaaquairon(II) (with a vacant coordination site) and hydrogen peroxide separated from each other by a little more than 4 Å with a set of atomic momenta that will lead to further separation. This configuration we take as the starting point for our reaction pathway and we reverse all atomic velocities to obtain a set of momenta that will lead to approaching reactants. Also, the velocities of the fictitious plane wave coefficient dynamics are reversed as well as the velocity of the Nosé thermostat variable. Here our reaction pathway starts, with now atomic velocities that will lead to approaching reactants.

The simulation was now continued without the bond distance constraints. Due to this difference with the separation process, the system initially tracks back onto the trajectory before the velocities were reversed, but soon diverges from it strongly, finding a new route which leads to coordination of H_2O_2 to the iron complex. Indeed, at $t = 6.5$ ps, the hydrogen peroxide coordinates again to the iron complex, but bonds now with the other oxygen, denoted O^{α}, to iron (see again figure 7.1). As soon as H_2O_2 coordinates to the complex, O-O lysis takes place, and an iron(III)hydroxo moiety is formed together with an $OH^{\cdot}$ radical. At about $t = 6.9$ ps, the $OH^{\cdot}$ radical grabs the Fe(III)-OH hydrogen to form a water molecule and the ferryl ion.

The mechanism followed by this pathway will be referred to as the rebound mechanism, because the $OH^{\cdot}$ radical that splits off in the O-O lysis step rebounds to abstract the hydrogen from the hydroxo ligand. The rebound mechanism differs from pathways in which the $OH^{\cdot}$ radical shunts, via a hydrogen bond wire of solvent water molecules,

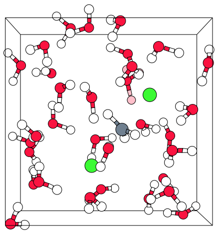

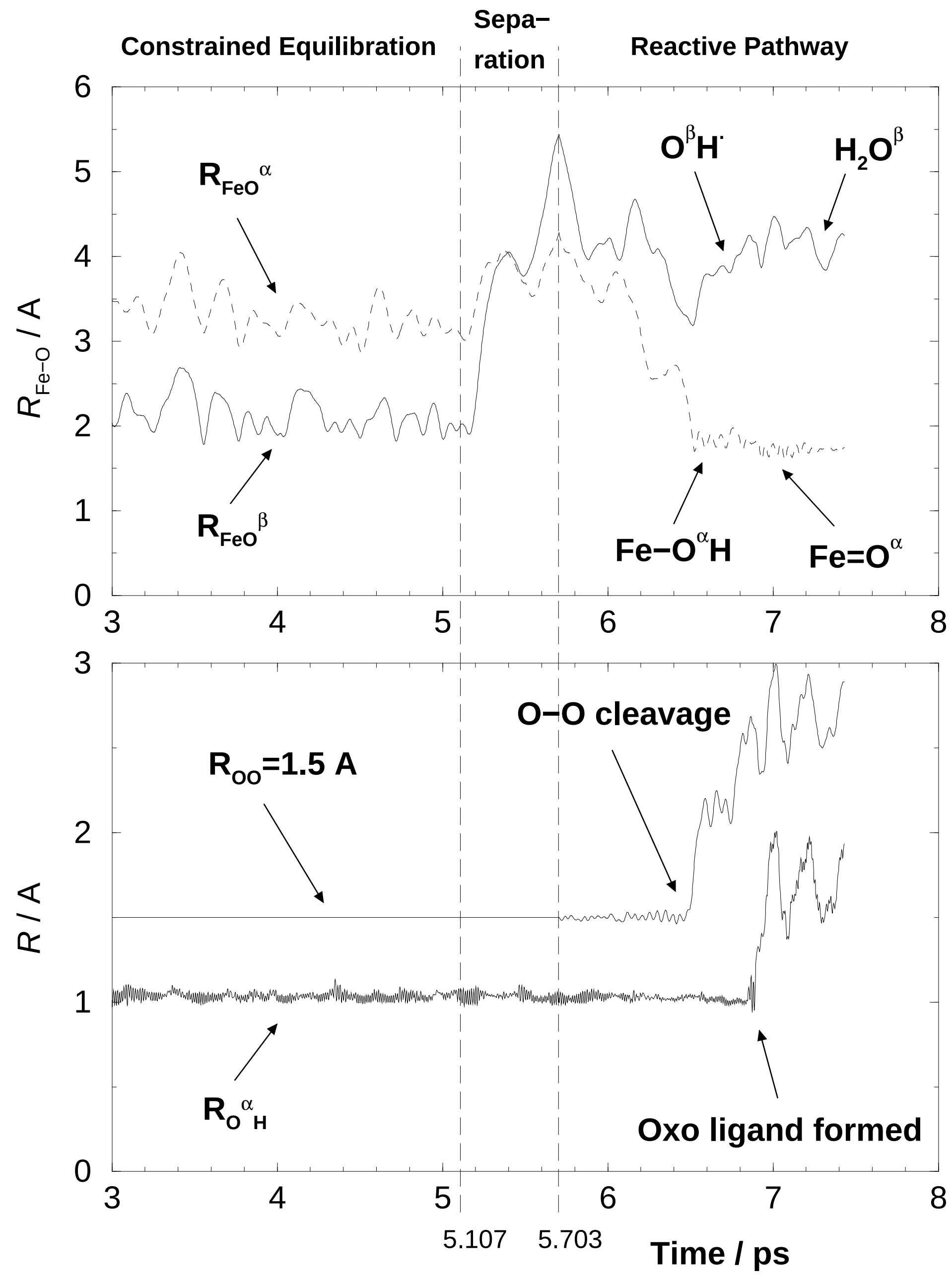

Figure 7.1: *Upper graph: The two Fe-O (H_2O_2 oxygens) distances as a function of time, starting from the last part of the equilibration phase (coordinated Fe-H_2O_2 complex). At t=5.1 ps H_2O_2 is driven away from Fe^{II}. At t=5.7 ps the velocities are reversed. Lower graph: The O-O distance is initially fixed until t=5.7 ps. At t=6.5 ps O-O bond cleavage takes place. The $O^\alpha H$ ligand bond is broken at t=6.85 ps, when the $O^\beta H^\cdot$ radical grabs the $O^\alpha H$ hydrogen.*

to a terminating water ligand, which was observed when starting from hydrogen peroxide coordinated to pentaaqua iron(II) in water [171]. In the latter case, a dihydroxo

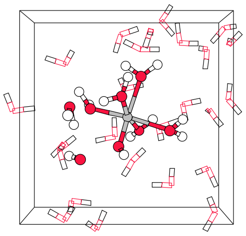

iron(IV) species was formed (much as predicted by the DFT calculations of the complex *in vacuo*), which transformed via proton exchange with the solvent into the ferryl ion a few picoseconds later. We will refer to this mechanism as the two-step mechanism. The main question that remains concerning the rebound pathway is: to what extent is the found reaction pathway dictated by the manipulation at time $t = 5.1$ ps, and is it thus a representative pathway? We attempt to answer this question by applying the transition path sampling method to generate pathways that will have no memory of this preparation strategy.

7.3 Computational details

The microscopic reaction pathways presented in this paper were computed using the Car-Parrinello method. [49] This method combines classical molecular dynamics (MD) with a quantum mechanical computation of the electronic structure. The forces on the nuclei are obtained from the electronic ground-state energy, rather than from an empirical forcefield, which is why Car-Parrinello MD often is referred to as *ab initio* molecular dynamics (AIMD). The Car-Parrinello technique differs from other AIMD methods by the dynamical optimization method, known as simulated annealing, for the electronic wavefunction degrees of freedom (*i.e.* the basis set expansion coefficients) which can be treated simultaneous with, and on the same footing as, the Newtonian nuclear dynamics. The parameter of inertia, usually called “fictitious electronic mass”, controlling the response of the basis set coefficients to the potential in the simulated annealing approach, is chosen much smaller than the atomic masses. This way, the wavefunction adapts instantaneously to the moving nuclei, keeping the electrons sufficiently close to the correct ground-state. The Verlet algorithm is used to integrate the equations of motion for the nuclear dynamics and for the coefficient optimization. In the present work, the fictitious electron mass was chosen 500 a.u. ($\approx 4.555 \cdot 10^{-28}$ kg), which limits the time step to 0.145 fs.

The electronic structure is calculated with density functional theory (DFT). [46] We used the Becke-88 [36] and Perdew-86 [38] gradient corrected functionals for exchange and electron correlation respectively. The Car-Parrinello simulations were performed using the CP-PAW program developed by Blöchl, [24] who integrated the projector augmented wave (PAW) method with the *ab initio* molecular dynamics. The PAW method uses an augmented plane-wave basis for the electronic valence wavefunctions and, in the current implementation, frozen atomic wavefunctions for the core states. The plane-wave basis expansion was cut off after functions with a kinetic energy of 30 Ry. The 1s electrons of oxygen and up to the 3p electrons for iron were kept frozen. For the augmentation for H and O, one projector function per angular momentum quantum number was used for *s*- and *p*-angular momenta. For Fe, one projector function was used for *s*- and *p*- and two for *d*-angular momenta.

The advantage of PAW over the more commonly used pseudopotential approach is that transferability problems should be largely avoided. However, as with all methods in which the core is represented approximately, there will be some loss of accuracy. Extensive tests are therefore required and we have previously shown that bond energies and geometries of small molecules and complexes computed with CP-PAW agree very well with highly

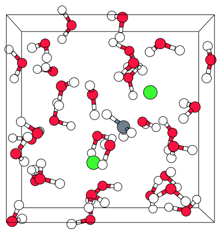

Table 7.1: *Bond dissociation energies and rearrangement energies in kcal/mol for isolated ("gas phase") complexes, calculated with the Amsterdam Density Functional program (ADF) and the CP-PAW program using the Becke-Perdew exchange correlation functional.*

	Gas phase reaction			CP-PAW	ADF	ΔΔE
A	$Fe^{II}(H_2O)_6$	→	$Fe^{II}(H_2O)_5 + H_2O$	21.7	22.1	-0.4
B	$Fe^{II}(H_2O)_6$	→	$Fe^{II}(H_2O)_5\text{–}H_2O$	-2.3	-3.5	1.2
C	$Fe^{II}(H_2O)_5 + H_2O_2$	→	$Fe^{III}(H_2O)_5OH + OH^{\cdot}$	-8.4	-2.1	-6.3
D	$Fe^{III}(H_2O)_5OH + OH^{\cdot}$	→	$Fe^{IV}(H_2O)_5O + H_2O$	-30.8	-28.7	-2.1

accurate all-electron DFT results obtained with the ADF [70] program [144]. However, we have in the course of the present work noted that reaction energies of chemical reactions involving a change in the formal oxidation state of iron sometimes exhibit relatively large (several kcal/mol) discrepancies with accurate (large basis set, all-electron) ADF calculations. Table 7.1 shows four reaction energies of gas phase reactions involving simple aqua iron complexes, calculated with CP-PAW and with ADF. The same exchange-correlation functional was used in both calculations. The Kohn-Sham orbitals were expanded in the ADF calculation a large even-tempered all-electron Slater-type basis set containing: 4 s, 2 p, and 1 d functions for hydrogen; 6 s, 4 p, 2 d, and 1 f functions for oxygen; and 11 s, 7 p, 5 d, and 1 f functions for iron [175]. The CP-PAW calculation used plane-waves with a cut-off of 30 Rydberg. Reaction A and B, show the typical small differences in the order of 1 kcal/mol due to the differences in basis set and the frozen core approximation used with PAW. However, reactions C and D, which involve a change in the iron oxidation state, show larger discrepancies, up to 6.3 kcal/mol for the reaction in which iron(II) is oxidized to iron(III). The error does not seem to be due to the plane-wave cutoff of 30 Ry (it is not reduced when going to 50 Ry) and can be attributed to the partial waves for the inner region of the valence electrons and the projector functions used in the PAW calculations. The purpose of the present work is the application of transition path sampling in order to obtain reaction pathways which have lost the memory of their initial artificial construction. This memory effect, as we will see, is related to the solvent motion and the formation and breaking of H-bond networks in the solvent, which are well represented by the present type of CPMD simulations, as demonstrated earlier [144]. We therefore feel the present CPMD method can be applied to this type of study, but we have to take the limitations due to the limited accuracy of the reaction energetics in mind; obviously one cannot realistically calculate a reaction rate with this type of CP-PAW for a reaction involving change of oxidation state of Fe.

For the AIMD simulations of the Fenton reaction in aqueous solution in this paper, we applied periodic boundary conditions to a cubic box with an edge of 9.900 Å, containing one iron ion, one hydrogen peroxide molecule and 31 water molecules. The positive 2+ charge of this system was compensated by a uniformly distributed counter charge. In the reaction path sampling technique, we quenched the fictitious basis set coefficient

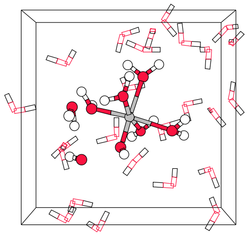

Figure 7.2: *Schematic representation of the free energy landscape with two stable, attractive wells separated by a transition state ridge, which connects the highest free energy points of all possible paths connecting the reactant and product states. The dotted line represents a new trajectory that was branched of at point p from an old trajectory (bold line) and surpasses the TS ridge at a lower point.*

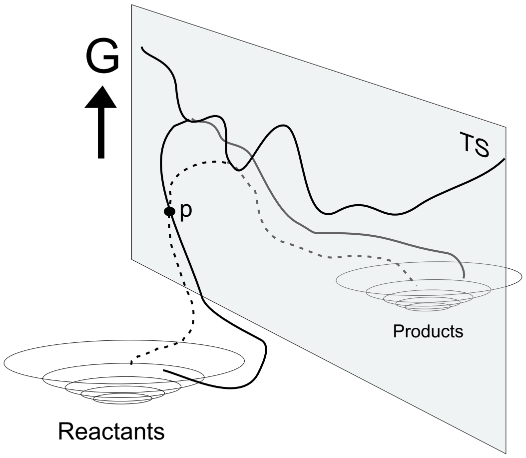

dynamics after every fourth reaction pathway generation, to avoid deviations from the Born-Oppenheimer surface. A Nosé thermostat [69] maintained a constant temperature of $T = 300$ K.

7.4 Transition path sampling

The technical details of transition path sampling and its potential to study the dynamics of rare events are described in a number of interesting papers by Bolhuis, Dellago, Geisler and Chandler [125, 212, 213]. The part that we are interested in, namely the generation and relaxation of reaction pathways, is schematically illustrated in figure 7.2.

In the rugged multidimensional free energy landscape, we find two stable states: the reactant state and the product state, which are separated from each other by an irregular energy barrier depicted by the line in the plane in figure 7.2. This line, in fact, connects all highest points of all the possible (reaction) pathways from the reactant state to the product state. We can define the transition path ensemble as the ensemble of all possible trajectories connecting the two stable states, within a certain finite time. The two stable states can be regarded as basins of attraction so that an MD simulation of the system started from a configuration in the neighborhood of one of the stable states is very likely to sample only this stable state region and will not be seen to cross the barrier to the other stable state, unless we simulate for a very long time. Crossing the barrier ridge is of course more probable through a low-lying pass than via some high top on the ridge. However, if we manage to find a connecting pathway over the barrier by some artificial manipulation of the system (like we did for the hydrogen peroxide iron(II) complex, by first driving out H_2O_2 from the coordination shell), we are likely to find a too high barrier crossing point.

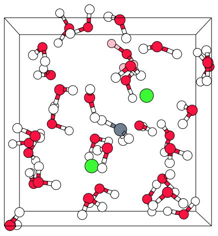

Such an initial pathway is depicted in figure 7.2 by the solid line from the reactant state to the product state. If the found pathway is indeed not a physically probable transition path, we can *relax* within the transition path ensemble from the improbable pathway to more probable paths by generating new pathways from our initial path. We therefore randomly pick a point p on the initial pathway, from where we branch off a new pathway, by making small random changes in the atomic momenta. Integration of the equations of motion forward and backward in time might result in a new pathway (called a new *generation*), represented by the dashed line. On this pathway, we can again randomly pick a new point p and again generate a trial pathway, etcetera. If the new trial pathway does not connect the two stable states (within some arbitrarily chosen finite time span), but instead remains in one of the stable states, we do not accept the new pathway but repeat the procedure starting from another point on the previous pathway. Success or failure of the pathway generation procedure depends on the following points:

1. the smaller the random changes of the atomic momenta, the larger the probability to succeed in finding a new reaction path

2. the closer point p is located to the ridge of the barrier tops, the larger the probability of succeeding in finding a new reaction path

On the other hand, the smaller the random changes of the atomic momenta the more the new pathway will follow the previous pathway, and the more pathways we have to generate in order to arrive at pathways which have no memory of the initial pathway. The magnitude of the momentum changes is thus a compromise, and we should therefore not strive for a 100% success rate in the pathway generation procedure. Dellago *et al.* have carried out a thorough efficiency analysis for a simple model system, finding that an acceptance probability in the range of 30-60% yields optimum efficiency. [214]

We want to make two more remarks on figure 7.2. First, it is possible that there exists more than one reaction "channel" separated from each other by an energy barrier. In figure 7.2, this is illustrated by the bump in the middle of the transition ridge, with lower lying passes on both sides (which even might lead to two different stable product states). Although in principle also pathways might be generated from the drawn pathway which pass through the right-hand-side channel, the chances of that become smaller as the separating bump increases. In practice another artificially initiated pathway would be needed as a starting point for the sampling of pathways through this second channel. The second remark regards the new definition of transition states within this theory. Instead of one transition state (TS) based on the intrinsic (zero Kelvin) reaction coordinate, an ensemble of transition states can be defined of all possible reaction pathways. The TS of each generated pathway is found by branching off a large number of new trajectories from a point p on the given pathway, starting with random momenta. From a point p close to one of the stable states most or even all trajectories will end up in the stable state. On the TS ridge however the chances are fifty-fifty to go either way, so that a point p from which half of the generated trajectories end up in each of the stable states can be identified as a point on the TS ridge. Of course, this TS point does not have to be connected to the highest potential energy along the pathway, since the TS is not only determined by the energy but also by the entropy. In particular, the potential energy along the pathway

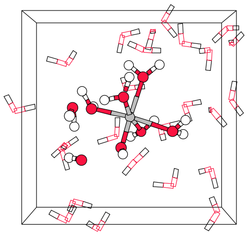

exhibits thermal fluctuation, which makes the maximum potential energy along the path a less useful parameter. We are *e.g.* not interested in the highest potential energy point if that high energy arises from motion (collision) of solvent molecules somewhere far from the reactants in the box. The TS point on a certain pathway should be a point on the *free energy* TS ridge. Having determined the TS points for a very large number (say, one thousand) of paths, interesting properties of the transition state ensemble (*i.e.* the ridge in figure 7.2) can be studied, such as the average solvent coordination in the transition state configurations. [125]

In the next section, we will first attempt to find the transition state for our initial pathway for the reaction between pentaaquairon(II) and hydrogen peroxide in water. Next we will use the transition path sampling technique to generate new pathways.

7.5 Results

7.5.1 Determination of the transition state on the initial reaction path

In the original transition path sampling procedure, to determine the transition state of a single reaction pathway, a large number of trajectories have to be initiated with random initial atomic velocities from some trial point along the pathway. From the ratio of the number of trajectories that end in the reactant well and the number of trajectories that end in the product well, it can be determined whether the trial point is located on the reactant side or the product side of the TS point. If more than 50 % of the trajectories ended in the reactant well, a new trial point is chosen located at the product side of the previous point (and *vice versa*), and this procedure is repeated until the TS point is found for which 50 % of the trajectories generated from this point end up in the reactant well and 50 % end up in the product well. Unfortunately, this technique is computationally very expensive in combination with Car-Parrinello MD for our system. Therefore, we introduce an alternative strategy to speed up the search for the TS point. Instead of branching off many trajectories from a trial point with random initial atomic velocities, we start one trajectory with zero atomic velocities. The initial direction of the system is therefore determined by the potential energy rather than the free energy, as was the case in the original strategy. If the system ends up in the reactant state, we try a new trial point located more to the products side along the pathway and *vice versa*. Due to the low temperature the system will have (starting from zero Kelvin) and since mainly the starting direction of the generated trajectory is relevant, a damped Nosé thermostat which heats up the system to $T = 300$ K is used to accelerate the search even more. Since we are however interested in the free energy transition state position, we will in the end nevertheless use the original generation procedure to find the exact location, but our "zero Kelvin" approach provides a very cheap means to obtain a good first guess for the expensive full procedure.

The left-hand-side graphs in figure 7.3, show the result of our "zero Kelvin" approach to narrow down the TS position on our initial pathway, defined in section 7.2, of the reaction between pentaaqua iron(II) and hydrogen peroxide in water. Note that the

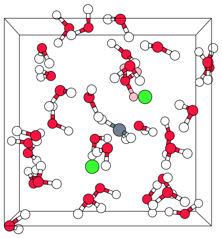

Figure 7.3: *Left-hand-side: estimation of the position of the transition state on the reaction path (bold line) by starting new trajectories from certain configurations (denoted with crosses) with zero velocities. Solid lines indicate trajectories which recross back to the reactant state; dashed lines are paths which lead to oxygen-oxygen lysis (products). Right-hand-side: testing the TS position estimate by initiating 20 trajectories with random velocities, starting in between point 4 and 5 of the left-hand-side trajectories. Indeed, half of them end up in the reactant state, and half in the product state.*

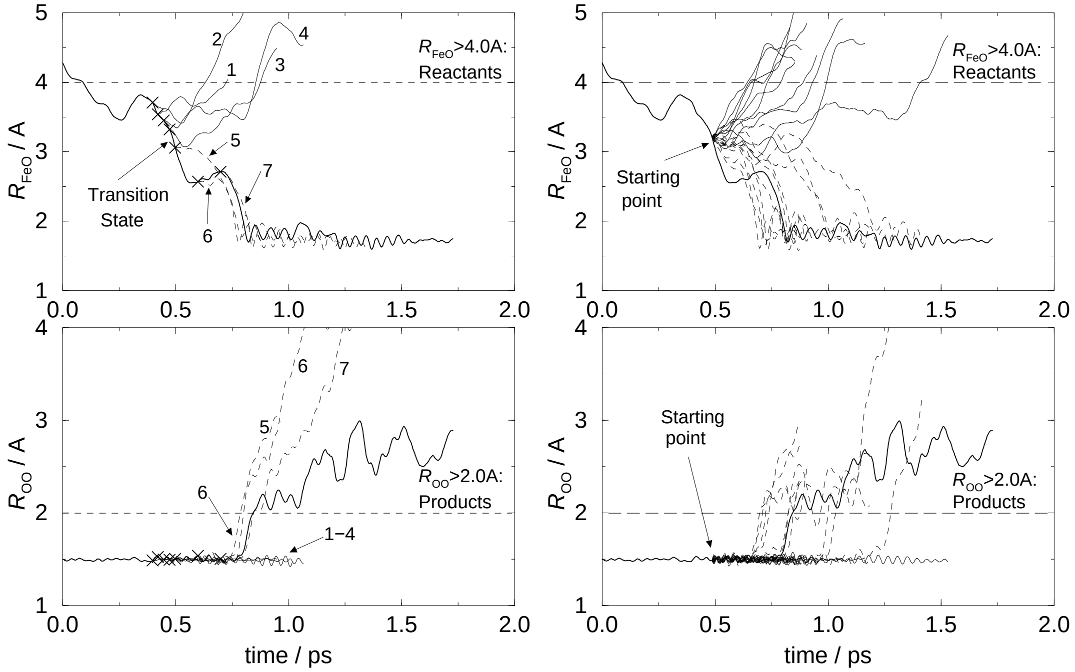

starting point of our initial path at $t = 5.703$ ps in figure 7.1 has been set to $t = 0$ in figure 7.3. The upper left-hand-side graph shows again the iron(II) oxygen distance (bold line), which equals $R_{\mathrm{FeO}} = 4.3$ Å at the start at $t = 0$ and decreases to $R_{\mathrm{FeO}} = 1.9$ Å 800 femtoseconds later, as hydrogen peroxide coordinates and bonds to iron and the oxygen-oxygen bond breaks (which is shown in the lower graph). The horizontal dashed lines depict our choice for the order parameters that define the stable states. That is, for $R_{\mathrm{FeO}^\alpha} > 4.0$ Å the system finds itself in the reactant well of separated iron(II) and hydrogen peroxide and for $R_{\mathrm{OO}} > 2.0$ Å the system finds itself in the product well of dissociated hydrogen peroxide. Note that this definition imposes no constraints—the final product may consist of the OH$^\cdot$ radical, a dihydroxo or oxo iron complex or something we had not thought of yet.

The crosses on the bold line in both of the left-hand-side graphs denote the trial points, from which trajectories were started with zero velocities. We see that the trajectories originating from the first four trial points all end up in the reactant well of $R_{\mathrm{FeO}} > 4.0$ Å (solid lines). The trajectories of the next three points all end up in the product state of $R_{\mathrm{OO}} > 2.0$ Å (dashed lines). We have thus narrowed down the estimate for the TS

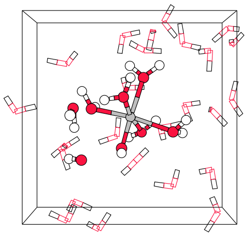

location between the fourth point at $t = 0.473$ ps ($R_{\mathrm{FeO}} = 3.3$ Å) and the fifth point at $t = 0.498$ ps ($R_{\mathrm{FeO}} = 3.1$ Å).

To verify this estimate of the TS location, we started 20 AIMD trajectories at the point at $t = 0.485$ ps (in the middle between point 4 and 5) where the iron-oxygen separation is $R_{\mathrm{FeO}} = 3.21$ Å. The initial atomic momenta were drawn from a gaussian (Boltzmann) distribution of a temperature of $T = 300$ K and corrected for any total momentum of the system. In the right-hand-side graphs of figure 7.3, the 20 trajectories have been plotted. Ten of them end up in the reactant well and the other ten end up in the product well. Perhaps a little fortuitously, apparently our approach resulted in a very good estimate of the transition state location on our reaction pathway, which could indicate that the TS point on the free energy surface (sampled by the original method, starting with random momenta) is not very different from the TS point on the potential energy surface (which determines the TS position resulting from our zero-Kelvin approach).

The large iron-oxygen separation of $R_{\mathrm{FeO}} = 3.21$ Å and the unchanged O-O distance in the transition state configuration indicates that the barrier is mainly determined by the solvent environment for our reaction pathway and not by the actual oxygen-oxygen lysis. Earlier, we had inferred that this barrier for hydrogen peroxide coordinated to iron(II) in aqueous solution must be small in the PAW calculation as we observed the spontaneous reaction to the ferryl ion or to an iron(IV)dihydroxo complex, during AIMD simulations [144, 171]. Also in the present simulation the barrier for O-O bond breaking is apparently small. It is possible that the barrier is underestimated in the PAW calculation, in view of the overestimation of higher oxidation states for iron as mentioned earlier in section 7.3. In ADF calculations (STO basis functions) for the isolated complex we have found a barrier, although a small one (6 kcal/mol), for the O-O lysis of the coordinated hydrogen peroxide in the pentaaqua iron hydrogen peroxide complex. The TS barrier in this case was found when the leaving O^{β}H radical was in the process of forming a bond to a H atom of an adjacent ligand, the calculations *in vacuo* preventing it to go into solution. [145] The TS position found in the present CPMD simulation in solution is clearly connected to a barrier in the ligand coordination process. This can be understood assuming that the approaching hydrogen peroxide has to break (partially) with the energetically favorable solvation shell before it can form an energetically favorable bond with the iron complex. The correspondence between the methods to estimate the TS position (namely "random momenta" and "zero-Kelvin") can be understood in the same way when we also assume that the entropy loss due to coordination is less important. For comparison, the free energy barrier for exchange of a water molecule from the first coordination shell of iron(II) in water was estimated to be 8.6 kcal/mol with NMR spectroscopy, which is indeed mainly energetic ($\Delta H^{\ddagger} = 7.7$ kcal/mol, $-T\Delta S^{\ddagger} = 0.9$ kcal/mol) [215].

7.5.2 Transition path sampling

In this section, new reactive pathways for the O-O bond breaking upon coordination of an hydrogen peroxide molecule to an iron(II) ion in aqueous solution will be generated, using the transition path sampling technique. To this end, a point on an existing reaction pathway has to be chosen as the starting configuration of a new pathway. In the present sampling procedure, a configuration file with the atomic configurations and wavefunction

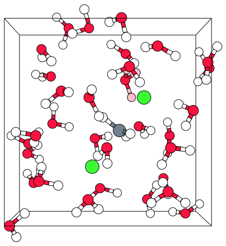

Figure 7.4: *R_{FeO} during the last four reaction pathways from sequence B, with their starting points denoted by the circles. That is, pathway no. 7 was generated by simulating backwards and forward in time starting from the configuration at t=3.303 ps of pathway no. 6. The configuration at pathway 7 at t=3.594 ps, was the starting configuration of pathway 8, etcetera. Note the shorter Fe^{IV}=O distance in pathway no. 7 (at about t=4 ps) compared to the Fe^{IV}-OH distance in the later pathways.)*

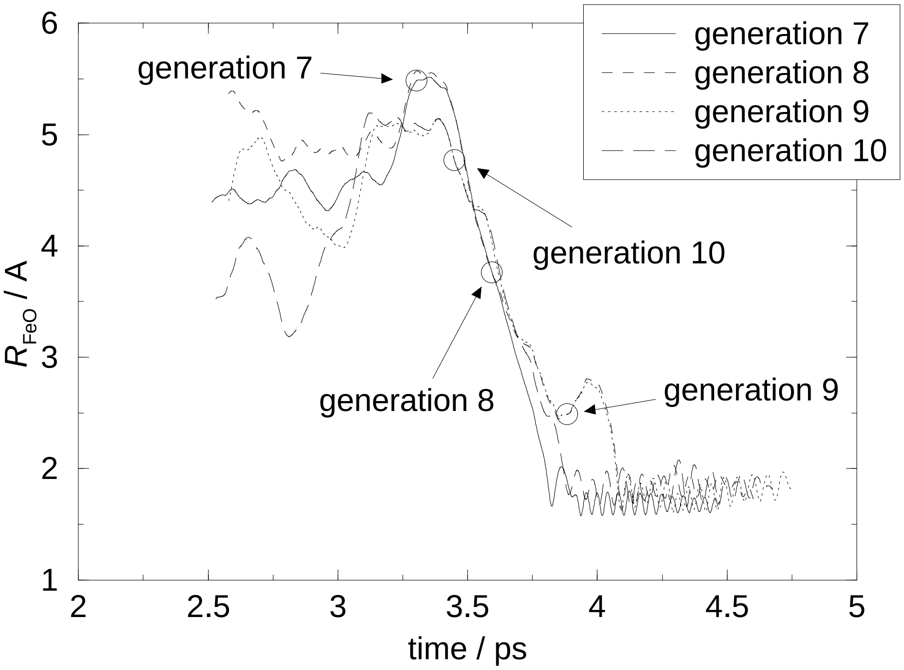

coefficients was saved every 1000 time steps (145 femtoseconds). One of the saved configurations was randomly chosen as the starting point for a new pathway. The first new successful reaction path initiated from a point on our initial pathway, will be referred to as the first generation path; a successful reaction path initiated from a point on this first generation path makes than a second generation path, etcetera. A *sequence* of reactive pathways is a series of subsequent generations. Figure 7.4 illustrates the procedure for four pathways; the circles denote the chosen starting points where on each n^{th} generation path a new $(n+1)^{\text{th}}$ generation path branches off. On a certain pathway, the time between its own starting point and the starting point of the next pathway, varied between 0.29 and 0.58 picoseconds, which is in a sense the time that the system is allowed to relax on a pathway before a next generation one branches off.

We calculated two sequences (sequence A and sequence B), each with a length of 10 generations. For the first generation of each sequence we took one of the 20 trajectories calculated earlier to verify the transition state location on the initial reaction pathway, shown in the right-hand-side plots of figure 7.3. That is, the first generation pathways for both sequences A and B branch off at the transition state point of our initial pathway, with random atomic momenta drawn from a T = 300 K Boltzmann distribution. Of

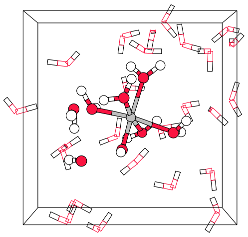

course, figure 7.3 shows only halves of reactive pathways (namely from the TS point to either the product state or the reactant state), so the other half was calculated, for our two first generations, by integrating the equations of motion backwards in time from the starting configuration of the reactive pathway (*i.e.* the TS point).

In table 7.2, which shows some characteristics of the computed pathways for sequence A (first 11 rows) and sequence B (last 9 rows), we see that the first generation pathways of sequences A and B are quite different from each other. For sequence A, the pathway does not show the direct mechanism of our initial pathway in which the ferryl ion ($\mathrm{Fe^{IV}O^{2+}}$) is formed via a rebound of the leaving $\mathrm{OH^{\cdot}}$ radical, which abstracts the hydrogen of the intermediate $\mathrm{Fe^{III}}$-OH. Instead, the leaving $\mathrm{OH^{\cdot}}$ radical jumps after a lifetime of $\tau_{\mathrm{OH}^{\cdot}} = 149$ fs via two solvent water molecules and terminates at a water ligand of a periodic image of the iron complex in a neighboring copy of the unit cell to form the dihydroxo iron(IV) moiety. This is indeed the first step of the two-step mechanism that we have seen before in simulations starting from hydrogen peroxide already coordinated to pentaaquairon(II). [146, 171] In a second step (see last column in table 7.2), the ferryl ion was formed by donation of a proton by one of the hydroxo ligands to the solvent. For sequence B, the first generation pathway shows the rebound mechanism, although also an incipient $\mathrm{OH^{\cdot}}$ radical shunt via two solvent water molecules is observed, but this $\mathrm{OH^{\cdot}}$-shunt is not completed, the motion of the solvent hydrogens is reversed when the $\mathrm{Fe^{III}}$-OH intermediate donates its hydrogen to the leaving $\mathrm{OH^{\cdot}}$ radical.

From these two first generation pathways, we successively generated new pathways by taking a configuration from a path and changing the atomic momenta. The momenta were changed by randomly drawing new momenta from a gaussian distribution of $T = 5$ K or $T = 10$ K and adding these to the old momenta (and correcting for any total momentum of the system). The success rate of obtaining a new pathway connecting reactants and products was about 50%. In both sequences, accidentally, the fifth generation pathway was started from an unsuccessful fourth generation pathway that started in the product well and recrossed back to the product well, although the iron-oxygen distances reached a separation of more than 4 Å (which is our order parameter defining the reactant well) in both fourth generation pathways.

Taking a closer look at table 7.2, we see trends along the two sequences which could indicate that indeed our initial pathway is an atypical one and relaxation towards more representative pathways does take place. For example, the time that the leaving $\mathrm{OH^{\cdot}}$ radical remains intact before abstracting a hydrogen from the complex or a solvent water (the lifetime $\tau_{\mathrm{OH}^{\cdot}}$, which is measured from the moment of O-O lysis, defined as $R_{\mathrm{OO}} > 2.0$ Å, until the first H-abstraction by $\mathrm{OH^{\cdot}}$), is seen to decrease in both sequences. Secondly, in both sequences the followed mechanisms change via or from the "long-wire two-step" mechanism (in which the $\mathrm{OH^{\cdot}}$ radical in the first step terminates via a wire of two or three solvent waters at a water ligand of the periodic image of the complex) to the "short-wire two step" mechanism. In the latter case, the leaving $\mathrm{OH^{\cdot}}$ radical terminates in the first step at an adjacent water ligand (thus stays in the same unit cell) via one bridging solvent molecule, forming the dihydroxo iron(IV) complex. Figure 7.5 shows in four snapshots the H_2O_2 coordination to iron(II), the O-O lysis, and the $\mathrm{OH^{\cdot}}$ radical shunt and termination, of such a short-wire step. In fact, this new "short-wire" reaction pathway was already predicted in previous work where we discussed the possibilities for a radical shunt in a

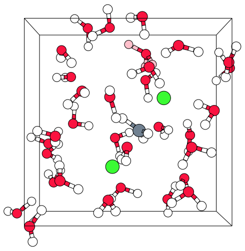

Table 7.2: *Compilation of the characteristics of the reaction paths generated in sequences A and B. The* $O^{\beta}H^{\cdot}$ *radicals formed in the paths of the first generations have relatively long lifetimes* $\tau_{OH^{\cdot}}$*. In sequence A already from the first generation no direct (i. e. rebound) mechanism is observed, but in the first generations, untill generation 7 (except for generation 3) the H abstraction takes place along a long wire to the next box, to a water ligand of the periodic "copy" complex to form dihydroxo iron(IV) (and ferryl ion in the second step). The* $O^{\beta}H^{\cdot}$ *radicals in later generation paths of sequence A live shorter and terminate via a short wire at an aqua ligand of the initial iron complex ("same"). In the second step the acidic dihydroxo iron(IV) species can transform into a trihydroxo species or a ferryl ion (last column). In the generations 1-7 of sequence B the* $O^{\beta}H^{\cdot}$ *radical abstracts the* $O^{\alpha}H$ *hydrogen to form the ferryl ion in one step (direct mechanism). Only in the later generations the transition paths relaxes to the abstraction through a H-bond wire, either a long wire (generations 8 and 9) or finally (generation 10) a short one.*

generation	mechanism	$\tau_{OH^{\cdot}}$ / fs	# H_2O in H-bond wire	terminating Fe complex	final obs. species
		Relaxation sequence A			
1	long wire	149	2	copy	ferryl
2	long wire	380	2	copy	ferryl
3	short wire	322	0	same	ferryl
5[a]	long wire	289	2	copy	$Fe^{IV}(OH)_3$
6	long wire	265	2	copy	$Fe^{IV}(OH)_3$
7	long wire	150	3	copy	ferryl
7	short wire	70	1	same	ferryl
8	short wire	73	1	same	$Fe^{IV}(OH)_3$
9	short wire	70	1	same	$Fe^{IV}(OH)_2$
9	short wire	65	1	same	$Fe^{IV}(OH)_3$
10	short wire	66	1	same	$Fe^{IV}(OH)_3$

table 7.2 continues on next page...

very large box containing a single pentaaqua iron(II) hydrogen peroxide complex. [171] In our present pathway relaxation procedure it indeed appears spontaneously.

The last column in table 7.2 displays the last observed iron complex. It shows that not always the ferryl ion is formed, but instead in many cases an $[Fe^{IV}(H_2O)_3(OH)_3]^+$ complex. This is due to the dynamic equilibrium between the acidic dihydroxo species and its conjugate base, the hydrolyzed trihydroxo species, by proton donation to the solvent:

$$\left[(H_2O)_4Fe^{IV}(OH)_2\right]^{2+} + H_2O \leftrightarrow \left[(H_2O)_3Fe^{IV}(OH)_3\right]^{+} + H_3O^{+} \quad (7.4)$$

Formation of the ferryl ion by H-donation of one of the dihydroxo ligands to the solvent

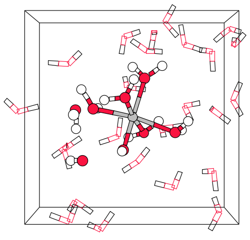

continuing table 7.2...

generation	mechanism	$\tau_{\mathrm{OH}^{\cdot}}$ / fs	# H_2O in H-bond wire	terminating Fe complex	final obs. species
		Relaxation sequence B			
1^b	both	101	2	both	ferryl
2	direct	121	0	same	ferryl
3	direct	133	0	same	ferryl
5^a	direct	251	0	same	ferryl
6	direct	248	0	same	ferryl
7	direct	141	0	same	ferryl
8	long wire	43	2	copy	$\mathrm{Fe}^{\mathrm{IV}}(\mathrm{OH})_3$
9	long wire	42	2	copy	$\mathrm{Fe}^{\mathrm{IV}}(\mathrm{OH})_3$
10	short wire	93	1	same	$\mathrm{Fe}^{\mathrm{IV}}(\mathrm{OH})_3$

[a] Accidentally, for both sequences the 4^{th} generation path was rejected because it recrossed from products to products, but was still used to generate a successful 5^{th} generation reaction path.

[b] The $\mathrm{O}^{\beta}\mathrm{H}^{\cdot}$ radical grabs simultaneously H^{α} and initiates an (unsuccessful) shunt to a periodic copy of the iron complex. See also text.

is only favorable if the system finds itself on the left-hand-side of equation 7.4. Most reaction pathways are however too short to observe the ferryl ion formation as the second step.

7.6 Discussion

The pathway relaxation from an artificially constructed reaction pathway to a pathway without the memory of the initial construction, was obtained in two steps (for both sequences A and B). The first step took place in the first pathway generation, namely by taking completely random atomic momenta at the starting point (which was the transition state configuration of the initial reaction pathway). The second part of the relaxation consisted of nine more sequential pathway generations, in which we observed (a) increasingly faster terminations of the leaving $\mathrm{OH}^{\cdot}$ radical due to shorter lifetimes $\tau_{\mathrm{OH}^{\cdot}}$ and (b) a shift from the direct rebound mechanism and the long-wire two-step mechanism to the short-wire two-step mechanism.

These changes along the two sequences of pathways can be understood as the result of the relaxation of the solvent environment of the reactants. As an illustration, figure 7.6 shows the hydrogen-oxygen distances $R_{\mathrm{O}^{\beta}\mathrm{H}}$ as a function of time for the solvent water hydrogens within a radius of 2 Å of the H_2O_2 oxygen, O^{β}, for the initial unrelaxed reaction pathway (upper graph) and the last pathway (no. 10) of sequence A (lower graph). The moment that the hydrogen peroxide O-O distance equaled $R_{\mathrm{OO}} = 2.00$ Å, which marks the moment of coordination and dissociation of the hydrogen peroxide to the iron complex, was taken for time $t = 0$, marked by the vertical dashed line. Before $t = 0$, we see the lines arising from the hydrogen bonded solvent water molecules to the yet intact hydrogen

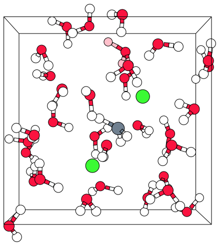

Figure 7.5: *Four snapshots of the 10^{th} generation reaction path of sequence A, which had a total length of 2.68 ps, showing the formation of the dihydroxo iron(IV) complex by H-abstraction from an H_2O ligand by the leaving $OH^{\cdot}$ radical via one bridging solvent water molecule. The bridging solvent molecule which is hydrogen bonded to H_2O_2 from t=0 ps is also shown, but for simplicity, the other solvent water molecules are left out.*

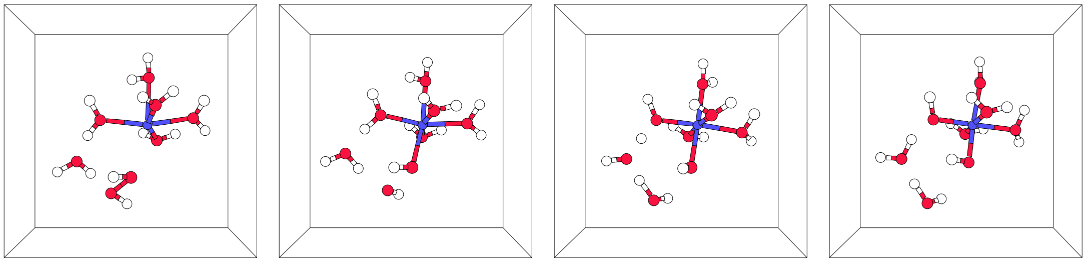

t = 1.342 ps   t = 1.387 ps   t = 1.451 ps   t = 1.467 ps

peroxide and from the $\mathrm{H_2O_2}$ hydrogen H^α (distinguished by the bold line in the graphs). The $R_{\mathrm{O}^\beta\mathrm{H}^\beta}$ distance, fluctuating around 1 Å has been left out for clarity. After $t = 0$, we see the lines arising from the hydrogen bonded solvent water molecules to the, at first, leaving $\mathrm{OH}^{\cdot}$ radical and later formed water molecule oxygen. Note that the change from $\mathrm{OH}^{\cdot}$ radical into water molecule occurs almost 300 fs later in the initial pathway compared to the relaxed pathway and that the $\mathrm{OH}^{\cdot}$ abstracts H^α (from the formed $\mathrm{Fe^{III}}$-OH^α) in the initial pathway but in the relaxed pathway it abstracts the hydrogen from one of the hydrogen bonded solvent molecules. Also, we see in the upper graph of the unrelaxed pathway jumps from two solvent hydrogens to the $\mathrm{OH}^{\cdot}$ radical between $t = 0 - 0.35$ ps, which however do not make it to a H atom at the water molecule that is formed; this is "achieved" by the H^α.

The initial reaction pathway was constructed by driving hydrogen peroxide out of the coordination shell from the $[\mathrm{Fe^{II}(H_2O)_5(H_2O_2)}]^{2+}$ complex, as shown earlier in figure 7.1 between $t = 5.1 - 5.7$ ps. We thus started from $\mathrm{H_2O_2}$, separated from the complex, that could hardly have formed a relaxed solvation shell, which however is expected to exist for separated reactants in the reactant well. This is seen in the upper graph of figure 7.6 from the absence of hydrogen bonds from solvent waters before $t = 0$. The lower graph, of reaction pathway no. 10, on the other hand, shows two solvent hydrogens with $R_{\mathrm{O}^\beta\mathrm{H}}$ distances between 1.5-2.0 Å [216], indicating the adoption of hydrogen bonds from the solvent network and thus indicating that relaxation of the solvent structure has occurred around hydrogen peroxide. Because hydrogen peroxide takes part in the three-dimensional solvent network via the formed hydrogen bonds between solvent molecules and $\mathrm{H_2O_2}$ before the reaction with iron (which is also illustrated in the first snapshots in figure 7.5) the leaving $\mathrm{OH}^{\cdot}$ radical can terminate much faster via H-bond wires in the network, resulting in the lower lifetime $\tau_{\mathrm{OH}^{\cdot}}$.

Have we now found the most likely mechanism for the iron(II) catalyzed dissociation of hydrogen peroxide? Let us first consider the alternative to the proposed two-step

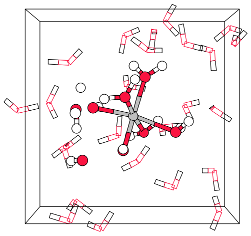

Figure 7.6: *Distances between solvent hydrogens and O^{β} (the hydrogen peroxide oxygen not bonded to iron) during the unrelaxed initial pathway (upper graph) and the last pathway of sequence A (lower pathway). The increased number of hydrogen bonds in the latter, especially before t=0 (the moment of dissociation defined as $R_{\mathrm{OO}} = 2.00$ Å) indicates the intended solvent relaxation*

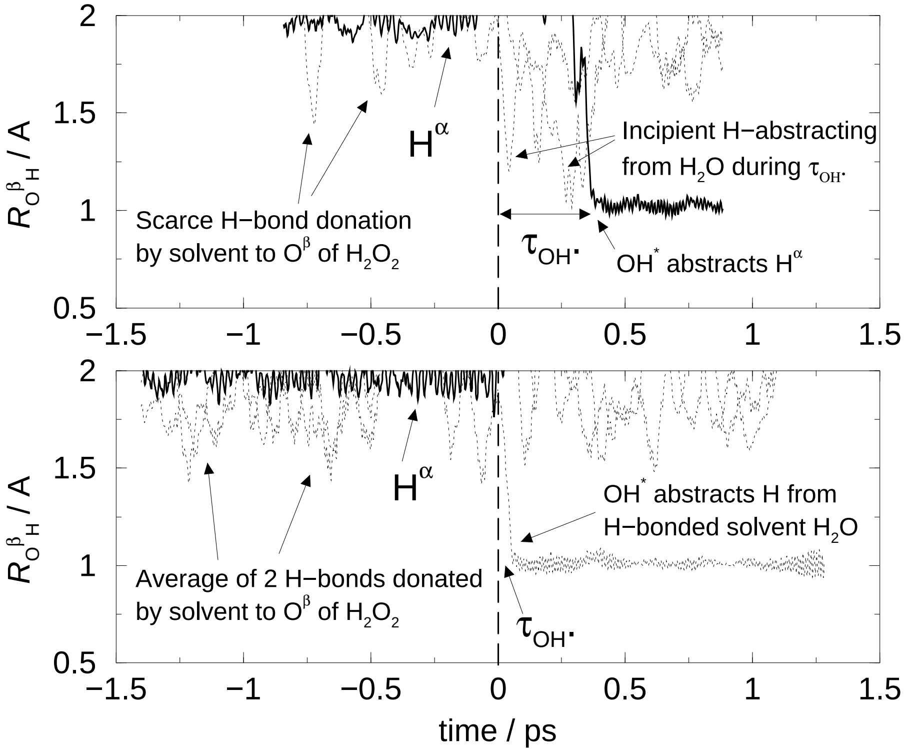

mechanism, namely the rebound mechanism. Of course, whether the two-step mechanism is indeed more favorable than this alternative can in principle only be established after generating a very large number of independent reaction pathways, and compare the probabilities of the two mechanisms. Our transition path sampling sequences indicate the rebound mechanism to have lower probability than the two-step mechanism. This can be rationalized from the following motive. In the rebound mechanism, the leaving $OH^{\cdot}$ has to abstract the Fe^{III}-OH^{α} hydrogen. From our results, however, we see that the leaving $OH^{\cdot}$ from the solvated hydrogen peroxide will jump rapidly along an H-bond wire to termination, which is much more probable, simply because the Fe^{III}-OH^{α} hydrogen is further away after the O-O lysis than the solvent molecules forming H-bonds.

The alternative mechanism to the two aforementioned ones (with a ferryl ion as the active intermediate) is Haber and Weiss' free radical mechanism. We have given arguments in references 146, 171 and 145 why we believe this mechanism to be unlikely. If we would still want to compare its probability to that of the two-step (ferryl ion producing) mechanism, we should consider that for the Haber and Weiss radical mechanism, the leaving $OH^{\cdot}$ radical has to become a "free radical" by jumping along an H-bond wire of

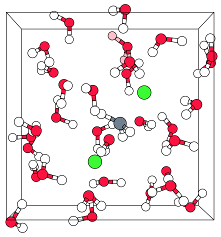

a number of solvent waters. The $OH^{\cdot}$ then should become disconnected, possibly by a thermal rotation of one of the involved solvent waters, so that the $OH^{\cdot}$ radical cannot jump back to terminate at the aquairon complex. In our rather small system, the occurrence or non-occurrence of the latter event cannot be adequately tested since an $OH^{\cdot}$ radical that leaves the complex to become a free radical via a short wire of, say, three solvent waters, is already too close to the periodic image of the iron complex at which it can terminate. For reaction path sampling of the Haber and Weiss free radical mechanism, a larger unit cell would be essential.

Let us finally note that the AIMD simulations are not without shortcomings. The box size was chosen rather small in order to make the computations feasible. The $OH^{\cdot}$ radical could therefore jump via a hydrogen bonded wire of three water molecules through the unit cell to a neighboring periodic copy of the cell. So, although the reactants have at least one complete hydration shell, and the major solvation contributions are included in the calculations, the long range effects are approximated and the simulations can, in the future when computers become faster, be improved by increasing the box size and the number of solvent molecules in the box. Other (minor) error sources are the neglect of pressure effects in the NVT ensemble, the classical treatment of the nuclear dynamics neglecting tunneling and zero point energy effects, and the accuracy of electronic structure method which is with the present exchange-correlation functions of DFT about 1 kcal/mol, and significantly larger (due to approximations in the PAW method) when changes in oxidation state of the metal are involved, see section 7.3.

7.7 Conclusion

We have successfully applied the reaction path generation technique used in transition path sampling in order to obtain relaxed reaction pathways of the reaction between pentaaqua iron(II) and hydrogen peroxide in aqueous solution. The initial reaction pathway which was the subject of this relaxation procedure showed a rebound mechanism in which the hydrogen peroxide O-O bond dissociated at H_2O_2 coordination to the iron(II) center, after which the leaving $OH^{\cdot}$ radical rebounded to abstract the intermediate Fe^{III}-OH hydrogen, forming the ferryl ion and a water molecule. We generated two sequences of ten reaction pathways from this initial path in order to obtain pathways which have lost the memory of the artificial construction of the initial pathway. Along these sequences, we found a shift to a new mechanism in which the leaving $OH^{\cdot}$ jumps via a solvent water molecule and abstracts the hydrogen from a water ligand forming a dihydroxo iron(IV) complex and a water molecule. The mechanistic change can be rationalized as the result of the proper reestablishing of the solvent structure around the reactants, which had been broken up in the artificial generation of the initial pathway. It is to be noted that the "mechanism" which emerges from these transition path sampling experiments is precisely the one found in our earlier AIMD simulation, starting from coordinated H_2O_2 [144], and was indeed already indicated by gas phase calculations [145]

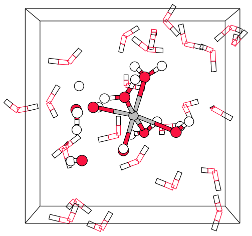

Acknowledgements

We acknowledge gratefully the support by the Prioriteits Programma Materialen - Computational Materials Science (PPM-CMS). We thank the foundation NCF of the Netherlands Foundation of Scientific Research (NWO) for computer time.

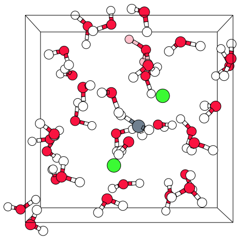

Chapter 8

Methane oxidation by the ferryl ion[*]

Previously, we have shown that the ferryl ion ($[Fe^{IV}O]^{2+}$) is easily produced from Fenton's reagent (*i.e.* a mixture of Fe^{2+} ions and H_2O_2 in aqueous solution), using DFT and Car-Parrinello MD calculations. In order to definitely conclude that the ferryl ion is indeed the active species in oxidation reactions with Fenton's reagent, we have in the present study studied the reactivity of the ferryl ion towards organic substrates, in particular the oxidation of methane to methanol. Our static DFT calculations on the $[(H_2O)_5Fe^{IV}O]^{2+}$–CH_4 complex *in vacuo* show a strong prevalance for the oxygen-rebound mechanism over the methane-coordination mechanism, which is in agreement with the results for methane oxidation by bio-catalysts MMO and P450, but not with those for methane oxidation by bare metal-oxo ions. The highest energy barrier in the oxygen-rebound mechanism is only 3 kcal/mol, whereas in the methane coordination mechanism the highest barrier is 23 kcal/mol. Overall the oxidation reaction energy is downhill by 47 kcal/mol. We also have computed the free energy barrier of the H-abstraction reaction from methane by the ferryl ion (*i.e.* the first step in the rebound mechanism) in aqueous solution by the method of constrained (first principles) molecular dynamics. The free energy barrier of 22 kcal/mol in solution is significantly higher that it is *in vacuo*. Nevertheless, in combination with our previous work, we must conclude that the ferryl ion is indeed the active intermediate in Fenton chemistry.

8.1 Introduction

Oxidation of organic compounds catalyzed by transition metal complexes is of great importance in industrial and biological processes. The most efficient oxidation catalysts are enzymes found in nature—examples are the chromophore P450, the anti-tumor drug bleomycin and methane monooxygenase (MMO). MMOs are a group of enzymes with two active iron centers, which are even capable of directly converting methane to methanol, whereas nowadays methanol is commercially produced in a two-step process via syn-

---

[*] B. Ensing, F. Buda, and E. J. Baerends, *submitted for publication*

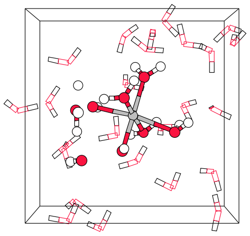

thesis gas, which is thermodynamically less efficient. In order to improve industrially applied catalysts, study of these enzymes can be very helpful. Oxidations by Fenton's reagent [128,155] (*i.e.* a mixture of Fe^{2+} and H_2O_2) are particularly interesting because it not only shows several mechanistic similarities with biochemical enzymes but it has also found industrial applications in for instance paper bleaching and polluted soil cleaning. However, the reaction mechanisms within Fenton chemistry, *i.e.* oxidation reactions initiated by Fenton's reagent, are still not fully understood, despite the intensive research for more than 60 years.

It is generally believed that the active species in Fenton chemistry is the free $OH^{\cdot}$ radical, which is produced by the iron catalyzed dissociation of hydrogen peroxide, as already proposed in 1932 by Haber and Weiss [156] (reaction equation 8.1).

$$\begin{aligned} Fe^{2+} + H_2O_2 &\rightarrow Fe^{3+} + OH^- + OH^{\cdot} && (8.1) \\ Fe^{2+} + H_2O_2 &\rightarrow FeO^{2+} + H_2O && (8.2) \end{aligned}$$

According to the most popular alternative, the active intermediate is a high-valent iron oxo species, the ferryl ion, which was actually already suggested in 1930, by Bray and Gorin [157](reaction equation 8.2). Due to the extremely short lifetimes of the proposed active intermediates, which makes direct detection experimentally very difficult, the controversy remains. The elucidation of the mechanism is further complicated by its complex dependence on the reaction conditions, such as the ligation of the metal, the solvent, the pH and the organic substrate.

We have recently performed static density functional theory (DFT) calculations on aquairon hydrogen peroxide complexes *in vacuo* as well as *ab initio* (DFT) molecular dynamics (AIMD) simulations on Fenton's reagent in aqueous solution, without an organic substrate. [145, 146, 171, 197] Our studies show that the ferryl ion is easily formed from hydrogen peroxide coordinated to pentaaqua iron(II), and from the energetic point of view much more likely than the formation of free $OH^{\cdot}$ radicals, thus favoring Bray and Gorin's proposal (reaction equation 8.2). However, to definitively accept the ferryl ion as the active species in aqueous Fenton chemistry, we need to investigate whether the ferryl ion is indeed capable of oxidizing organic substrates. This is the main goal of the present study.

For the organic substrate, we have chosen methane as our model system, which commends itself for a number of reasons. In the first place is the conversion of methane to methanol commercially very interesting, as mentioned before. Secondly, methane is a simple and small system which should limit the chemical complexity and also the computational requirements. In the third place, since the C-H dissociation energies of alkanes range from 103 kcal/mol (calculated at the DFT-BP+ZPE level of theory) for methane to about 90 kcal/mol for tertiary positions, oxidation of other alkanes by the ferryl ion should, at least thermodynamically, be no problem if the ferryl ion is shown to be capable of oxidizing methane. And in the last place, C-H bond activation of methane by transition metal complexes has already been investigated extensively, which makes it possible to compare the reactivity of the aqua iron oxo species to other iron-oxo moieties, such as the earlier mentioned enzymes. In practice, methane is not a Fenton's reagent substrate in aqueous solution, due to its very low solubility in water.

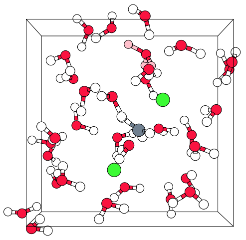

The bare FeO^+ ion has been shown to oxidize methane to methanol in the gas phase, under ion-cyclotron resonance conditions [217, 218], which has led to a number of theoretical investigations of oxidation reactions by FeO^+ and other bare metal oxo species [168, 170, 191–195]. Bare iron-oxo species were also believed to model the enzyme oxidations by cytochrome P450 [195] and MMO [170, 191, 192]. For the methane–to–methanol oxidation by FeO^{n+}, n=0,1,2 , Yoshizawa *et al.* found that a concerted reaction mechanism, via a four-centered transition state (with methane coordinated to iron) is energetically more favorable than a direct H-abstraction by the oxo ligand. Secondly, FeO^{2+} is much more effective for C-H bond cleavage in this *methane coordination mechanism* than FeO^+ and FeO. [170] Also, MnO^+, which is isoelectronic to FeO^{2+}, is most effective in C-H bond activation, compared to FeO^+ and CoO^+ [191,219]. Shaik *et al.* have proposed low-energy reaction paths, via a double crossing of the high-spin and low-spin energy surfaces—the so-called two-state reactivity [168, 195, 220].

The active states of the bioorganic molecules MMO [221–223] and cytochrome P450 [224,225], capable of hydroxylating and oxidizing organic substrates, also involve an $Fe^{IV}O$ intermediate. The latest theoretical (DFT) studies on methane–to–methanol oxidation by MMO [163, 164, 185, 186] and P450 [160, 190] confirm the consensus *oxygen-rebound mechanism* for these systems. The rate limiting step is the methane H-abstraction, via a linear $(Fe)O\cdots H\cdots C$ complex, forming a $^{\cdot}CH_3$ radical, which can rearrange to form the alcohol in the rebound step. The oxygen-rebound mechanism is supported by the high measured [226–228] and calculated [162,190] kinetic isotope effects. Ultrafast radical clock experiments, timing the rate of the rebound step, have however measured extremely short intermediate lifetimes, casting doubt on the presence of free radicals, which occur in a rebound mechanism [229,230]. Ogliaro *et al* explained the fast radical clock results for the P450 system with the aforementioned two-state reactivity [160]. For MMO, the radical clock experiments were explained by Siegbahn by an electron transfer of the substrate to the metal complex, forming a cation instead of a free radical [185].

We have calculated the reaction energy profiles for the oxidation of methane into methanol by the aqua iron(IV)oxo species *in vacuo* following the two mechanisms proposed in the literature. (A third mechanism, the so-called oxene-insertion, is now generally believed to be unlikely as it is characterized by very high energy barriers. [168]) First, the results for the methane coordination mechanism are presented in section 8.3.1, and next we discuss the results for the oxygen-rebound (radical) mechanism in section 8.3.2. To investigate the solvent effects on oxidation chemistry by the ferryl ion, we have also computed the free energy profile for the methane hydroxylation by the ferryl ion (according to the oxygen-rebound mechanism) in aqueous solution, using constrained *ab initio* molecular dynamics (section 8.4). We will first summarize the computational details, before presenting our results.

8.2 Method

All electronic structure calculations were performed using the density functional theory (DFT) method (see *e.g.* ref. 46). We used the Becke-88 gradient corrected exchange functional [67] and the Perdew-86 gradient corrected correlation functional. [38] For the

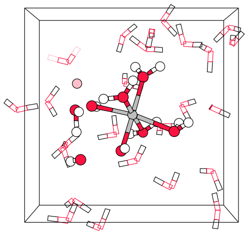

calculations of energies, frequencies and optimizations of geometries of the molecular structures *in vacuo*, we used the Slater type orbital based ADF package. [70] The Kohn-Sham orbitals were expanded in a large even-tempered all-electron Slater-type basis set containing: 4 s, 2 p, and 1 d functions for hydrogen; 6 s, 4 p, 2 d, and 1 f functions for carbon and oxygen; and 11 s, 7 p, 5 d, and 1 f functions for iron [175]. Finite-temperature reaction enthalpies at $T = 300$ K and the entropies were estimated using

$$\begin{aligned}
\Delta H^{300\mathrm{K}} &= \Delta E_0 + \Delta E_{\mathrm{ZPE}} + \Delta E_{\mathrm{int}}^{300\mathrm{K}} && (8.3)\\
\Delta E_{\mathrm{int}}^{300\mathrm{K}} &= \Delta E_T^{\mathrm{v}} + \Delta E^{\mathrm{t}} + \Delta E^{\mathrm{r}} && (8.4)\\
\Delta S &= R\ln(Q^{\mathrm{t}}Q^{\mathrm{r}}Q^{\mathrm{v}}) && (8.5)
\end{aligned}$$

with E_0 the sum of the electronic energy in a static nuclear field (Born-Oppenheimer approximation) and the nuclear electrostatic repulsion. The zero-point vibrational energy E_{ZPE} and the temperature dependent vibrational energy E_T^{v} were calculated from the unscaled DFT-BP frequencies, within the harmonic approximation. The change in translational energy ΔE^{t} and rotational energy ΔE^{r} were obtained using the ideal gas law, associating $\frac{1}{2}k_B T$ to each degree of freedom. The partition function Q is the product of translational, rotational and vibrational contributions (see *e.g.* chapter 20 in reference [78]).

The *ab initio* (DFT) molecular dynamics calculations of the systems including the solvent environment were done with the Car-Parrinello (CP) method [49] as implemented in the CP-PAW code developed by Blöchl [24]. The one-electron valence wave functions were expanded in an augmented plane wave basis up to a kinetic energy cutoff of 30 Ry. The frozen core approximation was applied for the 1s electrons of O, and up to 3p for Fe. For the augmentation for H and O, one projector function per angular-momentum quantum number was used for *s*- and *p*-angular momenta. For Fe, one projector function was used for *s* and *p* and two for *d*-angular momenta. The characteristic feature of the Car-Parrinello approach is that the electronic wave function, *i.e.* the coefficients of the plane wave basis set expansion, are dynamically optimized to be consistent with the changing positions of the atomic nuclei. The mass for the wave function coefficient dynamics was μ_e=1000 a.u., which limits the MD time step to $\delta t = 0.19$ fs.

The advantage of PAW over the more commonly used pseudopotential approach is that transferability problems should be largely avoided. However, as with all methods in which the core is represented approximately, there will be some loss of accuracy. Extensive tests are therefore required and we have previously shown that bond energies and geometries of small molecules and complexes computed with CP-PAW agree very well with highly accurate all-electron DFT results obtained with the ADF program [144]. However, we have in the course of the present work noted that reaction energies of chemical reactions involving a change in the formal oxidation state of iron sometimes exhibit relatively large (several kcal/mol) discrepancies with accurate (large basis set, all-electron) ADF calculations. Table 8.1 shows four reaction energies of gas phase reactions involving simple aqua iron complexes, calculated with CP-PAW and with ADF.

Reaction A and B, show the typical small differences in the order of 1 kcal/mol due to the differences in basis set and the frozen core approximation used with PAW. However, reactions C and D, which involve a change in the iron oxidation state, show larger discrepancies, up to 6.3 kcal/mol for the reaction in which iron(II) is oxidized to iron(III).

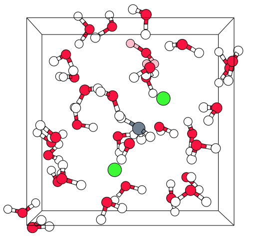

Table 8.1: *Bond dissociation energies and rearrangement energies in kcal/mol for isolated ("gas phase") complexes, calculated with the Amsterdam Density Functional program (ADF) and the CP-PAW program using the Becke-Perdew exchange correlation functional.*

	Gas phase reaction	CP-PAW	ADF	ΔΔE
A	$[\mathrm{Fe^{II}(H_2O)_6}]^{2+} \rightarrow [\mathrm{Fe^{II}(H_2O)_5}]^{2+} + \mathrm{H_2O}$	21.7	22.1	-0.4
B	$[\mathrm{Fe^{II}(H_2O)_6}]^{2+} \rightarrow [\mathrm{Fe^{II}(H_2O)_5}]^{2+}\text{–}\mathrm{H_2O}$	-2.3	-3.5	1.2
C	$[\mathrm{Fe^{II}(H_2O)_5}]^{2+} + \mathrm{H_2O_2} \rightarrow$ $[\mathrm{Fe^{III}(H_2O)_5OH}]^{2+} + \mathrm{OH^{\cdot}}$	-8.4	-2.1	-6.3
D	$[\mathrm{Fe^{III}(H_2O)_5OH}]^{2+} + \mathrm{OH^{\cdot}} \rightarrow$ $[\mathrm{Fe^{IV}(H_2O)_5O}]^{2+} + \mathrm{H_2O}$	-30.8	-28.7	-2.1

The error does not seem to be due to the plane-wave cutoff of 30 Ry (it is not reduced when going to 50 Ry) and can be attributed to the partial waves for the inner region of the valence electrons and the projector functions used in the PAW calculations. Also in this work, we will simulate a reaction involving a changing iron oxidation state (from iron(IV) to iron(III)) in aqueous solution. We will therefore only discuss the solvent effects on this reaction, by comparing the results with the same reaction *in vacuo*, rather than attempting to compute the reaction rate for this reaction in aqueous solution.

8.3 Gas Phase Calculations

8.3.1 The methane coordination mechanism

Figure 8.1 shows the energy profile and the complex geometries along the reaction coordinate for the reaction between tetraaqua iron(IV) oxo and methane, following the methane coordination mechanism. The sum of the energies of the optimized methane molecule and the optimized tetraaqua iron(IV) oxo complex (*i.e.* the reactants), is taken as the off-set for the energy scale. The initial step is the coordination of methane at the vacant coordination site of the metal center, forming a weekly bound reactant complex. The interaction energy is less than 6 kcal/mol. For comparison, the interaction of a fifth H_2O ligand at the $[\mathrm{Fe^{IV}O(H_2O)_4}]^{2+}$ complex equals 29.2 kcal/mol, which indicates that, in aqueous solution, the required CH_4/H_2O ligand exchange process is endothermic, by more than 20 kcal/mol. The transformation of the reactant complex into the product-complex of methanol bound to tetraaqua iron(II) occurs in two steps. In the first step, a hydrogen is abstracted from the weakly bound methane by the oxo-ligand, forming a hydroxo ligand and a (formally) CH_3^- ligand bound to iron(IV). This step is overall exothermic by 15.5 kcal/mol, but has a significant barrier of 22.8 kcal/mol, associated with a strained four-membered ring in the transition state. In the second step, the CH_3 group is transferred from the metal center to the oxygen of the hydroxo ligand, forming a bound methanol group. The oxidation state

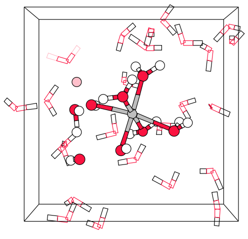

Figure 8.1: *Geometries and energy profile (in kcal/mol) of the intermediate steps along the methane coordination mechanism of the methane–to–methanol oxidation by the tetraaqua iron(IV)oxo species. The energy of the separated reactants is set to zero.*

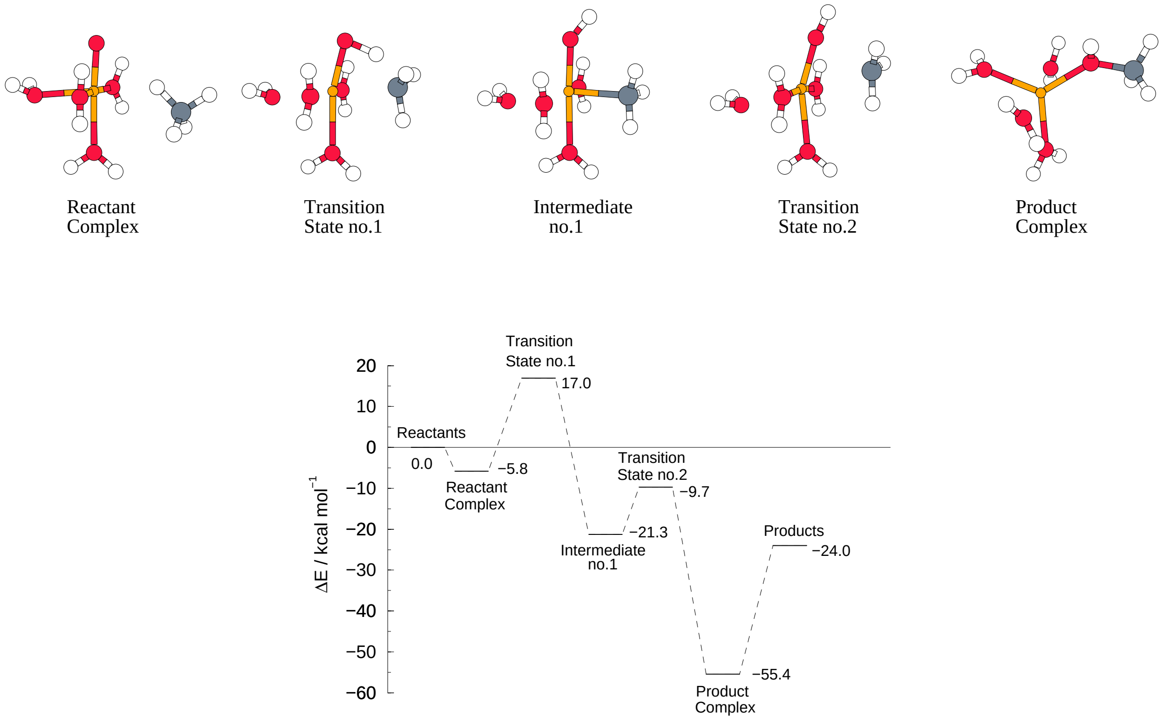

of iron is simultaneously lowered from Fe^{IV} to Fe^{II}, as both ligands (*i.e.* OH^- and CH_3^-) donate an electron to the metal d-manifold. The energy barrier for the, again exothermic, second step is not very high: 11.6 kcal/mol. The bonding of the methanol to $\text{Fe}^{\text{II}}(\text{H}_2\text{O})_4$ is found to be 31.4 kcal/mol strong. The final separation in aqueous solution can however be expected to be almost thermoneutral ($\Delta E = 5.4$ kcal/mol, neglecting solvent effects) if it is accompanied by the coordination of a solvent water to the vacant coordination site of the five-fold coordinated product complex, *i.e.*:

$$\begin{array}{llll} \text{Fe}^{\text{II}}(\text{H}_2\text{O})_4(\text{CH}_3\text{OH}) & + & \text{H}_2\text{O} \rightarrow \text{Fe}^{\text{II}}(\text{H}_2\text{O})_5(\text{CH}_3\text{OH}) & \Delta E = -20.3 \text{ kcal/mol} \\ \text{Fe}^{\text{II}}(\text{H}_2\text{O})_5(\text{CH}_3\text{OH}) & \rightarrow & \text{Fe}^{\text{II}}(\text{H}_2\text{O})_5 + \text{CH}_3\text{OH} & \Delta E = +25.7 \text{ kcal/mol} \end{array}$$

(methanol is stronger bonded to tetraaquairon(II) than to pentaaquairon(II) by $31.4 - 25.7 = 5.7$ kcal/mol).

Compared to the methane–to–methanol oxidation by bare metal–oxo species, for which the methane coordination mechanism was found to be the most likely mechanism, there are a number of differences. In the reactant complexes of methane coordinated to bare FeO, FeO^+ and FeO^{2+}, the binding of methane is η^2 or η^3-type, with Fe-C distances as

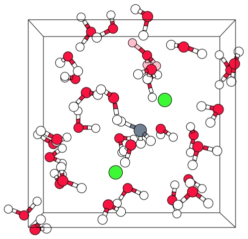

Table 8.2: *Relevant bond lengths (in Å) and angles as well as Mulliken charges and spin populations, for the reaction intermediates in the methane coordination mechanism of the methane–to–methanol oxidation by the tetraaqua iron(IV)oxo species.*

	Free Reactants	Reactant Complex	Trans. State 1	Inter-mediate	Trans. State 2	Product Complex	Free Products
RFeO	1.62	1.61	1.73	1.74	1.79	2.03	
ROH		2.51	1.13	0.98	0.97	0.97	0.97
RFeC		3.02	2.20	2.06	2.46	3.18	
ROC		3.62	2.34	2.70	2.18	1.48	1.43
RCH	1.10	1.12	1.30	2.90	2.40	2.02	1.96
$\angle$OFeC		98.	72.	90.	59.	21.	
qFe	1.22	1.24	1.43	1.40	1.32	1.25	1.28
qO	-0.16	-0.20	-0.25	-0.21	-0.30	-0.08	-0.09
qC	0.30	0.41	0.19	0.20	0.41	0.29	0.22
qH	-0.08	-0.11	0.03	0.08	0.08	0.06	0.07
sFe	3.10	3.07	3.68	3.74	3.87	3.82	3.84
sO	0.73	0.72	0.28	0.37	0.26	0.04	0.00
sC	0.00	0.04	-0.19	-0.32	-0.31	0.00	0.00
sH	0.00	0.01	0.05	0.02	0.01	0.00	0.00

short as 2.32, 2.36 and 2.07 Å respectively [170]. The interaction energy between CH_4 and FeO^{2+} was found to be extremely high, namely 70.3 kcal/mol, compared to 22.8 and 5.7 kcal/mol, for the high-spin methane FeO^+ and FeO complexes, respectively. The interaction energy with the MnO^+ ion (which is isoelectronic with FeO^{2+}) is only 16.2 kcal/mol [191]. Instead, we find for our aqua ligated complexes only a weak interaction between methane and the iron(IV) complex (5.8 kcal/mol), with methane bonded to the metal via a single hydrogen; the Fe-H bond distance being 2.17 Å, and a Fe-C distance of 3.02 Å. The relevant geometrical parameters, as well as Mulliken charges q and spin populations s are compiled in table 8.2, for the structures shown in figure 8.1. The Mulliken charge on iron of qFe=1.22 is relatively high compared to *e.g.* the five-fold coordinated $[Fe^{IV}(OH)_4(H_2O)]\cdot H_2O$ complex (qFe=0.85 [163]), due to the total +2 charge of our systems, and hardly changes after forming the reactant complex with methane. Also, the different basis sets used in our work and in that in the literature can give rise to differences in the Mulliken charges, so that these comparisons are to be regarded with reservation. The spin-density on iron(IV) of sFe=3.10, on the other hand, agrees very well that of other iron(IV) complexes, such as the tetrahydroxo complex (sFe=3.10 [163]) and in MMO models (sFe=3.11-3.55 [164, 185, 186]). The rest of the spin-density (the total spin-density is 4) is mainly located on the oxo ligand. The geometries of transition state no.1 (TS1) and the hydroxo intermediate agree qualitatively with the ones found for this first step for the bare $[FeO\text{-}HCH_3]^{2+}$ [170]. Quantitatively, the bond lengths differ in

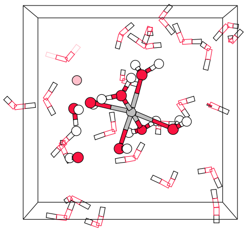

the order of 0.1 Å, with notably shorter Fe-O bond lengths of 1.614 Å and 1.675 Å for the TS1 and intermediate, respectively (where we find 1.73 Å and 1.74 Å), and a larger O-H bond distance of 1.443 Å for the transition state (we find 1.13 Å), in the case of the bare $[\mathrm{FeO\text{-}HCH_3}]^{2+}$ chemistry. The energetics are again very different. For the bare $[\mathrm{FeO\text{-}HCH_3}]^{2+}$ first step, the barrier is only 4.9 kcal/mol (here, 22.8 kcal/mol), whereas the overall transformation energy equals -52.0 kcal/mol (we find -15.5 kcal/mol). The $[\mathrm{MnO\text{-}CH_3}]^{+}$ profile shows only slightly better comparison, with a barrier of 9.4 kcal/mol and -36.1 kcal/mol overall. The CH_3 ligand interacts much more strongly with the metal center than CH_4, giving a bonding energy of -31.2 kcal/mol in the hydroxo intermediate. The positive Mulliken charge on the carbon in the hydroxo intermediate has decreased by 0.2 electron with respect to the reactant complex, and gained a spin density of 0.36. The spin density on iron of $s\mathrm{Fe}=3.74$ is in between the spins usually found for Fe(IV) and Fe(III). The second step, the formation of the methanol, which we found to be exothermic by 34.1 kcal/mol with a moderate barrier of 11.6 kcal/mol, was found to be energetically unfavorable for the bare $[\mathrm{FeOH\text{-}CH_3}]^{2+}$ case, and was not further discussed [170]. Also with manganese (*i.e.* bare $[\mathrm{MnOH\text{-}CH_3}]^{2+}$), this step is not exothermic (by 0.2 kcal/mol), and has a very high barrier, equal to 35.9 kcal/mol [191].

We conclude that the oxidation of methane to methanol by the tetraaqua iron(IV) oxo species is exothermic *in vacuo* following the methane coordination pathway, with a highest barrier for the hydroxylation step of 22.8 kcal/mol. If one were to start from pentaaqua iron(IV)oxo (as in aqueous solution), the first step is the water–methane ligand exchange reaction, which *in vacuo* is endothermic by 23.4 kcal/mol. The reaction energy profile shows large differences with that of methane oxidation by a bare FeO^{2+} ion, which casts doubt on the use of bare transition metal-oxo species as models for ligated transition metal oxo moieties, such as in enzymes and in solution.

8.3.2 Rebound mechanism

In this section, we present the results for the methane–to–methanol oxidation by the aqua iron(IV)oxo species, following the oxygen-rebound mechanism. This mechanism consists of two steps: first the hydrogen abstraction from methane by the iron(IV)oxo species, producing iron(III)hydroxo and a $^{\cdot}CH_3$ radical, and second, the collapse of the $^{\cdot}CH_3$ radical onto the iron(III)hydroxo oxygen, forming $\mathrm{Fe(II)CH_3OH}$. Figure 8.2 shows the energy profile for these reaction steps along with the intermediate complex geometries. For this mechanism, we have also computed the zero-point energy corrections, the temperature dependent enthalpy corrections for a temperature of $T = 300$ K and the entropy term $-T\Delta S$ (see table 8.3), the sum of which is added to the internal energy to give the free energy, indicated in figure 8.2 between parentheses.

The interaction between the methane substrate and the iron(IV)oxo complex is again very weak, equal to -2 kcal/mol. The first reaction step, the transfer of a CH_4 hydrogen from methane to the oxo ligand, forming an Fe(III)OH complex with a bound $^{\cdot}CH_3$ radical, is surprisingly easy. The overall reaction energy is +2.0 kcal/mol, and the barrier is only 3.4 kcal/mol (1.3 kcal/mol with respect to the free reactants). Release of the $^{\cdot}CH_3$ group, producing a free radical, was calculated from the energy difference of the separate geometry optimized structures to cost 14.4 kcal/mol. In contrast to H-abstraction from

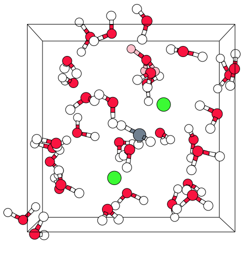

Figure 8.2: *Geometries and energy profile (in kcal/mol) of the intermediate steps along the oxygen-rebound mechanism of the methane–to–methanol oxidation by the pentaaqua iron(IV)oxo species. The energy of the separated reactants is set to zero. The free energies are indicated by the dotted levels and the numbers between parenthesis.*

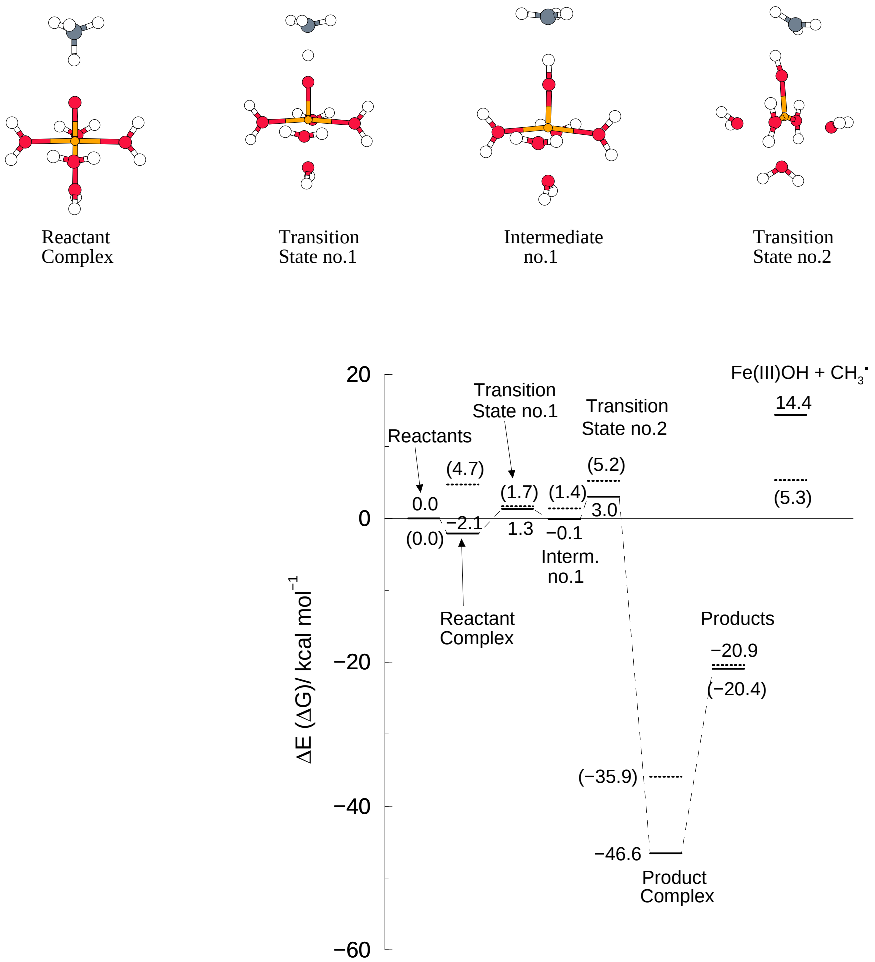

an isolated CH_4 molecule which costs 103 kcal/mol (calculated at the DFT-BP+ZPE level of theory), the energy surface is very flat due to the simultaneous formation of the OH bond with the breaking of the CH bond. Also compared to the formation of the free $^{\cdot}CH_3$ radical from the reactant complex, which costs 16.5 kcal/mol, the reaction energy needed to go from Fe(IV)O$\cdots$$HCH_3$ to Fe(III)OH$\cdots$$CH_3$ is very small. This is obviously due to fairly strong (14.5 kcal/mol) bond between the $^{\cdot}CH_3$ radical and the Fe(III)OH complex. We have not analyzed this bond in detail, but we note that there is a significant charge transfer contribution from CH_3 to the iron complex concomitant with the H-abstraction (see also the substantial absolute increase of qO and $q CH_3$ as ROH decreases and RCH increases in table 8.4, whereas the charge on CH_3 becomes zero for

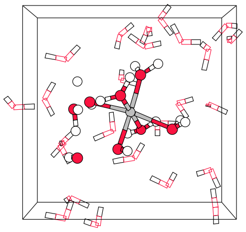

Table 8.3: *DFT energies (kcal/mol) for the intermediates in the oxygen-rebound mechanism of the methane–to–methanol oxidation by the pentaaqua iron(IV)oxo species (the proposed active species in the Fenton's reagent), compared to biochemical methane oxidations by MMO and P450. The lowest three rows show the zero-point energy correction, the temperature dependent corrections and the entropy term.*

	Reactant Complex	Trans. State 1	Inter-mediate	Free Radic.	Trans. State 2	Product Complex	Free Products
Fenton[a]	-2.1	1.3	-0.1	14.4	3.0	-46.6	-20.9
MMO[b]	2.3	13.8	2.8		7.6	-47.7	
MMO[c]	-1.5	23.2	11.3	23.7	20.6	-41.8	-34.3
P450[d]	-1.0	26.7	23.6		29.1	-36.9	
ΔZPE[a]	-0.8	-4.9	-3.3	-3.9	-3.5	1.8	0.1
$\Delta E_{\text{int}}^{300\text{K}}$[a]	0.4	-4.4	-1.7	-1.8	-2.1	4.2	-1.3
$-T\Delta S$ [a]	7.2	9.7	6.6	-3.4	7.8	4.6	1.7

[a] Our work. [b] P.E.M. Siegbahn, DFT-B3LYP + PCM, MMO compound Q model $(HCOO)_2$-$(C_3N_2H_4)Fe(\mu\text{-}O)_2(\eta^2\text{-}HCOO)Fe(C_3N_2H_4)(HCOO)(H_2O)$, ref. 185. [c] Basch *et al*, DFT-B3LYP, MMO compound Q model: cis-$(H_2O)(NH_2)Fe(\mu\text{-}O)_2(\eta^2\text{-}HCOO)_2Fe(NH_2)(H_2O)$, ref. 186. [d] Ogliaro *et al*, DFT-B3LYP, high-spin P450 compound I model: $FeO(C_{20}N_4H_{12})(SCH_3)$, ref. 160.

the free radical formation).

For the second step in the oxygen-rebound mechanism, we find the formation of methanol bound to pentaaqua iron(II) to be very exothermic (46.6 kcal/mol), with again a very small barrier, equal to 3.1 kcal/mol. We did not succeed in finding this second transition state from geometry optimization along the unstable mode of the Hessian, due to convergence problems (which is a notorious problem of weakly bound radicals to transition metal complexes, see *e.g.* ref. 185). However, from the potential energy surface shown in figure 8.3, we could determine the transition state structure to be the one shown in figure 8.2. This potential energy surface was computed from a geometry optimization for each point (indicated by the crosses) constraining only the C-O bond distance and the H-O-C angle. The oxygen of the hydroxo complex is situated at the coordinates (0,0) in the plot and the $R2 = 0$ axis is depicted to be along O-H. The energy of the Fe^{III}-$OH\cdots CH_3$ intermediate, which is a local minimum on the energy surface, was set to zero in figure 8.2 The potential energy surface shows that there exists a narrow channel, through which the bound methyl radical can rotate around the hydroxo hydrogen to bind with the oxygen. The channel is very flat up to an H-O-C angle of about 60 degrees, with a small maximum at an angle of 30 degrees (transition state no.2), but then enters a very steep well associated with the irreversible formation of methanol. From the zero-Kelvin energy, this second step seems thus much more likely than formation of the free methyl radical. However, if we include zero-point energy effects, temperature corrections and entropy effects, we see that the free energy barriers are similar, namely 5.2 and 5.3 kcal/mol,

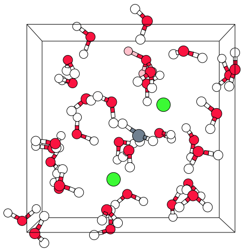

Table 8.4: *Relevant bond lengths (in Å) and angles as well as Mulliken charges and spin populations, for the reaction intermediates in the oxygen-rebound mechanism of the methane–to–methanol oxidation by the tetraaqua iron(IV)oxo species.*

	Free React.	React. Comp.	Trans. State 1	Inter-mediate	Free Radic.	Trans. State 2	Prod. Comp.	Free Prod.
RFeO	1.61	1.63	1.72	1.77	1.77	1.79	2.09	
ROC		2.91	2.55	2.78		2.50	1.47	
ROH		1.76	1.20	1.03	0.98	1.01	0.97	1.43
RCH	1.10	1.15	1.34	1.76		1.70	1.99	0.97
$\angle$HOC		1.	0.	1.		30.	108.	108.
$\angle$FeOH		179.	176.	155.	179.	151.	120.	
qFe	1.35	1.36	1.46	1.43	1.49	1.43	1.30	1.33
qO	-0.20	-0.30	-0.48	-0.36	-0.25	-0.37	-0.08	-0.09
qC	0.30	0.34	0.34	0.30	0.00	0.33	0.30	0.22
qCH$_3$	0.08	0.13	0.32	0.32	0.00	0.34	0.21	0.02
qH	-0.08	-0.11	0.04	-0.03	0.07	-0.02	0.05	0.07
sFe	3.14	3.40	3.97	4.11	4.20	4.08	3.83	3.85
sO	0.69	0.59	0.38	0.40	0.52	0.35	0.04	0.00
sC	0.00	-0.10	-0.50	-0.75	1.08	-0.65	0.00	0.00
sH	0.00	-0.04	-0.03	-0.01	0.03	-0.01	0.00	0.00

respectively (see figure 8.2).

This rebound mechanism has also been theoretically predicted to be the reaction mechanism for the methane-to-methanol oxidation by the enzymes P450 and MMO (as aforementioned in the introduction). In these complexes, a Fe^{IV}O species is ligated by either a porphyrin ring via four nitrogens (P450) or octahedrally by none-heme ligands via connecting oxygens (MMO), which makes especially the latter interesting to compare our results with. Literature values for the energetics are compiled along with our results in table 8.3. We see that also in these biological complexes the methane is initially very weakly bound in the reactant complex and that the overall formation of the product complex is very exothermic. The reaction barriers in between, however, are significantly higher for the oxidation by the enzymes than by the aqua ligated iron oxo species. For methane oxidation by P450, Ogliaro *et al.* found a barrier of 26.7 kcal/mol for the hydroxylation, and 29.1 kcal/mol for the rebound step, although the latter barrier vanishes if the system is allowed to cross to the low-spin surface [160]. Cytochrome P450 is known to be incapable of oxidizing methane, in contrast to MMO. Still, Basch *et al* find a barrier for H-abstraction by MMO which is almost as high as the one for P450, equal to 23.2 kcal/mol [186]. Siegbahn found a much lower barrier with MMO, namely 13.8 kcal/mol, which is still 11 kcal/mol higher than the barrier we find for the oxidation with aqua iron oxo [185]. The cited work on P450 and MMO was performed using

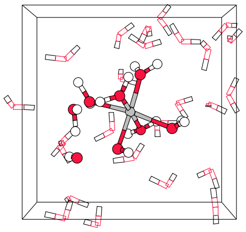

Figure 8.3: *Contour diagram of the potential energy surface of the bound $^{\cdot}CH_3$ radical in the neighborhood of the hydroxo ligand, which were both produced in the first step of the oxygen-rebound mechanism. Each mark ("+") indicates the carbon position of the methyl radical at which the energy was obtained from a geometry optimization of the complex, constraining only the C-O distance and the H-O-C angle. Oxygen is located at the point (0,0), and R2=0 axis is chosen to lie on the O-H bond, as indicated. With $^{\cdot}CH_3$ initially positioned close to (0,3), it can follow a bent channel with a small barrier of 3.1 kcal/mol, towards the steep well at (1.4,-0.5) forming methanol bound to iron(II).*

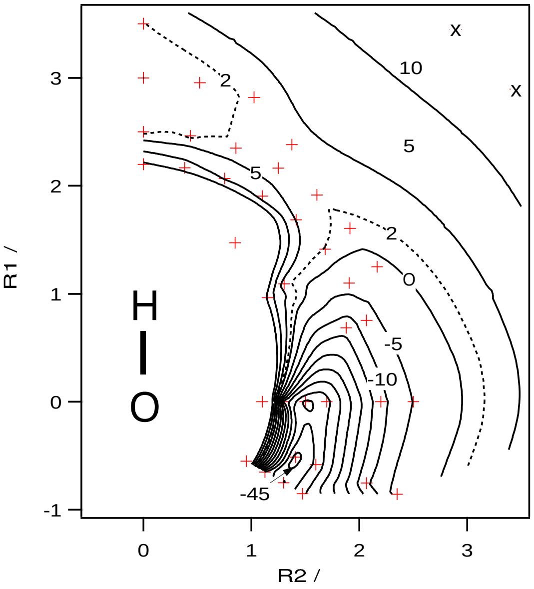

the hybrid B3LYP functional, which is known to sometimes give better transition state energies in cases where these barriers are underestimated by GGA functionals, see for example ref. 144. However, a comparison of these two functionals for the hydroxylation of H_2 by a bare iron oxo species showed that there is good agreement on the reaction barriers among the B3LYP and BP86 functionals, although the overall reaction exothermicy was found to be 10 kcal/mol smaller by the BP86 functional compared to the B3LYP functional [168]. Since discrepancies between the functionals are typically amplified in such small bare atom reactions, we expect much smaller discrepancies between energetics calculated with B3LYP and BP86 for the present complexes.

The O-H and C-H distances in the first transition state (*i.e.* the one for the hydroxylation step) (see table 8.4) are very similar to those found for the biochemical hydroxylations. For MMO, Siegbahn found R_{OH}=1.24 Å and R_{CH}=1.30 Å, and Basch *et al* found R_{OH}=1.21 Å and R_{CH}=1.33 Å, which compares well with the ones in our transition state (R_{OH}=1.20 Å and R_{CH}=1.34 Å). For the P450 transition state, Ogliaro *et al* found R_{OH}=1.09 Å and R_{CH}=1.50 Å, which lies relatively closer to the Fe^{III}-OH$\cdots$$CH_3$ intermediate state. Summarizing, we find that, apart from the higher barrier for hydrox-

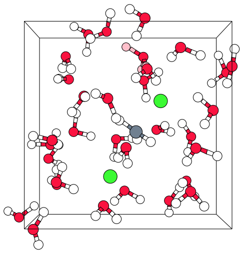

ylation in the MMO case, the rebound mechanism for methane–to–methanol oxidation by the pentaaqua iron(IV)oxo species is quite similar to the mechanism for the methane oxidation by MMO, calculated by Siegbahn. The hydrated ferryl ion *in vacuo* is found to be a highly reactive species, very well capable of hydroxylation and oxidation reactions with an organic substrate.

8.4 H-abstraction from methane by iron(IV)oxo in water

In this section, we will examine the solvent effects on the energetics of the hydroxylation of methane by the ferryl ion in aqueous solution. We have performed constrained molecular dynamics simulations to compute the free energy barrier, using the method of thermodynamic integration (see *e.g.* ref. 71). Since *in vacuo* the reaction barrier for the methane hydroxylation was found to be much higher in the methane coordination mechanism (22.8 kcal/mol) than in the oxygen-rebound mechanism (3.5 kcal/mol), the latter route is especially interesting to study in aqueous solution; also, because the required H_2O/CH_4 ligand exchange for the methane coordination mechanism adds an extra endothermicy of 23.4 kcal/mol *in vacuo*. On the other hand, one could argue that this ligand exchange reaction energy would be much less endothermic in aqueous solution, due to the hydrophobic repulsion between the methane substrate and the solvent in contrast to the hydrophilic interaction between the water molecule and the solvent. In principle, computation of the ligand exchange reaction (free) energy in aqueous solution is possible, although cumbersome and a complicated reaction coordinate would be required. Instead, using a simple bond constraint, the interaction between the methane molecule and the iron site can be computed and compared to the -6 kcal/mol attraction at an Fe-C distance of $R_{\mathrm{FeC}} = 3.0$ Å *in vacuo*. We therefore performed a short constrained molecular dynamics simulation of this system (see *e.g.* the reactant complex structure in figure 8.1) in water, with the Fe-C bond distance constrained to 3.0 Å. The resulting average force of constraint is repulsive by 0.008 a.u., and similarly, an average force of constraint equal to 0.022 a.u. is found for a Fe-C bond distance fixed at 2.5 Å (see figure 8.4). The CH_4 molecule is thus repelled from the iron coordination site in aqueous solution, so that we have concluded that the methane coordination mechanism does not offer a viable route in aqueous solution.

Proceeding with the oxygen-rebound mechanism, we performed 9 subsequent constrained molecular dynamics simulations at different points along the reaction coordinate of the reaction

$$[(\mathrm{H_2O})_5\mathrm{Fe^{IV}O}]^{2+} + \mathrm{CH_4} \rightarrow [(\mathrm{H_2O})_5\mathrm{Fe^{III}OH}]^{2+} + {}^{\cdot}\mathrm{CH_3} \tag{8.6}$$

in water. The cubic supercell with an edge of 10.13 Å and subject to periodic boundary conditions, contained one iron(IV)oxo molecule, one CH_4 molecule and a total number of 31 H_2O molecules. The total 2+ charge was balanced by a uniformly distributed counter charge. A Nosé thermostat maintained a temperature of T = 300 K. The constrained reaction coordinate, ξ, was chosen to be a function of the O-H bond distance, R_{OH}, the

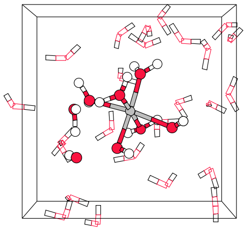

Figure 8.4: *The force of constraint (gray line) and a running average (black line) during a constrained AIMD simulation of* $[(H_2O)_4Fe^{IV}O(CH_4)]^{2+}$ *in aqueous solution. Constraining the Fe-C bond length to 3.0 Å results in a repulsive force of 0.008 a.u. After moving the constraint to 2.5 Å (at* $t \approx 4.25$ *ps) increases the average to 0.022 a.u.*

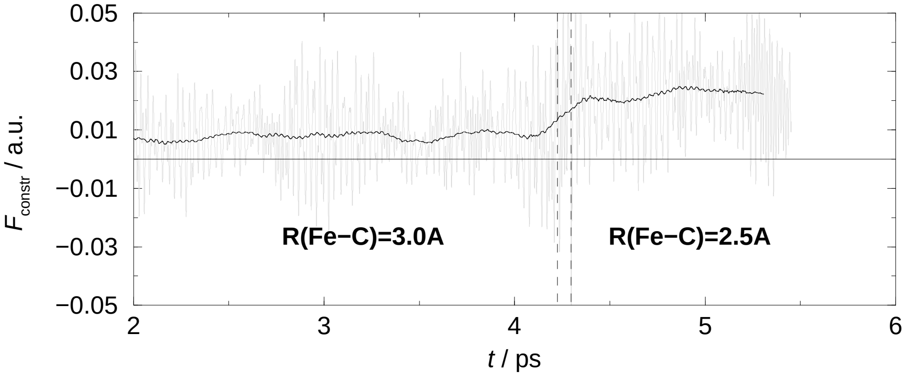

C-O bond distance, R_{CO}, and the angle between these bonds, $\angle_{HOC}$:

$$\xi = 1 - \frac{R_{OH} \cos \angle_{HOC}}{R_{CO}} \tag{8.7}$$

The second term is the ratio of the projection of the O-H bond distance onto the C-O axis and the C-O bond distance, which equals $\xi = 0.5$ when the hydrogen is in the middle of the oxo ligand and the carbon. For infinitely far separated reactants ξ goes to zero, and for infinitely far separated products ξ goes to one. Note that $\xi \geq 1$ for $\angle_{HOC} \geq 90°$, for instance when forming methanol and secondly, $\xi < 0$ if $R_{OH} > R_{CO}$, for instance in freely rotating CH_4. For our 9 MD simulations, we choose $\xi = (0.30, 0.35, 0.40, 0.45, 0.50, 0.54, 0.60, 0.65, 0.70)$. Each simulation started by bringing the constrained reaction coordinate ξ to the desired value during a short MD run, after which an equilibration MD run followed of at least 2.5 ps to adapt the system to the new constraint value, until there was no longer any drift in the fluctuating force of constraint. We then sampled the force of constraint, λ_ξ, during a 2 ps MD simulation. To correct λ_ξ for the bias introduced by imposing the constraint, which limits the sampling to a constrained NVT ensemble, instead of the desired true NVT ensemble, the true force of constraint $F(\xi)$ was calculated using

$$\begin{aligned} F(\xi) &= \frac{\langle \lambda_\xi Z^{-1/2} \rangle_\xi + \frac{1}{2} k_B T \langle Z_\xi^{-5/2} \sum_{i=1}^{N} \frac{1}{m_i} \nabla_i \xi \cdot \nabla_i Z \rangle_\xi}{\langle Z^{-1/2} \rangle_\xi} \\ Z &= \sum_i \frac{1}{m_i} \left(\frac{\partial \xi}{\partial \mathbf{r}_i} \right)^2 \end{aligned} \tag{8.8}$$

where T is the temperature, k_B is Boltzmanns constant, m_i and r_i are the mass and the position of atom i and λ_ξ is the sampled Lagrange multiplier associated with the holonomic constraint $\xi - \xi'(\mathbf{r}) = 0$ [17].

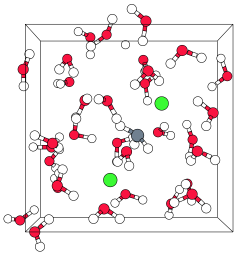

Figure 8.5: *The Helmholtz free energy profile ΔA (solid thin line) for methane hydroxylation by the ferryl ion in aqueous solution, obtained from the sampled mean forces of constraint (circles and dashed line; right-hand-side axis) of 9 constrained AIMD runs. The discrepancy between the reaction energies of the hydroxylation in vacuo for the all-electron ADF calculation (crosses) and the approximate PAW calculation (squares), results in a correction to $\Delta A_{\mathrm{aq,PAW}}$, the corrected ΔA_{aq} being given by the solid bold line* (cf. *text).*

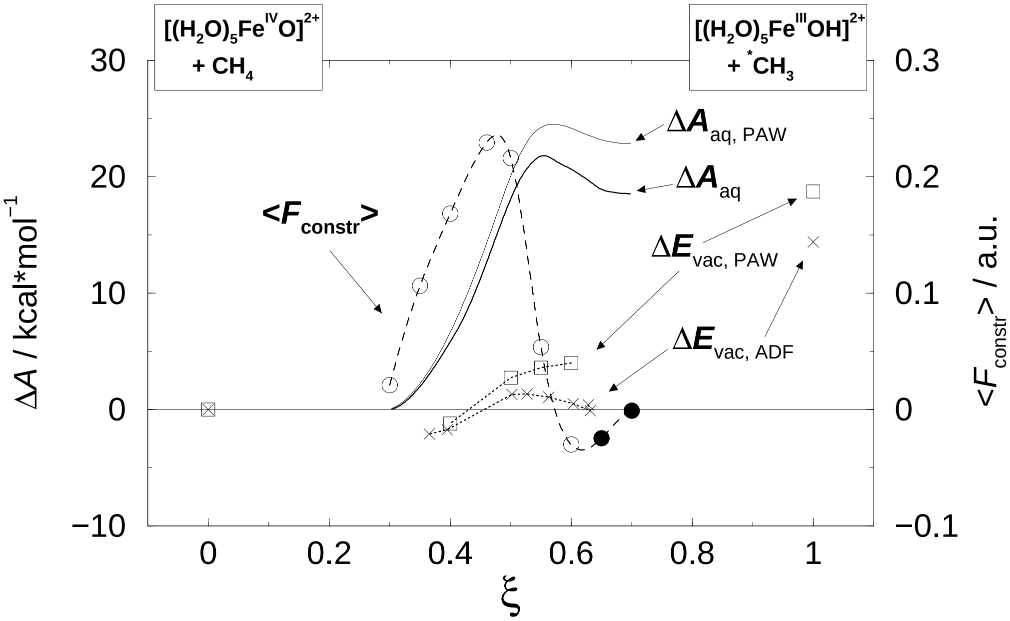

The results, the forces of constraint for nine points along the reaction coordinate, are shown in figure 8.5, indicated by the open and closed circles (and the right-hand-side axis) and fitted with a quadratic spline (dashed line). Due to the limited size of the supercell, the reaction coordinate value of $\xi = 0.3$ is practically the largest possible separation of the reactants in the box. The average distance between the oxo ligand and the methane carbon equals $R_{\mathrm{CO}} = 3.44$ Å at this constraint value (see figure 8.6, for the relevant average inter-atomic distances, R_{CO}, R_{OH}, R_{CH}, and R_{FeO} as a function of the reaction coordinate ξ). The average distance between the methane carbon and its hydrogen (that is to be transferred to the oxo ligand) is $R_{\mathrm{CH}} = 1.114$ Å at $\xi = 0.3$, which is almost equal to the other three average C-H bond distances (1.107 Å). The interaction between the reactants at $\xi = 0.3$ is indeed very small, but not completely zero, as seen from the small value for the mean force of constraint at $\xi = 0.3$ in figure 8.5. Moving along the reaction coordinate to larger ξ results initially in an increasing repulsive force, which comes to a maximum at $\xi = 0.477$ and then decreases again to cross the zero mean force of constraint at $\xi = 0.580$, which marks the transition state. Initially, the reactants are just pulled towards each other, as shown by the rapid decrease in the averages R_{CO} and R_{OH} (see figure 8.6). But beyond $\xi = 0.4$, also R_{CH} is seen to increase rapidly, indicating the transfer of the hydrogen from methane to the oxo ligand. The average

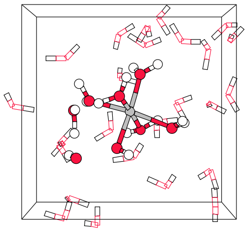

Figure 8.6: *The most relevant bond distances as a function of the reaction coordinate ξ. The bond distances in vacuo and the (average) distances in solution are very similar, except for R_{FeO}. In vacuo, the Fe-O distance for $[(H_2O)_5Fe^{IV}O]^{2+}$ ($\xi = 1$) is reached rapidly, as indicated by the horizontal dotted line, and similarly the Fe-O distance for $[(H_2O)_5Fe^{III}OH]^{2+}$ ($\xi = 0$) at the other end. In aqueous solution the average Fe-O bond length is always significantly larger.*

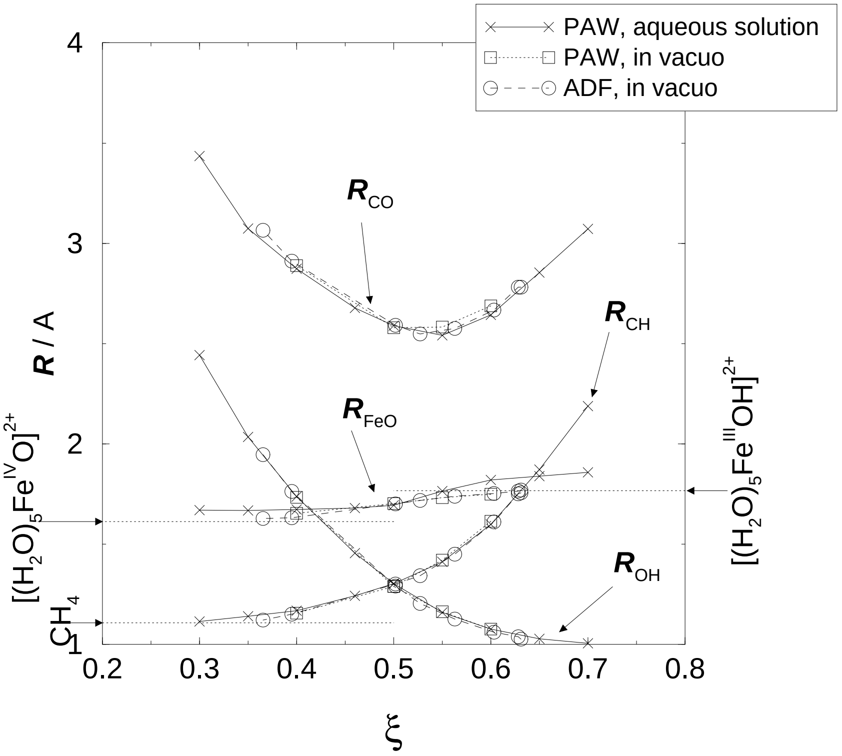

distance between the oxo ligand and the methane carbon, R_{CO}, has its minimum at the transition state position of $\xi = 0.580$. During the constrained MD simulation at $\xi = 0.65$ and $\xi = 0.70$ (distinguished by the black filled circles in figure 8.5), the coordination number of iron dropped by one to five, as in both simulations one of the five water ligands left the coordination shell and moved into the solvent. This event did not however have a significant effect on the (running) force of constraint.

The Helmholtz free energy profile is obtained by integrating the mean force of constraint with respect to ξ:

$$A(\xi) = \int F(\xi) d\xi + C \tag{8.9}$$

The result is shown by the thin solid line in figure 8.5 (connected to the left-hand-side axis). We choose C such that the free energy equals zero for our most left-hand-side point, $\xi = 0.3$. The bold solid line shows the modified free energy profile, ΔA_{aq}, for the hydrogen abstraction from methane by the ferryl ion in water, after correcting for the discrepancy

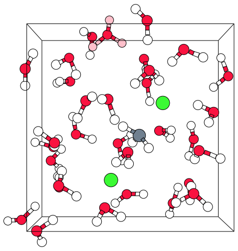

Figure 8.7: *Solvation of the reacting species during the hydroxylation in water measured by the coordination numbers of the oxo/hydroxo ligand oxygen (upper graph) and of the methane/methyl-radical carbon and hydrogens (lower graph). Circles, squares and solid lines show the average number of solvent hydrogens with a certain radius around the atom and crosses and dashed lines show the number of oxygens with a certain radius around the atom.*

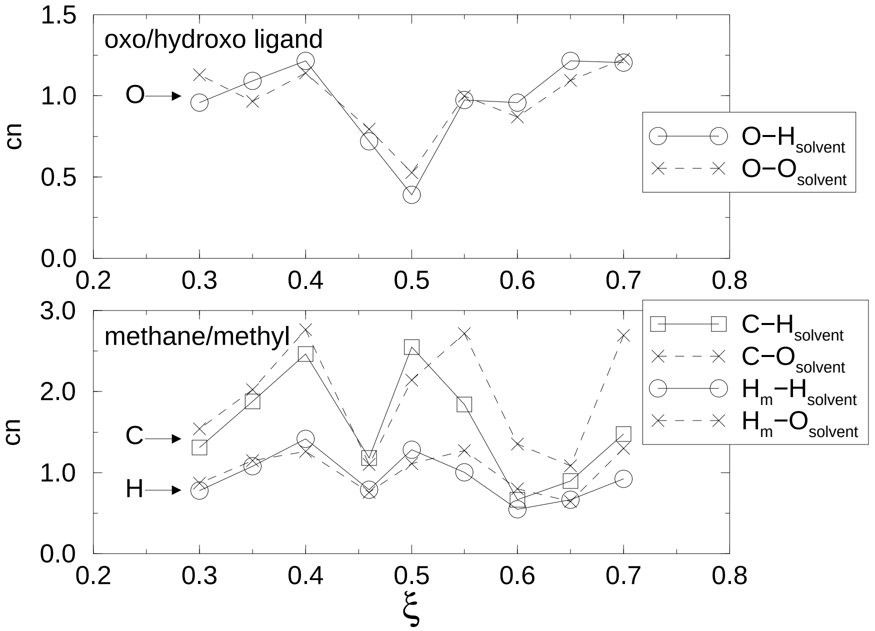

between results for the reaction energy of the hydrated complexes *in vacuo* obtained with the accurate all-electron ADF computation and with the approximate PAW approach, as explained in the method section 8.2. We have also plotted these reaction energies of the hydrated complexes *in vacuo* in figure 8.5 for comparison, using dotted lines and squares (labeled $\Delta E_{\mathrm{vac,ADF}}$) and crosses (labeled $\Delta E_{\mathrm{vac,PAW}}$). The reaction free energy barrier of 21.8 kcal/mol (with respect to the reactant complex at $\xi = 0.3$) is much higher than the zero-Kelvin energy barrier found for the H-abstraction *in vacuo* of 3.4 kcal/mol. Including the temperature dependent internal energy, $\Delta E_{\mathrm{int}}^{300\mathrm{K}} = -4.8$ kcal/mol, and the entropy contribution, $-T\Delta S = 2.5$ kcal/mol (see table 8.3) to this latter number, results in a free energy barrier of 1.1 kcal/mol *in vacuo*, making the difference in energetics even larger[†]. The large difference between the free energy profile in aqueous solution and the reaction energy *in vacuo* is rather striking. Moving further to the product side, ΔA_{aq} slowly decreases again by 3.3 kcal/mol, to 18.5 kcal/mol with respect to the reactant state at $\xi = 0.3$.

Clearly, the aqueous solution has a strong effect on the energetics of the hydrogen abstraction reaction from methane by the ferryl ion. The hydration of the iron complex

---

[†] The zero-point energy is not included in the computed Helmholtz free energy of the reaction in solution and is therefore also omitted in this number for the reaction *in vacuo*.

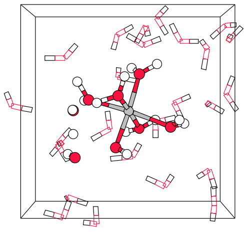

and the methyl by the surrounding dipolar water molecules plays an important role, as the charge distribution over the reactants changes along the reaction coordinate, leading to changes in the solvation energy. We have expressed the hydration of the oxo atom and the carbon and its (three) hydrogens in solvent coordination numbers, *cn*, by integrating the radial distribution functions of these atoms with respect to the solvent hydrogens and solvent oxygens up to certain radii. For the oxo/hydroxo ligand oxygen, the radial distributions, $g_{\mathrm{OH_s}}(r)$ and $g_{\mathrm{OO_s}}(r)$ showed clear peaks due to the hydration by, on average, one water molecule and the upper integration limit was therefore chosen at the minimum after the peaks at $r_{\mathrm{OH_s}} = 2.25$ Å and $r_{\mathrm{OO_s}} = 3.00$ Å. For the methane/methyl carbon and hydrogens, the hydrophobic solvation does not result in sharp peaks in the radial distribution functions, so that here the integration limits were chosen arbitrarily to be $r_{\mathrm{CH_s}} = 3.0$ Å, $r_{\mathrm{CO_s}} = 3.5$ Å, $r_{\mathrm{H_mH_s}} = 2.5$ Å, and $r_{\mathrm{H_mO_s}} = 3.0$ Å (the subscript s meaning solvent and m meaning methyl). Figure 8.7 shows these solvent coordination numbers for the oxo/hydroxo ligand (upper graph) and the methane/methyl substrate (lower graph).

The hydration of the hydrogen abstracting oxygen shows a clear picture: at the reactant side, the oxo ligand is coordinated by on average one water molecule and at the product side the hydroxo ligand also accepts on average one (1.2) hydrogen bond from a solvent molecule. In between, the hydration decreases to a minimum of about 0.4 hydrogen bonded solvent molecule at $\xi = 0.5$. This decrease is partly explained by the approaching methane which disrupts the solvent structure around the oxo-ligand as the distance between the oxygen and the methane carbon, R_{CO} (figure 8.6) decreases. However, the oxo coordination is not so small at $\xi = 0.55$ and $\xi = 0.60$ even though R_{CO} is still small. Most likely, the increased charge transfer (polarization) in the transition state complex relative to the reactant complex which we observed for the hydrated complexes *in vacuo* (see table 8.4), also takes place during the hydrogen transfer in solution. As a result the oxygen becomes more negative in the transition state configuration (at $\xi = 0.58$ in aqueous solution) and therefore more attractive for H-bond donating solvent molecules, hence the increased coordination number at $\xi = 0.55$ and $\xi = 0.60$, compared to $\xi = 0.50$.

The coordination number of the carbon (and methyl hydrogens) initially increases, as the methane molecule becomes polarized when one C-H becomes slightly elongated (lower graph in figure 8.7). But again *cn* drops when the distance between methane and the oxo ligand, R_{CO}, and part of the solvation shell of methane has to make space for the oxo ligand to enter. Also here, the minimum in *cn* is again followed by a significant increase which must be due to the increased (now positive) charge on $\mathrm{CH_3}$, which we also noticed *in vacuo* (table 8.4).

Can the ferryl ion still be expected to be the active intermediate in oxidation reactions by Fenton's reagent? For the oxidation of methane in aqueous solution, the reaction free energy barrier of more than 20 kcal/mol for the rate determining step (*i.e.* the H-abstraction) is on the high side. However, as explained in the introduction, the reaction barrier for methane hydroxylation serves as an upper limit. The C-H bond energy in a more typical organic substrate, such as tartaric acid (as was used by H.J.H Fenton himself [128, 155]) is in the order of 10 kcal/mol less than in methane. The remaining 10 kcal/mol for the barrier of the hydroxylation, is not very high at all, so that this result in combination with our previous work on the ferryl ion formation from Fenton's reagent leads us to conclude that the ferryl ion is indeed the most likely candidate for the active

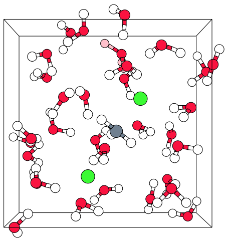

species in Fenton chemistry. Moreover, in most other solvents the screening effects will be less, which can now be expected to lower the barrier for the H-abstraction more.

8.5 Conclusion

We have performed static DFT calculations as well as *ab initio* (DFT) molecular dynamics simulations to study the ability of the ferryl ion $[\mathrm{Fe^{IV}O}]^{2+}$ to oxidize organic substrates in aqueous solution. The static DFT calculations show that the hydrated ferryl ion $[\mathrm{H_2O})_5\mathrm{Fe^{IV}O}]^{2+}$ is indeed very reactive and can oxidize methane to methanol, via two mechanisms.

Via the so-called methane coordination mechanism, with one water ligand replaced by methane, the weakly interacting reaction complex first forms a iron(IV)-hydroxo-methyl complex by hydrogen transfer from the methane to the oxo ligand. Then, methanol is formed in a second exothermic step by transfer of the CH_3 group from the metal to the hydroxo oxygen. The first step is the rate limiting step with a barrier of 22.8 kcal/mol. The energetics for the methane coordination mechanism in our aquairon complex are quite different from that of the methane oxidation by bare metal oxo species, for which this mechanism was found to be the most likely one. The water-methane ligand exchange reaction preceding the actual H-abstraction is endothermic by 23.4 kcal/mol.

Via an alternative mechanism, the so-called oxygen-rebound mechanism, the methane–to–methanol oxidation is practically barrierless *in vacuo* and also proceeds in two steps. In the first step, a hydrogen is abstracted from methane by the oxo ligand, forming an $[\mathrm{Fe^{III}OH}\cdots{}^{\cdot}\mathrm{CH_3}]^{2+}$ complex. In the second step, the bound ${}^{\cdot}CH_3$ radical can transfer via a narrow channel to the hydroxo oxygen, forming again methanol. Overall, this mechanism shows strong similarities with methane oxidation by the enzyme methane monooxygenase and, to a lesser extent, with oxidation by cytochrome P450, although the calculated barriers in the cases of these bio-catalysts are significantly higher.

Solvent effects are important when dealing with charged reactants. We have therefore studied the solvent effects on the initial methane hydroxylation step in the oxygen-rebound mechanism in aqueous solution. The free energy barrier of the H-abstraction from methane in aqueous solution is estimated to be 22 kcal/mol, using the method of constrained molecular dynamics. The reaction barrier and the overall endothermicy of this first step are significantly higher in solution than they are *in vacuo*, which is due to the decreased hydration of the reacting oxo/hydroxo ligand in the transition state and the higher energy of solvation for the iron(IV)oxo ion compared to the iron(III)hydroxo ion.

In combination with our previous work on Fenton's reagent (a mixture of iron(II) ions and hydrogen peroxide in water), which showed the spontaneous formation of the much contested ferryl ion, this work strongly supports the mechanism proposed by Bray and Gorin for the oxidation of organic substrates by Fenton's reagent, with the ferryl ion as the active species.

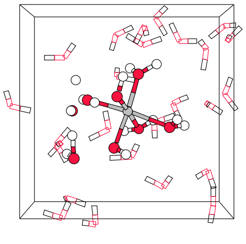

Acknowledgements

We acknowledge gratefully the helpful discussions with Michiel Gribnau from Unilever in Vlaardingen and the support by the Prioriteits Programma Materialen - Computational Materials Science (PPM-CMS). We thank the foundation NCF of the Netherlands Foundation of Scientific Research (NWO) for computer time.

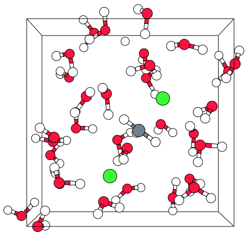

Chapter 9

Summary

Biochemical processes and environmentally friendly applied chemistry typically take place in aqueous solution. The solvent-solute interactions, particularly between charged or polar reactants and the water environment, are strong enough to have a dramatic impact on the chemistry taking place in solution. For example, the free energy barrier of the prototype S_N2 reaction between Cl^- and CH_3Cl, studied in chapter 3 is changed from 9 kcal/mol in the gas phase to 27 kcal/mol in aqueous solution, leading to a difference of 13 orders of magnitude (!) in the reaction rate at a temperature of $T = 300$ K. Besides the effect of solvation, the solvent molecules can be actively involved in chemical reactions, for example via their ability to transfer protons and hydrogen atoms as was shown in *e.g.* chapters 5 and 6. This way, the solvent environment can completely change reaction mechanisms by opening new reaction pathways. Both types of solvent effects, we have studied on a variety of chemical reactions in water on a microscopic scale using the method of *ab initio* molecular dynamics (AIMD).

AIMD is a very powerful simulation technique as it combines electronic structure calculations by way of the density functional theory (DFT) method with classical dynamics of the nuclei, so that both chemical reactions and solvent dynamics can be accurately modeled. The performance of AIMD to model liquid water and ionic solutions such as HCl(aq) (chapter 3) and $FeCl_2$(aq) (chapter 5) was found to be very good for structural parameters such as radial distribution functions and coordination numbers and reasonably accurate for dynamic properties, *e.g.* the self-diffusion coefficient of bulk water and the acidity constant of $[Fe^{III}(H_2O)_5]^{3+}$(aq) (chapter 4). The accuracy of the intra- and intermolecular interactions was found to be in general in the order of 1 kcal/mol. Although the AIMD technique is without doubt the state-of-the-art of the computer simulation methods available for these systems, calculations on ”chemistry in water” are still far from trivial, simply because chemical reactions typically occur on a much longer time scale ($\approx 10^{-9} - 10^{-3}$ s) than the time scale accessible to AIMD ($\approx 10^{-12} - 10^{-10}$ s), so that reactions during AIMD simulations are considered rare events.

A very effective technique to obtain information on the rare but important moment of transition state barrier crossing is the method of constrained molecular dynamics. With this technique, the system can be constrained to move only in the sub-space at a certain (fixed) point on a reaction coordinate. In chapter 3, we employed the method

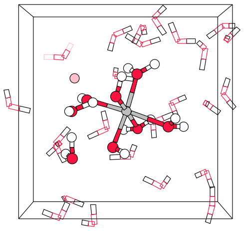

of constrained molecular dynamics to compute the free energy barrier of the textbook identity S_N2 reaction between Cl^- and CH_3Cl in aqueous solution. The solvent environment not only causes a dramatic increase of the barrier height, but affects the total free energy surface, which in the gas phase has the typical double-well shape. In aqueous solution however, endothermic solvent rearrangements approximately cancel the 11 kcal/mol exothermic reactant-complex formation, so that the free energy profile becomes unimodal. Our result for the free energy barrier of the S_N2 reaction in aqueous solution of 27 kcal/mol is in surprisingly good agreement with the experimental number of 26.6 kcal/mol, considering we encountered two important error sources for which we had to correct. In the first place, we found that DFT with the Becke-Perdew exchange-correlation functional underestimates the transition state energy barrier by as much as 8 kcal/mol, which could be attributed to an artifact in the description of symmetrical "three-center four-electron" bonds, such as the σ-bond in Cl-C-Cl by present-day GGA exchange functionals. Secondly, the free energy profile showed a hysteresis leading to an error of 3.2 kcal/mol in the barrier height, which was traced back to result from a too slowly adapting solvent environment. We found strong indications that the rearrangements in the solvation shells of the attacking and leaving Cl's (the coordination numbers of which change from five and one respectively in the reactant state to two and two respectively in the transition state) are in fact activated transformations. Although the trivial solution to the hysteresis problem would be to perform (much) longer constrained molecular dynamics simulations, one should be aware that the computed potential of mean force is a function of the chosen reaction coordinate and always will result in too low a barrier if activated environmental changes are not described by the reaction coordinate. An important lesson is to always check on the amount of hysteresis by repeating the constrained molecular dynamics exercise in the reverse reaction direction. Nevertheless, we showed that we can very accurately compute the energetic and entropic effects of the solvent environment on a prototype chemical reaction, using AIMD.

After this instructive study on the elementary S_N2 reaction, we devoted chapters 5 till 8 to the very versatile Fenton chemistry. The term Fenton chemistry denotes a broad range of oxidation and radical reactions initiated by the application of a mixture of iron(II) ions and hydrogen peroxide in aqueous solution, also known as Fenton's reagent. Although Fenton's reagent has found many applications and has been the subject of countless studies which have led to an even further broadening of the field by incorporating other transition metals, metal ligands and solvents, understanding of this type of oxidation catalysis was still clouded by many open questions concerning, most importantly, the reaction mechanism(s) and the nature of the reactive intermediate(s). The main experimental difficulty, the detection of the very short-lived reactive intermediates (possibly hydroxyl radicals or high-valent iron-oxo species), is not a problem for theoretical methods. Modeling of Fenton chemistry is nevertheless very challenging because it requires an accurate description of a number of complicated and simultaneously occurring processes, in particular, 1) the aqueous solvation dynamics, 2) the transport of protons and hydroxyl radicals along H-bond wires in the solvent, 3) the changing oxidation state, charge and spin-state of transition metal complexes, and 4) a number of chemical reactions, among which the O-O lysis of H_2O_2, hydrogen abstraction and hydroxylation of organic substrates, hydrolysis of metal ligands and radical reactions.

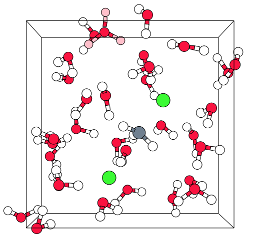

In chapter 5, we set out with the computation of the energetics of the two main reaction mechanisms proposed in literature for the reaction between iron(II) ions and hydrogen peroxide, starting from the $[Fe^{II}(H_2O)_5(H_2O_2)]^{2+}$ complex *in vacuo*. We found that the more popular Haber and Weiss mechanism, in which the very reactive hydroxyl radical is formed, is endothermic by 21 kcal/mol. The alternative Bray and Gorin mechanism, producing the much contested ferryl ion ($[Fe^{IV}O]^{2+}$) via an iron(IV)dihydroxo intermediate on the other hand is exothermic by 8 kcal/mol, with two minor reaction barriers, the highest being 6 kcal/mol. These preliminary static DFT calculations already revealed the importance of solvent effect, as *e.g.* the micro-solvation of a single H_2O molecule reduces the second reaction barrier from 18 to less than 4 kcal/mol. Using AIMD, we computed reaction pathways of the reaction between an iron(II) ion and hydrogen peroxide in aqueous solution, with two different starting configurations. Starting from H_2O_2 coordinated to the hydrated Fe^{2+} ion in water, we observed the formation of the ferryl via a two-step mechanism, very similar to the static DFT results *in vacuo*. That is, first O-O bond lysis takes place, forming $[Fe^{III}(H_2O)_5(OH)]^{2+}$ and an $OH^{\cdot}$ radical. The $OH^{\cdot}$ is very short-lived and travels rapidly via H-abstractions along a H-bond wire through the solvent to terminate at a water ligand of an iron complex in a neighboring periodic supercell, thus forming $[Fe^{IV}(H_2O)_4(OH)_2]^{2+}$ (and a water molecule). The acidic iron(IV)dihydroxo species is seen to be in a dynamic equilibrium with its conjugate base, via hydrolysis taking place at the water ligands. In the second step, the ferryl ion is formed as hydrolysis takes place at one of the OH ligands, donating a proton to the solvent, which was not seen to return. In the second starting configuration, we included the coordination process by starting from separated but approaching reactants, H_2O_2 and $[Fe^{II}(H_2O)_5]^{2+}$ (which has a vacant coordination site) in water. Again the ferryl ion was formed spontaneously, but now via a direct mechanism, as the intermediate $OH^{\cdot}$ radical produced after coordination and simultaneous O-O lysis, directly abstracts the Fe^{III}-OH hydrogen.

Visualization of the computed AIMD trajectories by movies, showing at a microscopic scale and in slow-motion the coordination and subsequent chemical reactions, gives a very clear impression of the mechanisms and relative time scales of these complex processes, which chemists denote with such abstract reaction equations as: $Fe^{II}(aq) + H_2O_2(aq) \rightarrow Fe^{IV}O^{2+}(aq) + H_2O(l)$. A disadvantage of our limited number of illustrative reaction pathways is of course the poor statistics, which do not allow *e.g.* to predict which of the two observed mechanisms (*i.e.* two-step vs. direct mechanism) is more favorable, let alone to compute a reaction rate. Another problem is the construction of the initial configurations of the systems, which in all cases involved unphysical geometric constraints, which could make the simulations less representative. In chapter 7, we attempt to tackle these problems, by generating new reaction pathways using the transition path sampling technique. Starting from the computed trajectory in which the separated reactants coordinate and react via the direct mechanism, we generated two new reactive pathways by randomly choosing a snapshot of the old trajectory, making small random changes to the atomic momenta and integrating the equations of motion forward and backward in time. On connecting the reactant state and the product state, the new pathways were accepted and used to branch of again two new pathways and so forth. This way, we computed two sequences of both 10 reactive pathways in order to obtain relaxed pathways, which no longer have a memory of the artificial construction of the initial pathway.

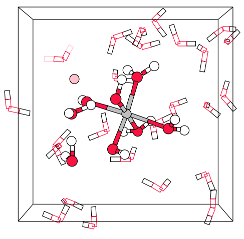

In both sequences of pathways, the reaction mechanism changes from the initial direct mechanism to the two-step mechanism. In the first new pathways following the two-step mechanism, the $OH^{\cdot}$ radical jumps via two or three solvent H_2O molecules to a neighboring periodic supercell to termination, forming the iron(IV)dihydroxo intermediate as already seen when we started from the $[Fe^{II}(H_2O)_5(H_2O_2)]^{2+}$(aq) complex. But in the last generated pathways, the $OH^{\cdot}$ radical terminates at the same iron complex as where H_2O_2 coordinated (instead of a periodic image) via a very short H-bond wire involving only one H_2O molecule. This trend was rationalized in chapter 7 from the fact that, along the sequences of reactive trajectories, the solvent relaxes in particular around the reactants as it loses the memory of the artificial preparation of the starting pathway. The H-bond wires in the solvent which are formed during the solvent relaxation are followed by the $OH^{\cdot}$ radical after O-O lysis, which makes the two-step mechanism more favorable than the direct mechanism.

Having established the reaction mechanism and the formed reactive species for the reaction between iron(II) and hydrogen peroxide in water, we focused on the mixture of iron(III) and hydrogen peroxide (known as the Fenton-like reagent) as iron(III) can be formed in Fenton chemistry, and the Fe^{3+}/H_2O_2 mixture is known to be also capable of oxidizing organic substrates, albeit less reactively than Fenton's reagent. In chapter 6, we show that O-O lysis of hydrogen peroxide coordinated to pentaaquairon(III) is energetically unfavorable in contrast to the iron(II) case. The formation of a Fe(III)-OOH species by donation of H^+, as proposed in literature cannot realistically be modeled by static DFT without the proper inclusion of the solvent, which screens the strong electrostatic interactions during this charge separation process. In a number of AIMD simulations of Fe^{3+} and H_2O_2 in aqueous solution, we indeed observe the spontaneous formation of the iron(III)hydroperoxo species. The DFT calculations show that homolysis of the Fe-O bond and the homolysis of the O-O bond are likely candidates for a second step in the Fenton-like mechanism, in particular favoring the latter in which both a ferryl ion and a hydroxyl radical are formed, when hydrolysis of the iron complexes is taken into account. Still, the reaction energy of this O-O homolysis of $[Fe^{III}(H_2O)_4(OH)(OOH)]^+$ is $+26$ kcal/mol *in vacuo*. In aqueous solution, we have computed the free energy barrier of the O-O homolysis to be $\Delta A^\ddagger = 21$ kcal/mol using the method of constrained molecular dynamics. Hydrolysis is indeed seen to play an important role as we observe the increasing acidity of the iron complex during the reaction. Analysis of the vibration spectra of the iron(III)hydroperoxo species in water confirms a reduced O-O bond strength and an increased Fe-O bond strength when the high-spin ($S = 5/2$) iron complex is brought to the low-spin ($S = 1/2$) state, as suggested by Raman spectroscopy studies. Using metal ligands that induce the low-spin state, we expect therefore a further reduction of the O-O homolysis endothermicity.

The observed spontaneous formation of the ferryl ion from Fenton's reagent alone is no prove that the ferryl ion is indeed the active intermediate capable of oxidizing organic substrates. In chapter 8, we have therefore studied the oxidation of methane to methanol by the ferryl ion in aqueous solution. We have investigated in particular two reaction mechanisms suggested in the literature: 1) the methane-coordination mechanism, in which the methane molecule first coordinates to the metal and transfers a hydrogen to the oxo ligand forming the $[Fe^{IV}(H_2O)_4(CH_3)(OH)]^{2+}$ intermediate, after which the CH_3^- ligand

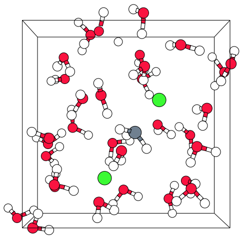

is transferred from the metal to the hydroxo ligand, forming methanol in the second step, and 2) the oxygen rebound mechanism, in which the ferryl ion first abstracts a hydrogen from the methane molecule forming an pentaaquairon(III)hydroxo intermediate and the $CH_3^{\cdot}$ radical which rebounds in a second step back to the oxygen forming the methanol. Our DFT calculations strongly favor the oxygen rebound mechanism, as the reaction energy barrier for the hydrogen abstraction from methane is only 3 kcal/mol compared to 23 kcal/mol in the methane coordination mechanism. Moreover, the water-methane ligand exchange required for the methane coordination mechanism adds an endothermicity of 23 kcal/mol *in vacuo*. Overall, the oxidation of methane by the ferryl ion is exothermic by 47 kcal/mol. Our results show strong similarities with the methane oxidation by enzymes, such as methane mono-oxygenase and cytochrome P450. Inclusion of the full solvent environment again shows the importance of these effects when dealing with charged species. Using constrained AIMD, we estimated the free energy barrier for the H-abstraction in the oxygen rebound mechanism to be 22 kcal/mol, much higher than in the gas phase.

We have shown that correct inclusion of the solvent effects usually changes severally the results of computer simulations on chemistry in aqueous solution. Not only the chemical reaction energetics is almost always modified dramatically, but also the extra degrees of freedom provided by the solvent molecules can open new mechanistic routes, which are not found for the reaction *in vacuo*. These effects should not be neglected, when studying chemical reactions that typically take place in water. We found that the Car-Parrinello molecular dynamics simulation method is a most powerful technique to compute physical properties of chemicals in solution and to obtain microscopic insight in solvent structure and solvation dynamics. The most important limitations that we encountered involve the quality of the present-day DFT exchange-correlation functionals and the rather high computational demand of the method in combination with our systems. Nevertheless, first principles computer simulation of rare events in aqueous solution is no longer out of reach, not even the simulation of such complicated systems as transition metal catalyzed oxidation reactions in water.

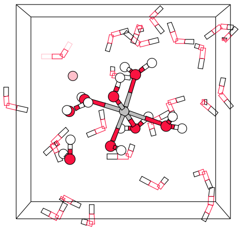

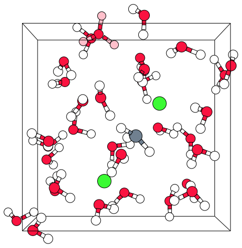

Chapter 10

Nederlandstalige samenvatting

Het is een goed gebruik om een proefschrift dat geschreven is in het Engels te besluiten met een min of meer letterlijke vertaling van de samenvatting in de moedertaal van de auteur. Omdat niet zozeer de Engelse taal als wel het gebruik van wetenschappelijke vaktaal een belemmering betekent voor de leesbaarheid van de “summary” voor de meeste belangstellenden onder niet-vakgenoten, probeer ik hier een samenvatting in begrijpelijk Nederlands te geven en verwijs ik vakkundigen graag naar de Engelstalige variant.

Het lijdt geen twijfel dat tegenwoordig de computer niet meer is weg te denken in het scheikundig onderzoek bij bedrijven en universiteiten. Commerciële software voor het ontrafelen van de structuur en de eigenschappen van nieuwe chemische stoffen en het bestuderen van chemische reacties tussen geïsoleerde moleculen biedt een onmisbare aanvulling op dure, gevaarlijke en milieuverontreinigende experimenten of kan deze zelfs overbodig maken. Veel interessante chemische reacties vinden plaats in waterig milieu, bijvoorbeeld de chemische processen in levende cellen zoals in het menselijk lichaam, maar ook in de steeds meer in opkomst rakende milieuvriendelijk chemische processen in de industrie. De invloed van water als oplosmiddel op chemische reacties is groot, vooral als de opgeloste chemicaliën een ionische of polaire aard hebben waardoor de wisselwerking met de watermoleculen sterk is. Bijvoorbeeld, de reactie tussen methylchloride en chloride ionen (deze was onderwerp van studie in hoofdstuk 3) verloopt in de gas toestand ongeveer 10^{13} (één met 13 nullen!) keer zo snel als wanneer de reagerende chemicaliën opgelost zijn in water. Bovendien kunnen de watermoleculen actief deelnemen in chemische reacties waardoor het oplosmiddel het verloop van reacties, oftewel het reactiemechanisme, verandert; voorbeelden hiervan zijn bestudeerd in hoofdstuk 5 en 6. Desalniettemin wordt in de huidige theoretische modellen de invloed van het oplosmiddel meestal verwaarloosd of hooguit in beperkte benadering meegenomen. Daarnaast zijn de microscopische mechanismen achter de oplosmiddeleffecten nog weinig onderzocht en daardoor vrijwel onbegrepen.

Dit proefschrift beschrijft mijn onderzoek naar de invloed van water als oplosmiddel op chemische reacties met behulp van theoretische methoden. Het model dat we hiervoor hebben gebruikt is de Car-Parrinello (”first principles”[*]) moleculaire dynamicasimulatie

---

[*] First principles: veel gebruikte vertaling van het Latijnse ”ab initio”, wat ”vanuit de eerste beginselen” betekent, om het onderscheid met klassieke moleculaire dynamica te maken waar de krachten middels empirisch bepaalde vergelijkingen worden bepaald i.p.v. vanuit de elektronenstruktuur.

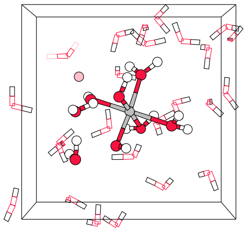

techniek. Deze rekenkundige methode verenigt in zich 1) een algoritme om de bewegingen van de atomen en moleculen in de tijd te voorspellen volgens de klassieke natuurwetten samen met 2) een kwantummechanische bepaling van de elektronenstructuur volgens het principe van de dichtheid functionaal theorie (DFT). Dit laatste, kennis van de elektronenstructuur in moleculen, maakt het mogelijk om chemische reacties tussen moleculen te voorspellen en te begrijpen terwijl met behulp van moleculaire dynamica de wisselwerkingen van de bewegende oplosmiddelmoleculen in vloeibaar water kunnen worden gemodelleerd. Echter, zelfs met deze geavanceerde methode is het simuleren van chemische reacties nog verre van triviaal. Dit komt doordat de langste tijdschaal die we met de allersnelste supercomputers kunnen simuleren, voor een typisch systeem van 100 atomen, slechts in de orde van 10^{-12}-10^{-10} seconden is. Dat is dus niet lang genoeg om chemische reacties waar te nemen, want reacties vinden typisch plaats op een tijdschaal van 10^{-9}-10^{-3} seconden. Het probleem is min of meer vergelijkbaar met het proberen om zonsverduisteringen te bestuderen door willekeurige filmpjes van strandvakanties te bekijken; de kans om zo een eclips te zien is te klein.

Een krachtige techniek om met behulp van moleculaire dynamicasimulaties toch informatie te verkrijgen over het relatief zeldzame maar beslissende moment van het plaatsvinden van een chemische reactie oftewel het moment waarop de moleculen de reactie-energiebarrière weten te overbruggen, is de “constrained” moleculaire dynamica methode. Hiermee kunnen de bewegingen van de moleculen worden gedwongen zich te beperken tot een vast (“constrained”) punt op een reactiecoördinaat, bijvoorbeeld in de reactantentoestand of in een (zonder “constraint” onwaarschijnlijke) overgangstoestand. In hoofdstuk 3 hebben we de constrained moleculaire dynamica methode toegepast om de invloed van water te bestuderen op de chloor uitwisselingsreactie tussen methylchloride en een chloride ion. Dit schoolvoorbeeld van een onder organisch chemici bekende bi-moleculaire nucleofiele substitutie (S_N2) reactie, is goed beschreven in de literatuur en derhalve een goede test voor onze berekeningen. Het model blijkt nauwkeurig de oplosmiddeleffecten te voorspellen van water op de reactie (vrije) energiebarrière; de hoogte van de barrière die we berekenden op 27 kcal/mol komt goed overeen met het experimenteel bekende getal van 26.6 kcal/mol. Dat de overgangsbarrière van de S_N2 reactie veel hoger is in oplossing dan in de gasfase (9 kcal/mol) komt doordat in oplossing met name de chloor atomen/ionen in het reactiecomplex minder sterk worden gesolveerd door watermoleculen in de overgangstoestand dan in de reactantentoestand en de productentoestand. Hierdoor is de energie van de overgangsenergie ten opzichte van de energie van de reactantentoestand (oftewel de reactiebarrière) veel hoger in oplossing dan in de gastoestand.

De berekeningen waren niet zonder technische complicaties. Ten eerste vonden we dat de elektron dichtheid functionaal (de Becke Perdew exchange-correlatie functionaal) de overgangsbarrière onderschat met 8 kcal/mol, vanwege een onjuiste modellering van symmetrische “drie-centra vier-elektron” bindingen, zoals de σ-binding in de Cl-C-Cl overgangstoestand door de huidige GGA exchangefunctionalen. Ten tweede vonden we hysterese in onze bepaling van het reactie vrije-energieprofiel (oftewel de vorm van het gemeten (berekende) profiel $f(x)$ bleek af te hangen van de richting waarin we de reactiecoördinaat x variëerden) doordat de vloeistofmoleculen zich te langzaam bleken aan te passen aan de veranderende reactiecoördinaat. We vonden sterke aanwijzingen dat de vereiste veranderingen in het omringende water ge-activeerd zijn, dat wil zeggen dat

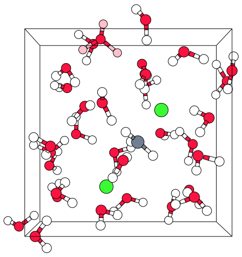

voor de veranderingen in de hydratatieschillen van chloor gedurende de chemische reactie extra barrières moeten worden overbrugd die niet door de toegepaste reactiecoördinaat worden ge-"constrained". Een belangrijke les die hieruit volgt is, om bij toepassing van de constrained MD techniek, de reactie zowel in voorwaartse als achterwaartse richting te simuleren, en zodoende de mate van hysterese vast te stellen. Voor beide genoemde complicaties konden we correcties toepassen. Als gezegd, bleken de oplosmiddeleffecten op de reactie goed beschreven door het gebruikte model.

Na deze leerzame teststudie van de oplosmiddeleffecten op de elementaire S_N2 reactie wierpen we ons op het onderzoeken van deze effecten op een overgangsmetaal gekatalyseerde oxidatiereactie, namelijk de Fenton reactie. De Fenton reactie is de opsplitsing van waterstofperoxide (de oxidator, H_2O_2) door reactie met een ijzer(II) ion (de katalysator, Fe^{2+}) in zeer reactieve deeltjes die in staat zijn organische moleculen, zoals tartaarzuur, te oxideren. Hoewel deze reactie al in 1876 door H.J.H. Fenton werd ontdekt en sindsdien onderwerp van ontelbaar veel studies is geweest, is het reactiemechanisme en de aard van de zeer reactieve deeltjes meer dan een eeuw later nog steeds niet met zekerheid bekend. Het grootste experimentele probleem is dat de reactieve deeltjes slechts een zeer korte tijd bestaan voordat ze reageren, zodat ze nauwelijks direct in een meting zijn waar te nemen. Desalniettemin wordt de Fenton reactie (en varianten hierop) veelvuldig toegepast in de industrie. Voor onze theoretische methode is de korte levensduur geen enkel probleem. Bovendien is de Fenton reactie als modelsysteem een praktische keuze voor ons onderzoek doordat het relatief kleine moleculen betreft (hetgeen de rekentijd van de simulaties beperkt) en anderzijds een veelzijdige uitdaging voor onze simulatiemethoden door de tegelijkertijd optredende complexe processen die moeten worden gemodelleerd. Processen die voor de theoretische methoden veeleisend zijn, zijn ondermeer de veranderende oxidatie toestand, elektron spin toestand en lading van het metaal ion gedurende de reactie, de veranderende zuurgraad van het complex, de vorming van radicalen, het sprongsgewijze transport van protonen en hydroxyl radicalen via het waterstof gebonden netwerk van de waterige oplossing, de vloeistof dynamica in de hydratatieschillen van de reactanten en een aantal chemische reacties, waaronder O-O lysis van waterstofperoxide, waterstof abstractie en hydroxylatie van organische substraten, hydrolyse van metaal liganden en radicaal reacties.

Na een aantal inleidende vingeroefeningen (waaronder moleculaire orbital analyse van ijzercomplexen en de berekening van de zuurgraad van ijzer(III) in waterige oplossing) beschreven in hoofdstuk 4, zijn we in hoofdstuk 5 begonnen met de berekening van de reactieenergieprofielen van de twee belangrijkste reactiemechanismen die voorgesteld zijn voor de Fenton reactie in de literatuur. De beginconfiguratie van deze statische (nul Kelvin) DFT berekeningen was het $[Fe^{II}(H_2O)_5(H_2O_2)]^{2+}$ reactanten complex in vacuum. We vonden dat het populaire mechanisme waarin de zeer reactieve $OH^{\cdot}$ radicalen worden gevormd (voor het eerst voorgesteld door Haber en Weiss in 1934) energetisch vrij ongunstig is met een reactieenergie van 21 kcal/mol. Het omstreden alternatief van Bray en Gorin (uit 1932), waarin een $[Fe^{IV}O]^{2+}$ ion (ook ferryl ion genaamd) wordt gevormd, blijkt energetisch wel gunstig met een reactieenergie van -8 kcal/mol, via een tweestappenreactie waarin eerst het $[Fe^{IV}(H_2O)_4(OH)_2]^{2+}$ intermediair wordt gevormd. De reactieenergiebarrières van respectievelijk 6 en 4 kcal/mol zijn bovendien bijzonder laag, waarbij opgemerkt dat zonder een (micro-) gesolveerd watermolecule (gevormd in de eerste stap)

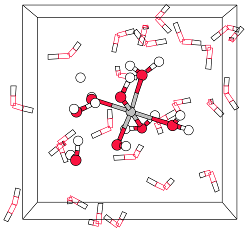

de energie barrière van de tweede stap 18 kcal/mol zou zijn—een aanwijzing dat (water) oplosmiddeleffecten wel eens een belangrijke rol zouden kunnen spelen. Dynamicasimulaties van ijzer(II) en waterstofperoxide opgelost in water lieten twee verschillende reactiemechanismen zien afhankelijk van de begincondities. Geprepareerd met H_2O_2 reeds in de coördinatieschil van het gehydrateerde ijzer(II) ion, dissocieerde het peroxide spontaan in een hydroxo ligand ($[(H_2O)_5Fe^{III}(OH)]^{2+}$(aq) vormend) en een zeer kort levend $OH^{\cdot}$ radicaal dat via drie watermoleculen aan een aqua (=water) ligand termineerde en zo $[(H_2O)_4Fe^{IV}(OH)_2]^{2+}$(aq) vormde. Dit dihydroxo deeltje bleek zuur te zijn en in de simulatie voortdurend een H^+ van een aqua ligand uit te wisselen met het oplosmiddel. Dit dynamische evenwicht werd na circa 3 ps beeindigd door de donatie van een H^+ door een hydroxo ligand, het ferryl ion vormend. Het tweede reactiemechanisme vond plaats vanuit van elkaar gescheiden opgeloste H_2O_2 en Fe^{2+} reactanten, zodat ook de coördinatie werd gesimuleerd. Onmiddellijk na coördinatie vond de O-O dissociatie plaats, maar het afgescheiden $OH^{\cdot}$ abstraheerde zonder tussenkomst van oplosmiddelmoleculen het H atoom van het gevormde ijzer(III)hydroxo deeltje, zodat in één stap het ferryl ion werd geproduceerd.

Chemische reacties worden door scheikundigen weergegeven met eenvoudige reactievergelijkingen, zoals $Fe^{II}(aq) + H_2O_2(aq) \rightarrow Fe^{IV}O^{2+}(aq) + H_2O(l)$. Hieruit blijkt duidelijk wat de reactanten en de producten van de reactie zijn, maar hoe het reactiemechanisme in zijn werk gaat (met name de volgorde van het breken en vormen van bindingen) blijft onduidelijk. Visualisatie van een simulatietraject door middel van een filmpje waarin in slow-motion de atomen bewegen terwijl de moleculen met elkaar reageren geeft een goed beeld van een reactiemechanisme en de relatieve tijdschalen waarin de verschillende processen plaats vinden ten opzichte van elkaar. Na echter een paar van deze filmpjes van één bepaalde reactie in oplossing gezien te hebben, wordt duidelijk dat er ontelbaar veel verschillende routes zijn die leiden van reactanten tot producten. Zelfs wanneer al deze reactieroutes tot hetzelfde globale reactiemechanisme zijn te classificeren (wat in principe niet het geval hoeft te zijn), dan is nog steeds een statistische afspiegeling nodig (van veelal duizenden trajecten) om interessante grootheden als de reactiesnelheidsconstante te kunnen bepalen. Met de enkele dynamicasimulaties van de Fenton reactie, hierboven beschreven, is deze bepaling dus niet mogelijk; sterker nog, we kunnen zelfs niet bepalen welk van de twee geobserveerde mechanismen waarschijnlijker is. Daar komt nog bij dat voor de preparatie van de systemen on-fysische technieken zijn gebruikt, (er werden geometrische beperkingen opgelegd) om de observatie van de chemische reactie in de beperkte simulatietijd waarschijnlijker te maken, die de relevantie van de trajecten als illustratie van de werkelijkheid negatief beïnvloeden. In hoofdstuk 7 hebben naar een manier gezocht om het illustratieve karakter van onze eerdere reactietrajecten te vergroten met behulp van een nieuwe techniek, genaamd "transition path sampling". Met deze techniek kan vanuit een bestaand, al dan niet realistisch, reactiepad, nieuwe reactiepaden worden gegenereerd, hetgeen we als volgt hebben toegepast op het eerder genoemde traject van de gescheiden H_2O_2 en Fe^{2+} reactanten die zonder tussenkomst van oplosmiddelen tot het ferryl ion reageerden. We namen de configuratie (van posities en snelheden van de nucleï en de bijbehorende elektron golffunctie en zijn afgeleide in de tijd) van een willekeurig gekozen tijdstip van ons bestaande reactietraject en maakten vervolgens kleine willekeurige veranderingen in de snelheden van de nucleï. Integratie van

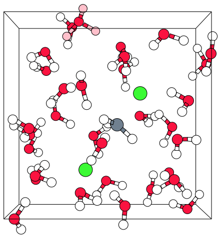

de bewegingsvergelijkingen (oftewel dynamicasimulatie) vanaf deze vernieuwde configuratie vooruit en achteruit in de tijd, leidde zo tot een nieuw traject, dat, hoe meer de tijd vorderde (in beide richtingen), meer en meer afweek van het oorspronkelijke traject. Wanneer dit nieuwe traject een nieuwe route vormde tussen de reactanten toestand (terug in de tijd) en de producten toestand (vooruit in de tijd), accepteerden we dit nieuwe traject om hiermee vervolgens de voorgaande handelingen te herhalen. Zo niet dan probeerden we het nogmaals met het oudere traject door een nieuw willekeurig tijdstip en willekeurige nuceï snelheden te kiezen. Op deze wijze genereerden we een reeks van reactiepaden (n.b. dit zijn normaal gesproken onwaarschijnlijke gebeurtenissen in onze computersimulaties). Door het ergodische (chaotische) karakter van het dynamische systeem, wijkt een volgend gegenereerd reactiepad in de reeks steeds meer af van het oorspronkelijke pad. Dit betekent, wanneer ons initiële reactiepad van de Fenton weinig realistisch zou zijn, bijvoorbeeld omdat het systeem een onwaarschijnlijk hoge reactiebarrière neemt als gevolg van de preparatie van het systeem, dat het hoogstwaarschijnlijk is dat paden verderop in de reeks hun weg hebben gevonden naar realistische illustratieve routes, omdat ze zozeer afwijken van het initiële pad dat ze geen "herinnering" meer hebben van de preparatie van het systeem. Voor ons eerder genoemde pad van de Fenton reactie hebben op deze wijze twee reeksen van paden gegenereerd. In beide reeksen was reeds na tien paden het reactiemechanisme veranderd van het directe mechanisme naar het twee-staps mechanisme. Nadere bestudering toonde aan dat met name de oplosmiddel structuur rond de reactanten in het initiële pad zich in een ongunstige configuratie bevond, hetgeen zich verderop in de reeksen aanpaste en leidde tot het "twee-staps" reactiemechanisme.

Nadat we aldus overtuigend hadden aangetoond dat het twee-staps mechanisme, het meest waarschijnlijke mechanisme achter de Fenton reactie is, waarbij eerst het ijzer(IV)-dihydroxo intermediair wordt gevormd alvorens het ferryl ion te produceren, was het slechts een kleine stap om ook de reactie tussen ijzer(III) en waterstofperoxide te bestuderen. Dit mengsel wordt algemeen met het Fenton-*like* reagens aangeduid en is ook in staat om organische substraten te oxideren, al is de reactiviteit veel minder dan bij het ijzer(II)/H_2O_2 mengsel. Dit laatste is enigszins verrassend, daar het verschil tussen het Fenton reagens en het Fenton-like reagens immers slechts één elektron betreft. In hoofdstuk 6 lieten we met behulp van statische DFT berekeningen aan de ijzercomplexen in vacuüm zien dat het verbreken van de O-O binding in $[(H_2O)_5Fe^{III}(H_2O_2)]^{3+}$ energetisch zeer ongunstig is, in tegenstelling tot dat bij het Fenton reagens. In de literatuur is het ijzer(III)hydroperoxo ($[Fe^{III}OOH]^{2+}$) deeltje voorgesteld als mogelijk reactief intermediair, wat gevormd kan worden vanuit het Fe^{III}-H_2O_2 complex door de donatie van een proton (H^+). Echter, het modelleren van deze 'ladingsscheiding" reactie is niet goed mogelijk zonder rekening te houden met de vloeistofeffecten, omdat deze de sterke elektrostatische interactie tussen de ladingen afschermt ("screening effect"). In dynamicasimulaties van het Fenton-like reagens opgelost in water zien we inderdaad spontaan het ijzer(III)hydroperoxo deeltje ontstaan en niet de O-O binding breken zoals bij het Fenton reagens in water. Homolyse van de O-O binding in het hydroperoxo intermediair, waarbij een ferryl ion en een hydroxyl radicaal (twee zeer reactieve deeltjes) ontstaan lijkt in eerste instantie energetisch zeer ongunstig (43 kcal/mol in vacuüm). Als echter de mogelijkheid van hydrolyse van het zure ijzer(III) complex wordt meegenomen, vermindert de endothermiteit naar 26 kcal/mol door de verminderde lading van het complex van 3+

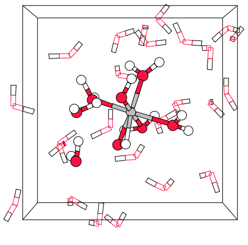

naar 2+. Met behulp van de eerder genoemde constrained moleculaire dynamica techniek hebben we de vrije energiebarrière van de homolyse van het ijzer(III)hydroperoxo complex in water berekend op $\Delta A^{\ddagger} = 21$ kcal/mol. Deze berekening bevestigt bovendien het hydrolyse effect—de simulaties laten eens te meer zien dat de ijzercomplexen zuurder worden naarmate de formele oxidatie toestand van het metaal toeneemt. Ten slotte hebben we de (infrarood) vibratie spectra van het ijzer(III)hydroperoxo intermediair bepaald voor het metaal, zowel in de elektronische hoog-spin toestand ($S = 5/2$, dit is de grond-toestand voor de aqua geligeerde ijzercomplexen) en in de laag-spin toestand ($S = 1/2$). De spectra bevestigen het beeld dat de in de laag-spin toestand de O-O binding zwakker, en de Fe-O binding sterker, is vergeleken met die in de hoog-spin toestand, zoals gesuggereerd in de literatuur aan de hand van Raman spectroscopie. Met andere woorden, wanneer het ijzer wordt gecoördineerd met andere liganden (dan water) die een laag-spin complex induceren wordt verwacht dat homolyse van een hydroperoxo complex energetisch gunstiger zal zijn dan nu het geval is.

Het ontstaan van het ferryl ion uit ijzer(II) en waterstofperoxide, en in mindere mate ook uit ijzer(III) en waterstofperoxide, alleen is niet voldoende bewijs dat het ferryl ion ook inderdaad het reactieïntermediar is in Fenton chemie, verantwoordelijk voor de oxidatie van organische substraat moleculen. In hoofdstuk 8 hebben we daarom onderzocht of het ferryl ion in staat is om methaan te oxideren tot methanol. Hierbij hebben we ons andermaal geconcentreerd op twee uit de literatuur bekende mechanismen, te weten: 1) het methaan-coördinatie mechanisme, waarbij methaan eerst coördineert aan een vrije coördinatie plaats aan het ijzer(IV) en een waterstof afstaat aan het oxo ligand, zodat het $[\mathrm{Fe^{IV}(H_2O)_4(CH_3)(OH)}]^{2+}$ intermediair gevormd wordt, waarna in een tweede stap het methanol wordt gevormd door transfer van het $\mathrm{CH_3^-}$ ligand van het metaal naar het hydroxo zuurstof, en 2) het terugkaatsmechanisme, waarbij het ferryl ion eerst een H van methaan abstraheert om een $\mathrm{Fe^{III}OH}$ intermediair te vormen en een $\mathrm{CH_3}^{\cdot}$ radicaal dat in tweede instantie wordt teruggekaatst en reageert met het hydroxo ligand tot methanol. Alhoewel de totale reactieenergie in beide gevallen zeer gunstig is (minder dan -45 kcal/mol), laten onze DFT een duidelijke voorkeur zien voor het terugkaatsmechanisme. De reactiebarrière is slechts 3 kcal/mol in het geval van het terugkaatsmechanisme terwijl de hoogste barrière voor het methaan coördinatie mechanisme 23 kcal/mol is. Dit is in tegenspraak met de resultaten van eerder gerapporteerde DFT berekeningen aan methaanoxidatie door kale (dat is, zonder liganden) ijzer-oxo moleculen, waarmee we aantonen dat het verwaarlozen van de ligandveldeffecten, zoals soms (gedeeltelijk) wordt gedaan bij de modellering van grote bio-complexen, van doorslaggevende betekenis kan zijn. Bovendien is het vervangen van een waterligand door het methaan ligand in het methaan coördinatie mechanisme als initiële stap energetisch ongunstig (23 kcal/mol in vacuüm). Onze resultaten vertonen opvallende gelijkenis met de DFT resultaten van oxidatie reacties door enzymen, zoals methaan mono-oxogenase en het chromofoor cytochroom P450. Het meenemen van de oplosmiddel omgeving in de simulatie laat nogmaals zien hoe belangrijk de oplosmiddeleffecten zijn op de chemie wanneer het reacties tussen één of meer geladen deeltjes betreft. Constrained moleculaire dynamicasimulaties van de H-abstractie van methaan door het ferryl ion in waterige oplosmiddel laat een vrije energiebarrière zien van 22 kcal/mol; veel hoger dan in de gas toestand. Omdat het primaire koolstof atoom in methaan veel moeilijker is te oxideren dan de secundair en ter-

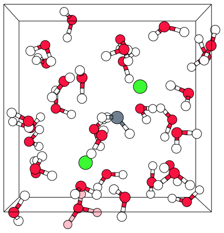

tiair vertakte koolstof atomen van de gebruikelijke Fenton substraten, is de buitengewone reactiviteit van het ferryl ion hiermee afdoende aangetoond.

Ik heb laten zien dat de resultaten van computer simulaties van chemie in water meestal significant beïnvloed worden wanneer de oplosmiddeleffecten niet correct worden meegenomen. Niet alleen verandert het energieprofiel van de reactie nagenoeg altijd, maar ook kunnen de extra vrijheidsgraden van de vloeistofmoleculen zorgen voor nieuwe reactiepaden in het mechanisme, die zonder het oplosmiddel niet gevonden worden. Deze effecten zijn allerminst verwaarloosbaar bij de bestudering van chemische reacties die in de praktijk plaatsvinden in waterig milieu. De Car-Parrinello moleculaire dynamicasimulatie methode bleek een bijzonder krachtig hulpmiddel voor het berekenen van fysische eigenschappen van chemicaliën in oplossing en voor het verkrijgen van microscopisch inzicht in de structuur van het oplosmiddel en de dynamica van de solvatatie. De belangrijkste beperkingen van de methode hebben te maken met 1) de nauwkeurigheid van de hedendaagse DFT exchange-correlatie functionalen en met 2) de grote rekenkracht die nodig is voor dit soort simulaties aan deze grote systemen. Desalniettemin bevinden nauwkeurige *first principles* computer simulaties van chemische reacties in waterige oplossing zich niet langer buiten het bereik van de onderzoeker.

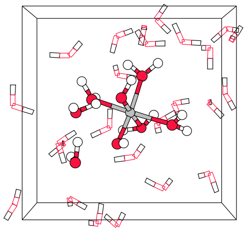

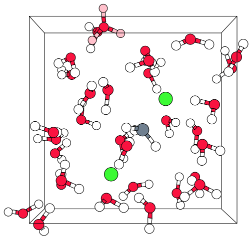

Dankwoord

Als u op deze pagina bent geraakt door alle voorgaande te lezen zult u begrijpen dat ik ze onmogelijk allemaal heb kunnen schrijven zonder de hulp en inspiratie van anderen, die ik hieronder van harte wil bedanken. Bovendien sluit ik hiermee niet alleen dit proefschrift af, maar ook een kleurrijke periode in mijn leven, zodat ik graag van de gelegenheid gebruik maak een aantal vrienden te bedanken voor het helpen kleuren.

In de eerste plaats bedank ik mijn promotor Evert Jan Baerends: ik ben je dankbaar voor de grote mate van vrijheid en vertrouwen die je me schonk en voor hetgeen je me geleerd hebt, met name je helicopter view, het presenteren van m'n resultaten en het waarderen van kleine succesjes als de grote nog even uitblijven. Evert Jan Meijer, mijn begeleider gedurende het eerste jaar, bedank ik ten eerste natuurlijk voor het aannemen van mij destijds (goede keuze, red.) en daarnaast voor dat je me hebt ingewijd en op weg hebt geholpen in de wereld van de Car-Parrinello simulaties. Francesco Buda, I very much enjoyed teaming up with you and discovering and exploring Fenton chemistry together. I thank you gratefully for the numerous discussions we had, and for sharing your priceless experience with CPMD techniques with me. Pieter Vernooys, zonder jou hulp, met programmeren en debuggen van unix scripts and fortran codes en bovenal met het omzeilen van batchqueue limieten op de supercomputers, zou de statestiek van mijn berekeningen niet half zo goed zijn, bedankt. I gratefully want to acknowledge Peter Blöchl the creater of the PAW program for letting me use his ingenious life-work for free. Michiel Gribnau, het idee om de Fenton chemie te bestuderen, als toepassing van overgangsmetaal gekatalyseerde oxidatie chemie in water, kwam van jou, en dat bleek al snel een veelzijdige uitdaging waaraan ik met erg veel plezier gewerkt heb. Ik wil je bedanken voor je enthousiasme en je waardevolle adviezen vanuit de praktijkervaring bij Unilever.

Ik heb erg veel geleerd tijdens de talrijke PPM-CMS sessies door de nauwe samenwerking met verschillende Nederlandse chemische industrieën, ik dank met name de coördinator Rob Meijer (DSM), Erik Kirchner (Akzo-Nobel), Betty Coussens (DSM), Michiel Gribnau (Unilever), Lou-Fé Feiner (Philips) en de dynamica groep van Rob de Groot te weten Gilles de Wijs, Joost Hageman, Peter van Gelderen en Rob zelf (Universiteit van Nijmegen). Bedankt Olivier Visser, door jou praktische tips, waardoor ondermeer het porten van PAW naar Teras in "no time" lukte, ben ik twee jaar eerder klaar. Vincent Osinga met jou heb ik heel veel plezier beleeft op de VU, denk maar aan de InVUtasie kampen, lesgeven in R117, de congressen en zomerscholen in bijvoorbeeld Han-sur-Lesse en Lund maar bovenal de ontelbare 10-minuut rallies Mortal Pongbat. Bedankt voor alles, al ben ik door het laatst genoemde wel twee jaar later klaar.

Misschien zijn niet alle bijdragen aan mijn onderzoek van mijn theoretische chemie

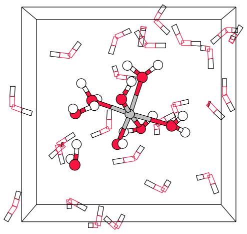

vakgroepgenoten even duidelijk aan te wijzen in dit proefschrift. Desalnietemin bedank ik Eric van Lente voor zijn kritische vragen, niet geremd door enige kennis van MD simulaties, waardoor ik regelmatig weer aan het denken werd gezet. Stan van Gisbergen bedankt voor je fijne ADF basis sets. Ik bedank Jeroen Groeneveld, Pieter Schipper, Vincent Osinga en Arno de Lange (MrB's), Ruud, Marijke, Douwe, Hans, Meindert, Winita en Fetze voor de fantastische skie en snowboard vakanties in Frankrijk. Drew jij gaf het laatste duwtje dat ik nodig had om over te stappen op Apple MacIntosh; wie had dat vier jaar geleden kunnen voorspellen? Oleg, your enthousiasm concerning electron exchange-correlation kernels and the Russian revolutions has been a great inspiration. Theodoor, de levendige koffiepauze overschrijdende maatschappelijke discussies met jou hebben mij wel eens bijna de waarde van wetenschap doen relativeren (N.B. Spreuken 19:20). Manuel Louwerse, bedankt voor het corrigeren van vele typvouten in het manuscript, en heel veel succes toegewenst. Celia, je hebt me als geen ander voorbereid op de valkuilen van het promoveren. Walter Ravenek, dankzij het begeleiden van jouw practica spreek ik nu een aardig woordje C. Matthias, je hebt me, wellicht onbewust, geleerd hoe ik de scheikundige kant van mijn resultaten het best kan presenteren, en dat is heel nuttig gebleken. Roar, bedankt dat je de liefde voor de onderwaterwereld in me hebt aangewakkerd. Pier bedank ik voor solide en oppervlakkige discussies, Myrta voor potentiele en functionele discussies, Wolfgang voor verlichtende discussies, Luuk voor relativerende discussies en Joost voor nauwkeurig gecorreleerde discussies. Ik bedank natuurlijk de secretaressen, Antoinette, Sophie, Roxaan, Nasreen en Laura. En de vele gasten en tijdelijke vakgroep genoten, met name Steve, Jeff, Angela, Paula, Benoit, Jordi, Timo en Markus, bedank ik voor de gezellige tijd.

Promoveren kan niet zonder afwisseling, ontspanning en afleiding. Wat dat betreft, ben ik mijn trouwe huisgenoot en drinkebroeder Hans veel dank verschuldigd. Zonder jou humor en hartverwarmende samenwerking om mijn tegenvallers te verdrinken zou dit boekje het levenslicht nooit gezien hebben. Pier bedank ik wat dit betreft voor de relaxte momenten in cafe Uilenstede en voor dat hij me heeft geintroduceerd in de Amsterdamse jazz scene. Muziek is een ideale vlucht uit de allerdaagse probleempjes gebleken, en ik bedank derhalve de jongens van Jazz or No, Vincent, Maarten, Pier, Marieke, Sebastiaan, Michiel en Paul en de beste band van Enschede: GQ, oftewel Lesly, Marylinn, Mark, Lennard, Messias, Erwin, Rudsel, Frank, Edu en Eddie voor de bijzonder inspirerende muziekale sessies, optredens en alles eromheen. De (voormalige) Enschede gang, Wilco, Anne Corien, Meindert, Allard, Bart en Martine bedank ik voor de vele bijzondere uurtjes waar ik het eigenlijk allemaal voor doe. Mijn ouders en familie ben ik dankbaar voor hun eindeloze vertrouwen in dat wetenschappelijke geneuzel dat mij kennelijk van de straat houdt. Mijn mooiste ontdekking deed ik in de wandelgangen van de VU, zal zelfs de Nobelprijscommissie moeten toegeven. Winita, nu zal eindelijk het grote geld binnen gaan rollen; begin maar vast met uitgeven. Trust me, I am a doctor...

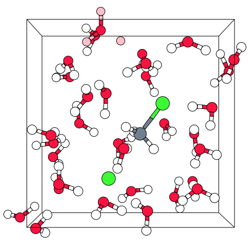

Publications

1. **Methane oxidation by the ferryl ion**
   B. Ensing, F. Buda, and E. J. Baerends.
   submitted for publication.

2. **O_2 evolution in the Fenton reaction**
   F. Buda, B. Ensing, M. C. M. Gribnau, and E. J. Baerends.
   submitted for publication.

3. **Fenton-like chemistry in water: oxidation catalysis by Fe(III) and H_2O_2**
   B. Ensing, F. Buda, and E. J. Baerends.
   submitted for publication.

4. **Reaction path sampling of the reaction between iron(II) and hydrogen peroxide in aqueous solution**
   B. Ensing and E. J. Baerends.
   J. Phys. Chem. A **106**, 7902-7910 (2002).

5. **A Car-Parrinello study of the formation of oxidizing intermediates from Fenton's reagent in aqueous solution**
   B. Ensing, F. Buda, P. E. Blöchl, and E. J. Baerends.
   Phys. Chem. Chem. Phys. **4**, 3619-3627 (2002).

6. **Chemical involvement of solvent water molecules in elementary steps of the Fenton reaction**
   B. Ensing, F. Buda, P. E. Blöchl, and E. J. Baerends.
   Angew. Chem. Int. Edit. **40**, 2893-2895 (2001).

7. **DFT studie of the active intermediate in the Fenton reaction**
   F. Buda, B. Ensing, M. C. M. Gribnau, and E. J. Baerends.
   Chem. Eur. J. **7**, 2775-2783 (2001).

8. **Solvation effects on the S_N2 reaction between $CH_3Cl + Cl^-$ in water**
   B. Ensing, E. J. Meijer, P. E. Blöchl, and E. J. Baerends.
   J. Phys. Chem. A **105**, 3300-3310 (2001).

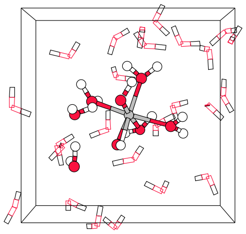

9. **Comparison of the accurate Kohn-Sham solution with the generalized gradient approximations (GGAs) for the S_N2 reaction, $F^- + CH_3F \rightarrow FCH_3 + F^-$: A qualitative rule to predict success or failure of GGAs**
   O. V. Gritsenko, B. Ensing, P. R. T. Schipper, and E. J. Baerends.
   J. Phys. Chem. A **104**, 8558-8565 (2000).

10. **A combined molecular dynamics ab initio study of H_2 adsorption on ideal, relaxed, and temperature-reconstructed MgO(111) surfaces**
    K. Hermansson, M. Baudin, B. Ensing, M. Alfredsson, and M. Wojcik.
    J. Phys. Chem. **109**, 7515-7521 (1998).

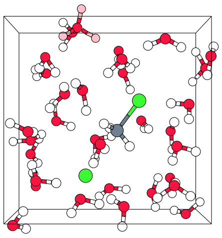

About the author

Bernd Ensing first saw the light of day on February 16, 1972 in Delfzijl (the Netherlands) and grew up in a friendly village named Wagenborgen, which lies somewhere in the flat and green countryside of the Groningen province. In 1990, he completed the havo at the Fivel-college in Delfzijl and a year later he graduated at the atheneum at the same college. He moved to Enschede to study Chemical Technology at the technical university of Twente. Although educated to become an chemical engineer, he choose his mayor in the field of chemical physics at the group of professor Wim Briels, who send him to Sweden for a three-month traineeship at the computational chemistry group of professor Kersti Hermansson, situated at the Uppsala University. Here, he performed his first calculations and completed a study entitled "ab initio and DFT computations of H_2 absorption on reconstructed MgO(111) surfaces obtained from molecular dynamics snapshots", which led to his first scientific publication. In August 1996, he graduated his Master of Science with a study on argon adsorption in the pores of $AlPO_4$-5 zeolites, which he completed partly in Hermansson's group in Uppsala and in the chemical physics group in Enschede. Two months later he moved to Amsterdam and started his Ph.D. study on first principles dynamics simulations of solvent effects on chemical reactions, in the theoretical chemistry group of professor Evert Jan Baerends, of which this thesis is the result. In November 2003, he will move to Philadelphia to start a post-doctoral study in the group of professor Mike Klein at the University of Pennsylvania. In the mean time he hopes to one morning wake up and find himself being able to play as good a saxophone as Charly *Bird* Parker...

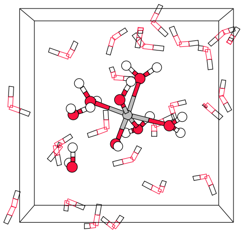

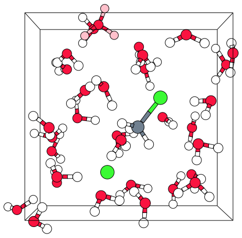

About the simulation movies in this thesis

English version on the next page

Op bijna alle bladzijden van dit proefschrift staat onderaan een plaatje van een kubische doos met moleculen. Wanneer u de pagina's snel door uw vingers laat glijden, vormen de plaatjes een filmpje van een *first principles* moleculaire dynamicasimulatie van een chemische reactie in water. Op de even genummerde pagina's ziet u een voorbeeld van de S_N2 reactie tussen methyl chloride en een chloor ion (welke we bestudeerden in hoofdstuk 3). Op de oneven genummmerde pagina's laten de bewegende beeldjes een reactiepad zien van de eerste stap van de Fenton reactie, die we bespraken in de hoofdstukken 5 en 7.

Even genummerde pagina's: een onrealistische S_N2 reactie. In deze simulatie (zie ook het linker plaatje hieronder) manipuleerde ik het systeem van methyl chloride en een chloor ion in waterige oplossing zodanig dat er een reactie plaats vindt in minder dan een halve picoseconde. Het illustreert een berucht misbruik van de zogenaamde "constraint" methode die in de literatuur soms misleidend "method of slow-growth" wordt genoemd. In dit geval wordt het chloor ion naar het methyl chloride ion getrokken en tegelijkertijd word het ander chloor weggeduwd, zonder rekening te houden met de omringende water moleculen die zich zo snel niet kunnen aanpassen aan de veranderende situatie. Het juiste gebruik van de constraint methode heb ik laten zien in hoofdstuk 3.

Oneven genummerde pagina's: een realistische Fenton reactie. Dit filmpje laat een realistische simulatie zien van een typisch reactiepad van de reactie tussen waterstofperoxide en een ijzer(II) ion, oftewel de Fenton reactie. De vloeistof moleculen zijn nu slechts schematisch weergegeven (zie ook het rechter plaatje hieronder), behalve één water molecule dat chemisch deelneemt in de reactie. De totale duur van de simulatie was 2.68 ps. Het filmpje begint op $t = 1273$ femtoseconde (fs) op pagina 1, alwaar de reactanten nog ruim 3 Å van elkaar gescheiden zijn. Rond bladzijde 97 (110 fs later) breekt de zuurstof-zuurstof binding om het pentawater ijzer(III) hydroxo intermediair te vormen en het $OH^{\cdot}$ radicaal. Het radicaal springt via het oplosmiddel water molecule naar het voorste water ligand waarmee het reageert tot het ijzer(IV) dihydroxo intermediair en een water molecule, ergens in de buurt van bladzijde 157 ($t = 1454$ fs). Het toenemende zuurgehalte van het complex gedurende de reactie blijkt uit de poging tot proton donatie van het linker waterligand aan het oplosmiddel op het eind. Een filmpje van de tweede stap van de Fenton reactie waarbij het ferryl ion wordt gevormd staat gepland voor de tweede druk van dit proefschrift...

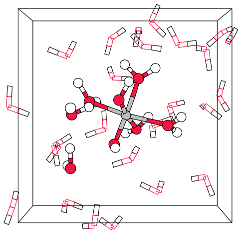

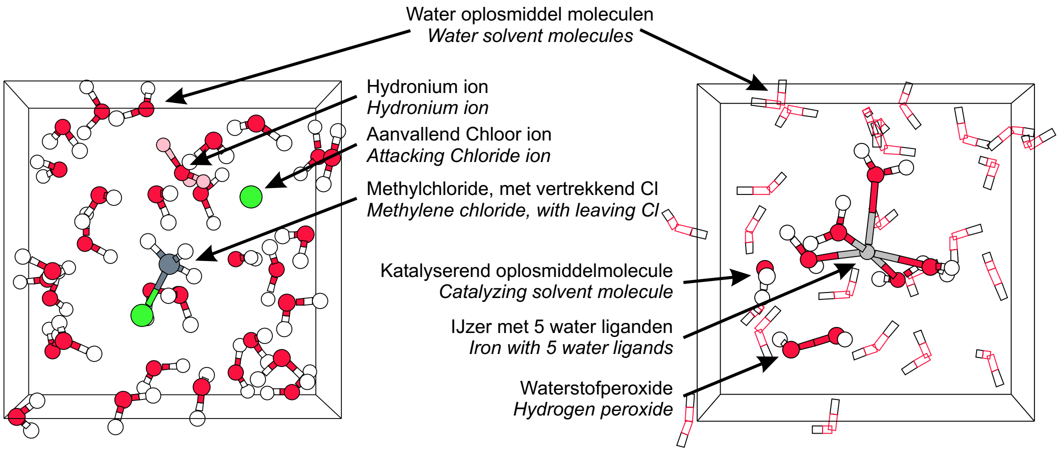

Most pages of this thesis contain in the lower corner a picture of a cubic box filled with molecules. Rapidly flipping the pages will result in a motion picture showing a trajectory of a first principles computer simulations of a chemical reaction in aqueous solution. On the even pages, you can see an illustration of the S_N2 reaction between CH_3Cl and Cl^- (see chapter 3. The odd pages show the first step of the Fenton reaction from a simulation discussed in chapter 7.

On the even pages: an unrealistic S_N2 reaction. In this simulation (see also the left-hand-side picture above) we enforced the reaction between CH_3Cl and Cl^- to occur in less than half a picosecond, by using a constraint that simultaneously pulls the chloride ion towards the methylene chloride carbon and pushes the other chlorine away from carbon. It illustrates nicely a typical abuse of the method of constraint, sometimes misleadingly called "method of slow growth". Close inspection of the movie shows that the solvent molecules hardly change position during the enforced reaction, because the solvent structure has no time to adapt, which leads to an useless unphysical picture. The correct way to apply the method of constraint was applied in chapter 3.

On the odd pages: a realistic Fenton reaction. This movie shows a realistic simulation of a typical reaction path of the reaction between hydrogen peroxide and an iron(II) ion, aka the Fenton reaction. The solvent molecules are now only drawn in draft for clarity (see also the right-hand-side snapshot above), except for one H_2O molecule which is chemically involved in the reaction. The total length of the simulation was 2.68 ps. The movie starts at t=1273 femtosecond (fs) on page 1 with the reactants still separated by 3.0 Å. Around page 97 (110 fs later), the oxygen-oxygen bond breaks, producing the pentaaquairon(III)hydroxo intermediate and an $OH^{\cdot}$ radical. This $OH^{\cdot}$ radical jumps via the solvent water molecule to termination at the water ligand producing the iron(IV)dihydroxo intermediate and a water molecule somewhere close to page 157 ($t = 1454$ fs). The increasing acidity of the complex along the reaction results in attempts to proton donation by the left-hand-side water ligand in the final state. A movie of the second step, which is the barrierless transformation of the dihydroxo intermediate into its oxo isomer, the ferryl ion, is planned for the second edition of this thesis...

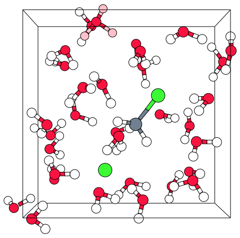

Bibliography

[1] Adams, D., *The Hitchhiker's guide to the galaxy.*

[2] Zwanzig, R., *Acc. Chem. Res.* **1990**, *23*, 148.

[3] Onsager, L., *Phys. Rev.* **1931**, *37*, 405.

[4] Kramers, H. A., *Physica* **1940**, *7*, 284.

[5] Eyring, H., *J. Chem. Phys.* **1935**, *3*, 107.

[6] Grote, R. F., Hynes, J. T., *J. Chem. Phys.* **1980**, *73*, 2715.

[7] Hänggi, P.; Talkner, P.; Borkovec, M., *Rev. Mod. Phys.* **1990**, *62*, 2551.

[8] Briels, W. J., Han-sur-Lesse Summer-school Theoretical Chemistry and Spectroscopy, lecture notes, 1999.

[9] Yamamoto, T., *J. Chem. Phys.* **1960**, *33*, 281.

[10] Chandler, D., *J. Chem. Phys.* **1978**, *68*, 2959.

[11] den Otter, W. K., *Molecular Dynamics Simulation of Barrier Crossings in the Condensed Phase*, PhD thesis, University of Twente, 1998.

[12] Bolhuis, P.; Chandler, D.; Dellago, C., CECAM Tutorial on Transition Path Sampling, lecture notes, 1999.

[13] Patey, G. N., Valleau, J. P., *J. Chem. Phys.* **1975**, *63*, 2334.

[14] Torrie, G. M., Valleau, J. P., *J. Comp. Phys.* **1977**, *23*, 187.

[15] Chandler, D., *An introduction to modern statistical mechanics*, Oxford university press, New York, 1987.

[16] Carter, E. A.; Ciccotti, G.; Hynes, J. T.; Kapral, R., *Chem. Phys. Lett* **1989**, *156*, 472.

[17] den Otter, W. K., Briels, W. J., *J. Chem. Phys.* **1998**, *109*, 4139.

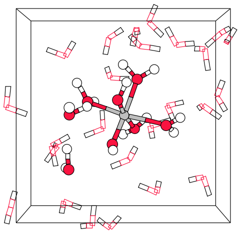

[18] Pastore, G.; Smargiassi, E.; Buda, F., *Phys. Rev. A* **1991**, *44*, 6334.

[19] Blöchl, P. E., Parrinello, M., *Phys. Rev. B* **1991**, *45*, 9413.

[20] Tassone, F.; Mauri, F.; Car, R., *Phys. Rev. B* **1994**, *50*, 10561.

[21] Marx, D., Hutter, J., Ab initio molecular dynamics: theory and implementation, in *Modern Methods and Algorithms of Quantum Chemistry*, edited by Grotendorst, J., p. 301, John von Neumann Institute for Computing, Jülich, NIC Series, 2000.

[22] Remler, D. K., Madden, P. A., *Mol. Phys.* **1990**, *70*, 921.

[23] Galli, G., Parrinello, M., Ab initio molecular dynamics: principles and practical implementation, in *Computer simulation in material science*, edited by Meyer, M., Pontikis, V., p. 283, Kluwer Academic Publishers, 1991.

[24] Blöchl, P. E., *Phys. Rev. B* **1994**, *50*, 17953.

[25] Hamann, D. R.; Schlüter, M.; Chiang, C., *Phys. Rev. Lett.* **1979**, *43*, 1494.

[26] Troellier, N., Martins, J. L., *Phys. Rev. B* **1991**, *43*, 1993.

[27] Bachelet, G. B.; Hamann, D. R.; Schlüter, M., *Phys. Rev. B* **1982**, *26*, 4199.

[28] Vanderbilt, D., *Phys. Rev. B* **1985**, *41*, 7892.

[29] Laasonen, K.; Car, R.; Lee, C.; Vanderbilt, D., *Phys. Rev. B* **1991**, *43*, 6796.

[30] Slater, J. C., *Phys. Rev.* **1937**, *51*, 846.

[31] Marcus, P. M., *Int. J. Quant. Chem.* **1967**, *1S*, 567.

[32] Andersen, O. K., *Phys. Rev. B* **1975**, *12*, 3060.

[33] Petrilli, H. M.; Blöchl, P. E.; Blaha, P.; Schwarz, K., *Phys. Rev. B* **1998**, *57*, 14690.

[34] Blöchl, P. E., *Phys. Rev. B* **2000**, *62*, 6158.

[35] Ceperley, D. M., Alder, B. J., *Phys. Rev. Lett.* **1980**, *45*, 566.

[36] Becke, A. D., *Phys. Rev. A* **1988**, *38*, 3098.

[37] Lee, C.; Yand, W.; Parr, R. G., *Phys. Rev. B* **1988**, *37*, 785.

[38] Perdew, J. P., *Phys. Rev. B* **1986**, *33*, 8822.

[39] Perdew, J. P., *Phys. Rev. B* **1992**, *46*, 6671.

[40] Mok, D. K. W.; Handy, N. C.; Amos, R. D., *Mol. Phys.* **1997**, *92*, 667.

[41] Proynov, E. I.; Sirois, S.; Salahub, D. R., *Int. J. Quant. Chem.* **1997**, *64*, 427.

[42] Ernzerhof, M., Scuseria, G. E., *J. Chem. Phys.* **1999**, *111*, 911.

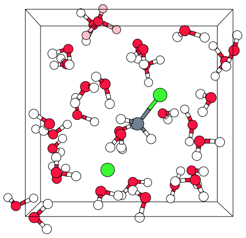

[43] Perdew, J. P., Zunger, A., *Phys. Rev. B* **1981**, *23*, 5048.

[44] van Leeuwen, R., Baerends, E. J., *Phys. Rev. A* **1994**, *49*, 2421.

[45] Baerends, E. J., Gritsenko, O. V., *J. Phys. Chem. A* **1997**, *101*, 5383.

[46] Parr, R. G., Yang, W., *Density-Functional Theory of Atoms and Molecules*, Oxford University: New York, 1989.

[47] Dreizler, R. M., Gross, E. K., *Density-Functional Theory: An approach to the many-body problem*, Springer-Verlag: Berlin, 1990.

[48] Bickelhaupt, F. M., Baerends, E. J., *Rev. Comp. Chem.* **2000**, *15*, 1.

[49] Car, R., Parrinello, M., *Phys. Rev. Lett.* **1985**, *55*, 2471.

[50] Laasonen, K.; Sprik, M.; Parrinello, M., *J. Chem. Phys.* **1993**, *99*, 9080.

[51] Sprik, M.; Hutter, J.; Parrinello, M., *J. Chem. Phys.* **1996**, *105*, 1142.

[52] Tuckerman, M.; Laasonen, K.; Sprik, M.; Parrinello, M., *J. Phys. Chem.* **1995**, *99*, 5749.

[53] Tuckerman, M.; Laasonen, K.; Sprik, M.; Parrinello, M., *J. Chem. Phys.* **1995**, *103*, 150.

[54] Meijer, E. J., Sprik, M., *J. Phys. Chem. A* **1998**, *102*, 2893.

[55] Meijer, E. J., Sprik, M., *J. Am. Chem. Soc.* **1998**, *120*, 6345.

[56] Deng, L.; Branchadell, V.; Ziegler, T., *J. Am. Chem. Soc.* **1994**, *116*, 10645.

[57] Botschwina, P., *Theor. Chem. Acc.* **1998**, *99*, 426.

[58] Glukhovtsev, M. N.; Pross, A.; Radom, L., *J. Am. Chem. Soc.* **1995**, *117*, 2024.

[59] Glukhovtsev, M. N.; Bach, R. D.; Pross, A.; Radom, L., *Chem. Phys. Lett.* **1996**, *260*, 558.

[60] Vetter, R., Zülicke, L., *J. Am. Chem. Soc.* **1990**, *112*, 5136.

[61] Streitwieser, A.; Choy, G. S.; Abu-Hasanayn, F., *J. Am. Chem. Soc.* **1997**, *119*, 5013.

[62] Dougherty, R. C.; Dalton, J.; Roberts, J. D., *Org. Mass. Spectr.* **1973**, *8*, 77.

[63] Barlow, S. E.; van Doren, J. M.; Bierbaum, V. M., *J. Am. Chem. Soc.* **1988**, *110*, 7240.

[64] Larson, J. W., McMahon, T. B., *J. Am. Chem. Soc.* **1985**, *107*, 766.

[65] Chandrasekhar, J.; Smith, S. F.; Jorgensen, W. L., *J. Am. Chem. Soc.* **1985**, *107*, 154.

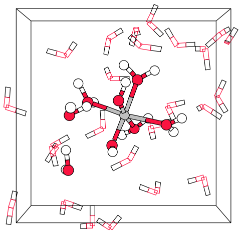

[66] Albery, W. J., Kreevoy, M. M., *Adv. Phys. Org. Chem.* **1978**, *16*, 87.

[67] Becke, A. D., *J. Chem. Phys.* **1992**, *96*, 2155.

[68] Verlet, L., *Phys. Rev.* **1967**, *159*, 98.

[69] Nosé, S. J., *J. Chem. Phys.* **1984**, *81*, 511.

[70] Baerends, E. J.; Ellis, D. E.; Ros, P., *Chem. Phys.* **1973**, *2*, 41.

[71] Frenkel, D., Smit, B., *Understanding molecular simulation*, Academic, San Diego, CA, 1996.

[72] van Gunsteren, W. F., in *Computer simulations of biomolecular systems: theoretical and experimental applications*, edited by van Gunsteren, W. F., Weiner, P. K., volume 1, ESCOM Leiden, The Netherlands, 1989.

[73] Ryckaert, J. P.; Ciccotti, G.; Berendsen, H. J. C., *J. Comp. Chem.* **1977**, *23*, 327.

[74] Neria, E.; Fischer, S.; Karplus, M., *J. Chem. Phys.* **1996**, *105*, 1902.

[75] Margl, P.; Lohrenz, J. C. W.; Ziegler, T.; Blöchl, P. E., *J. Am. Chem. Soc.* **1996**, *118*, 4434.

[76] Sprik, M., Ciccotti, G., *J. Chem. Phys.* **1998**, *109*, 7737.

[77] Blöchl, P. E., *J. Chem. Phys.* **1995**, *103*, 7422.

[78] Atkins, P. W., *Physical Chemistry*, Oxford university press, New York, 1990.

[79] Curtiss, L. A.; Raghavachari, K.; Redfern, P.; Pople, J. A., *J. Chem. Phys.* **1997**, *106*, 1063.

[80] Pople, J. A.; Head-Gordon, M.; Raghavachari, D. J. F. K.; Curtiss, L. A., *J. Chem. Phys.* **1989**, *90*, 5622.

[81] Curtiss, L. A.; Jones, C.; Trucks, G. W.; Raghavachari, K.; Pople, J. A., *J. Chem. Phys.* **1990**, *93*, 2537.

[82] in *Tables of interatomic distances and configuration in molecules and ions*, edited by Sutton, L., The Chemical Society, London, 1965.

[83] Callomon, J. H.; Hirota, E.; Kuchitsu, K.; Lafferty, W. J.; Maki, A. G.; Pote, C. S., in *Structure data of free polyatomic molecules, Landolt–Börnstein, New Series, Group II*, edited by Hellwege, K. H., Hellwege, A. M., volume 7, Springer, Berlin, 1976.

[84] Huber, K. P., Herzberg, G., in *Molecular spectra and molecular structure IV: Constants of diatomic molecules*, Van Nostrand Reinhold, New York, 1979.

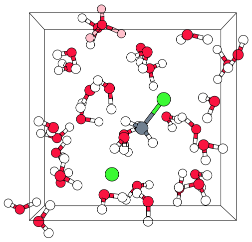

[85] Harmony, M. D.; Laurie, V. W.; Kuczkowski, R. L.; Schwendeman, R. H.; Ramsay, D. A.; Lovas, F. J.; Lafferty, W. J.; Maki, A. G., *J. Phys. Chem. Ref. Data* **1979**, *8*, 619.

[86] Kim, K., Jordan, K. D., *J. Phys. Chem.* **1994**, *98*, 10089.

[87] Tuma, C.; Boese, A. D.; Handy, N. C., *Phys. Chem. Chem. Phys.* **1999**, *1*, 3939.

[88] Klopper, W., Lüthi, H. P., *Mol. Phys.* **1999**, *96*, 559.

[89] Hobza, P.; Bludski, O.; Suhai, S., *Phys. Chem. Chem. Phys.* **1999**, *1*, 3073.

[90] Xantheas, S. S., Dunning, T. H., *J. Chem. Phys.* **1993**, *99*, 8774.

[91] Schütz, M.; Brdarski, S.; Widmark, P. O.; Lindh, R.; Karlström, G., *J. Chem. Phys.* **1997**, *107*, 4597.

[92] Halkier, A.; Koch, H.; rgensen, P. J.; Christiansen, O.; Nielsen, I. M. B.; Helgaker, T., *Theoret. Chim. Acta (Berl)* **1997**, *97*, 150.

[93] Bentwood, R. M.; Barnes, A. J.; Thomas, W. J. O., *J. Mol. Spectrosc.* **1980**, *84*, 391.

[94] Odutola, J. A., Dyke, T. R., *J. Chem. Phys.* **1980**, *72*, 5062.

[95] Curtiss, L. A.; Frurip, D. L.; Blander, M., *J. Chem. Phys.* **1979**, *71*, 2703.

[96] Reimers, J. J.; Watts, R. O.; Klein, M. L., *Chem. Phys.* **1982**, *64*, 9.

[97] van Duijneveldt-van der Rijdt, J. G. C. M., van Duijneveldt, F. B., *J. Chem. Phys.* **1992**, *97*, 5019.

[98] *MP2 limit estimates: Feyereisen* et al*:*−4.9±0.1 *[231]; Schütz* et al*:*−4.94±0.02 *[91]; Xantheas:*−4.9 *[232]; Hobza* et al*:*−5.029 *[89]; Halkier* et al*:*−4.94±0.1 *[92]; Klopper* et al*:*−4.99 .

[99] Perdew, J. P., Wang, Y., *Phys. Rev. B* **1986**, *33*, 8800.

[100] Combariza, J. E., Kestner, N. R., *J. Phys. Chem.* **1995**, *99*, 2717.

[101] Dunbar, R. C.; McMahon, T. B.; Thölmann, D.; Tonner, D. S.; Salahub, D. R.; Wei, D., *J. Am. Chem. Soc.* **1995**, *117*, 12819.

[102] Xantheas, S. S., *J. Phys. Chem.* **1996**, *100*, 9703.

[103] Hiraoka, K.; Mizuse, S.; Yamabe, S., *J. Phys. Chem.* **1988**, *92*, 3943.

[104] Sieck, L. W., *J. Phys. Chem.* **1985**, *89*, 5552.

[105] Yamabe, S.; Furumiya, Y.; K.Hiraoka; Morise, K., *Chem. Phys. Lett.* **1986**, *131*, 261.

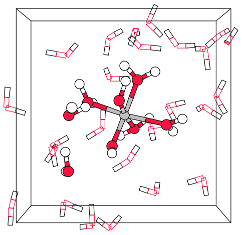

[106] Tromp, R. H.; P.Posterino; Neilson, G. W.; Ricci, M. A.; Soper, A. K., *J. Chem. Phys.* **1994**, *101*, 6210.

[107] in *CRC Handbook of Chemistry and Physics*, edited by Lide, D. R., Chemical Rubber, Boca Raton, Fl, 1994.

[108] Jorgensen, W. L.; Chandrasekhar, J.; Madura, J. D.; Impey, R. W.; Klein, M. L., *J. Chem. Phys.* **1983**, *79*, 926.

[109] van der Stoel, D.; van Maaren, P. J.; Berendsen, H. J. C., *J. Chem. Phys.* **1998**, *108*, 10220.

[110] Watanabe, K., Klein, M. L., *Chem. Phys.* **1989**, *131*, 157.

[111] Liu, Y., Ichiye, T., *J. Phys. Chem.* **1996**, *100*, 2723.

[112] Chandra, A., Ichiye, T., *J. Chem. Phys.* **1999**, *111*, 2701.

[113] Narten, A. H.; Danford, M. D.; Levy, H. A., *Discussions Faraday Soc.* **1967**, *43*, 97.

[114] Narten, A. H., Levy, H. A., *J. Chem. Phys.* **1971**, *55*, 2263.

[115] Krynicki, K.; Green, C. D.; Sawyer, D. W., *Faraday Discuss. Chem. Soc.* **1978**, *66*, 199.

[116] Sprik, M.; Klein, M. L.; Watanabe, K., *J. Phys. Chem.* **1990**, *94*, 6483.

[117] Laasonen, K., Klein, M. L., *J. Am. Chem. Soc.* **1994**, *116*, 11620.

[118] Laasonen, K., Klein, M. L., *J. Phys. Chem. A* **1997**, *101*, 98.

[119] Chandrasekhar, J.; Spellmeyer, D. C.; Jorgensen, W. L., *J. Am. Chem. Soc.* **1984**, *106*, 903.

[120] Newsome, J. R.; Neilson, G. W.; Enderby, J. E., *J. Phys. C: Solid State Phys.* **1980**, *923*, 13.

[121] Enderby, J. E., Neilson, G. W., *Rep. Progr. Phys.* **1981**, *44*, 38.

[122] Enderby, J. E.; Cummings, S.; Herdman, G. J.; Neilson, G. W.; Salmon, P. S.; Skipper, N., *J. Phys. Chem.* **1987**, *91*, 5851.

[123] *This value includes the zero-point energy, which we estimated within DFT-BP:* $\Delta E_{\rm ZPE}^{\rm RC} < |-0.1|$ *kcal/mol* .

[124] Gritsenko, O. V.; Ensing, B.; Schipper, P. R. T.; Baerends, E. J., *J. Phys. Chem. A* **2000**, *104*, 8558.

[125] Geissler, P. L.; Dellago, C.; Chandler, D., *J. Phys. Chem. B* **1999**, *103*, 3706.

[126] Sprik, M., *Faraday Discuss.* **1998**, *110*, 437.

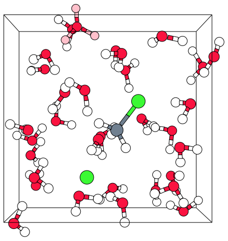

[127] Sprik, M., *Chem. Phys.* **2000**, *258*, 139.

[128] Fenton, H. J. H., *Chem. News* **1876**, *190.*

[129] Imlay, J. A., Linn, S., *Science* **1988**, *240*, 1302.

[130] Lindahl, T., *Nature* **1993**, *362*, 709.

[131] Chen, K., Que Jr., L., *J. Am. Chem. Soc.* **2001**, *123*, 6327.

[132] Costas, M.; Chen, K.; L. Que Jr., *Coord. Chem. Rev.* **2000**, *200*, 517.

[133] Catalytic decomposition of hydrogen peroxide in bleaching; a radical approach to a complex mechanism, Technical report, Akzo Nobel, 2000.

[134] Nagano, T.; Hirano, T.; Hirobe, M., *J. Biol. Chem.* **1989**, *264*, 9243.

[135] Balch, A. L., *Inorg. Chim. Acta* **1992**, *198*, 297.

[136] de Laat, J.; Gallard, H.; Ancelin, S.; Legube, B., *Chemosphere* **1999**, *39*, 2693.

[137] de Laat, J., Gallard, H., *Environ. Sci. technol.* **1999**, *33*, 2726.

[138] Gallard, H., de Laat, J., *Wat. Res.* **2000**, *34*, 3107.

[139] Gallard, H., de Laat, J., *Chemosphere* **2001**, *42*, 405.

[140] M. C. M. Gribnau, Unilever, V., *private communication* **1998**, .

[141] Gimarc, B. M., *J. Am. Chem. Soc.* **1970**, *92*, 266.

[142] Solomons, T. W. G., *Organic Chemistry*, Wiley, New York, 1992, Table 7.1.

[143] Baes, C. J., Mesner, R. E., in *The Hydrolysis of cations*, edited by Krieger., Malabar, India, 1986.

[144] Ensing, B.; Meijer, E. J.; Blöchl, P. E.; Baerends, E. J., *J. Phys. Chem. A* **2001**, *105*, 3300.

[145] Buda, F.; Ensing, B.; Gribnau, M. C. M.; Baerends, E. J., *Chem. Eur. J.* **2001**, *7*, 2775.

[146] Ensing, B.; Buda, F.; Blöchl, P. E.; Baerends, E. J., *Phys. Chem. Chem. Phys.* **2002**, *4*, 3619.

[147] Guùrdia, E., Padró, J. A., *Chem. Phys.* **1990**, *144*, 353.

[148] Herdman, G. J., Neilson, G. W., *J. Phys. :Condens Matter* **1991**, *4*, 649.

[149] Brunschwig, B. S.; Creutz, C.; Macartney, D. H.; Sham, T. K.; Sutin, N., *Faraday Discuss. Chem. Soc.* **1982**, *74*, 113.

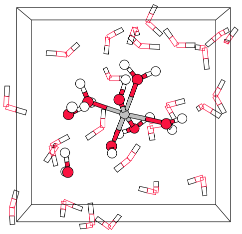

[150] Ohtaki, H., Radnai, T., *Chem. Rev.* **1993**, *93*, 1157.

[151] Pasquarello, A.; Petri, I.; Salmon, P. S.; Parisel, O.; Car, R.; Toth, E.; Powell, D. H.; Fischer, H. E.; Helm, L.; Merbach, A. E., *Science* **2001**, *291*, 856.

[152] Benfatto, M.; D'Angelo, P.; Della Longa, S.; Pavel, N. V., *Phys. Rev. B* **2002**, *65*, 174205.

[153] Li, J.; Fisher, C. L.; Chen, J. L.; Bashford, D.; Noodleman, L., *Inorg. Chem.* **1996**, *35*, 4694.

[154] Jr., C. M. F., *Chem. Rev.* **1984**, *84*, 31.

[155] Fenton, H. J. H., *J. Chem. Soc.* **1894**, *65*, 899.

[156] Haber, F., Weiss, J., *Proc. R. Soc. London* **1934**, *147*, 332.

[157] Bray, W. C., Gorin, M. H., *J. Am. Chem. Soc.* **1932**, *54*, 2124.

[158] Roelfes, G.; Lubben, M.; Hage, R.; Que Jr., L.; Feringa, B. L., *Chem. Eur. J.* **2000**, *6*, 2152.

[159] Blomberg, M. R. A.; Siegbahn, P. E. M.; Babcock, G. T.; Wikström, M., *J. Am. Chem. Soc.* **2000**, *122*, 12848.

[160] Ogliaro, F.; Harris, N.; Cohen, S.; Filatov, M.; de Visser, S. P.; Shaik, S., *J. Am. Chem. Soc.* **2000**, *122*, 8977.

[161] Harris, D., Loew, G. H., *J. Am. Chem. Soc.* **1998**, *120*, 8941.

[162] Yoshizawa, K.; Kagawa, Y.; Shiota, Y., *J. Phys. Chem. B* **2000**, *104*, 12365.

[163] Siegbahn, P. E. M., Crabtree, R. H., *J. Am. Chem. Soc.* **1997**, *119*, 3103.

[164] Basch, H.; Mogi, K.; Musaev, D. G.; Morokuma, K., *J. Am. Chem. Soc.* **1999**, *121*, 7249.

[165] Tung, H.; Kang, C.; Sawyer, D. W., *J. Am. Chem. Soc.* **1991**, *114*, 3445.

[166] Hage, J. P.; Llobet, A.; Sawyer, D. W., *Bioorg. Med. Chem.* **1995**, *3*, 1383.

[167] Kremer, M. L., *Phys. Chem. Chem. Phys.* **1999**, *1*, 3595.

[168] Filatov, M., Shaik, S., *J. Phys. Chem. A* **1998**, *102*, 3835.

[169] Bärsch, S.; Schröder, D.; Schwarz, H., *Helv. Chim. Acta* **2000**, *83*, 827.

[170] Yoshizawa, K.; Shiota, Y.; Yamabe, T., *Organometallics* **1998**, *17*, 2825.

[171] Ensing, B.; Buda, F.; Blöchl, P. E.; Baerends, E. J., *Angew. Chem. Int. Edit.* **2001**, *40*, 2893.

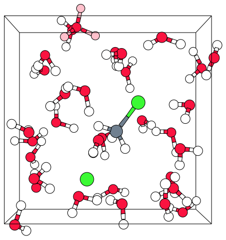

[172] Marx, D.; Sprik, M.; Parrinello, M., *Chem. Phys. Lett.* **1997**, *273*, 360.

[173] Kalman, E.; Radnal, T.; Palinkas, G.; Hajdu, F.; Vertes, A., *Electrochim. Acta* **1988**, *33*, 1223.

[174] Powel, D. H.; Neilson, G. W.; Enderby, J. E., *J. Phys. :Condens Matter* **1993**, *5*, 5723.

[175] Chong, D. P., *private communication: high-quality even-tempered all-electron STO basis set* .

[176] Tachiev, G.; Roth, J. A.; Bowers, A. R., *Int. J. Chem. Kin.* **1999**, *32*, 24.

[177] Bernadou, J., Meunier, B., *Chem. Comm.* **1998**, , 2167.

[178] *The observation of the spontaneous expulsion of a water ligand by the tetraaqua dihydroxo iron(IV)oxo complex in a short AIMD simulation is unexpected, because water ligands of octahedral surrounded iron complexes typically have residence times in the order of* 10^{-7} *sec. and more. Why we observe it here needs further investigation.* .

[179] Rahhal, S., Richter, H. W., *J. Am. Chem. Soc.* **1988**, *110*, 3126.

[180] Rush, J. D., Koppenol, W. H., *J. Am. Chem. Soc.* **1988**, *110*, 4957.

[181] Barb, W. G.; Baxendale, J. H.; George, P.; Hargrave, K. R., *Trans. Faraday. Soc.* **1951**, *47*, 591.

[182] Walling, C., Weil, T., *Int. J. Chem. Kin.* **1974**, *6*, 507.

[183] Kremer, M. L., Stein, G., *Trans. Faraday. Soc.* **1959**, *95*, 595.

[184] Geissler, P. L.; Dellago, C.; Chandler, D.; Hutter, J.; Parrinello, M., *Sci.* **2001**, *2121*, 291.

[185] Siegbahn, P. E. M., *J. Biol. Inorg. Chem.* **2001**, *6*, 27.

[186] Basch, H.; Mogi, K.; Musaev, D. G.; Morokuma, K., *J. Phys. Chem. A* **2001**, *105*, 3615.

[187] Torrent, M.; Musaev, D. G.; Morokuma, K., *J. Phys. Chem. B* **2001**, *105*, 4453.

[188] Dunietz, B. D.; Beachy, M. D.; Cao, Y.; Whittington, D. A.; Lippard, S. J.; Friesner, R. A., *J. Am. Chem. Soc.* **2000**, *122*, 2828.

[189] Siegbahn, P. E. M., Blomberg, M. R. A., *Chem. Rev.* **2000**, *100*, 421.

[190] Ogliaro, F.; Filatov, M.; Shaik, S., *Eur. J. Inorg. Chem.* **2000**, , 2455.

[191] Yoshizawa, K.; Shiota, Y.; Yamabe, T., *J. Am. Chem. Soc.* **1998**, *120*, 564.

[192] Yoshizawa, K.; Shiota, Y.; Yamabe, T., *J. Chem. Phys.* **1999**, *111*, 538.

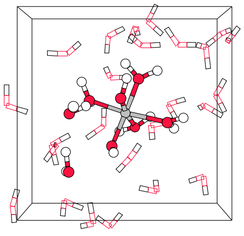

[193] Yoshizawa, K.; Shiota, Y.; Kagawa, Y.; Yamabe, T., *J. Phys. Chem. A* **2000**, *104*, 2552.

[194] Schröder, D.; Schwarz, H.; Shaik, S., *Struct. Bond.* **2000**, *97*, 92.

[195] Shaik, S.; Filatov, M.; Schröder, D.; Schwarz, H., *Chem. Eur. J.* **1998**, *4*, 193.

[196] Halperin, J., Taube, H., *J. Am. Chem. Soc.* **1952**, *74*, 380.

[197] Ensing, B., Baerends, E. J., *J. Phys. Chem. A* **2002**, *106*, 7902.

[198] Ensing, B.; Buda, F.; Baerends, E. J., in preparation.

[199] Girerd, J. J.; Banse, F.; Simaan, A. J., *Struct. Bond.* **2000**, *97*, 145.

[200] Ho, R. Y. N.; Roelfes, G.; Hermant, R.; Feringa, B. L.; Que Jr., L., *J. Am. Chem. Soc.* **1999**, *121*, 264.

[201] Ho, R. Y. N.; Roelfes, G.; Hermant, R.; Hage, R.; Feringa, B. L.; Que Jr., L., *Chem. Comm.* **1999**, , 2161.

[202] Simaan, A. J.; Döpner, S.; Banse, F.; Bourcier, S.; ; Bouchoux, G.; Boussac, A.; Hildebrandt, G.; Girerd, J. J., *Eur. J. Inorg. Chem.* **2000**, , 1627.

[203] Neese, F., Solomon, E. I., *J. Am. Chem. Soc.* **1998**, , 12829.

[204] Ahmad, S.; McCallum, J. D.; Shiemke, A. K.; Appelman, E. H.; Loehr, T. M.; Sanders-Loehr, J., *Inorg. Chem.* **1988**, *27*, 2230.

[205] Shiemke, A. K.; Loehr, T. M.; Sanders-Loehr, J., *J. Am. Chem. Soc.* **1984**, *106*, 4951.

[206] Nienhuys, H. K.; van Santen, R. A.; Bakker, H., *J. Chem. Phys.* **2000**, *112*, 8487.

[207] Trout, B. L., Parrinello, M., *Chem. Phys. Lett.* **1998**, *288*, 343.

[208] Mohr, M.; Marx, D.; Parrinello, M.; Zipse, H., *Chem. Eur. J.* **2000**, *6*, 4009.

[209] Aagaard, O. M.; Meier, R. J.; Buda, F., *J. Am. Chem. Soc.* **1998**, *120*, 7174.

[210] Mann, D. J., Hase, W. L., *Phys. Chem. Chem. Phys.* **2001**, *3*, 4376.

[211] van Speybroeck, V., *Theoretische studie van chemische reacties met statische en dynamische ab initio methoden*, Universiteit Gent, Belgium, 2001, Thesis, Chapter 8.

[212] Dellago, C.; Bolhuis, P. G.; Csajka, F. S.; Chandler, D., *J. Chem. Phys.* **1998**, *108*, 1964.

[213] Bolhuis, P. G.; Dellago, C.; Chandler, D., *J. Chem. Phys.* **1998**, *108*, 9236.

[214] Dellago, C.; Bolhuis, P. G.; Chandler, D., *J. Chem. Phys.* **1999**, *110*, 6617.

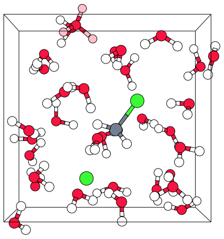

[215] Swift, T. J., Connick, R. E., *J. Chem. Phys.* **1962**, *37*, 307.

[216] The average H-bond length in liquid water was earlier estimated to be 1.73 Å from the radial distribution functions obtained with AIMD simulations in ref. 144.

[217] Schröder, D., Schwarz, H., *Angew. Chem. Int. Edit.* **1990**, *29*, 1433.

[218] Schröder, D.; Schwarz, H.; Clemmer, D. E.; Chen, Y.; Armentrout, P. B.; Baranov, V. I.; Bohme, D. K., *Int. J. Mass Spectrom.* **1997**, *161*, 175.

[219] Ryan, M. F.; Fiedler, A.; Schröder, D.; Schwarz, H., *J. Am. Chem. Soc.* **1995**, *117*, 2033.

[220] Fiedler, A.; Schröder, D.; Shaik, S.; Schwarz, H., *J. Am. Chem. Soc.* **1994**, *116*, 10734.

[221] Feig, A. L., Lippard, S. J., *Chem. Rev.* **1994**, *94*, 759.

[222] Waller, B. J., Lipscomb, J. D., *Chem. Rev.* **1996**, *96*, 2625.

[223] Solomon, E. I.; Brunold, T. C.; Davis, M. I.; Kemsley, J. N.; Lee, S.-K.; Lehnert, N.; Neese, F.; Skulan, A. J.; Yang, Y.-S.; Zhou, J., *Chem. Rev.* **2000**, *100*, 235.

[224] de Montellano, P. R. O., *Cytochrome P450: structure, mechanism, and biochemistry*, Plenum, New York, 1995.

[225] Sono, M.; Roach, M. P.; Coulter, E. D.; Dawson, J. H., *Chem. Rev.* **1996**, *96*, 2841.

[226] Nesheim, J. C., Lipscomb, J. D., *Biochemistry* **1996**, *35*, 10240.

[227] Lipscomb, J. D., Que Jr., L., *J. Biol. Inorg. Chem.* **1998**, *3*, 331.

[228] Brazeau, B. J.; Waller, B. J.; Lipscomb, J. D., *J. Am. Chem. Soc.* **2001**, *123*, 10421.

[229] Toy, P. H.; Newcomb, M.; Hollenberg, P. F., *J. Am. Chem. Soc.* **1998**, *120*, 7719.

[230] Newcomb, M.; Shen, R.; Choi, S. Y.; Toy, P. H.; Hollenberg, P. F.; Vaz, A. D. N.; Coon, M. J., *J. Am. Chem. Soc.* **2000**, *122*, 2677.

[231] Feyereisen, M. W.; Feller, D.; Dixon, D., *J. Phys. Chem.* **1996**, *100*, 2993.

[232] Xantheas, S. S., *J. Chem. Phys.* **1996**, *104*, 8821.